Modélisation numérique du contrôle climatique sur l'érosion des versants. Développement d'un nouveau modèle et application au dernier cycle glaciaire-interglaciaire dans le Nord-Ouest de l'Europe

Benoît Bovy

Université de Liège - Université de Grenoble

Numerical modelling of the climate control on hillslope erosion

Model development and application to the Last Glacial-Interglacial Cycle in NW Europe

Thèse réalisée par
Benoît Bovy
sous la direction de
Alain Demoulin (Université de Liège, UGPQ)
et
Jean Braun (Université de Grenoble, ISTerre)
pour l'obtention du titre de
Docteur en sciences de l'Université de Liège
et
Docteur de l'Université de Grenoble
(spécialité : Terre, Univers, Environnement)

Jury composé de :
M. Niels Hovius (Lecturer, University of Cambridge, Rapporteur),
M. Arjun Heimsath (Associate Professor, Arizona State University, Rapporteur),
M. Louis François (Chargé de cours, Université de Liège, Président),
M. Stéphane Bonnet (Maître de Conférences, Université de Toulouse 3, Examinateur),
M. Yves Cornet (Chargé de cours, Université de Liège, Examinateur),
M. Jean Braun (Professeur, Université de Grenoble, Co-directeur de thèse),
M. Alain Demoulin (Maître de recherches FNRS, Université de Liège, Co-directeur de thèse)

Résumé

Modélisation numérique du contrôle climatique sur l'érosion des versants. Développement d'un nouveau modèle et application au dernier cycle glaciaire-interglaciaire dans le Nord-Ouest de l'Europe.

L'évolution des versants est le résultat de l'action combinée des processus d'altération et de transport sédimentaire. Même si il est généralement admis que l'efficacité de ces processus varie en fonction du climat, la quantification de l'influence climatique sur l'érosion des versants reste encore peu développée aujourd'hui. S'inscrivant dans cette problématique, notre étude est consacrée au développement d'un nouveau modèle numérique d'érosion des versants, ayant pour objectif de mieux représenter, à différentes échelles de temps, les multiples aspects du contrôle climatique sur les processus de transport de sol. Ce modèle numérique permet de simuler l'évolution de l'épaisseur de sol et du relief à l'échelle d'un versant; il repose sur une paramétrisation simple de la production de sol couplée à une paramétrisation multi-processus du transport de sol, qui comprend plusieurs variables en étroite relation avec le climat (débit de ruissellement, épaisseur de couche active). Le calcul de ces variables est réalisé sur base de séries temporelles de précipitation et de température avec l'aide d'un modèle de transfert de chaleur et d'un modèle de bilan hydrologique. Le comportement du modèle a été étudié au travers de quelques exemples génériques et d'analyses de sensibilité. Les résultats obtenus montrent des différences significatives dans la façon dont se comporte chaque processus de transport sous conditions climatiques variables, et également dans la manière dont chaque processus affecte l'érosion globale des versants. Ces résultats mettent ainsi en lumière l'importance de la paramétrisation multi-processus du transport de sol dans la modélisation de la réponse des versants aux changements climatiques. Nous avons également développé une méthode associant le modèle d'érosion de versant à un algorithme d'inversion (Neighbourhood Algorithm). Cette méthode a permis de caractériser de manière quantitative l'évolution des versants ardennais (NE Belgique) lors du dernier cycle glaciaire-interglaciaire, sur base d'un scénario climatique simple et de nombreuses données topographiques et d'épaisseurs de sol. Les résultats de l'inversion produisent des prédictions en accord avec certaines observations sur la morphologie des versants ardennais ainsi qu'avec des taux d'érosion estimés indépendamment sur base de concentrations en isotopes cosmogéniques, même si on montre que la distribution actuelle des épaisseurs de sol ne renferme pas assez d'information pour déterminer entièrement les taux de production et de transport de sol lors des périodes froides et tempérées du dernier cycle climatique. Les résultats de l'inversion suggèrent des taux de transport de sol bien plus élevés lors de la période froide que lors de la période tempérée, produisant une succession de systèmes limités par la production de sol d'une part (période froide), et par le transport de sol d'autre part (période tempérée). Un pic de transport de sol est prédit lors des transitions entre ces périodes. Les résultats laissent également suggérer qu'un équilibre dynamique en terme d'épaisseur de sol a été récemment atteint dans les parties convexes des versants, alors que des sols peu épais observés dans les parties concaves pourraient correspondre à des traces de la distribution des épaisseurs de sol qui prévalait lors de la dernière glaciation.

Abstract

Hillslope evolution results from the combined action of weathering and sediment transport processes, which are thought to be both influenced by climate. Yet, the strength and nature of the connection between climate and hillslope erosion remain poorly understood at a quantitative level. In this study, we present a new numerical model of soil production and transport, which aims to better represent, at different time scales, the climate control on soil transport. The numerical model operates at the scale of a single hill and predicts the rates of soil thickness and elevation change, by using a simple parametrization of soil production and a multi-process parametrization of soil transport which includes climate-dependent variables (overland flow discharge and active-layer depth). Simple ground heat transfer and water balance models are used for calculating these variables from time-series of precipitation and temperature. The behaviour of the model has been studied through a few simulation examples and sensitivity analysis. The results highlight the importance of considering multi-process parameterization of soil transport when modelling the response of the hillslope system to climate variations, as these results display significant differences on how each transport process behaves under various climatic conditions and on how each process affect the evolution of the system. Our numerical model has also been combined with an inversion scheme (Neighbourhood Algorithm) to extract quantitative information on the evolution of hillslopes in the Ardenne (Belgium, NW Europe) during the Last Glacial-Interglacial Cycle, using a simple climatic scenario and a unique set of topographic and soil thickness data. Model predictions based on inversion results are consistent with independent observations on hillslope morphology and cosmogenic nuclide-derived erosion rates, although the inversion results show that soil production and transport rates under both the cold and warm phases of the last climatic cycle cannot be fully constrained by the present-day soil thickness distribution. The inversion results suggest that soil transport is by far more efficient during the cold climatic phase than during the warm phase, resulting in the succession of weathering-limited (cold phase) and transport-limited (warm phase) systems. Maximum soil transport rates are predicted during the transitions between the cold-warm phases. The results also suggest that a soil thickness dynamic equilibrium has been recently reached on convex regions of the hillslopes, while shallow soils found in convergent areas may be the relics of the soil thickness distribution that formed during the cold phase.

Contents

Introduction

In hilly and mountainous regions, long-term downslope movement of soil on hillslopes can play a crucial role governing the rate at which landscape evolves through time. Indeed, hillslopes represent the most important part (over 90 %) of landscapes that are not currently glaciated, the remainder part of these landscapes consisting of river channels and their floodplains (Kirkby, 2008). Although river incision is often considered to mainly drive landscape response to tectonic or climatic change (Whipple and Tucker, 1999; Ouimet et al., 2009), hillslope erosion processes produce and deliver sediments to channels, which are known to influence river incision rates either as tools for erosion or as a cover protecting the underlying bedrock from erosion (Gilbert, 1877; Turowski and Rickenmann, 2009). Considering weathering and hillslope transport processes is therefore vital to understand how landscape evolves in response to climatic variations.

Indeed, it is well accepted that climate does directly influence the rate and style of hillslope evolution (Bull, 2001), but in light of contrasting evidence for both strong linkages (e.g., Kirkby and Cox, 1995; Tucker and Slingerland, 1997; Miller et al., 2001; Hales and Roering, 2005) and poor correlations (e.g., Riebe et al., 2001) between weathering, soil transport, and climate properties, the strength and nature of the connection between climate and hillslope erosion remain poorly understood at a quantitative level (Tucker et al., 2011). Climate control on hillslope erosion has often been partially and indirectly studied—at different temporal scales—through sediment delivery at larger spatial scales, including catchments (e.g., Hovius, 1998; Bogaart et al., 2003b; Trauth and Bookhagen, 2003; Restrepo et al., 2006), sedimentary basins (e.g., Leeder et al., 1998; Van der Zwan, 2002; Castelltort and Van Den Driessche, 2003), mountain belts (e.g. Willett, 2010) and even the continental or global scale (e.g., Donnelly, 1982; Zhang et al., 2001; Molnar, 2004; Willenbring and von Blanckenburg, 2010). However, little attention has been paid to the quantitative effects of climate variations on long-term hillslope dynamics. Yet, the mechanisms of hillslope erosion have been intensively studied so far, based either on field measurements or theoretical modelling approaches, even though most researchers have focused their work on specific environments characterized by the predominance of well-known processes, e.g., cold regions and periglacial processes (e.g., Matsuoka, 2001; Anderson, 2002), temperate regions and biogenic activity (e.g., Dietrich et al., 1995; Heimsath et al., 1997) or semiarid to arid regions (e.g. Yair, 1990; Abrahams et al., 1994; Poesen et al., 1998)

A major difficulty in quantifying the climatic influence on long-term erosion rates is that these rates are not directly measurable. Recently, methods have been developed to infer long-term

erosion rates using concentrations of cosmogenic radionuclides (see reviews in, e.g., Lal, 1991; Nishiizumi et al., 1993; Cerling and Craig, 1994). In active mountain belts, long-term denudation rates can also be inferred from low-temperature thermochronology data (e.g., Braun, 2002; Braun et al., 2006; Valla et al., 2010a). Both methods have been widely applied and provide, with topography, useful information to constrain surface processes models (SPMs). By performing a spatial and temporal integration of the data, these models permit, in turn, to test in a quantitative manner the plausibility of hypotheses suggested by the data. A great number of numerical SPMs have been developed during the last two decades (see reviews in, e.g., Willgoose, 2005; Codilean et al., 2006; Tucker and Hancock, 2010), in which both hillslope and channel processes are involved. However, these SPMs are designed for relatively large spatial scales, from catchments to orogens, and thus mainly put emphasis on channel processes, the link between these processes and climate being currently well-represented (e.g., Tucker and Slingerland, 1997; Tucker et al., 2001b; Bogaart et al., 2003a; Lague et al., 2005). By contrast, the representation of hillslope erosion in SPMs is still relatively simple; it generally consists of a diffusion equation, which is based on the old principle that sediment transport is a linear function of local slope (Davis, 1892; Gilbert, 1909). Many alternative, more advanced parameterizations of soil transport on hillslopes have been recently proposed (e.g., Roering et al., 1999; Prosser and Rustomji, 2000; Braun et al., 2001), but only a few of these parameterizations involve explicit link between transport processes and climate (e.g., Kirkby, 1994; Kirkby and Cox, 1995; Tucker and Bras, 2000; Anderson, 2002).

Research goals

Within the framework of surface processes modelling, the aim of this study is to enhance our representation of hillslope erosion, through the development of a new surface processes numerical model, which operates at the hillslope scale and in which both soil production and transport processes are involved. Moreover, emphasis is put on the climate control on hillslope sediment transport by the use of a specific, multi-process parameterization of soil transport, which includes variables—e.g., overland flow discharge and active-layer depth—that can be derived from climatic properties such as temperature and precipitation. Our motivation in developing such a new numerical model is to provide a modelling framework which allows climate-independent calibration of soil transport processes. Indeed, the parameters of simple hillslope erosion models—like the diffusion equation—are often assumed constant, although they must certainly vary with climatic variables and other material or environmental properties (Carson and Kirkby, 1972). Application of these simple models is thus limited either to environments where climate variations has only affected landscape evolution to second or higher order (e.g., Heimsath et al., 2000), or to studies that focus on average landscape evolution on time scales much longer than time scales of geomorphologically effective climate variations (e.g., the glacial-interglacial cycles) (Tucker, 2009a). The new numerical model proposed in this work should, at least partially, address this particular issue.

In addition to model development and testing, we therefore propose using the numerical model to study hillslope evolution in the Ardenne Massif (Belgium, NW Europe), which underwent drastic environmental changes during the last glacial-interglacial cycle of the Quaternary

(Vandenberghe et al., 2004). As, in the model, climate is—with hillslope topography—one of the main driving variables controlling hillslope erosion, we expect that cold and temperate environments that alternated or succeeded one another during the past 120 kyr in the Ardenne may help to constrain the parameterization of soil transport defined in the model. In turn, forward modelling may bring new insights on how hillslopes have responded—in terms of soil thickness distribution, hillslope morphology, denudation rates and sediment supply to channels—to the succession of cold and temperate climatic phases, and on the time needed by hillslope processes to fully respond—i.e., evolve towards a new equilibrium—to the transitions between these climatic phases.

Although fluvial processes are not included in the model, predictions of sediment supply can provide good basis to achieve better hillslope-channel coupling. Indeed, this last decade as seen the emergence of sediment-flux dependent river incision models (Whipple and Tucker, 2002; Sklar and Dietrich, 2006). However, in these models, sediment supply is often treated as simple external forcing (e.g., Hancock and Anderson, 2002), and a detailed hillslope-channel coupling is missing. Our model of hillslope erosion, if coupled with one of these sediment-flux dependent river incision models, would provide a framework to investigate the response of the whole landscape to climate variations.

Outline of the thesis content

This thesis is subdivided into three chapters. In chapter 1, we present our new numerical model of hillslope erosion. After a brief review of the landscape evolution modelling context in which the model has emerged, each development step of the model are described in detail. Through some examples, we then show the basic control of climate on modelled soil transport processes, before discussing the potential applications and the limitations of the model. In chapter 2, we explore, under different climatic scenarios, the complex and variable behaviours of the model in relation to the parameters of soil transport (with emphasis on the response time of the hillslope system). In chapter 3, we propose to use current soil thickness and elevation data to constrain both soil production and transport rates in the Ardenne Massif for the last glacial-interglacial cycle. To achieve this goal, our model is coupled with an inversion algorithm, and a simple climatic scenario is defined for the past 120 kyr in the Ardenne. A detailed discussion on the evolution of the hillslope system within both cold and temperate phases of the climatic cycle follows the presentation of the inversion results. Finally, we give an overview of what has been gained within this thesis, and discuss some additional topics, which may form the basis for future work.

Chapter 1

The CLImate Control on Hillslope Erosion (CLICHE) model: Description and basic applications

1.1 Introduction

In this chapter, we present the CLImate Control on Hillslope Erosion (CLICHE) model, a new geomorphic model, which aims to overcome some of the limitations of previous geomorphic models, notably about their relatively simplistic representation of hillslope erosion processes and the quasi-absence of explicit link between the efficiency of these processes and climate. The CLICHE model deals with most of the latest advances made in numerical modelling of surface processes (e.g., parameterization of regolith generation, multi-process parameterization of sediment transport mechanisms, irregular spatial discretization, stochastic treatment of rainfall and runoff, single or multiple flow directions for overland flow), summarized by Tucker and Hancock (2010). Another feature that makes CLICHE a new original model is the dependence of sediment transport on ground temperatures (more precisely, its frozen/unfrozen state). By developing a new numerical model of hillslope evolution, our purpose is to remove the 'climatic component' from the calibration of the geomorphic transport laws that are included in the model such that the control of climate on hillslope erosion is fully achieved by climatic inputs (e.g., times series of temperature and precipitation). Thus, CLICHE provides an extensible computational framework for developing insights on hillslope response to climate variations, by testing climate scenarios of arbitrary level of complexity (from constant climate to real climatic scenarios).

This chapter is organized as follows: we begin by briefly reviewing previous work in landscape evolution modelling; we then give a detailed description of each step of the CLICHE model development (model parameterization, numerical scheme, hydrological and heat transfer models) before showing some examples of the basic behaviour of the model; we finally discuss on the possible applications of CLICHE and its limitations.

1.2 Background

The development of the CLICHE model is made in the context of the growing number of landscape evolution models (or surface processes models - SPMs) that have been proposed during the last decades. Many geomorphological applications have demonstrated the usefulness of these models, whose predictions help researchers test simple to complex hypotheses on the nature of landscape evolution. SPMs also provide connection between small-scale, measurable processes and their long-term geomorphic implications (Tucker et al., 2001b). Below, we give a brief overview of SPMs, their history and their conceptual basis.

1.2.1 Surface processes models

The roots of landscape evolution theory can be found in the pioneering work of Gilbert (1877), who proposed a set of hypotheses to relate various landforms to the mechanisms of weathering, erosion and sediment transport. The first quantitative models appeared later in the 1960s (e.g., Culling, 1960; Scheidegger, 1961; Ahnert, 1970; Kirkby, 1971). These models formalize the concepts of Gilbert (1877) to the development of hillslope profiles. A few years later, these models were extended to two dimensions, although still focused on hillslope morphology (e.g.

Ahnert, 1976; Kirkby, 1986). During the last two decades, as computers continued to get faster, a number of sophisticated numerical SPMs have been developed, mainly focusing on watershed or mountain belt evolution (e.g., Willgoose et al., 1991; Howard, 1994; Tucker and Slingerland, 1997; Braun and Sambridge, 1997; Densmore et al., 1998; Tucker et al., 2001b; Crave and Davy, 2001; Coulthard et al., 2002). Both hillslope and fluvial processes are involved in these models, which differ from each other by the parameterization of these processes and their numerical resolution. For a complete overview of surface processes modelling and the recent SPMs, the reader is referred to the numerous reviews on that topic (Beaumont et al., 1999; Coulthard, 2001; Martin and Church, 2004; Willgoose, 2005; Codilean et al., 2006; Bishop, 2007; Tucker and Hancock, 2010).

Most of the recent SPMs are still based on the principle that landforms result from a unique suite of surface processes (Roering et al., 2004). For example, channel gradients tend to decrease with increasing drainage area in bedrock rivers because incision is proportional to stream power.

Hillslope erosion: the diffusion equation

Formulations for hillslope erosion are mainly derived considering hillslope form (e.g., convex, convex-concave, planar). In many SPMs, sediment transport rate on hillslopes is assumed to be equal to a linear function of topographic gradient (equation 1.2). Such an expression has its origin in the pioneering studies of convex hillslopes by Davis (1892) and Gilbert (1909). Combined with the application of mass conservation (equation 1.1), this leads to the diffusion equation 1.3 that describes the rate of elevation change $\partial z/\partial t$:

$$\frac{\partial z}{\partial t} = -\nabla \cdot \mathbf{q_s} \tag{1.1}$$

$$\mathbf{q_s} = -K\nabla z \tag{1.2}$$

$$\Leftrightarrow \frac{\partial z}{\partial t} = K\nabla^2 z \tag{1.3}$$

where z is elevation, $\nabla\cdot$ is the spatial divergence operator, ∇z is the topographic gradient (i.e., the local slope), $\mathbf{q_s}$ is the soil flux in the positive direction of ∇z, and K is the hillslope diffusivity.

1.2.2 Soil production functions

A few modelling studies considered the evolution of soil mantle in addition to the evolution of topographic surface (e.g., Ahnert, 1976; Dietrich et al., 1995; Heimsath et al., 1999; Braun et al., 2001). Soil production, or rock weathering, is the result of a variety of chemical and mechanical processes. It is, however, difficult for geomorphologists to consider each of these processes separately while studying the form of the landscape. Bedrock weathering rates are thus usually estimated using empirical soil production functions, i.e., relationships between weathering rates and soil depth. A substantial review of the history of soil production functions has been made by Humphreys and Wilkinson (2007). Here again, the roots of soil production functions

can be found in Gilbert (1877). This author suggested that a minimum soil cover is needed for bedrock weathering, as soil acts as a reservoir of water essential to weathering processes such as freeze-thaw or solutional processes. At depths beyond which soil production is maximised, soil production is self limiting as thicker soil progressively buffers the underlying bedrock from weathering. This behaviour can be represented by a 'humped' function (Cox, 1980) (Figure 1.1, curve ii). This relationship has been assumed for 100 years, but has not been quantitatively tested until recently. Heimsath et al. (1997, 1999) have first applied field methods and cosmogenic dating to hillslopes in northern California to determine soil production rates as a function of soil depth. These observations suggest an exponential decrease in soil production with increasing soil depth (Figure 1.1, curve i), as proposed earlier by (Dietrich et al., 1995). Both humped and exponential soil production functions are supported at other study sites (e.g., Small et al., 1999; Heimsath et al., 2000; Wilkinson et al., 2005), although unequivocal field evidence for either of these functions is still absent (Wilkinson and Humphreys, 2005).

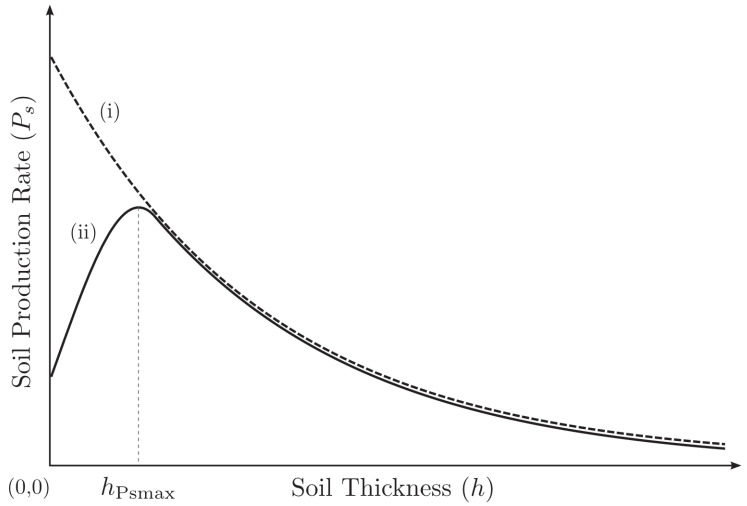

Figure 1.1: Schematic representation of (i) the exponential soil production function proposed by Dietrich et al. (1995) and Heimsath et al. (1997, 1999), and (ii) the humped soil production function initially proposed by Gilbert (1877), where $h_{P\mathrm{max}}$ corresponds to the optimal depth of soil production. Redrawn from (Humphreys and Wilkinson, 2007).

1.2.3 Modelling soil transport and hillslope erosion

Although the linear dependence of soil transport on local slope has been widely assumed (e.g., Ahnert, 1967; Nash, 1980; Dietrich et al., 1995; Fernandes and Dietrich, 1997; Heimsath et al., 1999; Martin, 2000), only a few observations support this relationship (McKean et al., 1993; Small et al., 1999). Morevover, it is well admitted that sediment transport on hillslopes result from a variety of processes (Figure 1.2), such as landsliding, rain-splash, depth-dependent creep, or overland flow (Nemcok et al., 1972; Carson and Kirkby, 1972; Selby, 1993; Hovius et al., 1997; Prosser and Rustomji, 2000). Other transport laws have therefore been proposed. These laws, still based on the process/form principle, state that transport rates depend non-linearly on local slope (e.g., Anderson, 1994; Howard, 1994; Roering et al., 1999), on depth of soil movement (e.g., Selby, 1993; Heimsath et al., 2005; Roering, 2008) and/or on drainage area or overland

flow discharge (e.g., Prosser and Rustomji, 2000). A review of many geomorphic transport laws has been made by Dietrich et al. (2003). Recently, some authors have proposed new SPMs using parameterization of soil transport which involves several processes, i.e., in which soil transport on slopes results from the combination of multiple geomorphic transport laws (Schoorl et al., 2000; Braun et al., 2001; Schoorl et al., 2002; Herman and Braun, 2006).

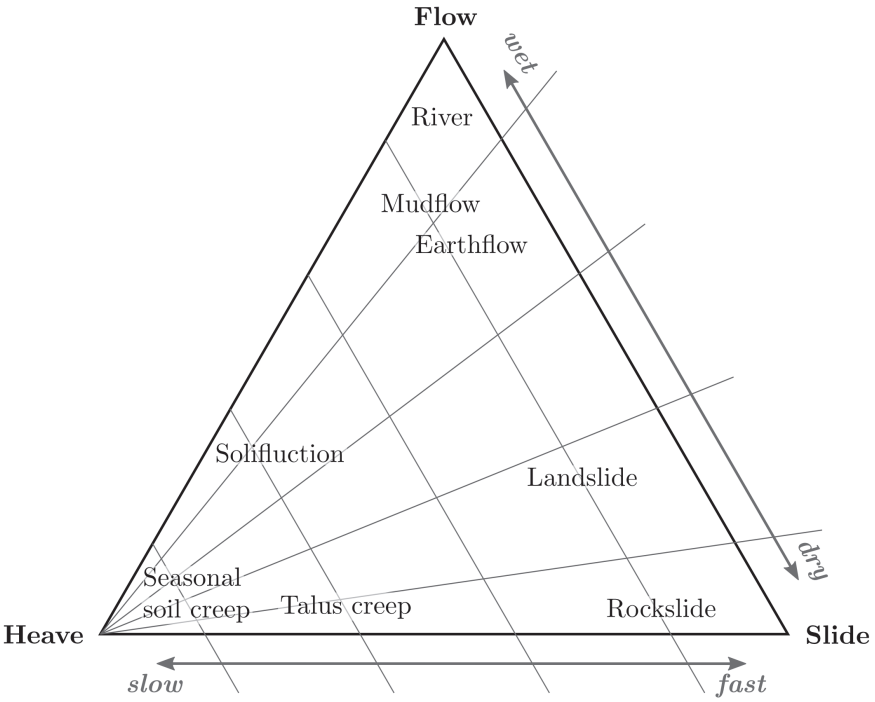

Figure 1.2: Classification of mass movement processes, after Carson and Kirkby (1972).

In surface processes modelling, a key issue to address is the calibration of the parameters of the transport laws. Most of these laws have only a limited physical basis, and their parameters are calibrated by comparing model predictions and observations (Furbish et al., 2009). These parameters are often assumed constant, although they must certainly vary with material properties, environmental or climatic variables such as rainfall and temperature, and biological activity (Carson and Kirkby, 1972). Calibrated values of these parameters are therefore related to specific environments. For example, Fernandes and Dietrich (1997) and Martin (2000) have synthesized many field-estimates of the diffusion-like coefficient K in equation 1.2, each related to a specific soil material and climate. The aim of our work is closely related to this calibration issue. By developing the parameterization of soil transport, our purpose is to remove the climatic dependence from the calibration of the parameters of soil transport laws. Calibrated values could therefore be valid in a larger range of environments, and also in environments that underwent drastic climatic changes.

Note that, beside the surface processes modelling framework discussed so far, a number of alternative hillslope erosion models coexist. Recent studies have proposed a representation of hillslope processes using a stochastic approach (e.g., Tucker and Bradley, 2010), a particle-based approach (e.g., Heimsath et al., 2002; Furbish et al., 2009) or a non-local theory of soil transport (Foufoula-Georgiou et al., 2010; Furbish and Haff, 2010). A number of soil erosion models also

emerged in the field of environmental and soil research (Merritt et al., 2003), either empirically-based (e.g., USLE or RUSLE, Renard et al., 1994), or conceptual or physically-based (e.g., WEPP, Laflen et al., 1991). These models have, however, been rarely used by geomorphologists for several reasons (e.g., assumption of constant or static topography, too detailed description of erosion mechanisms to be applied at large spatial and temporal scales); they provide frameworks that are considered out of the scope of the work we propose here.

1.3 CLICHE model overview and main assumptions

The CLICHE model simulates the evolution of a topographic surface and its subjacent soil mantle under a set of driving soil production and transport processes, at the scale of a single hill. Although it imposes no limitation on spatial scales used to investigate geomorphic systems, the model is not designed for river catchments because we have not included fluvial processes. The model conceptual framework, illustrated in Figure 1.3, is similar to the framework used in previous modelling studies (Carson and Kirkby, 1972; Dietrich et al., 1995; Heimsath et al., 1999; Braun et al., 2001). Conservation of mass is applied for a uniform column of soil. The term 'soil' used here refers to all the weathered material above intact bedrock, i.e., the regolith, which corresponds to a larger definition than the uppermost, highly altered portions of the regolith commonly used by pedologists (Phillips, 2010). Mobilization is possible for all the weathered material; a non-mobile saprolite layer is not considered here. The boundary between soil mantle and the underlying bedrock is thus assumed to be abrupt. This boundary is defined by the mechanical disruptions of the bedrock rather than by a chemical-weathering front associated with infiltrating water (Heimsath et al., 1999).

The rate of soil production is modelled by a unique, climate-independent soil production function. This weathering rate is, however, indirectly influenced by soil transport (Gilbert, 1877), which is modelled using a parameterization that combines multiple processes. This parameterization includes climate-dependent variables which are indirectly derived from time series of temperature and precipitations. In addition to the modelled transport processes, a threshold for downhill soil movement is based on the frozen/unfrozen state of the soil (no transport is allowed for frozen soil). The simple assumption underlying this threshold is that frozen soils usually have higher strength to deformation than unfrozen soils, due to the cohesion of the ice matrix that is added to the frictional resistance of the soil particles (Czurda and Hohmann, 1997), although the strength of frozen soils is generally time-dependent (i.e., the 'long-term' strength is much smaller than the 'short-term' strength, similarly to pure ice) and is largely influenced by the ice and unfrozen water contents, the grain size distribution, the mineral content and the soil density (Smith, 1996; Bell, 2000).

CLICHE is a two-dimensional numerical model that uses an irregular spatial discretization scheme (Braun and Sambridge, 1997; Tucker et al., 2001a). All soil properties (e.g., composition of the solid fraction, particle size, bulk density or thermal properties) are assumed temporally and spatially uniform. This assumption is reasonable considering the scale of a single hill, and allows the use of spatially-averaged models to calculate heat transfer from the ground surface to the soil base and to simulate water transfer at the soil/air interface, as needed to calculate soil transport

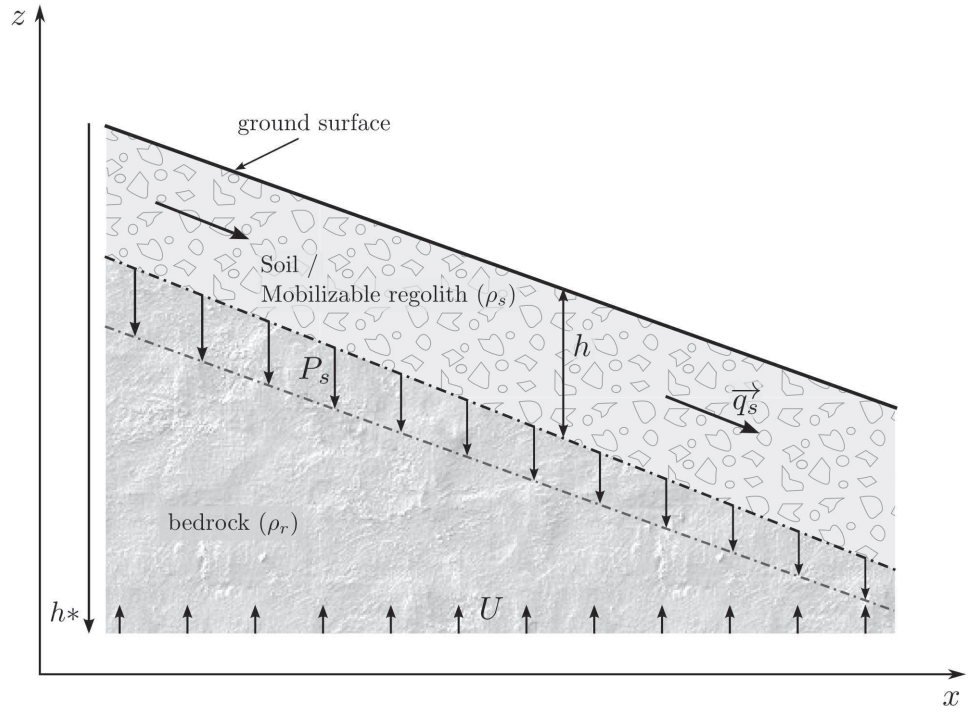

Figure 1.3: Coordinate system, conservation of mass and rates which control the evolution of soil thickness and surface elevation. Soil thickness h and depth below the ground surface $h*$ are both measured vertically. z is the elevation of the ground surface surface above any fixed reference level. P_s is rate of conversion of rock into soil. q_s is the downhill mass transport resulting from the action of multiple processes. U is the apparent rate of uniform mass uplift (tectonic or isostatic uplift or river incision). Modified from Dietrich et al. (1995).

rates. These models, as well as the parameterization of soil production and transport and its numerical resolution, will be described in detail below, with emphasis on the set of hypotheses we made at each step of the CLICHE model development.

1.3.1 Continuity of mass: soil thickness and elevation change

Considering no aeolian input nor significant loss by dissolution, the local rate of soil thickness change, $\partial h/\partial t$ (m·yr^{-1}), is determined by the balance between soil production and soil transport (Figure 1.3):

$$\rho_s \frac{\partial h}{\partial t} = \rho_r P_s - \rho_s \nabla \cdot \mathbf{q_s} \qquad \Leftrightarrow \qquad \frac{\partial h}{\partial t} = \kappa P_s - \nabla \cdot \mathbf{q_s} \tag{1.4}$$

where soil thickness h (m) is measured vertically, ρ_r is rock density, ρ_s is soil bulk density (κ is the ratio of rock density to soil density), P_s is the rate of bedrock weathering or soil production (m·yr^{-1}), $\mathbf{q_s}$ is the total downhill soil flux, and $\nabla\cdot$ is the spatial divergence operator.
Soil bulk (dry) density of most soils varies within the range of 1.1-1.6 g·cm^{-3}, while the density of soil particles (i.e., the bedrock weathered material) has a short range of 2.6-2.7 g·cm^{-3} in most mineral soils (Hillel, 1980). A value of $\kappa \sim 2$ is therefore acceptable.

The local rate of surface elevation change, $\partial z/\partial t$ (m·yr^{-1}), is related the rate of soil thickness change:

$$\frac{\partial z}{\partial t} = \frac{\partial h}{\partial t} - \kappa P_s + U \tag{1.5}$$

where U (m·yr^{-1}) is a source term that can either represent the rate of incision of channel streams at the hillslope boundaries or uniform uplift.

1.4 Parameterization of soil production and transport

To describe the rates of soil production and soil transport, we mainly follow the parameterization used in Braun et al. (2001). It consists of an empirical soil production law and three empirical or process-based transport laws, to which we add a specific transport law for modelling slow mass wasting in cold environments. Note that landslides and other rapid processes are not considered here.

1.4.1 Soil production function

Bedrock weathering is modelled using the exponential soil production function used by Heimsath et al. (1997, 1999) (Figure 1.1). The rate of weathering P_s (m·yr^{-1}) is given by:

$$P_s = P_0 \exp(-\frac{h}{h_0}) \tag{1.6}$$

where P_0 is expressed in (m·yr^{-1}) and h_0 (m) is a characteristic soil depth (soil production 'damping' depth) at which $P_s = (1/e)P_0$.
This soil production law has been calibrated at different sites (in northern California and southern Australia) using both soil thickness and cosmogenic radionucleides (CRN) measurements (Heimsath et al., 1999, 2000). For these sites, the authors reported values of P_0 between $5{\cdot}10^{-5}$ and $8{\cdot}10^{-5}$ m·yr^{-1} and a value of $h_0 \sim 0.5$ m.

1.4.2 Soil transport laws

The local rate of downhill soil transport involves four possible processes in our model (though additional processes can easily be implemented): transport by overland flow, simple creep, depth-dependent creep and periglacial solifluction. The total downhill soil flux, $\mathbf{q_s}$, results from the combination of these processes:

$$\mathbf{q_s} = \mathbf{q_r} + \mathbf{q_d} + \mathbf{q_{dd}} + \mathbf{q_g} \tag{1.7}$$

where $\mathbf{q_s}$ is the the depth-integrated, bulk volumetric soil flux per unit contour width (m^2·yr^{-1}). Expressions for transport by overland flow, simple creep and depth-dependent creep are already well described in the literature. However, only a few models for solifluction have been proposed

to date (Kirkby, 1995; Anderson, 2002). We will therefore argue in more detail the expression we have chosen for the latter process.

Transport by overland flow

The soil transport rate per unit width by flowing water, $\mathbf{q_r}$, is modelled as a power function of topographic gradient ∇z and surface water discharge per unit width q_w ($\mathrm{m^2 \cdot yr^{-1}}$):

$$\mathbf{q_r} = -K_r (q_w)^m (\nabla z)^n \tag{1.8}$$

Note that $(\nabla z)^n$ is short-hand for $||\nabla z||^{n-1} \nabla z$, as soil flux is oriented in the direction of the topographic gradient (like for the other transport laws).
This expression corresponds to a simplified form of the usual expression of sediment transport by water flow (Howard, 1980), in which the transport rate is assumed to be equal to the local carrying capacity, which is itself a function of boundary shear stress or stream power per unit width (Tucker and Hancock, 2010). We consider additionally no threshold for particle entrainment. The exponents m and n have values between 1 and 2 (Willgoose et al., 1991; Howard et al., 1994; Tucker and Bras, 1998; Prosser and Rustomji, 2000; Bogaart et al., 2003a). Whereas many surface processes models assume steady, 'geomorphologically effective' water discharges, in CLICHE, discharges are derived from daily precipitation time series (their calculation will be detailed in section 1.9).

Simple creep

The parameterization of soil transport used here includes the widely-used transport law which states that transport rate depends linearly on topographic gradient (see section 1.2.1). As pointed out by (Fernandes and Dietrich, 1997), this law—here termed as 'simple creep'—has in fact been used to represent a variety of transport processes such as creep (e.g. Culling, 1963; Armstrong, 1987), biogenic activity (e.g., Dietrich et al., 1987; Heimsath et al., 1999, 2002) or rain splash (e.g., De Ploey and Savat, 1968; Dunne et al., 2010). Downslope simple creep is commonly regarded as operating in a shallow superficial layer (Braun et al., 2001). Similarly to equation 1.2, we write:

$$\mathbf{q_d} = -K_d \nabla z \tag{1.9}$$

Note that because of the multi-process parameterization of soil transport, the coefficient K_d is not necessary equivalent to the coefficient of diffusion-based models (equation 1.2). Its value is also clearly scale-dependent (Dietrich et al., 1995), like the 'K' scale parameters of the other transport laws included in our model.

Depth-dependent creep

Beside linear creep, a few field observations but numerous laboratory and modelling studies have supported depth-dependent, viscous-like flow of soil (e.g. Ahnert, 1967; Selby, 1993; Braun et al., 2001; Furbish and Fagherazzi, 2001; Heimsath et al., 2005; Roering, 2008). The general expression for depth-dependent creep is given by:

$$\mathbf{q_{dd}} = -K_{dd}\, h^p\, (\nabla z)^l \tag{1.10}$$

Different authors have provided different values for the soil thickness and topographic gradient exponents. For example, Heimsath et al. (2005) used $p = l = 1$, although, generally, the velocity of soil displacement declines exponentially with depth (Roering, 2004). Due to a lack of constraints, Braun et al. (2001) have adopted values from Manning's equation for liquid flow ($p = 1.67$ and $l = 0.5$), which is consistent with constrained values obtained by Herman and Braun (2006) (p ranges from 1.5 to 2.0 and l ranges from 0.5 to 1.0).

Solifluction

Solifluction corresponds to one of the processes implied in depth-dependent creep, specific to cold environments. According to the modern broad terminology, solifluction may be defined as the slow mass wasting associated with freeze-thaw action (Ballantyne and Harris, 1994; French, 1996). In fact, solifluction is the result of the combined action of various processes that are difficult to distinguish. These processes include frost-creep, i.e., the downslope movement of soil particles originating from diurnal or seasonal frost heaving normal to the slope—due to ice-lens growth—followed by nearly vertical thaw consolidation; and gelifluction, i.e., the saturated soil movement associated with seasonal ground thawing (Washburn, 1979). While solifluction processes have been studied intensively in the field (Matsuoka, 2001, 2006) and in the laboratory (e.g., Harris et al., 2003, 2008), only a few parameterizations of solifluction rates have been proposed to date. Anderson (2002) has modelled frost-creep as a linear diffusive process where the diffusivity depends on the frequency of the frost events and the 'characteristic' depth of the frost penetration. Kirkby (1995) has proposed a model of gelifluction where the saturated soil layer is assumed to undergo uniform shear at a rate proportional to the surface gradient, although Harris et al. (2003) later suggested that gelifluction may rather be viewed as an elasto-plastic soil deformation than a viscous flow. Here, we adopt a simple parametrization of solifluction, which presents similarities to the models of Kirkby (1995) and Anderson (2002). Only seasonal freeze-thaw action is considered. To simplify the model formulation, we also assume that soil is completely saturated at the time when solifluction operates. Except for very dry climates, this assumption is reasonable since the addition of rain or meltwater during seasonal thawing also raises the moisture content of a thawing slope (Smith, 1988). Moreover, the model of Kirkby (1995) predicts only a weak control of soil deficit below saturation on gelifluction rates. We formulate the solifluction flux as follows:

$$\mathbf{q_g} = -K_g\, (h_a)^e\, (\nabla z)^g \tag{1.11}$$

Where h_a is the annual active layer depth (m), i.e., the depth of the seasonally thawed soil layer underlain by a frozen soil layer (a more detailed definition is given in section 1.8).
Soil velocity profiles resulting from the action of solifluction can have variable forms depending on the predominance of frost creep or gelifluction (Matsuoka, 2001, Fig. 1 p. 109). Data collected in both high-mountain and high-latitude cold environments have been synthesized by Matsuoka (2001) and suggest that solifluction rate varies roughly linearly with the annual freeze-thaw depth (except in non-permafrost sites characterized by deep seasonal frost penetration), while the gelifluction model of Kirkby (1995) is defined by a square dependence of the gelifluction rate on the active layer depth. The active layer exponent, e, is therefore assumed to have values between 1 and 2. The dependence of $\mathbf{q_g}$ on the local topographic gradient is less clear. Whereas increasing solifluction rates with slope have been reported from several high-latitude sites (e.g., Washburn, 1967; Hirakawa, 1989; Akerman, 1996), the data summarized by Matsuoka (2001) suggest a weak trend with $\mathbf{q_g}$ decreasing with slope. The author has proposed the downslope accumulation of frost-susceptible fine debris and/or the downslope increase of moisture availability as possible explanations for increasing solifluction rates with decreasing slope. In fact, the direct influence of slope on solifluction rates may be masked by the spatial variation in other factors, which themselves depend on slope (Harris, 1981). Despite the possible—but non-unique—inverse relationship between solifluction rate and local slope, solifluction is in essence a gravity-induced downslope movement of soil and we therefore adopt positive, though small (≤ 1), values for the slope exponent g.

1.5 Spatial framework

Equations 1.4 and 1.5 respectively describe the evolution of soil thickness and surface elevation on hillslopes. However, solving these partial differential equations (PDEs) is non-trivial and numerical methods are needed to perform their integration in space and time (for a given set of initial and boundary conditions). This step requires the discretization of the terrain surface, $z(x, y)$, and soil thickness, $h(x, y)$, into a finite number of 'hillslope elements', i.e., a lattice of connected points (x_i,y_i) and their associated cells (i.e., the part of the hillslope they represent) at which the solution of the PDEs is calculated. Here, we describe how the hillslope terrain is discretized in CLICHE and how the continuity of mass implied by equation 1.4 is applied within each hillslope element.

1.5.1 Irregular mesh: Delaunay triangulation and Voronoi diagram

While most of the surface processes numerical models were based on a regular spatial discretization, Braun and Sambridge (1997) first proposed to use irregular meshes, with their CASCADE model. They were rapidly joined by Tucker et al. (2001a,b) with the CHILD model. Here, we choose to use an irregular spatial discretization scheme similar to the CASCADE and CHILD models to numerically solve the geomorphic equations. The advantages of using irregular grids will be further detailed in section 1.11. The computational mesh, illustrated in Figure 1.4, is created in three stages: (1) The 2D planimetric space is first discretized as a set of points in any

arbitrary configuration, (2) these points are then connected using the Delaunay triangulation (Voronoi, 1908; Delaunay, 1934) to form the nodes of a Triangulated Irregular Network (TIN), and (3) the Voronoi diagram, which corresponds to the dual graph of the Delaunay's TIN, is constructed. Initial values of surface elevation and soil thickness are then assigned to each node. These values will be updated every time step of a CLICHE simulation (see section 1.6).

The Delaunay triangulation and the Voronoi tessellation are well established in the field of computational geometry (e.g., Fortune, 1992; Sambridge et al., 1995; Du, 1996). The Delaunay triangulation of a set of irregularly spaced points may be defined as the unique triangulation for which the circles passing through the three vertices of each triangle do not contain any other node. Unlike other triangulation methods, this triangulation has the useful property of minimizing the maximum internal angles, thus providing the most 'equable' triangulation of the original set of points. In the Delaunay's TIN, each node is connected to a set of neighbours called the 'natural neighbours'. Its dual Voronoi diagram may be defined as the set of contiguous polygons (cells) formed by intersecting the perpendicular bisectors of the Delaunay triangles. The Voronoi cell about a node is the region of the plane that is closest to the node; it may be regarded as the 'neighbourhood' of the node. To build the mesh in CLICHE, we use the CASCADE implementation code of the Delaunay-Voronoi meshing algorithms. For a more detailed description of methods and theory of Delaunay triangulation and its implementation, the reader is referred to Sambridge et al. (1995) and Braun and Sambridge (1995, 1997).

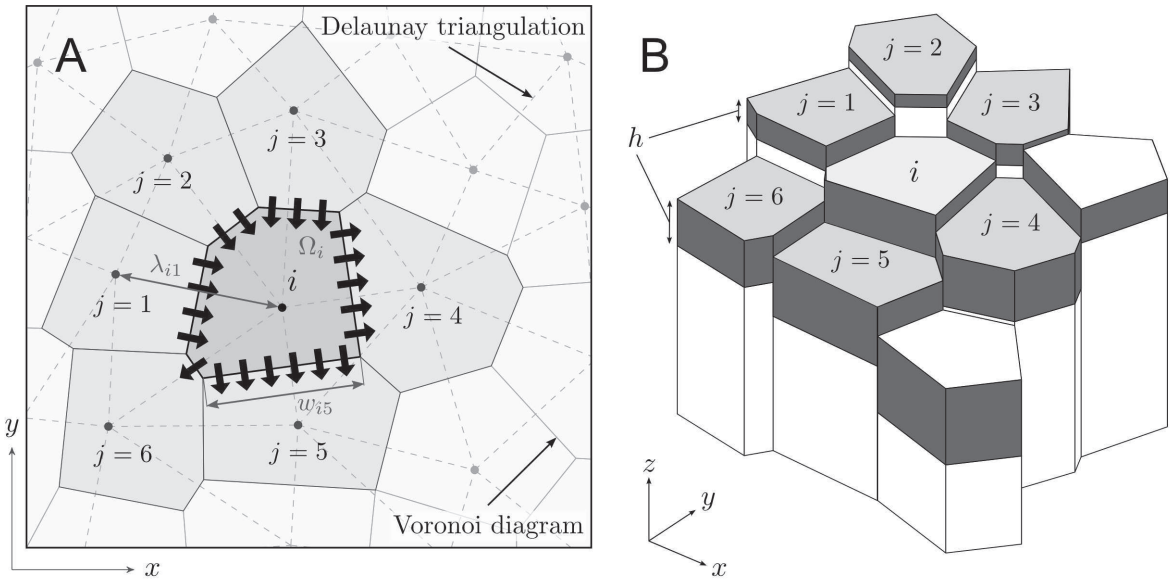

Figure 1.4: A mesh sample illustrating the discretization of the hillslope landscape in CLICHE. A. Planimetric view showing the mesh nodes (points), the edges of the Delaunay triangles (dashed gray lines) connecting the nodes, and the edges of the corresponding Voronoi cells (plain lines). The thick arrows illustrate the soil fluxes—more precisely, their normal component—across the Voronoi polygon edges shared by the node i and its 'natural neighbours'. As examples, Ω_i is the area of the Voronoi cell of the node i; λ_{i1} is the planimetric distance between i and its 1st neighbour; and w_{i5} is the width of the Voronoi edge between the node i and its 5th neighbour (the order of the neighbours doesn't have any importance here). B. 3D representation of a subset of the Voronoi diagram showing the average elevation (height of the 'columns') and the average soil thickness (depth of the dark-gray volumes) associated to each Voronoi cell.

1.5.2 Application of the finite-volume approach

As pointed out by Tucker et al. (2001b), the dual Delaunay-Voronoi framework lends itself to a numerical solution of the continuity equation 1.4 using the Finite-Volume (FV) approach (Eymard et al., 2000). Applying this approach in our two-dimensional problem consists of integrating the equation 1.4 over small areas ('finite-volume' cells) surrounding the nodes of the mesh, which here correspond to the Voronoi cells associated to each node. Hereafter, we illustrate the application of the FV method to the node i and its associated Voronoi cell of surface area Ω_i (Figure 1.4A). Using the divergence theorem[1], the integral over Ω_i of the divergence of the soil flux, $\nabla \cdot \mathbf{q_s}$, can be expressed as the integral of the soil fluxes at the boundary of the Voronoi cell:

$$\iint_{\Omega_i} \nabla \cdot \mathbf{q_s} \, d\Omega_i = \oint_{\omega_i} \hat{\mathbf{n}} \cdot \mathbf{q_s} \, d\omega_i \approx \sum_{j=1}^{nb_i} w_{ij} \, q_{s,ij} \tag{1.12}$$

where ω_i is the total length of the boundary of the Voronoi cell, $\hat{\mathbf{n}}$ is the unit vector normal to the boundary and pointing outward, nb_i is the number of natural neighbours connected to the node i, w_{ij} is the width of the edge shared by adjacent Voronoi cells associated to the node i and its neighbour j, and $q_{s,ij}$ is the total bulk volumetric soil flux across this edge per unit width (Figure 1.4 A).
The flux $q_{s,ij}$ is calculated using equation 1.7. By substituting equations 1.8 to 1.11 into equation 1.7, we note that this flux depends on the local topographic gradient across—and normal to—the shared Voronoi edge between the nodes i and j. This gradient is approximated as the topographic gradient between the nodes themselves:

$$||(\nabla z)_{ij}|| \approx S_{ij} = \frac{z_j - z_i}{\lambda_{ij}} \tag{1.13}$$

where z_i and z_j are the surface elevation associated to the nodes i and j, respectively, and λ_{ij} is the planimetric distance between these nodes.
Considering the downslope movement of soil, the substitution of equation 1.13 into equations 1.8 to 1.11 indicates that $q_{s,ij}$ is positive if the net soil flux is from i to j, and negative if the net flux is from j to i. Note also that FV methods are conservative, i.e., that the flux entering (or leaving) a given cell equals the flux leaving (or entering) the adjacent cell ($q_{s,ij} = -q_{s,ji}$). Finally, integrating both sides of equation 1.4 over Ω_i gives:

$$\frac{dh_i}{dt} = \kappa P_{s,i} - \frac{1}{\Omega i} \left(\sum_{j=1}^{nb_i} w_{ij} \, q_{s,ij} \right) \tag{1.14}$$

Intuitively, equation 1.14 simply states that a non-zero net soil flux out of the Voronoi cell surrounding the node i would result in a general decrease of soil thickness within this cell if the net flux is not balanced by the rate of soil production (inversely, a non-zero net flux entering the

[1] also called the Gauss' or Gauss-Ostrogradski's theorem

cell will always result in accumulation of soil within the cell). Note that in FV applications, the cells—and not the nodes of the mesh—are the primitive elements of the spatial discretization. Because the soil fluxes acting inside the cells are not considered, by using the divergence theorem it is only possible to describe the average rate of soil removal or accumulation, dh/dt, within each cell. This should be taken into account when setting the locations of the irregularly spaced nodes. When mentioning values of soil thickness, h_i, and surface elevation, z_i, assigned to the node i, we thus refer to the averages over the corresponding Voronoi cell (Figure 1.4 B).

1.6 Temporal framework

In CLICHE, the time evolution of soil thickness and surface elevation is treated explicitly, i.e., the values at the beginning of the next time step are fully determined by the values at the beginning of the 'current' time step. The time integration of equations 1.4 and 1.5 gives:

$$h_i(t + \Delta t) = h_i(t) + \frac{dh_i}{dt}\Delta t \tag{1.15}$$

$$z_i(t + \Delta t) = z_i(t) + \left(\frac{dh_i}{dt} - \kappa P_{s,i} + U\right)\Delta t \tag{1.16}$$

where Δt is the duration of the time steps, and where the values of $P_{s,i}$, U and all time-dependent variables used to calculate dh_i/dt (i.e., the variables involved in the expressions of the soil fluxes, equations 1.8 to 1.11) are those at the beginning of the current time step.

Using an explicit time integration scheme, the length of the time steps must be less than a certain time to ensure numerical stability (i.e., to avoid any exponential magnification of approximation errors or numerical artefacts as the simulation proceeds). As we focus on the control of climate on hillslope erosion, the time discretization must also deal with the time scales of the climate phenomena that are known to play a significant role on short to long-term hillslope evolution, such as the frequency and the magnitude of precipitation events (e.g., Kirkby, 1994; Kirkby and Cox, 1995; Tucker and Bras, 2000), as well as the periodic variation of air temperature and its propagation into near-surface soils (Anderson, 2002). These two aspects of the intrinsic climate variability are partially handled by CLICHE: precipitation events are approximated on a daily basis and only the seasonal variability of air and soil temperatures is considered (Figure 1.5) (more details will be given in sections 1.8 and 1.9). The fixed length of each time step therefore corresponds to a day. However, for simulations involving hillslope erosion over hundreds of thousands of years, it becomes computationally intractable to simulate individual days. This problem is overcome by virtually elongating the duration of the seasonal—or annual—cycles and, consequently, the length of the 'daily' time steps (a similar solution has been proposed by Tucker and Bras, 2000). The simulation time t and the time step duration Δt are given by:

$$\Delta t = \frac{T_c}{365} \qquad T_c \geq 1 \tag{1.17}$$

$$t = T_c\,(n_c + t_c) \qquad n_c \in (0, 1, 2\ldots) \quad t_c \in \left(0, \frac{1}{365}, \frac{2}{365} \ldots \frac{364}{365}\right) \tag{1.18}$$

where T_c is the annual cycle elongation factor (years), n_c increments of one unit each time the simulation enters into a new elongated annual cycle, and t_c is the relative time within the annual cycle (unitless).
Basically, the cycle elongation factor may correspond to the number of years during which the same annual sequences of daily precipitations rates and temperatures are repeated, each day of each of these years being then aggregated into one 'elongated day'. The impact of T_c on simulated hillslope evolution will be further discussed.

1.7 Adjustment of the soil transport fluxes

A straightforward application of the equations 1.15 and 1.16 would lead to incorrect or undesirable results for two reasons. The first obvious reason is that, during a time step, the amount of soil leaving a cell cannot exceed the amount of mobilizable soil available within the cell. This amount of soil is function of the average soil thickness within the cell, but can also be limited by the depth—from the surface—of the non-frozen soil layer, as we assumed that frozen soils cannot be mobilized. The second reason is that even with small, though reasonable, time steps, numerical instability may be locally initiated by too-rapid removal or accumulation of soil (which dramatically increases the slope between a node and one or several of its neighbours, which in turn will cause an increase of the soil flux and at the next time step, etc...) To ensure that this undesirable effect will never occur during a simulation, we assume that the amount of soil leaving a cell cannot either produce a lowering of surface elevation greater than the difference—multiplied by a factor α (< 1)—of elevation between the cell and its highest downslope adjacent cell. Contrary to the former restriction, this arbitrary limitation has no physical basis. Nevertheless, most of the soil transport processes modelled in CLICHE are very slow, thus never producing a sudden, rapid evolution of soil thickness or terrain surface at the scale of a time step. Because these diffusive processes tend to smooth out the roughness of the terrain surface, they are not favourable to the initiation of numerical instability. In fact, the addition of a maximum threshold of elevation lowering is only imposed by the action of transport by overland flow that is simulated at the 'daily' time scale. The stochastic generation of daily precipitation rates may produce extreme—but rare—events of large water discharge on convergent areas of the hillslopes, which may result in very high soil fluxes and create conditions that can potentially lead to numerical instability. The elevation lowering threshold is therefore necessary to deliver acceptable numerical solutions even for the most extreme generated rainfall rates.

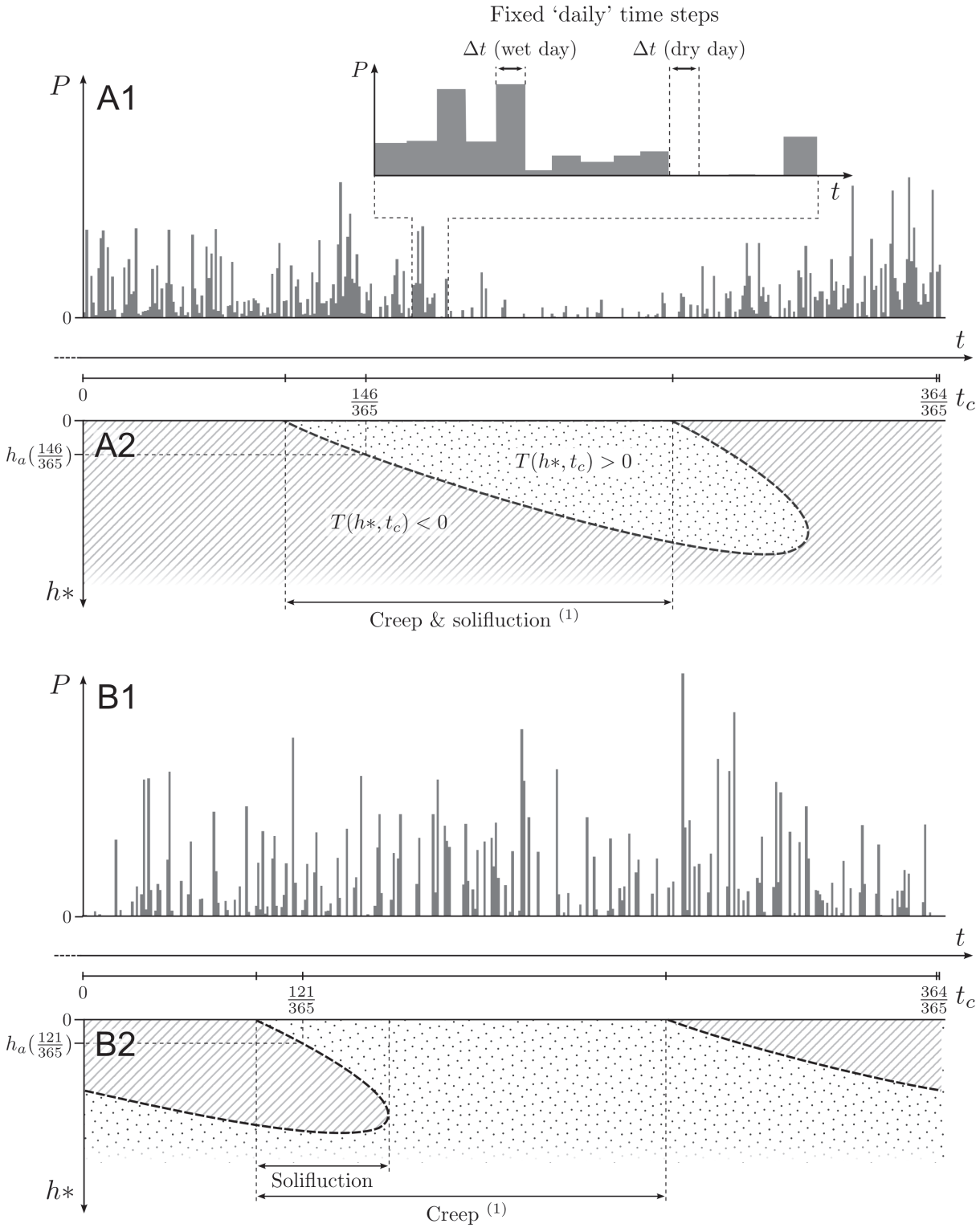

(1) And transport by overland flow if surface runoff occurs

Figure 1.5: Schematic illustration of model operations during one seasonal cycle, in the cases of (A) a negative Mean Annual Air Temperature (MAAT) with high seasonal precipitation variability and (B) a positive MAAT with low seasonal precipitation variability (B). A1-B1: Stochastically generated daily mean precipitation rates and fixed daily time steps (see section 1.9.1). A2-B2: Seasonal evolution of the frozen/non-frozen state of soil (see section 1.8), active layer depth for two values of t_c, and periods of action of modelled transport processes. See text for the definitions of the illustrated variables.

The restrictions described here above can be expressed as the following set of inequalities:

$$\frac{\Delta t}{\Omega_i} \sum_j w_{ij}\, q_{s,ij}^{out} \leq h_i \tag{1.19}$$

$$\leq h_{a,i} \tag{1.20}$$

$$\leq \alpha(z_i - z_m) \tag{1.21}$$

where $q_{s,ij}^{out}$ (≥ 0) is the flux of soil leaving the Voronoi cell of the node i and entering to the adjacent cell of its neighbour j, $h_{a,i}$ is the depth of the non-frozen soil layer assigned to the node i (see section 1.8), and z_m is the surface elevation associated to the highest downslope neighbour of i.

To meet these restrictions for any amount of available soil and/or soil fluxes of any magnitude, a solution consists of adequately reducing the potential soil fluxes if needed. The inequalities 1.19, 1.20 and 1.21 are always satisfied if each flux $q_{s,ij}^{out}$ is multiplied by a factor given by:

$$sf_i = \begin{cases} \min\left(\dfrac{\min(h_i,\ h_{a,i},\ \alpha(z_i - z_m))}{\Delta t\ \Omega_i^{-1}\ \sum_j\ w_{ij}\ q_{s,ij}^{out}},\ 1\right) & \text{if } \sum_j q_{s,ij}^{out} > 0 \\ 0 & \text{if } \sum_j q_{s,ij}^{out} = 0 \end{cases} \tag{1.22}$$

where sf_i is comprised between 0 and 1 (unitless).

A value of 1 means that the amount of soil is sufficient to satisfy the fluxes of soil leaving the cell of the node i, whereas values close to 0 imply effective soil fluxes that are much lower than the potential fluxes. Because the fluxes of soil coming from the adjacent cells (noted $q_{s,ij}^{in}$, and < 0) are equivalent to the fluxes leaving those cells ($q_{s,ji}^{out}$), the former fluxes also have to be adjusted adequately. Including the factors sf in equation 1.14 yields :

$$\frac{dh_i}{dt} = \kappa P_{s,i} - \frac{1}{\Omega i}\left(\sum_j sf_j\ w_{ij}\ q_{s,ij}^{in} + sf_i \sum_j w_{ij}\ q_{s,ij}^{out}\right) \tag{1.23}$$

1.8 Soil temperature profiles and 'active layer' depth

An important criterion for the mobilization of soils, specific to our model, is the state of the soil—frozen or non-frozen—, which is also involved in the calculation of the solifluction fluxes. The estimation of soil temperature is thus required at each time step. In most instances, conduction is the principal mode of energy transport in soils (de Vries, 1975; Schaetzl and Anderson, 2005), although energy may also be transferred by radiation in very shallow layers or by convection in water or air-filled pores (Kane et al., 2001). Assuming that soil behaves as an homogeneous, solid material, one can therefore apply Fourier's law (Fourier, 1955) (equation 1.24) and the conservation of energy (equation 1.25) to describe the conductive heat flow and the evolution of soil temperature along a vertical section of the soil layer:

$$\mathbf{q_T} = -\lambda_T \frac{\partial T}{\partial h*} \tag{1.24}$$

$$\rho_s C_T \frac{\partial T}{\partial t} = \frac{\partial \mathbf{q_T}}{\partial h*} \qquad \Leftrightarrow \qquad \rho_s C_T \frac{\partial T}{\partial t} = -\lambda_T \frac{\partial^2 T}{(\partial h*)^2} \tag{1.25}$$

where T is soil temperature, $\mathbf{q_T}$ is the heat flux in the positive $h*$-direction (here measured vertically), λ_T is the thermal conductivity of soil, and C_T is the soil specific heat capacity.
Some important assumptions are made at this stage. Firstly, soil temperatures are estimated using a one-dimensional heat transfer model. The same vertical profile of soil temperature is predicted everywhere on the hillslope (lateral heat fluxes are assumed negligible compared to the vertical fluxes). Secondly, thermal conductivity and specific heat of the soil are assumed constant in space and time, whereas these parameters are known to vary with water content, composition of the solid fraction (mineral type and particle size) and bulk density (e.g. de Vries, 1963; Abu-Hamdeh and Reeder, 2000; Ochsner et al., 2001; Abu-Hamdeh, 2003; Schaetzl and Anderson, 2005). The control of these soil properties is, however, weaker on thermal diffusivity, i.e., the ratio of thermal conductivity on specific heat ($\lambda_T/(\rho_s\, C_T)$) (Ochsner et al., 2001). Finally, the model ignores heat flows carried by precipitation or meltwater and latent heat effects induced by water phase change. Note for example that Overduin et al. (2006) have observed significant changes in the apparent thermal conductivity and the apparent heat capacity of soil during a seasonal freeze-thaw cycle. A detailed description of potential, non-conductive, heat transfer processes in permafrost affected grounds or seasonally frozen soils can be found in Kane et al. (2001).

Despite all the simplifications implied by its application to natural soils, the heat equation 1.25 has the advantage of providing an analytical solution for a set of specific boundary conditions. Given (1) a seasonal sinusoidal temperature variation at the soil surface ($h* = 0$),

$$T(0, t_c) = \text{MAAT} - T_a \cos(2\,\pi\, t_c) \tag{1.26}$$

and (2) that the surface temperature fluctuations completely die out at an infinite depth below the surface (assuming no heat flux at this 'boundary'),

$$T(\infty, t_c) = \text{MAAT} \tag{1.27}$$

we can write the solution of equation 1.25 as follows (de Vries, 1963; Turcotte and Schubert, 2002) :

$$T(h*, t_c) = \text{MAAT} - T_a \cos\left(2\,\pi\, t_c - \frac{h*}{h_T}\right) \exp\left(-\frac{h*}{h_T}\right) \tag{1.28}$$

where MAAT is the mean annual air temperature (°C) (used in place of ground surface temperature), T_a is half the annual air temperature variability, and h_T is a characteristic soil depth (the soil temperature seasonal damping depth) given by:

$$h_T = \sqrt{\frac{\tau\ \lambda_T}{\pi\, 10^{-3}\, \rho_s\, C_T}} \tag{1.29}$$

where τ is the period of the seasonal cycle (1 year), λ_T is here expressed in ($\mathrm{J{\cdot}yr^{-1}{\cdot}m^{-1}{\cdot}K^{-1}}$), C_T in ($\mathrm{J{\cdot}Kg^{-1}{\cdot}K^{-1}}$) and ρ_s in ($\mathrm{g{\cdot}cm^{-3}}$).
h_T is generally of the order of 0.5-1.0 m for soils (Kirkby, 1995). This parameter is kept constant despite the influence of soil states on thermal conductivity and heat capacity. Due to the model simplifications described above and the approximative boundary conditions, this solution (equation 1.28) provides only a crude estimation of soil temperatures, but reasonable when comparing the model results to the observed seasonal variation of soil temperatures (e.g., Wu and Nofziger, 1999; Elias et al., 2004). Calculating soil temperatures using this approach offers a good trade-off between accuracy, model complexity and computational time.

Predicted soil temperature profiles for several values of t_c are drawn in figure 1.6. These profiles clearly show the attenuation of the seasonal surface temperature fluctuations with increasing depth, and also the time lag due to the propagation of the heat wave from the surface. The coolest surface temperature occurs at the beginning of the seasonal cycle, which is here fixed at January 1. The limit between frozen and non-frozen soils corresponds to the 0°C isotherm of $T(h*, t_c)$ (Figure 1.5 A2-B2). From the temperature profiles, we can derive the depth of the 'active layer' at any time in the cycle. The active layer usually refers to the layer of ground which is subject to annual thawing and freezing in areas underlain by permafrost (French, 1996), but here we restrict its definition to soils while broadening the notion of depth of active layer to the depth above which the soil temperature is positive up to the surface:

$$h_a(t_c) = \begin{cases} h_{\mathrm{root}} \rightarrow T(h_{\mathrm{root}}, t_c) = 0 & \text{if} \quad T(h*, t_c) > 0;\ h* \in [0; h_{\mathrm{root}}[\\ 0 & \text{if} \quad T(0, t_c) \leq 0 \\ +\infty & \text{if} \quad T(h*, t_c) > 0;\ h* \in [0; +\infty[\end{cases} \tag{1.30}$$

where h_{root} is calculated numerically using a simple bisection algorithm applied to equation 1.28. Examples of the variable h_a for different values of t_c are illustrated in Figures 1.5 A2-B2 and 1.6. The active layer may be defined here as the layer within which the soil can freely move downslope. Its depth is therefore locally limited by the soil thickness:

$$h_{a,i}(t) = \min(h_a(t_c), h_i(t)) \tag{1.31}$$

The usual definition in the context of periglacial environments is, however, more appropriate to calculate the solifluction fluxes. These fluxes are set to zero if $h_a(t_c) = +\infty$ (Figure 1.5 B2), otherwise $h_{a,i}(t)$ is substituted into equation 1.11.

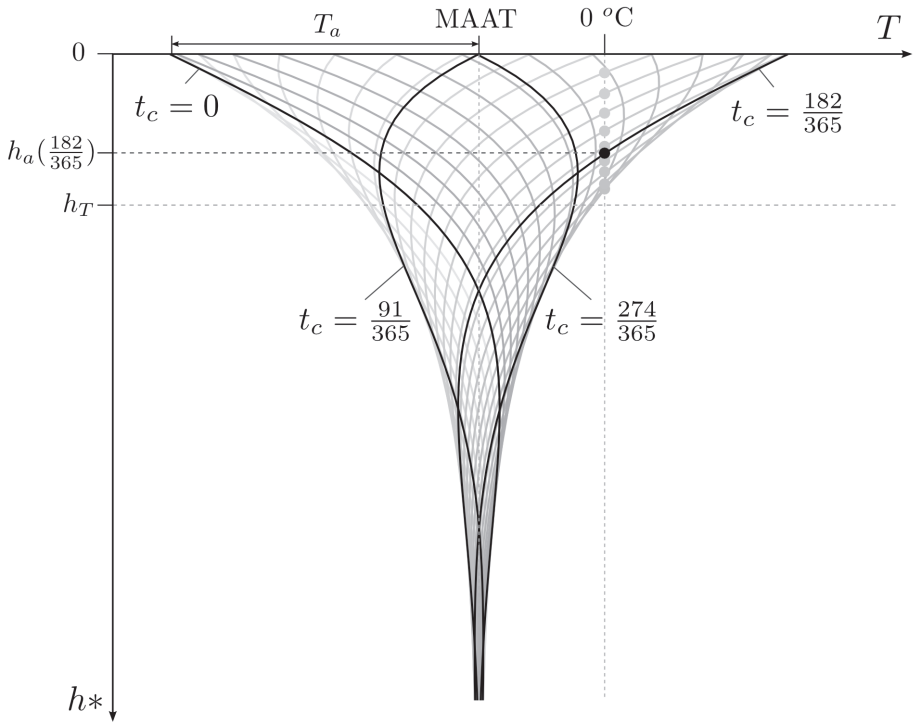

Figure 1.6: Soil temperature as a function of depth below the surface, predicted by the 1D-analytical model (equation 1.28) at regularly spaced times of the seasonal cycle (grey lines) and for specific values of t_c (black lines). MAAT is the mean annual air temperature (negative in this case) and T_a is half the annual air temperature variability. h_T is the depth at which the seasonal amplitude of temperature equals $1/e$ times the amplitude at the ground surface. Black and grey dots indicate the depth of the 'active layer', h_a (see definition in text and equation 1.20), for the correspondent temperature profiles (the active layer depth equals zero for the other profiles drawn in this figure).

1.9 Modelling hillslope hydrology

A simple precipitation-runoff model, averaged over the entire modelled hill and coupled to a stochastic precipitation generator, is used to simulate runoff on a daily basis. Bogaart et al. (2003c) applied the same model as a catchment-scale hydrological model, but its application to a single hill is conceptually straightforward because of the lumped character of the model (lateral water flow and its scale-dependence are not included). At the scale of a small hill, the time-response to daily hydrological events is assumed to be negligible (transfer functions or delayed runoff are not considered here). A steady-state hydrological system is assumed at each time step. CLICHE implements several algorithms to route the generated runoff across the terrain surface in order to calculate steady water discharges across the edges of the Voronoi diagram, as needed for calculating fluxes of soil transported by overland flow.

1.9.1 Stochastic generation of precipitation

Time series of daily precipitation rates are generated in two stages. Firstly, wet 'W' and dry 'D' days are distinguished by applying a first order stationary Markov chain model (Salas, 1993). This is a simple model that defines the state (W or D) on a day as a stochastic function

of the state on the previous day. The unconditional probability of a wet day $\Pr(W)$, related to its dry-day equivalent $\Pr(D)$, is given by:

$$\Pr(W) = 1 - \Pr(D) = \frac{1 - \Pr(D|D)}{2 - \Pr(D|D) - \Pr(W|W)} \tag{1.32}$$

where $\Pr(W|W)$ is the conditional probability that a wet days is followed by another wet day and $\Pr(D|D)$ is the dry-day equivalent (see Bogaart, 2003, pp. 121-122, for full definition of the Markov process and its mathematical development).
Time series of W/D days are then obtained by comparing the calculated value of $\Pr(W)$ to a sequence of pseudo-random generated numbers between 0 and 1.

Secondly, the amount of precipitation on each wet day, P (mm), is drawn stochastically from an exponential distribution:

$$d(P) = \frac{1}{\overline{P}} \exp\left(-\frac{P}{\overline{P}}\right) \tag{1.33}$$

where $\overline{P}$ (mm) is the mean precipitation rate on wet days.
Exponential (or Gamma) distributions are commonly used to describe precipitation rates at the scale of a day or a single storm (e.g., Hann, 1977; Eagleson, 1978; Richardson, 1981; Tucker and Bras, 2000; Bogaart et al., 2003c), based on the principle that heavy precipitation events occur less frequently than light ones (Gamma distributions imply that very light precipitation events are also less frequent, but it introduces an extra parameter which is not considered here).

The values for the parameters $\Pr(D|D)$, $\Pr(W|W)$ and $\overline{P}$ can be given on annual or monthly basis, which allows to study the impact on soil transport of diurnal, seasonal and inter-annual variability of precipitation. These parameters can be determined from the analysis of real precipitation data or from daily GCM outputs, using a small threshold of daily mean precipitation (e.g., < 0.01 mm) to differentiate between wet and dry days.

1.9.2 Runoff generation (using a lumped hydrological 'bucket' model)

To generate daily runoff on hillslopes, we apply a simplified version of PALEOFLOW (Bogaart et al., 2003c), which is itself a modified, lumped version of the spatially distributed RHINEFLOW model (Kwadijk and van Deursen, 1993, 1995). PALEOFLOW uses a one-layer water balance approach similar to the widely-applied concept of Thornthwaite & Mather (Thornthwaite and Mather, 1955). This method was originally based on monthly time steps, but can be theoretically applied at daily time steps (Thornthwaite and Mather, 1957). Two main storages are defined: storage as a snow cover, S_{snow}, and storage in the soil or unsaturated zone as shallow groundwater, S_{soil}. Both S_{snow} and S_{soil} are updated at each time step. These variables and all other quantities in the water balance model are expressed as water heights (mm) instead of rates. Multiplication by the (fixed) daily time steps converts these heights into traditional rates.

Rainfall & snowfall. The amount of precipitation on each wet day falls either as snowfall P_{snow} or rainfall P_{rain}, depending on air temperature $T(0, t_c)$ given by equation 1.26 and a

threshold temperature T_{snow}:

$$P_{\text{rain}} = \begin{cases} P & \text{if } T(0,t_c) > T_{\text{snow}} \\ 0 & \text{otherwise} \end{cases} \quad P_{\text{snow}} = \begin{cases} P & \text{if } T(0,t_c) < T_{\text{snow}} \\ 0 & \text{otherwise} \end{cases} \tag{1.34}$$

Snow storage and melt. Snow melt occurs when $T(0,t_c) > T_{\text{snow}}$. The amount of snow melt P_{melt} is calculated using a temperature-index approach (Ferguson, 1999), and is limited by the amount of available snow:

$$P_{\text{melt}} = \min(c_s(T(0,t_c) - T_{\text{snow}}), S_{\text{snow}}) \tag{1.35}$$

where c_s is the degree-day coefficient (mm·°C^{-1}).
The mass balance of the snow storage, ΔS_{snow}, is given by:

$$\Delta S_{\text{snow}} = P_{\text{snow}} - P_{\text{melt}} \tag{1.36}$$

Soil water storage. Water enters the soil storage S_{soil} as rainfall and/or snow melt $P_{\text{rain+melt}}$ and leaves by evapotranspiration E_a and/or (sub)surface runoff R_{total}:

$$\Delta S_{\text{soil}} = P_{\text{rain+melt}} - E_a - R_{\text{total}} \tag{1.37}$$

Evapotranspiration. Actual evapotranspiration E_a is a function of potential evapotranspiration E_p and soil water storage. E_p is estimated using the Priestley-Taylor method (Priestley and Taylor, 1972). When the total amount of water entering the soil storage exceeds E_p, actual evapotranspiration is assumed to be equal to E_p. Otherwise, water available in soil (S_{soil}) also contributes to E_a (equation 1.38). This contribution tends to decrease as soil moisture withdrawal increase (Rohli and Vega, 2011). This is modelled trough the accumulated potential water loss Ψ, introduced by Thornthwaite and Mather (1955), which corresponds to the potential deficiency of soil moisture associated with moisture contents below the soil storage capacity S_{smax} (equation 1.39).

$$E_a = \begin{cases} E_p & \text{if } P_{\text{rain+melt}} > E_p \\ P_{\text{rain+melt}} + \left(S_{\text{soil}} - S_{\text{smax}} \ \exp\left[-\dfrac{\Psi}{S_{\text{smax}}} \right] \right) & \text{otherwise} \end{cases} \tag{1.38}$$

$$\Psi = \begin{cases} 0 & \text{if } P_{\text{rain+melt}} > E_p \\ S_{\text{smax}} \ln\left[\dfrac{S_{\text{smax}}}{S_{\text{soil}}} \right] - (P_{\text{rain+melt}} - E_p) & \text{otherwise} \end{cases} \tag{1.39}$$

Equations 1.38 and 1.39 can be combined to show that actual evapotranspiration declines linearly with decreasing soil water availability, as assumed by Thornthwaite and Mather (1955):

$$E_a = \begin{cases} E_p & \text{if } P_{\text{rain+melt}} > E_p \\ P_{\text{rain+melt}} + \left(S_{\text{soil}} - S_{\text{soil}} \ \exp\left[\dfrac{P_{\text{rain+melt}} - E_p}{S_{\text{smax}}} \right] \right) & \text{otherwise} \end{cases} \tag{1.40}$$

Runoff. Runoff R_{total} only occurs if the total amount of water entering the soil storage exceeds both E_p and the amount of water needed to fill the soil storage to its full capacity:

$$R_{\text{total}} = \begin{cases} P_{\text{rain+melt}} + S_{\text{soil}} - E_p - S_{\text{smax}} & \text{if } P_{\text{rain+melt}} > E_p \text{ and } P_{\text{rain+melt}} + S_{\text{soil}} > S_{\text{smax}} \\ 0 & \text{otherwise} \end{cases} \tag{1.41}$$

Surface runoff R_{surface} is only a fraction of the total runoff:

$$R_{\text{surface}} = r \ R_{\text{total}} \tag{1.42}$$

where r is the fractionation parameter.
The rest of runoff is assumed to contribute to subsurface water flow or groundwater storage, of which the influence on surface water discharges at the hillslope scale is not considered. R_{surface} is finally converted into a spatially uniform runoff rate on the hillslopes:

$$R = \frac{365}{10^3} \, R_{\text{surface}} \tag{1.43}$$

where R is expressed in ($\text{m}\cdot\text{y}^{-1}$) (since each time step of a CLICHE simulation virtually represents a day, the generated daily runoff heights are not multiplied by the cycle elongation factor).

Apart from the well-known parameters of the Priestley-Taylor equation used to calculate E_p, the only parameters of the hydrological model are c_s, T_{snow}, S_{smax} and r. In a first approximation, T_{snow} is fixed to 0°C, though data-fitted snowfall probability curves—summarized for example in Kienzle (2008)—indicate a large range of probable transition temperatures from -2 to +6°C. The degree-day coefficient c_s implicitly represents all terms of the energy budget that account for the mass balance of a snow pack. It is therefore variable over time (Melloh, 1999), although time-dependent c_s has not always been applied with much success (Lindström et al., 1997). Here, this parameter is kept constant for simplicity. Values reported by many authors vary considerably from 0.6 to 14 $\text{mm}\cdot^\circ\text{C}^{-1}$ (e.g., Kwadijk and van Deursen, 1993; Haxeltine and Prentice, 1996; Singh et al., 2000). The parameters S_{smax} and r depend on soil properties and vegetation, which are both likely to change along with climate variations. In CLICHE, two different values can be fixed for both of these parameters, respectively for cold (MAAT < 0°C) and temperate (MAAT > 0°C) climates, though more detailed functional relationships are still to be defined. Each CLICHE simulation starts with soil water storage at its full capacity (i.e., $S_{\text{soil}} = S_{\text{smax}}$) and no snow cover. These simplified initial conditions are acceptable in semi-humid to humid climates, but can be very approximative in arid climates where several seasonal cycles are required to obtain

correctly calibrated hydrological simulations (Rohli and Vega, 2011). However, considering long-term simulation of hillslope erosion with relatively small values of T_c (i.e., a high number of elongated seasonal cycles), initial values of S_{snow} and S_{soil} should not have a great impact on the simulated long-term hillslope erosion.

Using the water balance model described here above, we assume that surface runoff is only due to excess soil storage capacity. Other runoff production mechanisms such as infiltration-excess (Hortonian) or saturation-excess are also known to have a significant impact on terrain morphology (e.g., Kirkby, 1987; Ijjasz-Vasquez et al., 1992; Tucker and Bras, 1998; Tucker et al., 2001b), although the influence of these mechanisms has been commonly discussed at the catchment scale. The vertical water balance approach proposed here has the advantage to have been widely applied in land surface schemes of Regional Climate Models or Global Circulation Models (GCMs) (Blyth, 2001), which will facilitate the use of GCM outputs as inputs of CLICHE.

1.9.3 Flow routing and overland flow discharge

The routing of water flow across the terrain surface is an important aspect of our modelling of hillslope hydrology because it determines the spatial distribution of overland flow discharges across the modelled hill. Algorithms for flow routing on regular meshes are well established. The algorithm used in nearly all grid-based surface processes models is the D8 method where the direction of steepest descent towards one of the eight neighbouring grid cells is used to represent the flow field (O'Callaghan and Mark, 1984; Jenson and Domingue, 1988). Other algorithms such as the D-∞ (Tarboton, 1997) and the DEMON (Costa-Cabral and Burges, 1994) algorithms have been proposed to provide a solution to the only eight possible flow-path directions allowed by the D8 algorithm. Contrary to these algorithms which are all based on the principle that water leaves a cell in a single direction (SD), several multiple flow direction (MD) algorithms allow divergent flow by partitioning the outflow from a cell between all of its downslope neighbours (MD8) (Freeman, 1991; Quinn et al., 1991). The most sophisticated algorithms to date include the MD-∞ proposed by Seibert and McGlynn (2007). The application of SD algorithms gives acceptable results in areas of convergent flows, but fails in convex terrain regions where MD algorithms may be more appropriate to represent divergent water flow (Garbrecht and Martz, 1999; Pelletier, 2008).

Besides grid-based algorithms, a number of TIN-based flow routing algorithms have been developed for hydrological modelling (e.g., Palacios-Velez and Cuevas-Renaud, 1986; Jones et al., 1990; Nelson et al., 1994; Banninger, 2007). However, most of these schemes are 'triangle-based' in the sense that they define flow pathways both across and between triangles, which is incompatible with our spatial discretization of soil transport and water flow defined across the edges of the Voronoi cells. We therefore use a 'Voronoi-based' approach similar to the one defined in the CASCADE and CHILD models (Braun and Sambridge, 1997; Tucker et al., 2001a), which consists of simply transposing the grid-based methods to the natural neighbourhood framework provided by the Voronoi tesselation. As hillslopes may present both convergent and divergent areas, CLICHE implements single flow and multiple flow methods (Figure 1.7). Each of these flow routing algorithms can be defined by the fraction d_{ij} of total flow leaving a cell that enters

into one of its downslope adjacent cells. In the SD case, d_{ij} is given by:

$$d_{ij} = \begin{cases} 1 & \text{if } S_{ij} = S_{i,\text{lowest}} \\ 0 & \text{otherwise} \end{cases} \tag{1.44}$$

where $S_{i,\text{lowest}}$ is the slope between the node i and its lowest downslope neighbour.
In the MD case, d_{ij} is proportional to the slope between the nodes i and j and the width of their shared Voronoi edge:

$$d_{ij} = \begin{cases} \dfrac{(S_{ij})^{\beta}\,(w_{ij})^{\delta}}{\sum_j (S_{ij})^{\beta}\,(w_{ij})^{\delta}} & \text{if } S_{ij} < 0 \\ 0 & \text{otherwise} \end{cases} \tag{1.45}$$

Where δ has a fixed value (we choose a value of 1 without any information found in the literature) and β can either take a fixed value or 'terrain-adaptive' values that are function of the maximum downslope gradient (Qin et al., 2007):

$$\beta = \gamma \cdot \ \min(|S_{i,\text{steepest}}|, 1) + 1.1 \tag{1.46}$$

where a γ value of 8.9 is suggested by the authors. For constant β, Freeman (1991) suggested a value of 1.1 whereas Holmgren (1994) proposed values of 4-6 to reduce flow dispersion, though these authors used regular meshes.
Unfortunately, MD and SD flow routing cannot be applied at the same time, respectively in the convex and concave regions of the modelled hill. Yet, the terrain-adaptive MD method proposed by Qin et al. (2007) produce highly divergent flow on gentle slopes and concentrated SD flow on very steep slopes. Computational cost is, however, higher using this method than using SD or uniform MD methods.

Upslope contributing area A is calculated from the area of each Voronoi cell Ω, using one of the implemented flow routing algorithms. Water discharge at the Voronoi edge shared by the nodes i and j is then given by:

$$Q_{w,ij} = d_{ij}\, R\, A_i \tag{1.47}$$

$$q_{w,ij} = \frac{Q_{w,ij}}{w_{ij}} \tag{1.48}$$

where $q_{w,ij}$ is the water discharge per unit width ($\text{m}^2 \cdot \text{yr}^{-1}$), substituted into equation 1.8.
Following the flow routing algorithm used, the calculated discharges characterize either channelized (using the SD method) or sheet (using the MD method) overland flow. Note however that, in the case of channelized flow, the width of the channels is not explicitly taken into account and is assumed to be equal to the width of the Voronoi edges.

Furthermore, SD and MD algorithms cannot route water outside of 'pits' (closed depressions). These pits may form in dynamic landscape models, either as the result of arbitrary

initial conditions or in response to simulated surface deformation (e.g., Howard, 1994; Tucker and Slingerland, 1996; Braun and Sambridge, 1997). Various methods have been developed to address the problem of water flowing across the pits. These mainly consist of removing the pits prior to route water flow (e.g. O'Callaghan and Mark, 1984; Jenson and Domingue, 1988), or identifying flooded regions and resolving outlets from those regions without altering the topography (Tucker et al., 2001a). In our case however, pits should never occur if the initial topography is defined appropriately, because of the introduced factor sf for effective soil fluxes (see section 1.7). Therefore, no pits-related specific procedure is implemented in CLICHE.

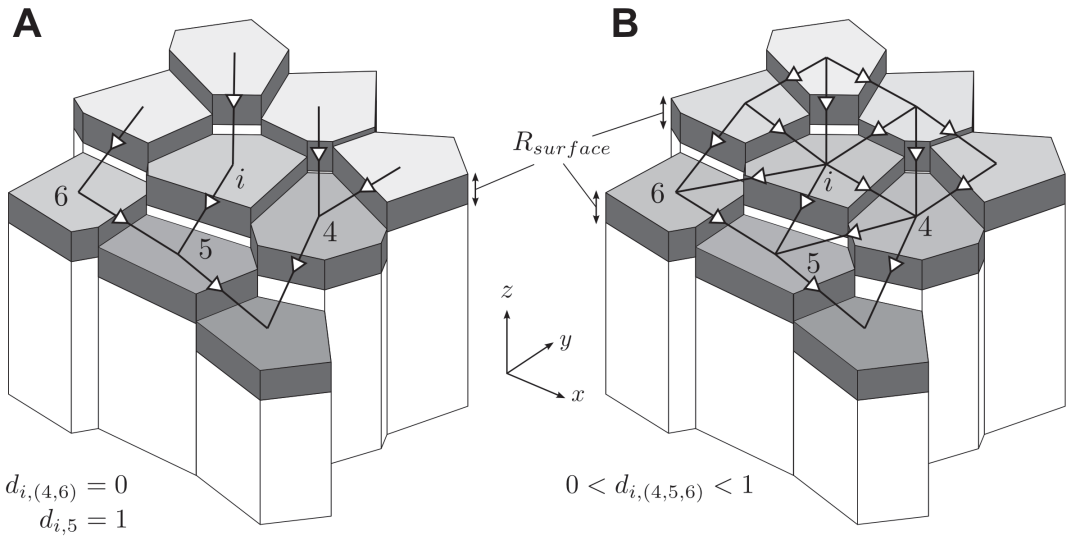

Figure 1.7: Illustration of the single flow (A) and multiple flow (B) routing algorithms implemented in CLICHE. Grey-filled Voronoi faces are proportional to drainage area. Black lines with white arrows indicates the direction of the water flow through the Voronoi edges (only the flow pathways between the represented cells are drawn). Dark-grey filled tops of Voronoi 'columns' illustrate the spatially uniform surface runoff.

1.10 Implementing and testing the numerical model

More than a model that is defined by a set of assumptions about how hillslope erosion works, CLICHE is a collection of software tools that provide a simulation environment for exploring the consequences of different hypotheses, parameters, boundary conditions and climate scenarios on hillslope soil dynamics and morphology evolution. The numerical model is implemented using the C programming language, excepted for the Delaunay-Voronoi meshing routines of the CASCADE model that are mainly written in FORTRAN. The code is then compiled as a Python extension. The Python language is used to implement all pre- and post-processing routines. The C/Python framework is computationally efficient while offering great flexibility and many possibilities, thanks to the numerous scientific and plotting libraries provided for Python. We have developed many tools dedicated to each aspect of a simulation environment (e.g., mesh creation tools, organization of many model runs and sensitivity analysis through the use of databases and parallel computing, characterization of terrain morphometry using irregular meshes, data visualization, file management and interface with existing inversion algorithms—see chapter 3). Most of the input/output data are stored in the sophisticated HDF5 (Hierarchical

Data Format) format (HDFGroup, 2011).

Figure 1.8 summarizes the main components of CLICHE described in the sections above. The generation of climatic time series and hydrological modelling are both performed separately of the simulation of soil production and transport. It allows to perform multiple model runs using the exactly the same climatic scenario, but in turn no feedback of soil dynamics on hillslope hydrology, soil thermal properties or climate is possible. Both flow routing algorithms and the calculation of the sf factor require processing of the mesh nodes ordered from the highest to the lowest elevations. Nodes ordering is achieved at every time step, using the quicksort algorithm (Press et al., 1992).

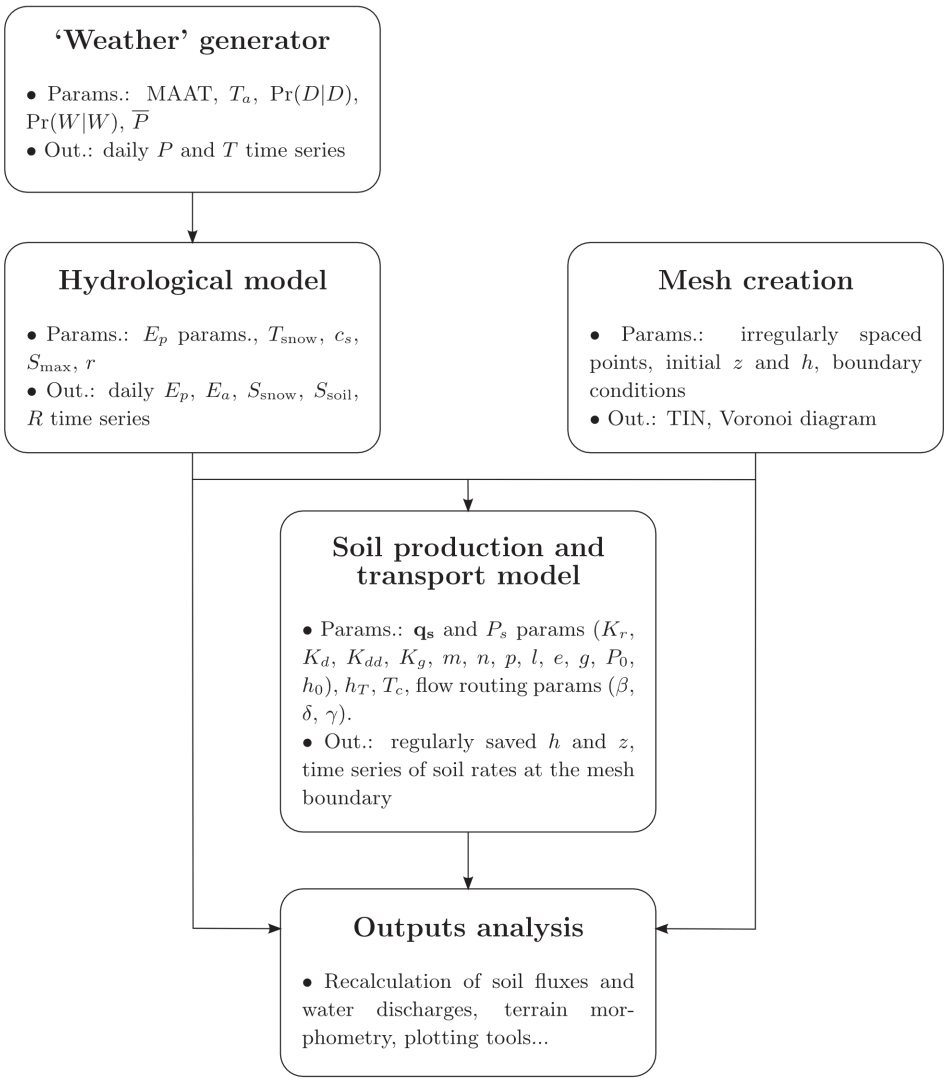

Figure 1.8: Summary of CLICHE components, main parameters and outputs (see text for definitions of parameters and variables). The weather generator makes reference to the stochastic generation of daily precipitation rates and the sinusoidal variation of the air (or ground surface) temperature.

The model implementation is made in a very flexible fashion, enhancing the researcher's ability to address a range of problems from very simple questions to complex study cases. For example, it is possible to make inactive one or several of the modelled soil transport processes. The model user can also easily define climatic scenarios at any level of complexity, by using real

data or GCM outputs or by arbitrarily fixing the values of the 'weather' generator parameters (Figure 1.8) (we provide tools for that purpose). Below we describe some basic examples of the behaviour of the modelled soil transport processes in relation to simple climate inputs. The numerical model is first tested against its analytical solution for a standard case (simple creep). The sensitivity of the simulated solifluction rates to air and soil temperatures is then analysed. Finally, we study the influence of the cycle elongation factor T_c with simulations of soil transport by overland flow.

1.10.1 A simple diffusion problem

The accuracy of the numerical approximation to the continuity equations 1.4 and 1.5 is difficult to evaluate due to the complexity of both the soil flux parameterization and the modelled surface topography. It is, however, possible to compare the numerical solution with an analytical solution for a simple case study. Considering only the action of linear creep (equation 1.9 is used and all other fluxes are set to zero), no uplift and an initial soil mantle thick enough to satisfy the creep flux, the equation 1.5 reduces to the diffusion equation 1.3 where the diffusion coefficient is equivalent to K_d. Analytical solutions of homogeneous diffusion—K_d is constant in space and time—can be derived for a specific set of initial and boundary conditions. If the initial hillslope topography is represented by the following Gaussian function,

$$z(x, y, t_0) = \frac{Z}{4\pi\ K_d\ t_0} \exp\left(\frac{-\left[(x - x')^2 + (y - y')^2\right]}{4\ K_d\ t_0}\right) \tag{1.49}$$

and both elevation and its gradient are zero at $|x| = |y| = \infty$, then the topography at the time $(t_0 + \Delta t)$ may be given by:

$$z(x, y, t_0 + \Delta t) = \frac{Z}{4\pi\ K_d\ (t_0 + \Delta t)} \exp\left(\frac{-\left[(x - x')^2 + (y - y')^2\right]}{4\ K_d\ (t_0 + \Delta t)}\right) \tag{1.50}$$

where t_0 is the initial time (> 0), x' and y' are the coordinates of the hill top, Z is a scaling constant, and Δt can have any value (the full demonstration for the one-dimensional case can be found in, e.g., Kelly, 2006, pp.140-141).

Figure 1.9 shows the results of several simulations of soil transport by linear creep, using an initial synthetic hill covered by a very thick soil mantle and shaped by applying equation 1.49 on a mesh of quasi-regularly spaced nodes (Figure 1.9 A). To show the control of the frozen/non-frozen soil criterion on the numerical solution, we vary MAAT from one simulation to another. The dimensions of the hill, the parameter K_d and the total simulation duration (100 kyr) were chosen to reduce the effects of the mesh boundaries on the simulated evolution of the hill topography, though non-negligible soil fluxes occur through these boundaries (Figure 1.9 C). Despite the finite extent and resolution of the mesh, the numerical solution agrees well with the analytical solution, but only for values of MAAT greater than the semi-annual amplitude of air temperature (T_a) (Figure 1.9 B). In the other cases, the numerical solution diverges from the analytical solution as MAAT progressively decreases below T_a. This particular behaviour

is due to the periodic occurrence—at least near the ground surface—of frozen soils, for which the downslope movement is not allowed by the model (as illustrated in Figure 1.9 C). For a fixed value of T_a, the period of possible soil transport decreases with MAAT (Figure 1.10 A), thus reducing the seasonal cycle averaged local soil fluxes and the apparent hillslope diffusivity, even though a unique value of K_d was fixed for all the simulations. For negative MAATs, the reduction of the soil fluxes and the apparent diffusivity along with MAAT is magnified due to the declining active layer depth (Figure 1.10 C). The extreme case of a non-evolving topography occurs when the soil is always frozen (i.e., MAAT $< -T_a$).

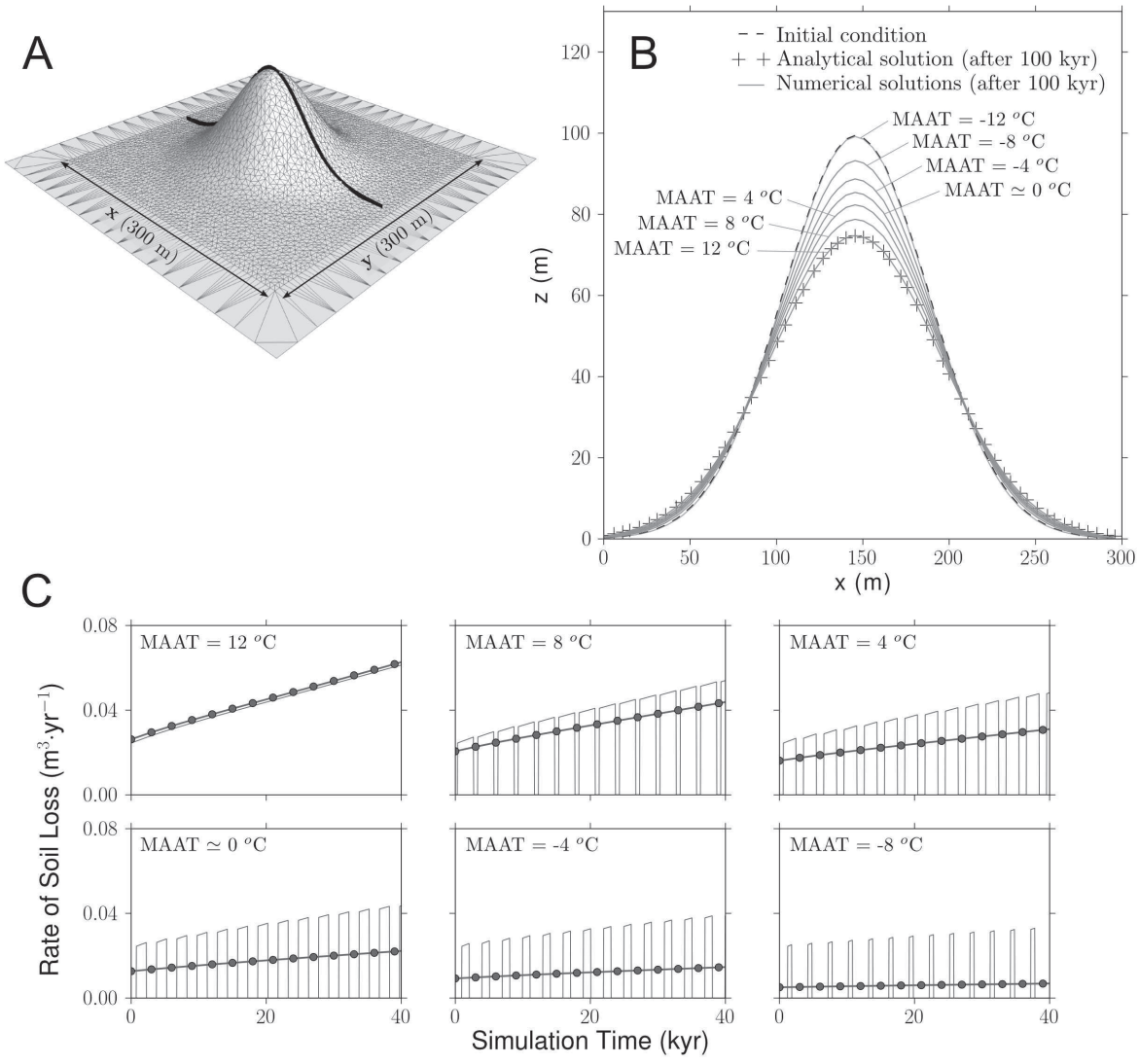

Figure 1.9: Simulation of only soil linear creep ($K_d = 0.003$ m^{2}yr^{-1}) on a synthetic hill for different values of MAAT ($T_a = 10$°C and $h_T = 0.7$ m). A. Computational mesh, which extends 300 m in both x and y directions (the mean distance between the nodes = 5 m), and initial ground surface elevation calculated by equation 1.49 ($t_0 = 3 \cdot 10^5$ kyr and Z is fixed so that hill is 100 m high). B. A cross-sectional profile of the initial hillslope topography (represented in A. by the thick black line) and elevation profiles obtained after 100 kyr of simulation, compared with the analytical solution (equation 1.50). C. 'Daily' rates of soil loss through the mesh boundaries (plain grey lines) and seasonal cycle averaged rates (black dot lines), during the first 40 kyr of the simulation ($T_c = 3000$ years).

1.10.2 Efficiency of solifluction

Despite the reduction of the length of time during the annual cycle when soil transport is possible with decreasing MAAT, our model is able to predict average soil transport rates that are much higher under cold climates than under warm or temperate climates, due to the action of other processes than simple creep. It may be the case of transport by overland flow if the amount of seasonal snowmelt is sufficient to generate high surface runoff rates, and possibly high soil transport rates. It is also the case of solifluction, which can only occur if temperature at the ground surface seasonally crosses the 0°C isotherm (i.e., $|\text{MAAT}| < T_a$). Simulations of solifluction with different MAATs show that the dependence of predicted solifluction rates on MAAT is highly non-linear and characterized by a more or less rapid decline of the transport rates when MAAT departs from 0°C (Figure 1.11). This particular behaviour is due to the combined effects of the active layer depth and the period of active solifluction, derived from the modelled soil temperatures, which both reach a maximum when MAAT equals 0°C (Figure 1.10 B-C). Increasing the value of the active layer exponent e will therefore increase the non-linear degree of the relationship between solifluction rates and MAAT. Note also that the period of active solifluction varies differently for positive and negative MAATs, which has a clear impact on the calculated solifluction rates. These rates are higher for negative MAATs than the equivalent positive MAATs. The difference would be greater if we considered that the annual amplitude of air temperature increases when MAAT decreases, as for example observed from reconstructed temperatures since the Last Glacial Maximum in northwestern and central Europe (Huijzer and Isarin, 1997; Huijzer and Vandenberghe, 1999; Vandenberghe et al., 2004).

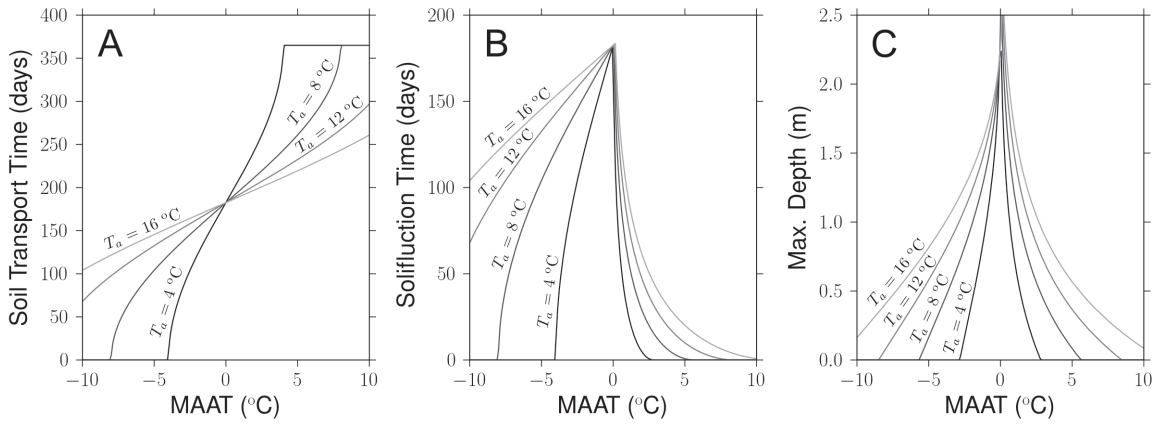

Figure 1.10: Variables derived from the modelled soil temperature profiles (see section 1.8), as functions of MAAT and T_a ($h_T = 0.7$ m). A. Total time of the seasonal cycle during which soil transport is allowed by the model. B. Total time of the seasonal cycle during which solifluction is active. C. Maximum depth of the seasonal frost-thaw penetration (the active layer in the periglacial context: values of $h_a = +\infty$ are not taken into account). See Figure 1.5 for illustrations of the variables plotted in A and B.

The behaviour of the modelled solifluction rates with respect to MAAT is consistent with global observations collected in present-day cold environments (Matsuoka, 2001). The observed volumetric solifluction rates tend to decrease towards very cold climates and more rapidly towards temperate climates, while the maximum transport rates are observed for MAATs comprised between -6 and -3°C. This temperature range corresponds roughly to the conditions favourable

to the occurrence of a warm—or discontinuous—permafrost (French and Slaymaker, 1993). It also corresponds to a transition where solifluction rates are influenced by the permafrost, the deep annual active layer and the diurnal freeze-thaw cycles. Below MAATs of -6 to -8°C, the presence of cold permafrost promotes the development of ice lenses in the basal active layer, which may generate 'plug-like' deep movement of soil on thawing and consequently high transport rates (Mackay, 1981; Harris et al., 2008). However, in very cold climates, the development of an annual active layer is missing and only shallow, diurnal freeze-thaw action can operate during the summer (Matsuoka and Moriwaki, 1992). Above MAAT of -6°C, near-surface velocities of soil movement rise with increasing MAAT and are mainly influenced by the diurnal freeze-thaw cycles (Matsuoka, 2001). But inversely, the depth of movement declines with MAAT, which combined with near-surface velocities results in a rapid decrease of volumetric solifluction rates above MAATs of -3°C. Although neither both diurnal freeze-thaw cycles nor the presence of cold or warm permafrost are explicitly considered in our model, observations suggest that the influence of these factors on solifluction rates end up being implicitly well represented by our parameterization of solifluction coupled to the modelled seasonal fluctuations of soil temperatures, despite the apparent truncation of the optimal MAAT. This truncation may be removed by the introduction of a correction factor between MAAT and the Mean Annual Ground surface Temperature (MAGT) (but it has not yet been implemented in our model). The difference ΔT between MAGT and MAAT is results from the insulating effects of the annual snow cover and vegetation (Delisle, 2007). Field studies yielded values of ΔT from +2 to +4°C in cold environments (e.g., Brown and Péwé, 1973; Chen, 2003; Delisle, 2007), which are consistent with the difference between the optimal MAAT for solifluction rates and MAAT of 0°C.

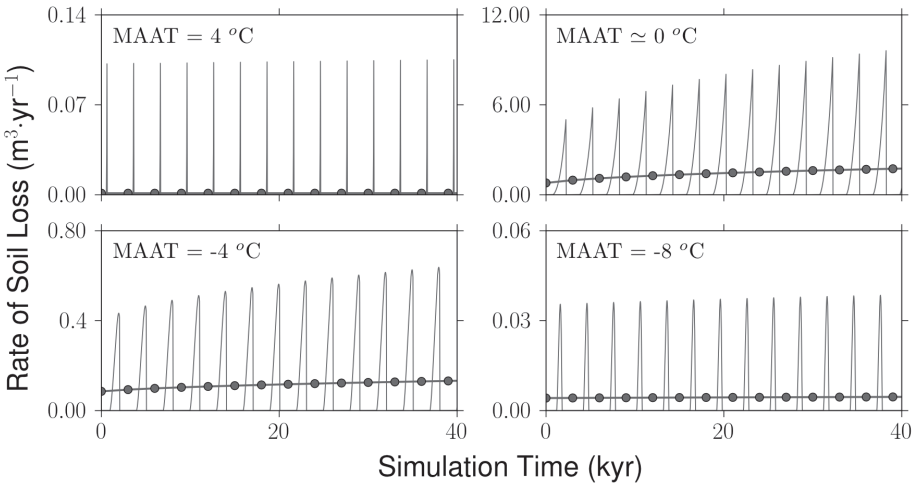

Figure 1.11: Simulation of only solifluction (K_g = 0.01 m^{2-e}yr^{-1}, e = 1.7 and g = 0.5) on a synthetic hill for different values of MAAT (T_a = 10°C and h_T = 0.7 m). 'Daily' rates of soil loss through the mesh boundaries (plain grey lines) and seasonal cycle averaged rates (black dot lines), during the first 40 kyr of the simulation. See Figure 1.9 for mesh configuration and other simulation parameters.

1.10.3 Testing the influence of the cycle elongation factor

Even though the cycle elongation factor T_c is a 'necessary evil' to keep some level of computational efficiency while simulating long-term hillslope erosion, some important facts must be considered when determining its value. Firstly, the inter-annual variability of climate—both temperatures and precipitations—is not represented for time spans smaller than T_c. The duration of an elongated seasonal cycle must therefore be (much) smaller than the extra-annual scales of climate variations considered in model applications. Secondly, if soil transport by overland flow is assumed to be a predominant mechanism, then T_c may theoretically have a significant impact on the simulated soil dynamics and hillslope erosion. From a statistical point of view, a higher value of T_c for a given simulation duration implies a smaller number of seasonal cycles, and thus fewer occurrences of time steps with extreme surface runoff rates. From a mechanistic point of view, the interaction between transport by overland flow and the other modelled processes may differ from small to high values of T_c. Indeed, a higher value of T_c also implies longer periods between runoff episodes, during which creep and/or solifluction processes can modify the terrain morphology more or less efficiently.

Figure 1.12 illustrates the 'statistical' influence of T_c on soil transport by overland flow for a relatively high frequency of runoff events. As expected, the simulated fluxes decrease when increasing the value of T_c (the relationship is slightly non-linear). The difference in soil rates between values of T_c close to each other is, however, not very strong. The same trend is found for mean denudation rates (Table 1.I). The inter-cycle variability of soil fluxes is also reduced for high values of T_c. This is caused by the factor sf, which limits the effective soil fluxes. For extreme runoff rates and high T_c values, this factor may have low values due to the large time step length Δt (equation 1.22), resulting in lower and less variable effective soil transport rates. The 'mechanistic' influence of T_c on the morphological evolution of a planar slope is shown in Figure 1.13. At low values of T_c, the formation and conservation of well-defined small 'channels' is results from an equilibrium between transport by overland flow—considering a channelized surface water flow (SD flow routing)—and creep. At high values of T_c, however, the action of creep during longer periods separating two successive runoff episodes leads to efficient healing of the scars, avoiding the formation of these channels.

Table 1.I: Simulation of overland flow on a intial planar slope (for the set of parameters given in Figure 1.12 caption): T_c vs. mean denudation rate (100 kyr average).

T_c	Mean denudation rate (mm·kyr^{-1})
100	52.23
200	52.47
300	52.09
400	50.07
800	45.21
1000	43.71
2000	36.23
3000	31.34

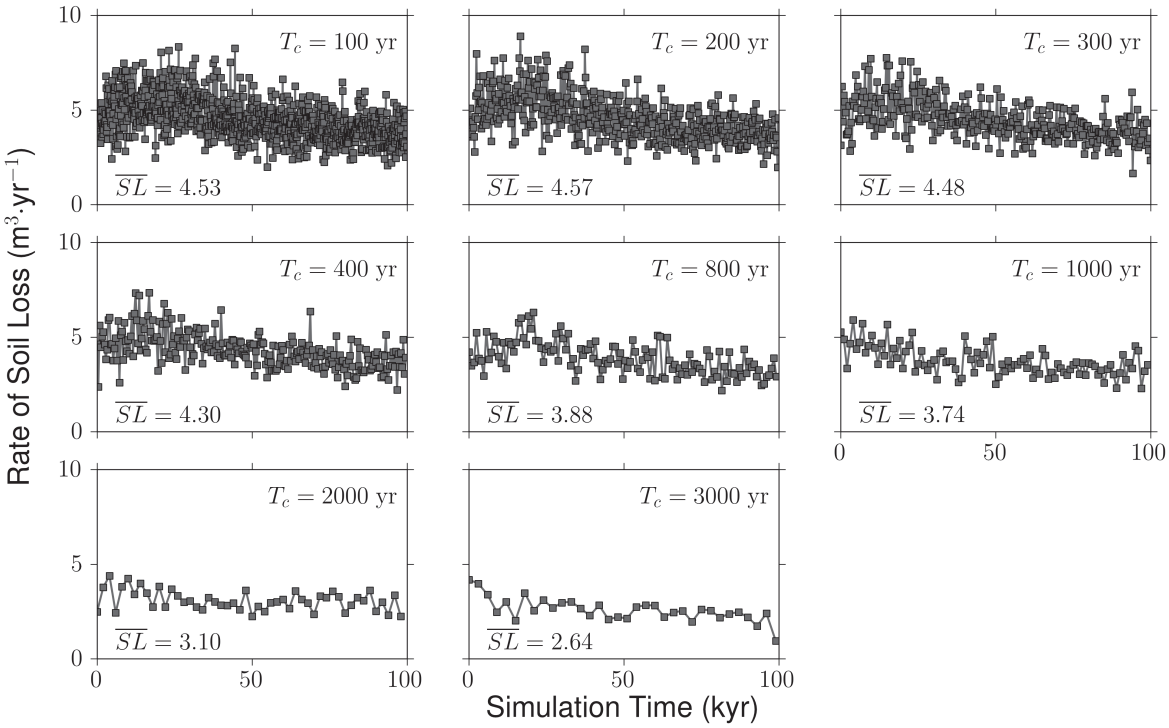

Figure 1.12: Simulation of only overland flow ($K_r = 10^{-5}$, $m = 1.7$ and $n = 1.3$) on a initial planar slope for different values of T_c. The dimensions of the pseudo-regular mesh = 300x300 m, the mean distance between the mesh nodes = 5 m and the initial max. difference of elevation = 100 m (elevations of the initial planar slope are locally slightly perturbed). Nodes at the bottom of the slope have a fixed, constant elevation. Initial soil mantle is thick enough to satisfy any soil flux. Soil temperatures are always positive (MAAT > T_a). Pr($W|W$), Pr($D|D$), $\overline{P}$ and all other hydrological parameters remain constant through the simulation and their values are fixed arbitrarily to produce ~ 60 episodes of surface runoff per elongated cycle, with a mean daily runoff rate ~ 3 mm. Water flow is routed using the SD algorithm. The plotted curves correspond to the cycle averaged rates of soil loss through the bottom slope boundary. $\overline{SL}$ is the average rate over the 100 kyr simulation.

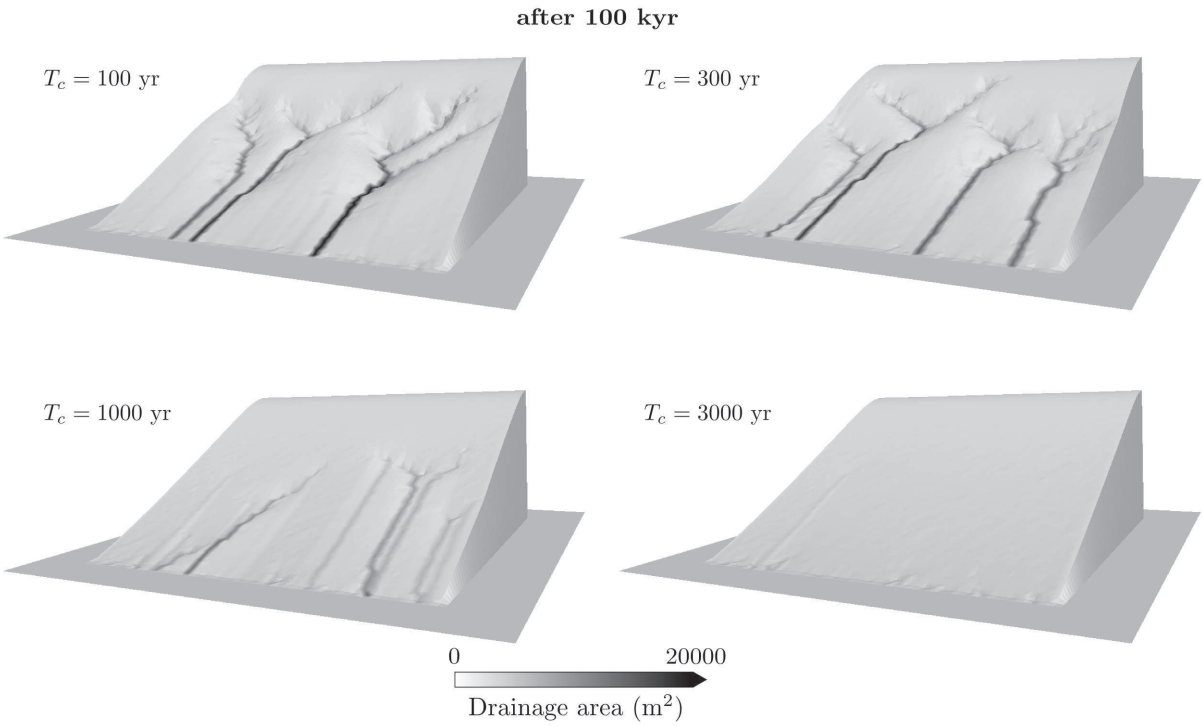

Figure 1.13: Results from 100 kyr simulation of both overland flow and simple creep ($K_d = 0.005$) on a intial planar slope for different values of T_c (See Figure 1.12 caption for all simulation parameters and mesh settings).

1.11 A brief discussion on CLICHE's potential applications and limitations

Models are simplified representations of our understanding of the physical reality. They all involve a trade-off between simplicity and realism (Tucker et al., 2001b), and are mostly designed for specific applications. CLICHE has been developed as a framework for modelling a variety of climate controls on hillslope erosion over a large range of time scales. In this model, the response of soil transport to climate change is represented in a more realistic manner than by simply and arbitrarily varying the scale coefficients ('K') of the soil transport laws. Our ultimate goal—not yet reached but already well started—is to remove the climate-dependency of these coefficients by several means: (1) the multi-process parameterization of soil transport mechanisms including climate-specific transport processes such as solifluction, (2) the addition of climate-dependent variables to the parameterization of the transport laws, as for example the surface water discharge for transport by overland flow and the active layer depth for solifluction, and (3) the introduction of thresholds for soil transport (e.g., frozen/non-frozen soils). Using this model it is possible to study the impact on hillsope erosion of climate variability at almost any time scale (from diurnal, seasonal to millennial or Quaternary time scales). The upper limit to time scale is dictated only by performance considerations and by the identified limitations of using large values for T_c. Although it is intended to serve a wide range of purposes, the CLICHE model's roots lie in mid- to long-term hillslope erosion in regions which underwent climate variations that deeply affected the environment such as the Quaternary glacial-interglacial cycles. Indeed, the dominant processes under both cold and warm climates are included in the model. Moreover, we have demonstrated that the frozen/unfrozen state of soil has a strong control on simulated soil transport rates, which may in turn affect the soil production rates. Finally, water balance at the soil/air interface accounts for snow accumulation and melt.

Another asset of the model is its irregular spatial discretization scheme. Although they mainly focused on large spatial scales (medium-size catchments to entire mountain belts), the authors of the CASCADE and CHILD models have demonstrated the considerable advantages of using TINs for modelling landscapes. For example, TIN-based meshing makes it possible to vary spatial resolution as a function of dominant surface process or landscape position (Tucker et al., 2001b). A variable-resolution mesh, if handled properly, may greatly improve the computational efficiency without altering the accuracy of the representation of modelled landscapes which potentially involve complex geometries. Irregular meshes also remove the directional bias introduced by rectangular meshes which forces streams to develop along four (or eight) preferred directions only (Braun and Sambridge, 1997). At the hillslope scale, examples of applications which may take advantage of an irregular spatial discretization include studying the development and evolution of channelized overland flow related landforms (e.g., Tucker et al., 2001b) or terraces and contour strips (e.g., Quine et al., 1999). The CASCADE and CHILD models also allow horizontal movements of the mesh nodes and implement dynamic, self-adaptive meshing, i.e., adding (or removing) nodes to (from) the mesh and then updating the Delaunay triangulation and the Voronoi tessellation. Although this feature is not yet fully implemented in CLICHE, horizontal movements of the mesh nodes may be useful for example for studying the influence

of river meandering, i.e., horizontally migrating base level, on hillslope retreating (by testing several hypotheses on boundary conditions). As pointed out by Perron and Hamon (2011, in review), only a few studies have emphasized the importance of considering both vertical and lateral components of erosion at the hillslope scale (e.g., Mudd and Furbish, 2005; Stark, 2010).

CLICHE includes many facets of our current understanding about how hillslope erosion works, but hypotheses and simplifications made at each step of the model development obviously imply some limitations. Probably most lacking is the representation of some remaining key aspects of climate control on hillslope erosion, notably via its influence on soil-particle size and vegetation (e.g., Dosseto et al., 2010), which is not explicitly considered here. Concerning the climate-dependent soil transport laws included in our model, vegetation is known to reduce solifluction rates by acting as a thermal insulator and by contributing to near-surface resistance to movement (Matsuoka, 2001), while the influence of vegetation on transport by overland flow is often considered through erosion thresholds (e.g., Tucker and Bras, 1998). The addition of such an erosion threshold in the overland flow law should be quite straightforward. However, characterizing the link between the erosion threshold and climate is more challenging. A possible solution may be the coupling of CLICHE with a vegetation model which could use the same climatic inputs than CLICHE, e.g., one recent version of the CARAIB model (François et al., 1998). In addition to soil transport, the representation of climate control is also incomplete concerning the parameterization of soil production, which is climate-independent. Yet, climate influences more or less chemical (e.g. White and Blum, 1995; Riebe et al., 2004) and mechanical rock weathering (e.g. Anderson, 1998; Hales and Roering, 2007). Models provided by Hales and Roering (2007) for bedrock frost-cracking and by Dixon et al. (2009a) for chemical weathering are good basis for future model improvements. The model proposed by Dixon et al. (2009a) requires, however, the modification of the conceptual framework shown in Figure 1.3 by the addition of a saprolite layer between soil and bedrock.

Furthermore, CLICHE shouldn't be applied to some specific environments, although only little improvements are needed to enhance its suitability in these environments. The model, in its current version, is not designed for example for steep slope environments. Indeed, for simplicity, soil thickness and depth below the ground surface are both measured vertically. This approximation is reasonable for gentle to moderate slopes but becomes very approximative for steep slopes. To improve model accuracy, we may add a slope correction factor in equation 1.5 (Braun et al., 2001), but it requires the calculation of the mean topographic gradient within each Voronoi cell, which is not trivial and demands additional computational effort. Moreover, the flux-based approach we use for soil transport is not compatible with rapid mass wasting processes such as landslides. Solutions have been recently proposed to capture landsliding by the use of non-linear transport laws (e.g., Kirkby, 1987; Anderson and Humphrey, 1989; Anderson, 1994; Howard, 1994; Roering et al., 1999). These expressions can easily be added to the parameterization of soil transport in CLICHE, but they are only slope-dependent and don't include any climate-dependent variable. By contrast, Montgomery and Dietrich (1994) have proposed a slope stability criterion of pore pressure–induced shallow landsliding, which is more climate-compliant but which requires a specific algorithm for routing the landslide debris (Tucker and Bras, 1998). Besides steep-slope areas, note that the runoff generation mechanism implemented in CLICHE

is not very suited for application in arid climates where Hortonian runoff dominates (Sharma, 1982). But apart from these specific restrictions, CLICHE provides a framework for investigating the evolution of hilly landscapes under a wide range of cold to temperate climates.

1.12 Concluding remarks

We have described, in this chapter, the development of a new numerical model of hillslope erosion through the action of soil production and transport processes. Trough a few examples, we have shown the basic behaviour of the model in relation to simple climatic inputs. These examples demonstrate, however, only some of the possibilities offered by the model. Under possible complex climatic scenarios, the concomitant action of all modelled transport mechanisms and their interaction with soil production—through soil thickness—should enable the prediction of topographic and soil thickness evolution with a high level of complexity and realism.

In our discussion, we have emphasized the usefulness of this model in bringing new insights into long-term hillslope evolution in response to Quaternary climate variations. Yet, potential applications of CLICHE are not necessarily limited to problems in fundamental geomorphology. At shorter, human time-scales, it is possible to realistically quantify the rate of soil erosion, transport and accumulation in response to scenarios of future climate change (using outputs of GCM experiments as CLICHE inputs). Although CLICHE predictions are currently limited to small hills—'upscaling' our advanced parameterization of erosion processes remains an unresolved issue—it could for example provide an accurate estimate of soil carbon storage/release in relation to climate change, considering its link with weathering and erosion (e.g., Stallard, 1998).

1.13 Symbols

A	Drainage area (upslope contributing area)	(m^2)
c_s	Snowmelt coefficient (degree-day factor)	($mm \cdot {}^\circ C^{-1}$)
C_T	Soil specific heat capacity	($J \cdot Kg^{-1} \cdot K^{-1}$)
d	Flow fractioning factor	(unitless)
E_p	Potential evapotranspiration	(mm)
E_a	Actual evapotranspiration	(mm)
e	Solifluction: 'active layer' depth exponent	(unitless)
f	Solifluction: soil water saturation exponent	(unitless)
g	Solifluction: slope exponent	(unitless)
h	Vertical soil thickness	(m)
$h*$	Vertical depth from the ground surface	(m)
h_0	Soil production 'damping depth'	(m)
h_a	'Active layer' depth	(m)
h_T	Soil temperature (seasonal) damping depth	(m)
K	Hillslope diffusivity	($m^2 yr^{-1}$)
K_r	Transport by overland flow coefficient	($m^{2-2m} yr^{n-1}$)
K_d	Simple creep coefficient	($m^2 yr^{-1}$)
K_{dd}	Depth dependent creep coefficient	($m^{2-p} yr^{-1}$)
K_g	Solifluction coefficient	($m^{2-e} yr^{-1}$)
MAAT	Mean Annual Air Temperature	(°C)
m	Transport by overland flow: discharge exponent	(unitless)
n	Transport by overland flow: slope exponent	(unitless)
nb	Number of Voronoi cell neighbours	(unitless)
p	Depth dependent creep: soil thickness exponent	(unitless)
l	Depth dependent creep: slope exponent	(unitless)
$\overline{P}$	Mean daily precipitation rate (only for wet days)	(mm)
P	Daily precipitation (rate)	(mm)
P_{rain}	Rainfall	(mm)
P_{snow}	Snowfall	(mm)
P_0	Maximum soil production rate	($m \cdot yr^{-1}$)
P_s	Soil production rate	($m \cdot yr^{-1}$)
$\Pr(W)$	Unconditional probability of a wet day	(unitless)
$\Pr(D)$	Unconditional probability of a dry day	(unitless)
$\Pr(W\|W)$	Conditional probability that a wet day is followed by another wet day	(unitless)
$\Pr(D\|D)$	Conditional probability that a dry day is followed by another dry day	(unitless)
q_s	Total soil flux per unit width	($m^2 \cdot yr^{-1}$)
q_r	Transport by overland flow soil flux	($m^2 \cdot yr^{-1}$)
q_d	Simple creep soil flux	($m^2 \cdot yr^{-1}$)

q_{dd}	Depth dependent creep soil flux	$(m^2 \cdot yr^{-1})$
q_g	Solifluction soil flux	$(m^2 \cdot yr^{-1})$
q_w	Surface water flow discharge per unit width	$(m^2 \cdot yr^{-1})$
Q_w	Surface water flow discharge	$(m^3 \cdot yr^{-1})$
r	Runoff fractioning coefficient	(unitless)
R_{surface}	Surface runoff	(mm)
R_{total}	Total runoff (surface + ground water recharge)	(mm)
R	Surface runoff rate	$(m \cdot yr^{-1})$
sf	Soil flux scaling factor	(unitless)
S	Slope	$(m \cdot m^{-1})$
S_{snow}	Snow storage	(mm)
S_{soil}	Soil (unsaturated layer) water storage	(mm)
S_{smax}	Soil water holding capacity	(mm)
t	Time	(yr)
t_c	Relative time in the annual cycle	(unitless [0;1])
T_c	Seasonal cycle elongation factor	(yr)
T	Soil temperature	(°C)
T_a	Annual semi-amplitude of air temperature	(°C)
T_{snow}	Threshold temperature of snowfall	(°C)
U	Uplift rate	$(m \cdot yr^{-1})$
w	Width of interface between adjacent Voronoi cells	(m)
z	Elevation	(m)
β	Flow partition slope exponent	(unitless)
δ	Flow partition width exponent	(unitless)
κ	Ratio of rock density to soil density	(unitless)
λ	Distance between mesh nodes	(m)
λ_T	Soil thermal conductivity	$(J \cdot yr^{-1} \cdot m^{-1} \cdot K^{-1})$
Ψ	Accumulated potential water loss	(mm)
ρ_r	Rock density	$(g \cdot cm^{-3})$
ρ_s	Soil bulk density	$(g \cdot cm^{-3})$
Ω	Area of Voronoi cells	(m^2)

Chapter 2

A CLICHE generic application: Climate, steady-state and hillslope response time

2.1 Introduction

Results from numerical simulations presented in chapter 1 have shown some features of the basic behaviour of soil transport modelled with CLICHE, the transport laws being considered separately. In this chapter, we propose to describe a few aspects of the general behaviour of the model, considering (1) the combination of all transport laws, (2) the combination of soil transport and soil production, and (3) more realistic climatic inputs. The spatio-temporal evolution of the modelled hillslope system can be characterized in many ways. However, considering each aspect of the system would be a long and hard task. We therefore mainly focus on the temporal evolution of some key characteristics (e.g., the evolution of averaged soil thickness and sediment supply to rivers), and more specifically on their transient behaviour and the establishment of a steady-sate (i.e., the apparent time-independence of these characteristics at the time when soil production is balanced by soil transport), as steady-state soil thickness is frequently assumed in models of soil, regolith, hillslope, and landscape dynamics, and in techniques used to estimate erosion and weathering rates (Phillips, 2010). In the context of Quaternary climate variations, we characterize the evolution of the modelled hillslope system for two specific, contrasted climates: a temperate climate (the present-day climate in NW Europe) and a cold climate (the reconstructed Pleniglacial climate in the same region).

Transient behaviour and evolution of the hillslope system towards a steady-sate follow a specific perturbation, i.e., imposed initial conditions or a change in boundary or limit—climatic or tectonic—conditions. As defined in Bull (2001), the time between the perturbation and the beginning of the adjustment of the hillslope system (regarding both soil thickness distribution across the hill and ground surface morphology) is called the reaction time. The time that is then needed to achieve a new equilibrium state between the new conditions and hillslope processes is called the relaxation time. The sum of the reaction time and the relaxation time is the response time. Here we propose to characterize the response time of the system for both the cold and the temperate defined climates, considering an initial bedrock surface on which soil thickness is initially assumed to be nil, and varying the relative efficiency of soil transport processes. We also briefly investigate the response times related to transitions between the cold and temperate climates.

Model experiments we make here presents many similarities—regarding the initial conditions and the model parameters—compared to the ones achieved in Braun et al. (2001). These authors have described in detail the behaviour of their model, which is based on a parameterization of soil production and transport mechanisms that is very close to the one used in CLICHE (see chapter 1). However, they focused their analysis on the comparison of their model predictions with a dataset collected by Heimsath et al. (2000) on a specific study site, the location of this site—in the Bega Valley, Australia—being specifically chosen to minimize the influence of past climate variations on soil production and transport. Braun et al. (2001) already provided a detailed description of the spatial distributions of soil thickness and transport rates predicted using a multi-process parameterization of soil transport. We propose here to characterize the difference in model behaviour when considering another, colder climate than the modern, warm temperate climate of the Bega Valley site.

2.2 Model setup

Here below, we describe the values of the model parameters, the climatic inputs (cold and temperate constant climates) and the geometry of the synthetic hill that we use in this chapter for simulating hillslope evolution with CLICHE. The initial geometry of the synthetic hill is a large-amplitude, symmetrical cosine bell on which a smaller amplitude trough has been added to create regions of varying curvature in both the x and y directions (Figure 2.1). The hill is 200 m high and extends 300 m in the x direction and 600 m in the y direction (the mean planimetric distance between the mesh nodes is $\sim$ 5 m). The initial geometry corresponds to bedrock elevation (soil thickness is nil), that is set to be the perturbation from which we analyse the response time of the system. Elevations of the mesh nodes at the lower boundaries of the hill remain constant during the simulations. These boundary conditions are chosen to simulate the presence of a stream removing soil. No uplift nor river incision is considered (i.e., $U = 0$).

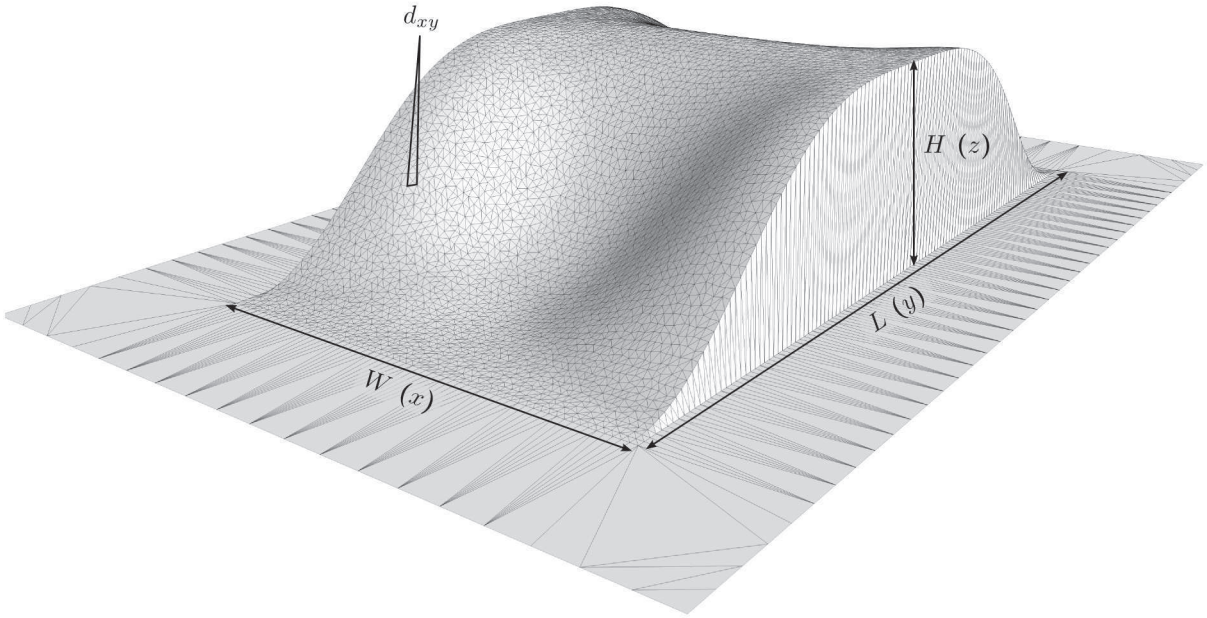

Figure 2.1: Shape and geometry of the synthetic hill used to simulate hillslope erosion (W: width, L: length, H: height, d_{xy}: mean planimetric distance between mesh nodes).

Furthermore, two different climates are considered (Table 2.I). On the one hand, a 'warm', or temperate climate is characterized by positive air and soil temperatures (no seasonal frost penetration occurs, Figure 2.2 D) and a moderate mean annual rainfall rate ($\sim$ 800 mm·yr^{-1}) with low seasonal variability. On the other hand, a 'cold' climate is defined by a high degree of continentality, with a more pronounced seasonal variability of temperatures and precipitations but low precipitation rates (the mean annual precipitation rate is about half the annual rate of the 'warm' climate). Under this cold climate, a thawing soil layer (i.e., an active layer) forms during the spring of each seasonal cycle (Figure 2.2 C). Subsets of the stochastically generated time-series of daily precipitation rates are shown for both climates in Figure 2.2 A-B. These climates are kept constant during the 150 kyr of each simulations. It allows setting a large, though

reasonable, value for the cycle elongation factor ($T_c = 500$ yr) to reduce the computational time of each model run. Basically, parameters used to generate the warm climate are derived from observed daily time series of the present-day climate in NW Europe (Klein Tank et al., 2002), while the cold climate is a reconstruction, from Global Circulation Model (GCM) experiments, of the Late Pleniglacial climate in the same region (Renssen and Isarin, 2001; Bogaart et al., 2003b). For a detailed discussion about these climate scenarios, the reader is referred to chapter 3, the context of which (i.e., application of CLICHE to field observations collected in NW Europe) is more appropriate than the context of this chapter (generic application).

The generated climatic time series are then used as input to the hydrological component of CLICHE. Figure 2.2 A-B shows very different runoff regimes between the cold and warm climates. The warm climate is characterized by sporadic runoff events, whereas the cold climate is characterized by well-defined seasonal runoff due to the amount of snowmelt that greatly contributes to exceeding soil storage capacity. As for the climate parameters, the values set for the hydrological parameters (Table 2.II) will be discussed in chapter 3. The multiple flow algorithm is used to route surface runoff (β and δ have fixed values of 1.1 and 1.0, respectively). Divergent flow is thus well-represented on the divergent regions of the synthetic hill, but the shape of the hill still produces convergent flow in the concave regions.

For the parameters of the soil production function and the exponents of the overland flow and depth-dependent creep transport laws, we use the same values than those used in Braun et al. (2001) (Table 2.II), although these authors have parameterized transport by overland flow in a slightly different manner—using drainage area as a proxy for overland flow discharge—than in the CLICHE parameterization. Without any information found in the literature, we set for the exponents of the solifluction law the same values than for the exponents of the depth-dependent creep law. These values fall in the acceptable range defined in chapter 1. For the parameters of the transport laws in general, it is important to note, at this point, that the field-calibrated values found in the literature are not necessary valid when used with the CLICHE model. Indeed, we have shown in chapter 1 that, using the exact same set of parameters values, simulation results can greatly differ following the climatic inputs, even when considering only the 'climate-independent' transport laws such as simple creep and depth-dependent-creep, due to the frozen/unfrozen soil criterion for transport.

Table 2.I: Parameters for the CLICHE's weather generator related to the 'warm' and 'cold' defined climates (given on the monthly basis). $\overline{T}_m$ is the monthly mean air temperature, $\overline{P}_m$ is the monthly averaged daily mean precipitation rate for wet days, $\Pr(D \mid D)$ is the probability that a dry day is followed by another dry day and $\Pr(W \mid W)$ is the equivalent for wet days (see chapter 1).

	J	F	M	A	M	J	J	A	S	O	N	D
'cold' climate												
$\overline{T}_m$ (°C)	-20.0	-18.0	-13.0	-7.0	0.0	6.0	8.0	6.0	0.0	-7.0	-13.0	-18.0
$\overline{P}_m$ (mm/d)	1.89	1.75	1.59	1.59	1.34	0.85	0.36	0.41	1.01	1.51	1.81	2.11
$\Pr(D \mid D)$	0.30	0.20	0.10	0.35	0.40	0.70	0.78	0.75	0.62	0.40	0.35	0.05
$\Pr(W \mid W)$	0.90	0.85	0.92	0.95	0.80	0.45	0.38	0.38	0.60	0.80	0.92	0.95
'warm' climate												
$\overline{T}_m$ (°C)	2.2	2.8	5.7	8.9	12.9	16.0	17.6	17.3	14.4	10.4	6.1	3.2
$\overline{P}_m$ (mm/d)	3.81	3.81	3.84	4.08	4.55	5.40	5.48	5.37	4.96	4.58	4.05	4.14
$\Pr(D \mid D)$	0.63	0.66	0.67	0.68	0.66	0.66	0.66	0.68	0.68	0.66	0.59	0.61
$\Pr(W \mid W)$	0.72	0.72	0.70	0.69	0.66	0.64	0.64	0.64	0.63	0.63	0.68	0.70

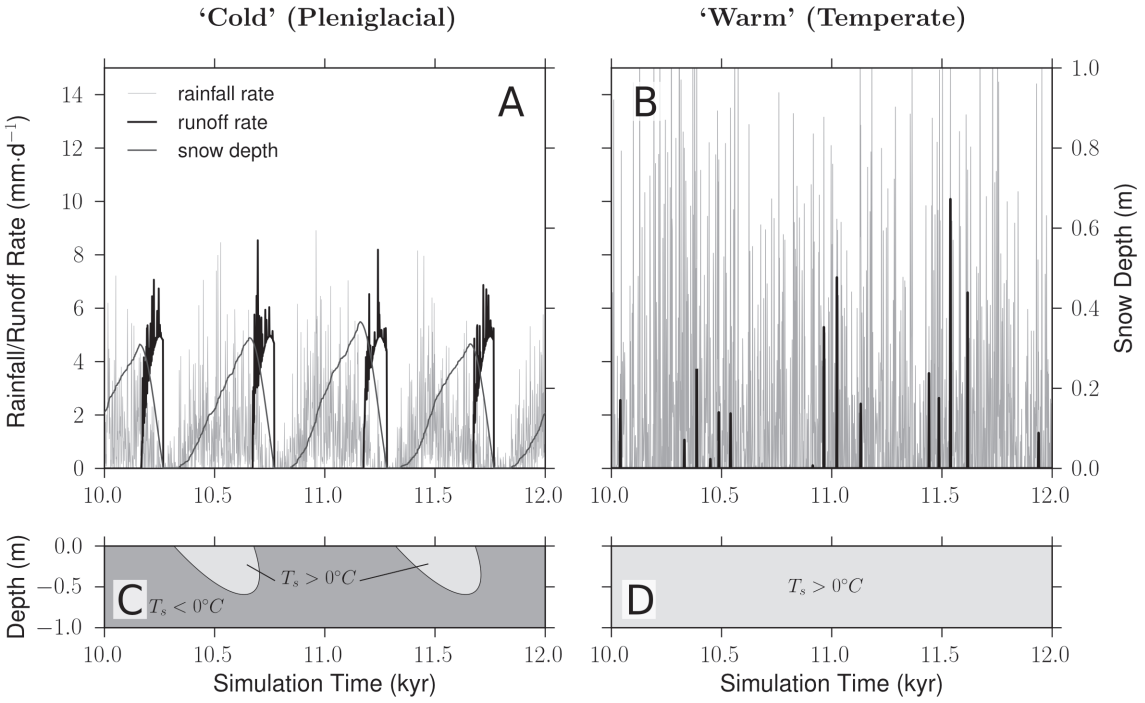

Figure 2.2: CLICHE's weather generator outputs for the two defined 'cold' (left column) and 'warm' (right column) climates. A-B. Short time spans showing the 'elongated' daily time series of mean rainfall rate generated by the weather generator and snow depth and surface runoff computed by the hydrological component of CLICHE (the cycle elongation factor $T_c = 0.5$ kyr). C-D. Soil state—i.e., frozen (dark grey) or unfrozen (light grey)—profiles as calculated by the thermal component of CLICHE for the same time spans than A-B. Note the presence of a seasonal active layer during the cold phase (C).

Table 2.II: Parameters values (or ranges) used in this chapter for CLICHE simulations.

parameter description	parameter	value or range	(units)
Hydrological/Thermal parameters			
Soil temperature damping depth	h_T	0.7	(m)
Snowmelt coefficient	c_s	0.7	(mm $^\circ$C^{-1})
Soil storage capacity (cold climate)	$S_{\mathrm{smax}}\|_{\mathrm{cold}}$	20.0	(mm)
Soil storage capacity (warm climate)	$S_{\mathrm{smax}}\|_{\mathrm{warm}}$	80.0	(mm)
Runoff separation coefficient (cold climate)	$r\|_{\mathrm{cold}}$	0.9	
Runoff separation coefficient (warm climate)	$r\|_{\mathrm{warm}}$	0.7	
Soil production fixed parameters			
Soil production max. rate	P_0	$5.3{\cdot}10^{-5}$	(m·yr^{-1})
Soil production damping depth	h_0	0.5	(m)
Ratio of bedrock to soil bulk density	κ	2.0	
Soil transport fixed parameters			
Overland flow exponents	m	1.7	
	n	1.3	
Depth-dependent creep exponents	p	1.7	
	l	0.5	
Solifluction exponents	e	1.7	
	g	0.5	
Parameters ranges			
Overland flow coef.	K_r	$10^{-7}; 10^{-4}$	(m^{2-2m}yr^{n-1})
Simple creep coef.	K_d	$10^{-4}; 10^{-2}$	(m^{2}yr^{-1})
Depth-dependent creep coef.	K_{dd}	$10^{-4}; 10^{-2}$	(m^{2-p}yr^{-1})
Solifluction coef.	K_g	$10^{-3}; 1.0$	(m^{2-e}yr^{-1})
Hill length	L	300; 900	(m)
Hill height	H	150; 250	(m)

2.3 Transient behaviour and steady-state

In this section, we analyse the influence of the relative efficiency of soil transport mechanisms on the transient behaviour of the system and the establishment of steady-state, under both cold and warm climates, using four different sets of values for the transport coefficients (i.e., the 'K' parameters of the transport laws). The system is analysed through the evolution of mean soil thickness (averaged over the entire synthetic hill) and sediment supply (i.e., the rate of soil loss at the hill lower boundaries).

The first set of values, which is taken as a reference, corresponds to the values obtained by Braun et al. (2001) after calibration (excepted for K_r), to which we add an arbitrary value for the solifluction coefficient ($K_g = 0.05$). Simulation results are shown in Figure 2.3 A1-A2. Considering the warm climate, the model reaches steady-state after ~ 50 kyr, similarly to what Braun et al. (2001) obtained from their modelling. This situation does not correspond, however, to a 'true geomorphic steady state'. Indeed, without any apparent uplift ($U = 0$), soil production and transport lead to ongoing lowering of the hill, thus progressively lowering the rates of soil transport as clearly shown by the curves of sediment supply in other model runs (e.g., Figure 2.3 B2-C1-D1-D2). Before reaching the quasi steady-state, the curve of sediment supply in Figure 2.3

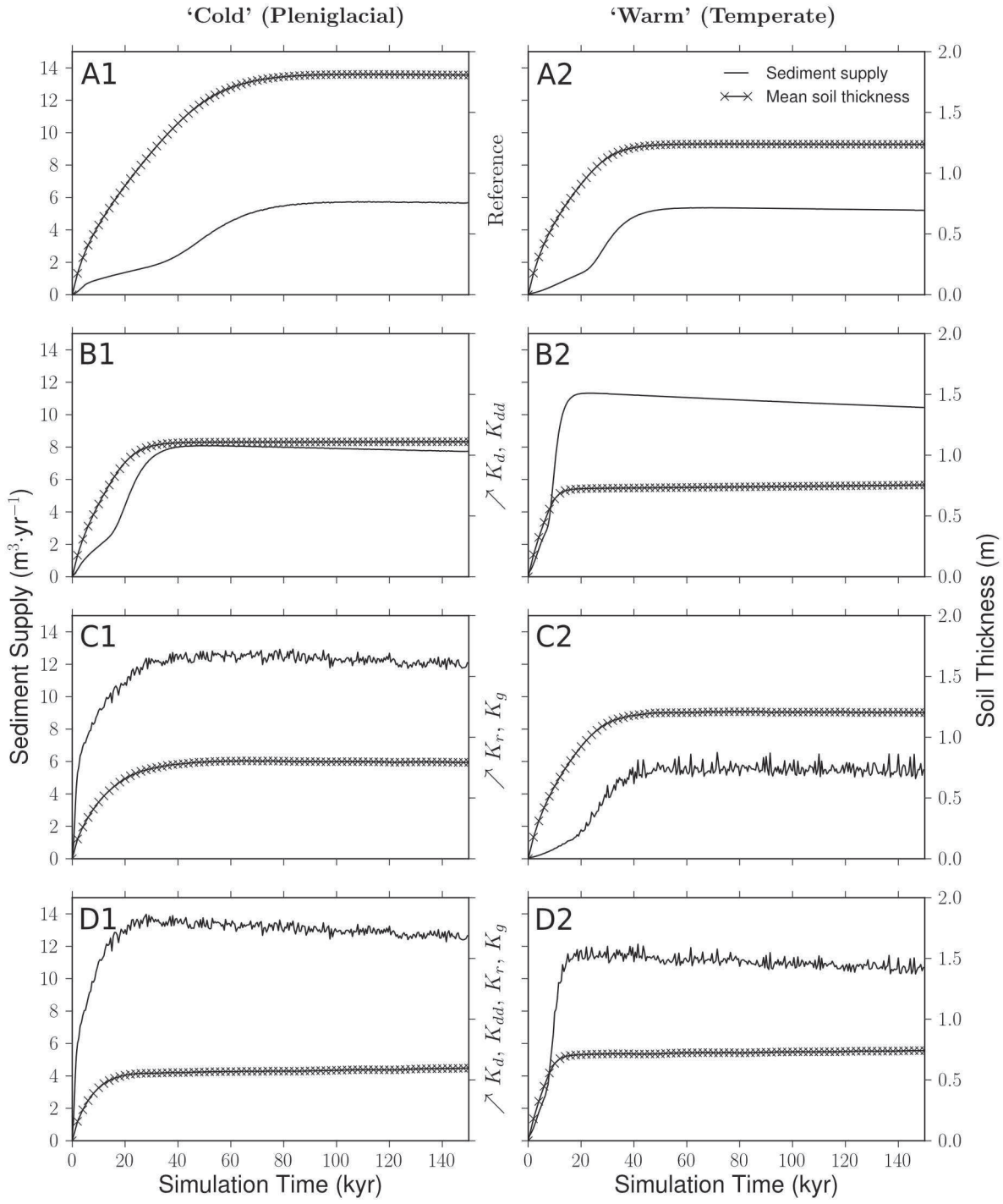

Figure 2.3: Simulation results using the cold (left column) and warm (right column) defined climates as inputs (see text for a description of these climates): seasonal cycle averaged sediment supply (i.e., rate of soil loss through the lower boundaries of the synthetic hill) and mean soil thickness (i.e., average over the whole hill). A. A reference case ($K_r = 10^{-7}$, $K_d = 0.003$, $K_{dd} = 0.003$ and $K_g = 0.05$). B. Higher values for K_{dd} (= 0.01) and K_d (= 0.01) than values in the reference case. C. Higher values for K_r (= 10^{-5}) and K_g (= 0.5). D. Higher values for all transport coefficients ($K_r = 10^{-5}$, $K_d = 0.01$, $K_{dd} = 0.01$ and $K_g = 0.05$). See Table 2.II for the values of the other model parameters.

A2 illustrates the specific transient behaviour of the system at the hill boundaries. As explained by Braun et al. (2001), at the beginning of the simulation, soil accumulation is maximum in regions of topographic convergence, after which the region of maximum soil accumulation shifts toward the lower boundaries of the hill due to the action of depth-dependent creep. This results in the downhill propagation of a 'soil transport wave'. The inflection point at about 20 kyr corresponds to the time when the wave reaches the hill lower boundary, causing an increase of the depth-dependent creep fluxes. This inflection point materializes the reaction time of depth-dependent creep at the hill boundary, while the response time of the system may be defined by the time needed by the wave to completely get out of the hillslope system. Although the curve of mean soil thickness doesn't seem to characterize the progression of this wave, it indicates steady-state at the same time than the curve of sediment supply. Mean soil thickness is mainly controlled by soil accumulation in the regions of topographic convergence and evolves non-linearly before reaching steady-state. Looking at Figure 2.3 A1, considering the cold climate, both curves of sediment supply and mean soil thickness have a similar shape than the respective curves under the warm climate. Steady-state is, however, reached later ($\sim$ 100 kyr) due to the periodic occurrences of unmovable frozen soil. The longer response time allows a greater amount of soil to accumulate in convergent areas, as shown by the curve of mean soil thickness.

From these reference simulations, we define another set of parameters, by increasing the values of the coefficients of overland flow (K_r) and solifluction (K_g) (Figure 2.3 C1-C2). Due to the difference in runoff regime between the cold and warm climates (Figure 2.2 A-B), transport by overland flow can potentially be much more efficient under the cold climate than under the warm climate. Likewise, the presence of an active layer under the cold climate implies the activation of solifluction, which is otherwise inactive under the warm climate. By choosing high values for K_r and K_g, we show that the impact on sediment supply and mean soil thickness is negligible under the warm climate (Figure 2.2 A2-C2), despite the increased inter-annual variability of sediment supply (i.e., the 'noise' of the curve of sediment supply in C2) due to transport by overland flow. By contrast, the evolution of the system is significantly different under the cold climate (A1-C1), for which the response time is reduced to $\sim$ 50 kyr and the transient behaviour of sediment supply doesn't show any inflexion point (the efficiency of depth-dependent creep at the boundary is less than the efficiency of solifluction and transport by overland flow).

Conversely, considering that simple creep and depth-dependent creep are more efficient under temperate environments, we may expect that increasing the value of their coefficient (K_d and K_{dd}) would affect the evolution of the system under the warm climate but not so much under the cold climate. Figure 2.3 B1-B2 shows that the response time is reduced under the warm climate ($\sim$ 20 kyr), but also under the cold climate ($\sim$ 40 kyr). In fact, under the cold climate, depth-dependent creep has a behaviour similar than solifluction (given the fact that the exponents of both transport laws have the same values). This outlines a limitation of the multi-process parameterization of soil transport in CLICHE, in which the transport laws may 'overlap' each other in their representation of soil transport processes. Furthermore, note that under the cold climate, the rate of sediment supply is about twice the corresponding rate under the warm climate, whereas the mean annual precipitation rate of the cold climate is about half the precipitation rate of the warm climate. This is a key point to consider when calibrating

transport law parameters using surface processes models that assume a steady 'geomorphically effective' rainfall rate.

We define a last set of parameters, in which all transport coefficients have high values. Model results show that both the response time ($\sim$ 25 kyr under the cold climate and $\sim$ 20 kyr under the warm climate) and the rate of sediment supply (and mean soil thickness) do not vary significantly from cold to warm climates (Figure 2.3 D1-D2).

Finally, we demonstrate from the simulation results presented in this section that the control of climate on the evolution of the hillslope system is highly dependent on the combination of coefficient set for the transport laws. The response time of the system can either be similar or vary significantly between two very different climates. Note also the inverse relationship between the difference in sediment supply and the difference in mean soil thickness from cold to warm climates.

2.4 Hillslope response time as a function of hill geometry and transport coefficients

The above examples provide only a limited description of the influence of transport coefficients on the evolution of the hillslope system. In this section we derive continuous relationships between the response—or characteristic—times of the system and the transport law coefficients (K_r, K_d, K_{dd}, K_g) and the geometry of the synthetic hill (i.e., its length L and its height H).

These relationships are derived using the results of a large number of model runs ($\sim$ 600) in which all parameters above are varied (the value range for each parameter can be found in Table 2.II). Thus, the computation of response time for each model run has to be made in an automatic fashion. This is quite straightforward for mean soil thickness, as the correspondent curves in Figure 2.3 present a smooth exponential shape. We therefore calculate the characteristic time of mean soil thickness evolution by adjusting the following exponential function to the curves of simulated mean soil thickness:

$$\overline{h}_n(t) = 1 - \exp\left(\frac{t}{\tau_{\mathrm{st}}}\right) \tag{2.1}$$

where t is simulation time (kyr), $\overline{h}_n$ is normalized mean soil thickness (m), and τ_{st} is a characteristic time (kyr). Equation 2.1 is adjusted using the downhill simplex algorithm (Press et al., 1992).
Although the calculation of τ_{st} is generally accurate, an estimation of uncertainty on the calculated τ_{st} value is provided by comparing the adjusted exponential curve to the curve obtained from the simulation. Note, however, that the characteristic time τ_{st} does not correspond to the response time of the system, even tough these variables are closely related, i.e., directly proportional.

In contrast to the calculation of τ_{st}, difficulties arise when calculating time responses using the curves of simulated sediment supply, as these curves can greatly differ from one model run

to another (regarding for example their transient shape or their smoothness, Figure 2.3). After many trials and errors, we have retained the following procedure that gives an accurate estimation of the response time τ_{sp} in most cases: (1) application of a median filter to the curve of sediment supply, (2) calculation of the first order derivative, (3) application of another median filter on the curve obtained at step 2, and (4) determination of τ_{sp} using a small threshold ($\gtrsim 0$) applied to the filtered curve of 1st derivative. This procedure is repeated several times by arbitrarily varying the size of the median filters and the threshold value, to provide an estimation of the uncertainty on the calculated τ_{sp} value. Although the calculation of τ_{sp} is less accurate than the calculation of τ_{st}, τ_{sp} corresponds to the 'real' response time of the system; its interpretation is therefore quite straightforward.

The following linearised model is then solved, using the Weighted Least Squares (WLS) method, from parameters and calculated response time associated to each model run:

$$\log(\tau) = p_1 \log(L) + p_2 \log(H) + p_3 \log(K_r) + \tag{2.2}$$

$$p_4 \log(K_d) + p_5 \log(K_{dd}) + p_6 \log(K_g) + \log(p_7) \tag{2.3}$$

where τ is either τ_{st} or τ_{sp}, and $p1$ to $p7$ are the parameters adjusted by WLS.

We obtain the following expressions for mean soil thickness evolution under both the cold and warm climates:

$$\tau_{st}|_{warm} = L^{0.85} H^{-0.40} K_r^{-0.04} K_d^{-0.05} K_{dd}^{-0.50} K_g^{-0.00} \cdot 2.54 \qquad (WR^2 = 0.95) \tag{2.4}$$

$$\tau_{st}|_{cold} = L^{0.99} H^{-0.28} K_r^{-0.14} K_d^{-0.01} K_{dd}^{-0.37} K_g^{-0.01} \cdot 0.91 \qquad (WR^2 = 0.72) \tag{2.5}$$

where WR^2 are the weighted coefficients of determination, which provide an estimation of the quality of the adjustments.
The expression associated to the warm climate (equation 2.4) is consistent with the results obtained by Braun et al. (2001). The signs of the adjusted parameters are also consistent with the simulation results presented in the previous section. Higher transport rates tend to decrease the response time, while lower relief (high value for L and/or low value for H) tends to increase the response time. Regarding the absolute values of the adjusted parameters, both expressions highlights the importance of relief and length scale in determining how quickly soil distribution reaches steady state on hillslopes. Under the warm climate, depth-dependent creep also appears to be determinant in the evolution of mean soil thickness towards steady-state. Under the cold climate, transport by overland flow also plays a non-negligible role (equation 2.5). As previously said, it is not very surprising that solifluction doesn't seem to influence τ_{st} in equation 2.5, since the depth-dependent creep law may also encompass solifuction processes under the cold climate.

For sediment supply, we obtain the following expressions:

$$\tau_{sp}|_{warm} = L^{0.67} H^{-0.16} K_r^{-0.09} K_d^{-0.12} K_{dd}^{-0.41} K_g^{-0.00} \cdot 3.14 \qquad (WR^2 = 0.71) \tag{2.6}$$

$$\tau_{sp}|_{cold} = L^{0.77} H^{-0.54} K_r^{-0.31} K_d^{-0.02} K_{dd}^{-0.15} K_g^{-0.07} \cdot 2.40 \qquad (WR^2 = 0.73) \tag{2.7}$$

These expressions are not very different compared to the expressions of τ_{st} (equations 2.4 and

2.5), except for hill geometry and for K_r which seems to have a greater impact on sediment supply than on mean soil thickness under the cold climate.

The empirical expressions derived here provide unique measures of the response time of soil mantled hillslopes to a specific perturbation. Because the response time is closely related, to a first order, to mean soil thickness at steady-state (Figure 2.4), these expressions may be useful in addressing the issue of upscaling hillslope processes in large-scale landscape evolution models. Note, however, that these expressions contain only partial information about the relationship between time response and soil transport coefficients and hillslope geometry, in the sense that they only provide an estimate of the sign and the non-linearity degree of the relationship.

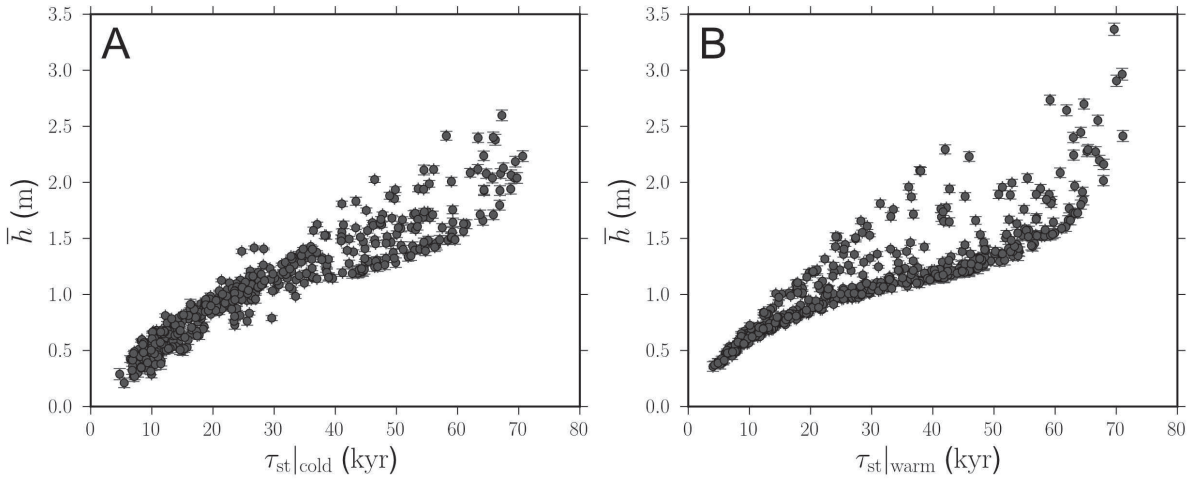

Figure 2.4: Characteristic response time τ_{st} (calculated using equation 2.1) and mean soil thickness at that time, for each model run. A. cold climate. B. warm climate.

2.5 Hillslope response time to climatic variations

So far, we have investigated the transient evolution of hillslope soil mantle starting from an initially bare-bedrock surface. Here we analyse the response of the system to climatic transitions between the warm and the cold climates. The total duration of the simulations is fixed to 300 kyr, so that steady-state is reached prior to the change in climate conditions, at 150 kyr. We firstly consider abrupt, instantaneous climatic transitions with the four sets of parameter values used in section 2.3. Results are shown in Figure 2.5. They reveal contrasted transient behaviours from one simulation to another. Yet, the reaction of both mean soil thickness and sediment supply to the climatic perturbation is quasi-instantaneous in all cases. This is due to (1) a sufficient soil cover in the lower and concave regions of the hill at the time of the perturbation, and (2) the direct adaptation of effective soil fluxes to the sudden change in climatic conditions, notably through the frozen/unfrozen soil threshold for transport, the active layer depth and the runoff regime (see chapter 1). Two types of reaction occur, depending on the set of parameter values and the transition from cold to warm or warm to cold climates. They consist of either a sudden decrease in sediment supply (and an increase in mean soil thickness) or, inversely, a sudden increase in sediment supply (and a decrease in mean soil thickness). In the first case, a new 'soil

transport wave' is generated by soil accumulation in the concave region of the synthetic hill. In the second case, such a wave is also generated, but by soil removal in the concave region. It is interesting to note that in both cases the time needed by the system to reach a new steady-state is nearly equivalent to the correspondent time response related to an initial bedrock surface (Figure 2.3). Consequently, the empirical expressions that we have derived in section 2.4 (equations 2.4 to 2.7) appear to be also valid in the case of a climatic perturbation.

Beside abrupt climatic transition, we also explored the impact of a perturbation of 10 kyr duration on soil dynamics. During this time span, all climatic parameters (Table 2.I) are assumed to vary linearly from one climate to the other. Results are shown in Figure 2.6. In all cases, the evolution of sediment supply during the transition greatly differs from the evolution in the case of an abrupt climatic transition. This is mainly due to the action of solifluction—and its interaction with other processes—, which peaks when the Mean Annual Air Temperature (MAAT) crosses 0°C (see chapter 1). For high K_g values, soil transport rates can be extremely high (e.g., Figure 2.6 C1-C2-D1-D2). However, these high soil fluxes don't seem to affect the response time of the system (except for the cases C1 and D1, where solifluction fluxes are much higher than in the other cases).

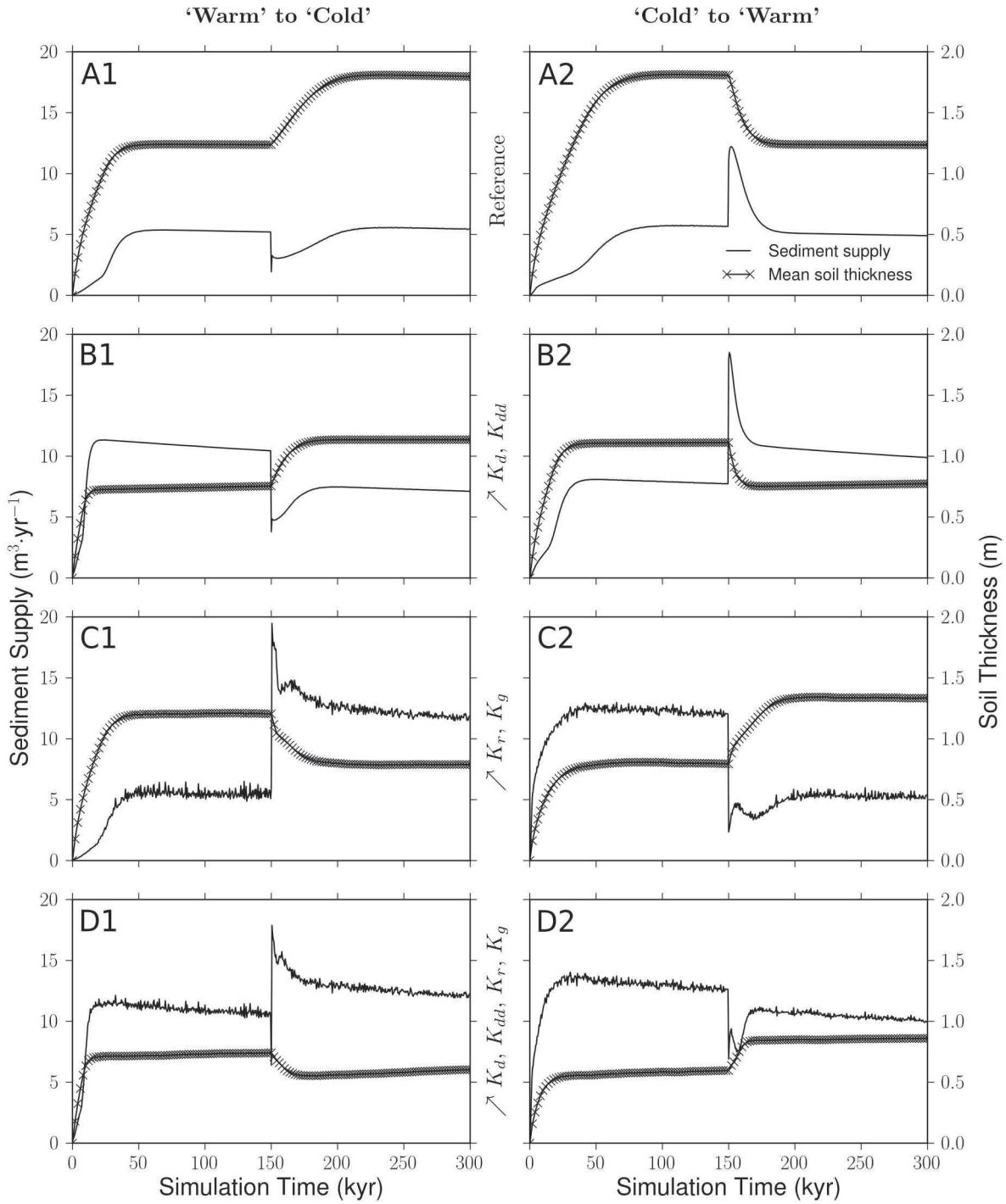

Figure 2.5: Simulation results using climatic scenarios characterized by an abrupt transition from the warm to the cold climate (left column) or from the cold to the warm climate (right column) (see text for a description of these climates): seasonal cycle averaged sediment supply (i.e., rate of soil loss through the lower boundaries of the synthetic hill) and mean soil thickness (i.e., average over the whole hill). A. A reference case. B. Higher values for K_{dd} and K_d than values in the reference case. C. Higher values for K_r and K_g. D. Higher values for all transport coefficients. See Figure 2.3 caption for values of the coefficients of the transport laws and Table 2.II for the values of the other model parameters.

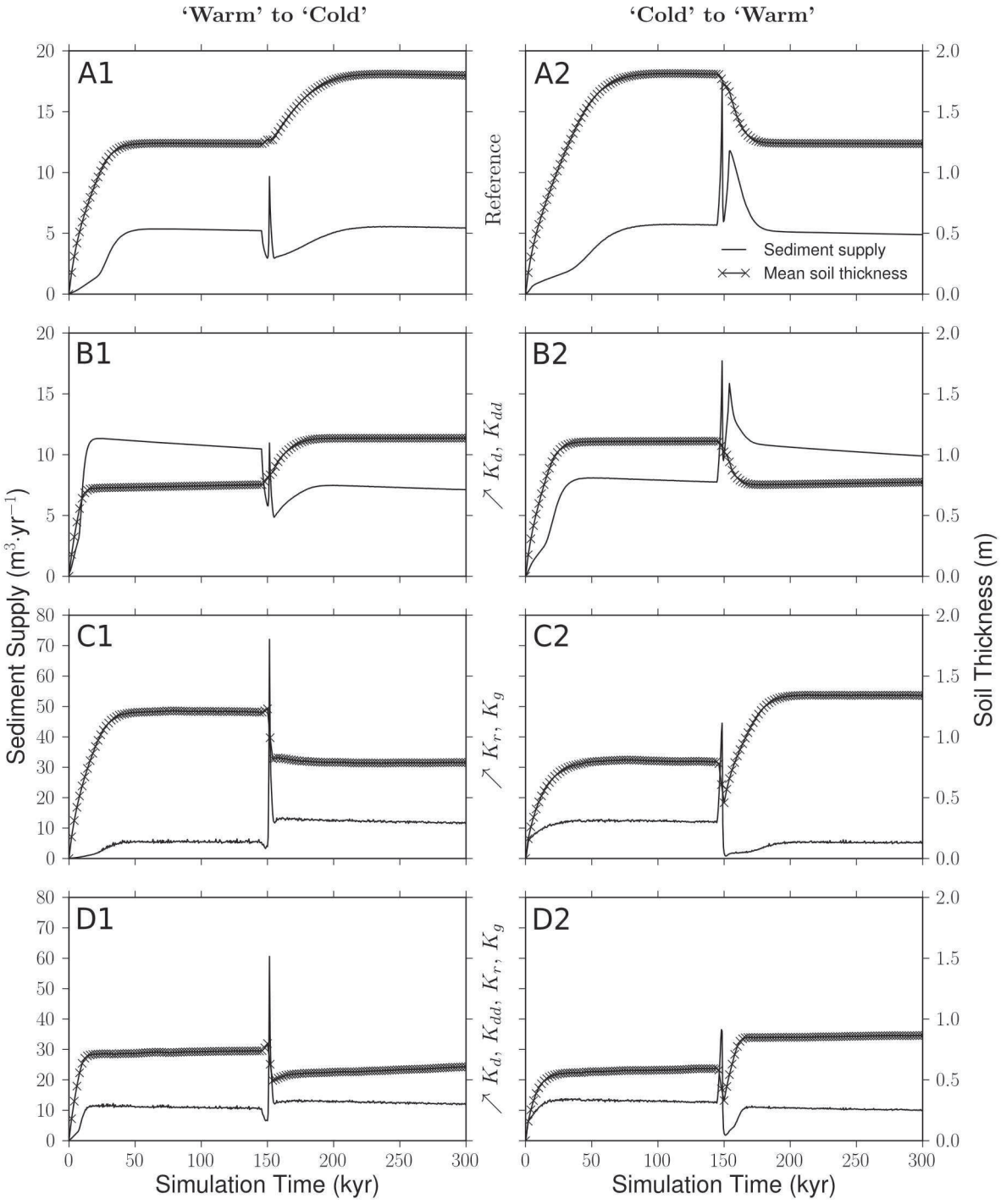

Figure 2.6: Simulation results using climatic scenarios characterized by a 10 kyr transition from the warm to the cold climate (left column) or from the cold to the warm climate (right column) (see text for a description of these climates): seasonal cycle averaged sediment supply (i.e., rate of soil loss through the lower boundaries of the synthetic hill) and mean soil thickness (i.e., average over the whole hill). Note the differences in the y-axis scale. See Figure 2.5 caption for more informations on the simulation setup.

2.6 Discussion and concluding remarks

Simulation results presented in this chapter clearly outline that hillslope geometry and soil transport parameters play important roles governing the style and rate at which the hillslope system evolves towards an equilibrium. As shown in Figures 2.3, 2.5 and 2.6, the difference in model behaviour between cold and temperate climates highly depends on the combination of values chosen for the transport parameters. It is for example possible, under the cold climate, to produce response times of the system that are shorter, longer or equivalent to response times under the temperate climate. Soil transport parameters similarly affect mean soil thickness and sediment supply at steady-state, as these variables are both closely correlated to response time (the correlation is positive for mean soil thickness and negative for sediment supply). The large range of possible model behaviours demonstrate the potential of CLICHE to address the problem of climatic variability in the assessment of field-based values for the parameters of the climate-independent transport laws. For example, field-estimates of hillslope diffusivity—i.e., the diffusion coefficient, using only the diffusion equation to simulate hillslope erosion—summarized in Fernandes and Dietrich (1997) show a strong increase in diffusivity from semi-arid to humid-temperate climates. By contrast, Bogaart et al. (2003a), who have compared diffusivities found in the literature (e.g. McKean et al., 1993; Martin and Church, 1997) with diffusivities derived from solifluction rate measurements (French, 1996), have concluded that hillslope diffusivities may not vary significantly between cold and temperate climates (the authors have, however, not considered the cold-temperate transitions). Depending on the combination of values chosen for the transport coefficients, it is possible, with CLICHE, to confirm either the poor or the strong correlation between climate and transport efficiency.

In fact, a poor correlation between climate and transport efficiency does not reflect the relative independence of soil transport processes with respect to climatic variations, but may rather result from the different behaviour of each transport process, as suggested by the sensitivity analysis made here. The difference in response time between the cold and the temperate climate seems to be function of the difference in parameter values between K_d and K_{dd} on one hand, and K_r and K_g on the other hand. The sensitivity analysis have also shown how each soil transport process affects differently the time response of the system, depending on whether the system is under the cold or the temperate climate. We therefore expect that natural experiments which have experienced high climate changes in the past provide good constraints on the soil transport parameters.

Chapter 3

Soil production and transport in mid-latitudes during the last glacial-interglacial cycle: A combined data and modelling approach

3.1 Introduction

In chapter 2, we have presented generic applications of CLICHE that have demonstrated the contrasted behaviours of the model in relation to cold and temperate climates and model parameters. Modelling hillslope processes is helpful to have access to the long-term soil and slope dynamics and to explore its complexity, but models need to be constrained by observations. Many authors relied on topographic data to test their model predictions (e.g., Rosenbloom and Anderson, 1994; Roering et al., 1999; Martin, 2000; Jiménez-Hornero et al., 2005). However, as pointed out by Furbish (2003) and Roering et al. (2004), additional information should often be considered when testing and calibrating the growing suite of landscape evolution models which continuously increase in complexity. In other studies, both soil thickness and topographic data were used to infer soil production, soil transport, and/or hillslope erosion rates (e.g., Dietrich et al., 1995; Heimsath et al., 1997, 1999, 2000; Braun et al., 2001; Herman and Braun, 2006; Roering, 2008; Pelletier and Rasmussen, 2009; Tucker et al., 2011).

In this chapter, we propose to use the extensive amount of existing soil thickness and elevation data in the Belgian Ardenne (NW Europe) to constrain both soil production and soil transport during the last glacial-interglacial cycle, with the help of the CLICHE model (see chapter 1) coupled with an inversion method (the NA-alogrithm: Sambridge, 1999a,b). The Belgian Ardenne is taken as a reference case of low to moderate-relief landscapes in mid-latitudes, that have been subjected to significant climate variations during the glacial-interglacial periods of the Quaternary (Vandenberghe et al., 2004), but where no evidence of former glacial activity has been found (Ehlers and Gibbard, 2004).

The work proposed here is very challenging for several reasons. Firstly, we only use current soil thickness and elevation data to constrain hillslope dynamics through the last 120 kyr. Braun et al. (2001) and Herman and Braun (2006) have successfully constrained a multi-parameter model of soil transport using data of soil thickness versus surface curvature (at least for soil creep processes, as their data contained little information about transport by overland flow). However, the authors also used other independent constraints on soil production rates, and their study area was specifically chosen to minimize the influence of former climate variations on soil dynamics. It is not the case in our study and difficulties may therefore arise, although we propose to explore the relationships of soil thickness not only to curvature, but also to other terrain attributes such as slope and drainage area. Secondly, both soil thickness and topographic data used here have a relatively low precision (i.e., only broad soil thickness classes are available in the database we use and the spatial resolution of the topographic data is equal to 20 m), whereas almost all studies mentioned here above took advantage of high resolution data (generally from 5 m to sub-meter resolution). Meter-resolution data is generally required as fine-scale topographic features are the signature of interesting and relevant transport processes, e.g., bioturbation and slow transport due to wetting-drying or freeze-thaw cycles (Roering, 2008). But other processes, which generally transport the soil at much longer scales (Furbish and Haff, 2010), have probably been active in the Ardenne during the glacial periods (Juvigné, 1993; Pissart, 1995; Rixhon and Juvigné, 2010). Thirdly, the extended data used here provides constraints to study hillslopes as a whole in our region of interest, contrary to high resolution data that are still not widely available

nowadays and therefore force the researchers to restrain their investigations to relatively small hill sites. But here again, complications may arise from lithologic, tectonic and/or topographic heterogeneities encountered in the study area, which may compromise the success of our inversion, although the topographic variety is handled by our methodology and all other heterogeneities are admittedly minor in the Ardenne (if put in a larger regional perspective). Finally, we define a very simple scenario for the climate of the last 120 kyr where both glacial and interglacial periods are characterized by a relative internal climatic stability. Reconstructions of global and European past climates (e.g., Genty et al., 2005; Kageyama et al., 2010; Singarayer and Valdes, 2010) show that this scenario is clearly unrealistic, at least for the glacial period, but such a simplified forcing should initially facilitate our comprehension of hillslope dynamics throughout the last glacial-interglacial cycle.

For all these reasons, we cannot state that this study does provide a precise calibration of the soil production and transport laws implemented in the CLICHE model. Despite careful handling of estimated data uncertainties in the model inversion procedure, we expect only a rough, but hopefully apparent, constraint level on soil production and transport mechanisms related to both the cold and temperate environments that alternated or succeeded one another during the past 120 kyr in the Ardenne. Nevertheless, we think that our inversion procedure may bring into light several quantitative aspects of hillslope dynamics under varying climate, e.g., the predominance, segregation and/or succession of specific transport processes or the responses to climate transitions in terms of denudation rate, sediment supply to the channels and the establishment of a dynamic equilibrium. Futhermore, as we perform our investigations in an extended study area, the outcome of the inversion should also indicate whether the climate control on hillslope dynamics prevails against other factors such as lithology or even tectonics. Indubitably, the inversion results should reveal which parameters can or cannot be constrained by present-day soil thickness and topographic data.

3.2 Study area and observational constraints

As a case study of hillslope soil production and transport under varying climatic conditions, the Ardenne Massif comprises most of the ingredients of a suitable natural experiment as proposed by Tucker (2009b). First, contrary to long-term fluvial incision of major streams which are often regarded as the erosional response to a tectonic uplift (Demoulin et al., 2009; Demoulin and Hallot, 2009; Rixhon et al., 2010; Sougnez and Vanacker, 2011), climate variability is supposed to be the main factor that has controlled hillslope erosion in the Ardenne Massif since 0.7 Ma (Demoulin et al., 2009). Interpretations of paleo-environmental data indicate that the landscape of NW Europe has drastically changed during the Quaternary climate variations (Vandenberghe et al., 2004). Although only a small number of slope deposits and landforms of the present-day Ardennian landscape have been explicitly attributed to the past periglacial activity (e.g. Alexandre, 1958; Pissart and Gullentops, 1967; Pissart, 1976), it is well accepted that erosion processes on hillslopes were by far more active under the periglacial environment the massif has experienced during the cold phases of the Quaternary than under the temperate environment of the Holocene (Pissart, 1995).

Within the massif, many of the landscape characteristics that are not explicitly taken into account in the CLICHE model can be roughly considered as spatially uniform at the regional scale and thus should not affect the robustness of our analyses. Indeed, from a geological point of view, the Ardenne Massif corresponds to the western prolongation of the Paleozoic Renish Shield. In the NE Ardenne, the Cambrian Stavelot massif is comprised of phyllites and quartzites and is surrounded by Ordovician and early Devonian slates mainly to the south and east, and middle and late Devonian sandstones, shales and limestones in the north and west (Demoulin et al., 2009). To avoid the limestones and related karst landscapes, we restricted our study area to three contiguous catchments of the NE Ardenne: the Vesdre (excluding the northern part of the basin), the Amblève and the Two Ourthes rivers which are tributaries or sub-tributaries of the Meuse river (Figure 3.1). Apart from the sub-horizontal plateaus (such as the Hautes-Fagnes plateau) and the alluvial plains, most of this area is covered by gravelly soils (Figure 3.2 A). As these soils are often chemically poor (Petit and Lambin, 2002), they are poorly suited for agriculture, which limits the impact of recent human activities on present-day soil mantle. Moreover, the relative small size of the study area (latitudinal extent $\sim$ 90km and longitudinal extent $\sim$ 60km), its location on the northern flank of the Ardenne Massif and its low to moderate relief (up to a few hundred meters) lead us to hypothesize that all catchments have been subjected to rather similar climatic conditions (Sougnez and Vanacker, 2011). At the same time however, the extent of the study area is large enough to encompass a wide range of hill configurations where local climatic, lithological or hydrological conditions have formed specific landforms and deposits (e.g., asymmetrical valleys firstly identified by Alexandre, 1958).

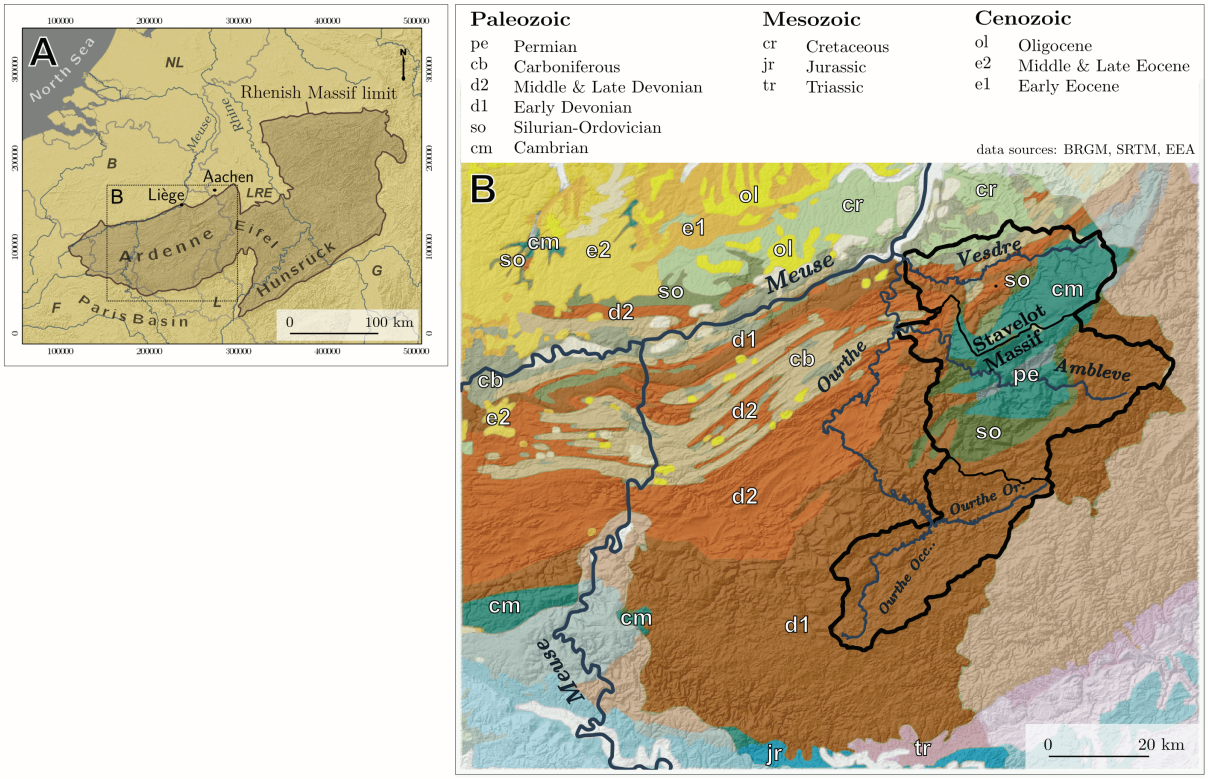

Figure 3.1: A. Localization of the Rheinish Massif (NW Europe) (B: Belgium; L: Luxembourg; F: France; D: Germany; NL: Netherlands; LRE: Lower Rhine Embayment). B. Simplified geological map of the Ardenne Massif and localization of the study area (thick black line).

Another great asset of the Ardenne Massif is the high amount of available topographical, geological and soil data. Here we make use of two data sources: a rather unique soil map covering the whole territory of Wallonia (S Belgium) and a gridded 20x20m Digital Elevation Model (DEM) provided by the Belgian National Geographical Institute (IGN) (IGN, 2007). The Digital Soil Map of Wallonia (DSMW) is an extensive cartographic database that contains, for contiguous polygons called soil units, much information on soil properties including information on soil thickness (Veron et al., 2005; PCNSW, 2007). This map is the result of a high-resolution intensive grid survey by augerings carried out during the last century. The limits of the mapped soil units —600 000 polygons in total—were drawn at field level, on cadastral plans at 1/5000 scale, before being transferred onto a topographical background.

Very high resolution ($\sim$ 1m) DEMs generated from LiDAR (Light Detection And Ranging) data also exist, but only for isolated areas spread over our region of interest. So we decided to work with the "DTM 1:10 000" of the IGN which entirely covers the Vesdre, Amblève and Ourthe catchments, but which in turn has a coarser resolution of 20m. This Digital Terrain Model is developed from photogrammetric derived points and structure-lines, airborne detail laser-scanning and field point observations (IGN, 2007). The "DTM 1:10 000" has the advantage of storing elevation values that correspond to the ground surface (not the top of the canopy) and has already been used in other geomorphological applications (Demoulin et al., 2007; Sougnez and Vanacker, 2011).

3.2.1 Surface derivatives vs. soil thickness in the Ardenne Massif

Inside the study area, we first attempt to quantify the hillslope morphology by deriving several terrain and topo-hydrological attributes from the DEM. However, the gridded DEM provided by the IGN contains several artefacts including a staircase-like behaviour of the modelled topography (Sougnez and Vanacker, 2011). This unwanted effect has a strong influence on the DEM-derived attributes and has to be removed. Re-interpolating the original 3D points over a 20x20m grid addresses the problem. Among the multiple interpolation schemes we have experimented with, we have retained the bicubic spline interpolation with Tykhonov regularization, implemented in GRASS GIS (Brovelli et al., 2004; GRASS Development Team, 2008), because it offers the best compromise between the reduction of the staircase-like behaviour and the smoothing of the real topography. Other reported DEM-artefacts like sinks in narrow valleys are less important for our purpose. The hydrological correction of the DEM has therefore been skipped in our case. Three basic variables are derived from the re-interpolated DEM: surface slope S, curvature C and drainage area A. Slope is the gradient of the terrain surface (i.e. the 1st order derivative, ∇z) and is approximated using a 3rd order finite difference scheme given by the Horn's formula implemented in GRASS GIS (Horn, 1981). Many geoprocessing softwares also implement algorithms to calculate profile or plan curvatures (i.e. curvatures of specifically-oriented sections of the surface), but the curvature derived here, noted $\nabla^2 z$, characterizes the surface in all directions and is more thus consistent with the generally accepted laws of soil transport (Dietrich et al., 2003). $\nabla^2 z$ is approximated using a 2nd order finite difference scheme that produces results similar to those from algorithm used by Dietrich et al. (1995) and Heimsath et al. (1999).

A multiple flow direction algorithm is finally applied to derive drainage area (Holmgren, 1994). In practice, all calculations described above are partially based on the elevation values of a DEM grid node and its eight nearest neighbours.

From the soil map, we then automatically select by a set of GIS operations the smallest gravel-soil units that are exclusively located on the hillslopes within the study area. The selection is made so that the values of the DEM-derivatives can roughly be considered as constant within each soil unit. The maximum planimetric extent accepted for a soil unit is fixed to 3600 m^2, which is equivalent to the area of the convolution kernels used to derive the terrain attributes from the DEM. To further narrow the selection while keeping a sufficient number of soil units, we also define by trial and error a maximum standard deviation threshold for each DEM-derivative sampled inside a soil unit. Measurements of soil thickness are not directly available in the soil map database, but two attributes of the database, named "PHASE_1" and "PHASE_2", give information on the depth to the substratum for each soil unit. These attributes take a numerical value that, depending on the soil type, can be related to a specific range of soil thickness. Four variable-size classes of soil thickness are identified after the interpretation of the map's legend (Table 3.I).

Table 3.I: Soil thickness classes for gravelly soils, reconstructed from the legend of the soil map, and number of selected soil units for each class c and DEM-derivative d ($N^o_{d,c}$ with $d \in [S, C, A, A*]$ and $A* = A^{-0.5}$). The number of selected soil units differs from one DEM-derivative to another due to the maximum standard deviation thresholds defined for each DEM-derivative (see text).

# class (c)	PHASE_1/2	class limits (cm)	$N^o_{S,c}$	$N^o_{C,c}$	$N^o_{A,c}$	$N^o_{A*,c}$
1	6	0 to 20	288	153	885	684
2	4, 5	20 to 40	2009	1418	2775	1989
3	2, 2_3, 3, 7	40 to 80	7155	5950	6423	3787
4	0_1, 1	$>$ 80	3127	2650	2446	1250

By averaging the values of DEM-derivatives over the extent of the selected soil units, we finally estimate the observed present-day distributions of each calculated DEM derivative d (i.e. slope, curvature and drainage area) for each soil thickness class c, which gives a total of 12 observed distributions. The normalized cumulative distributions—or empirical distribution functions—are given by:

$$F^o_{d,c}(x) = \frac{1}{N^o_{d,c}} \sum_{i=1}^{N^o_{d,c}} I_{d_i}(x) \tag{3.1}$$

where $F^o_{d,c}(x) \in [0;1] \forall x$, $I_{d_i}(x)$ is the indicator function, equal to 1 if $d_i \leq x$ and equal to 0 otherwise (d_i is the value of the DEM-derivative d assigned to the selected soil unit i), and $N^o_{d,c}$ is the number of soil units selected for the DEM derivative d that belong to the soil class c.

Preliminary results and discussion

The resulting map of soil thickness shown in figure 3.2 clearly outlines the dual character of the Ardenne landscape. The western part of the Ambleve basin and the south-western part of the

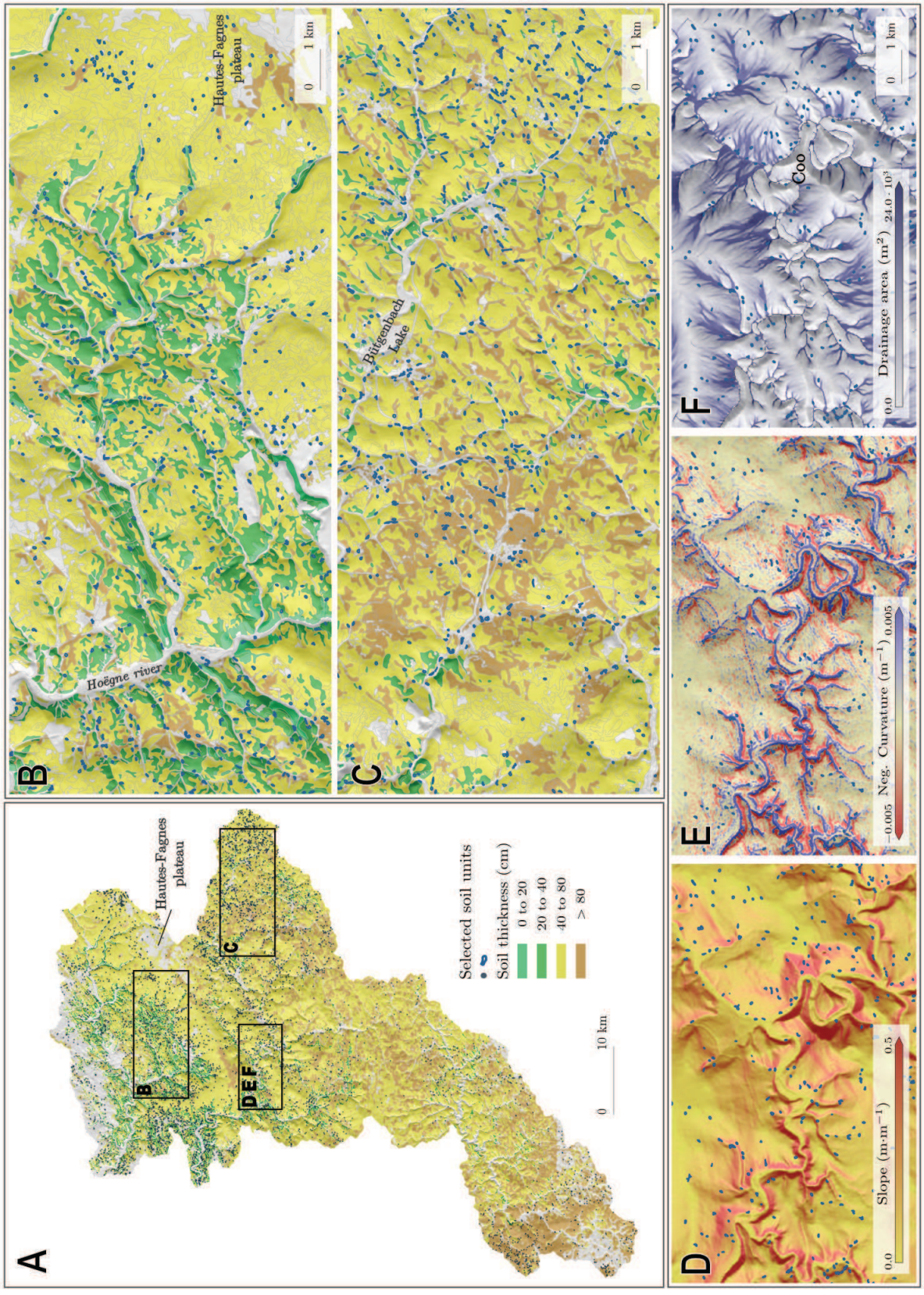

Figure 3.2: Study area: thickness map of gravel soils reconstructed from the Digital Soil Map of Wallonia (DSMW) (A,B,C), and terrain attributes derived from the re-interpolated IGN's DTM (D,E,F), with hill-shading. Soil units selected by an area threshold of 3600 m^2 are represented with the small blue points (A) or areas (B,C,D,E,F). B-C: map subsets showing respectively the moderate relief with shallow soils and the low relief with thicker soils (Contours of the soil map's contiguous soil units are drawn in light grey). Grey-filled soil units correspond to other soil layers than hillslope gravel soils (alluvial plains, sandy or organic soils...).

Vesdre basin present a moderate relief in which the major rivers and most of the main tributaries are well incised. The thickness of the soil mantle is variable and generally less than 40cm on the steepest valley-sides. This moderate relief contrasts with the low relief found in the upper part of the major rivers catchments (eastern Vesdre, eastern Ambleve and the Two Ourthes), where soil cover is uniformly thick. The contrast between these two landscapes is commonly regarded as the result of a fluvial erosion wave that has propagated into the Ardenne Massif since ~ 0.5 Ma (Rixhon et al., 2010; Demoulin et al., 2009). Channel incision has steepened the side slopes in the lowest valleys while the incomplete propagation of the erosion wave left slopes relatively unchanged in the upper part of the main catchments. In both cases however, soil mantle is sufficiently thick to qualify the present-day Ardenne landscape as a transport-limited landscape (i.e. the capacity to produce regolith is high in comparison to the capacity to mobilize regolith), contrary to weathering-limited landscapes that are bedrock-dominated (Kirkby, 1971; Carson and Kirkby, 1972; Dietrich et al., 2003).

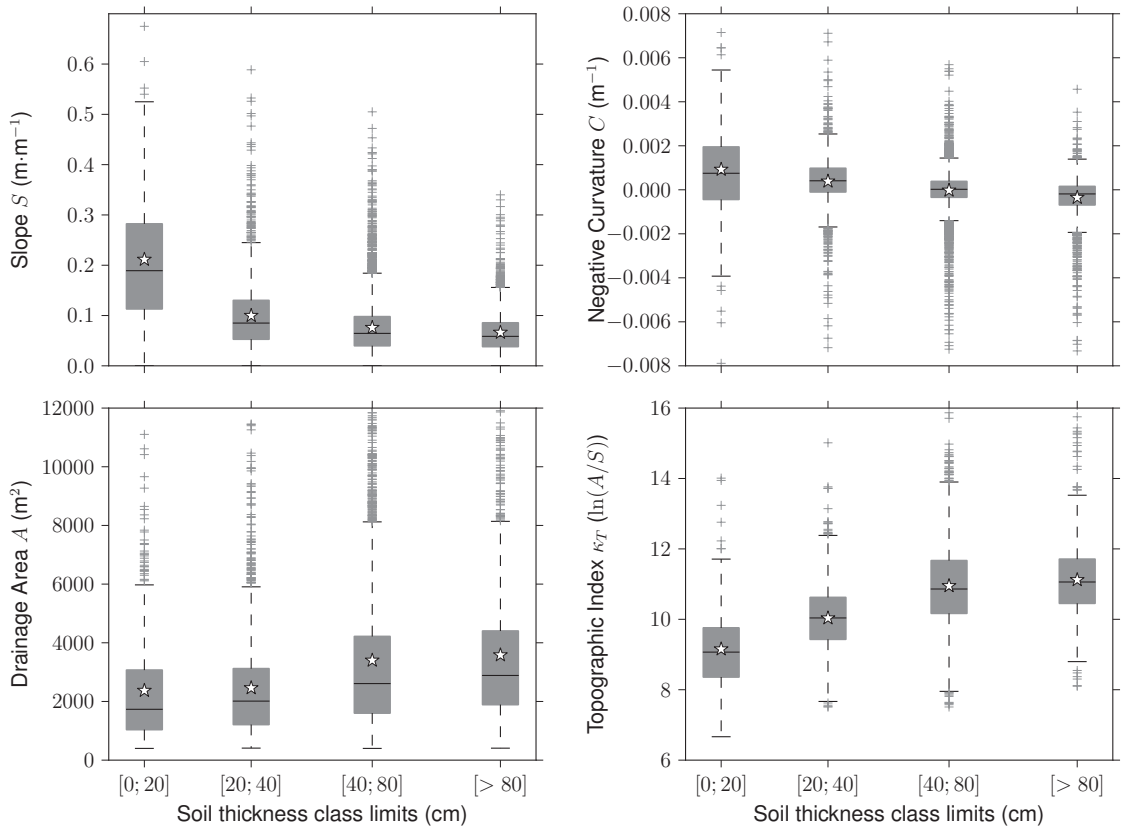

Figure 3.3: Boxplot representation of the distributions of the DEM derivatives values extracted from the selected soil units, for each soil thickness class defined by the soil map. The grey-filled boxes are bounded by the lower and upper quartiles and the bands near the middle of the boxes are the medians (the means are represented by white stars). The length of the whiskers are specified as 1.5 times the interquartile range and flier points in the distributions are those past the end of the whiskers.

Figure 3.3 also shows well-defined relationships between soil thickness and surface derivatives. If we consider the means or the medians of the distributions, we observe that negative curvature decreases with increasing soil thickness, as previously shown in data collected in northern California (Heimsath et al., 1997, 1999) and southeastern Australia (Heimsath et al., 2000).

This is expected if curvature is a surrogate for soil production and soil production decreases with soil thickness (Heimsath et al., 1997). But here the decrease is relatively small compared to the large variance observed for each distribution and the significant decline of the variance itself with increasing soil thickness. Possible causes of large variances also observed in northern California includes short-term variation in local thickness due to biogenic soil production and bedrock heterogeneity in resistance to weathering, as discussed by Heimsath et al. (1997). However, the resolution of the data we use here is not fine enough to deal with these small-scale heterogeneities. The presence of shallow soils in both high divergent and convergent areas remain unexplained and could be an artefact of the data or its resolution. Like curvature, slope and the variance of its distributions also decline with increasing soil thickness but, in this case, the relation is exponential. This means that thick soils are mainly located in sub-horizontal and flat areas such as the plateaus at the hill tops or at the base of the hills near the alluvial plains. The relationship between drainage area and soil thickness is not as clear as the slope or curvature vs. soil thickness relationships although a positive trend is perceptible. Nevertheless, a strong positive non-linear relation is obtained with the topographic index κ_T, defined from drainage area and slope ($\kappa_T = \ln(A/S)$). This index has been extensively used in the development and application of TOPMODEL, a spatially distributed hydrological model at the catchment scale (Beven and Kirkby, 1979). In TOPMODEL, the index is used as a measure of hydrological similarity (Beven, 1997). The well-defined relation observed in our data between this index and soil thickness lets us therefore suppose that transport of soil by water flow has been a dominant process on hillslopes in the Ardenne Massif.

3.3 Simulation of soil production and soil transport on a synthetic hill using the CLICHE model

By simulating soil production and soil transport on a synthetic hill, our purpose is to generate a spatial distribution of the soil mantle that can be compared to the observations. Although soil production is represented by a unique empirical law that does not depend on climate (mostly due to a lack of constraints), the parametrization of soil transport in CLICHE has been selected to simulate hillslope erosion under both temperate and periglacial environments.

Among the multiple transport laws implemented in CLICHE, we choose to represent here the total downhill soil flux by using four possible processes that are or have been predominant in the Ardenne: simple creep, depth-dependent creep, transport by overland flow and annual solifluction. The temperate rainfall regime and the modest slopes characterizing the Ardenne Massif ensure that soil transport by landsliding has been insignificant since the begin of the Holocene. Isolated hilly areas covered by loose sediments in surrounding regions are known to have been affected by old deep-seated landslides (Van Den Eeckhaut et al., 2005; Dewitte et al., 2008), but until now no trace of such events has been reported in the Ardenne Massif. However, recent observations made in high latitude environments (e.g. Lewkowicz, 1990) and evidence for the past presence of a discontinuous permafrost in the Ardenne (Vandenberghe and Pissart, 1993; Huijzer and Isarin, 1997) suggest that shallow active layer detachments or debris flows have occurred during the cold phases of the Quaternary with a non-negligible frequency, even if their

residual deposits are sparsely observed in the massif (Juvigné, 1993). The occurence of these rapid and shallow events depended less on the local slope than on slope instability caused by saturated moisture conditions within —or at the base of —the thawing active layer (Lewkowicz, 1990). One can therefore reasonably integrate their long-term averaged effects through the sub-continuous solifluction law parametrized in CLICHE, while keeping in mind that the processes involved are very different. Note that this solifluction law doesn't include processes governed by diurnal freeze-thaw cycles (e.g. diurnal frost creep). However, the latter have been shown to be become dominant only on steep slopes and where climate is devoid of seasonal variability (e.g., high altitude mountain environments) (Matsuoka, 2001). Beside slope processes, aeolian processes are known to have also been active during the cold phases of the Quaternary in NW Europe (Frechen et al., 2001). In CLICHE however, soil thickness is only controlled by the balance between local soil production from the underlying bedrock and removal or accumulation by slope processes, an thus aeolian inputs cannot be taken into account. Nevertheless, the sparse aeolian deposits actually found in the Ardenne let us presume that the influence of former aeolian activity on the present-day soil thickness can be considered as second order in our study area.

Futhermore, we consider that the simulation of hillslope erosion over the last glacial-interglacial cycle ($\sim$ 120 ky) only is sufficient to reproduce the spatial distribution of soil mantle observed in the Ardenne Massif. Simulations on such a short timespan can be made given: (1) the periodicity of the Quaternary climate variations, (2) the assumption of very efficient soil transport under periglacial conditions decreasing the time response of the Ardenne hillslopes to climate transitions (as shown in chapter 2) and (3) the unknown initial conditions. Our lack of knowledge on the state of the soil mantle 120 ky ago —at the end of the Eemian —compels us to define simplified initial conditions that consist of a uniform soil cover with a unknown thickness h_{t0} for the whole synthetic hill. Other initial (shape of the synthetic hill), limit (climate and tectonic settings) and boundary (connection between hillslope and river systems) conditions set for the CLICHE simulations are detailed in the sections below.

3.3.1 A simplified scenario of climate in NW Europe for the last glacial-interglacial cycle

A large amount of work has been devoted to the reconstruction of past climates and related environments, either from proxy data (e.g. ice cores, pollen records, aeolian activity, periglacial evidences) or Global Circulation Model (GCM) experiments. Bogaart et al. (2003b) have synthesized a great number of publications on temperature reconstruction and estimation of palaeo-precipitation rates for NW Europe and more particularly the Meuse catchment encompassing the Ardenne Massif. But unfortunately, most of these reconstructions are restricted only to the last glacial-interglacial transition (14 to 9 ^{14}C kyr BP). GCMs or Regional Climate Models (RCMs) are useful to physically reconstruct high resolution time series —time steps down to 1 day —needed to discriminate hydrological events which, for example, drive the transport of soil by overland flow in CLICHE. However, the majority of modelling studies with GCMs have also focused on recent key time periods in the last glacial-interglacial cycle (Singarayer and Valdes, 2010), including the Last Glacial Maximum (e.g. Kageyama et al., 2006; Laîné et al., 2008), the main warming events during the last glacial-interglacial transition (e.g. Renssen and

Isarin, 2001) and the Mid- to Late Holocene period (Wanner et al., 2008). The first results from a large set of GCM simulations covering the entire last glacial cycle have recently been published by Singarayer and Valdes (2010), although, in this study, the temporal resolution of the "snap-shot" simulations—from 4 ky up to 1 ky between successive model runs each of 500 years duration—was too long to catch the abrupt warming events that succeeded during the glacial period. These so-called 'Dansgaard-Oeschger' events have only recently been studied through the use of sophisticated GCMs (e.g., Flückiger et al., 2008; Kageyama et al., 2010) and their modelling remains a conceptual and technical challenge (Kageyama et al., 2010).

Table 3.II: Parameters for the CLICHE's weather generator related to the 'warm' and 'cold' phases of the climate scenario.

	J	F	M	A	M	J	J	A	S	O	N	D
'warm' phase												
$\overline{T}_m$ (°C)	2.2	2.8	5.7	8.9	12.9	16.0	17.6	17.3	14.4	10.4	6.1	3.2
$\overline{P}_m$ (mm/d)	3.81	3.81	3.84	4.08	4.55	5.40	5.48	5.37	4.96	4.58	4.05	4.14
$\Pr(D \mid D)$	0.63	0.66	0.67	0.68	0.66	0.66	0.66	0.68	0.68	0.66	0.59	0.61
$\Pr(W \mid W)$	0.72	0.72	0.70	0.69	0.66	0.64	0.64	0.64	0.63	0.63	0.68	0.70
'cold' phase												
$\overline{T}_m$ (°C)	-20.0	-18.0	-13.0	-7.0	0.0	6.0	8.0	6.0	0.0	-7.0	-13.0	-18.0
$\overline{P}_m$ (mm/d)	1.89	1.75	1.59	1.59	1.34	0.85	0.36	0.41	1.01	1.51	1.81	2.11
$\Pr(D \mid D)$	0.30	0.20	0.10	0.35	0.40	0.70	0.78	0.75	0.62	0.40	0.35	0.05
$\Pr(W \mid W)$	0.90	0.85	0.92	0.95	0.80	0.45	0.38	0.38	0.60	0.80	0.92	0.95

A weather generator like the one implemented in CLICHE has the ability to integrate the sparse time results of the multiple GCM experiments mentioned above, and eventually to correct GCM predictions that are known to be too cold or too warm, in order to reproduce continuously changing and more accurate time series of temperature and precipitations (Bogaart et al., 2003b). However, collecting and verifying the accuracy of many GCM predictions in our study area would be a long and hard task. We therefore preferred to initially adopt an extremely simple scenario for the climate of the last glacial-interglacial cycle, expecting that this scenario is likely to be refined in the future.

Both 'cold' and 'warm' phases of the cycle are here represented by a constant and stable climate. Each phase is characterized by the monthly average values of air temperature $\overline{T}_m$ and mean daily rainfall rate $\overline{P}_m$ and the conditional probabilities that a dry day is followed by another dry day $\Pr(D \mid D)$ and the equivalent for wet days $\Pr(W \mid W)$. These values are used as input parameters for the CLICHE's weather generator. Parameters for the warm phase are calculated from the analysis of observed daily time series of the present-day climate in NW Europe. These time series are provided by the European Climate Assessment and Dataset (Klein Tank et al., 2002) and the Aachen station (W Germany) is taken as the reference for our study area. Climate of the cold phase is based on the analysis of daily outputs of AGCM experiments for the Late Pleniglacial. These experiments are described in Renssen and Isarin (2001) and outputs for the Meuse catchment are presented in Bogaart et al. (2003b). All parameters are assumed to vary linearly during the transitions between cold and warm phases. Parameters for the cold and warm phases are shown in Table 3.II and the resulting time series, generated by the weather generator,

are plotted in Figure 3.4. The modelled last glacial-interglacial cycle starts at the end of a warm phase (the Eemian), then after a transition of 30 ky, a long cold phase holds for 75 ky until a short transition of 4 ky leads to the last warm phase (Holocene). The duration of the two transitions is fixed so that the evolution of mean annual temperature follows approximately the bottom envelope of the $\delta^{18}O$ curve as measured in the GRIP Greenland ice core (Figure 3.4A-B).

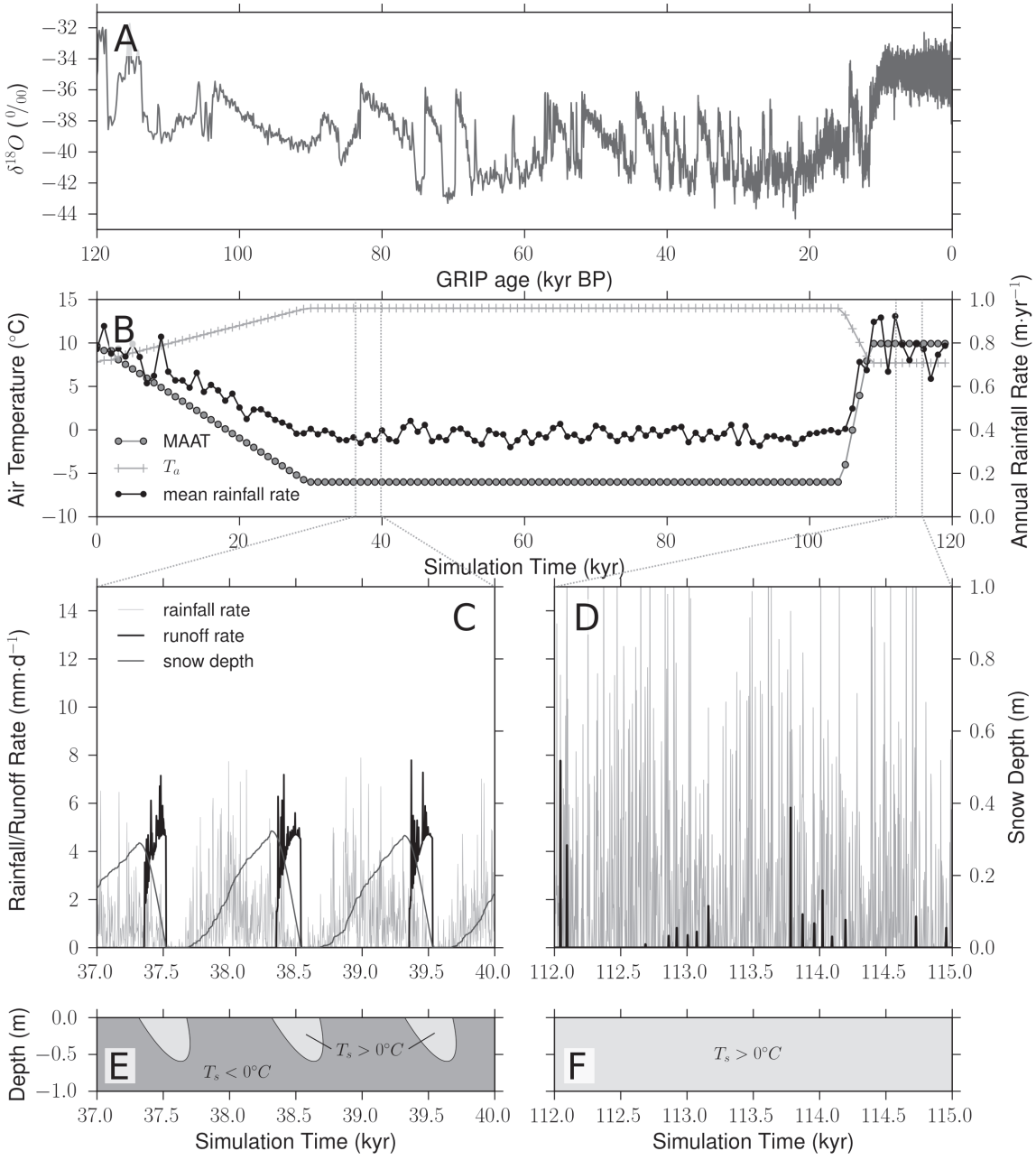

Figure 3.4: Climatic scenario for the last glacial-interglacial cycle. A. The GRIP $\delta^{18}O$ record since 120 kyr BP (Johnsen et al., 1997). B. Time series of Mean Annual Air Temperature (MAAT), semi-annual variation of air Temperature (T_a) and annual rainfall rate, extracted from the CLICHE's weather generator outputs for the whole glacial-interglacial cycle. C-D. Short time spans showing, for respectively the 'cold' and 'warm' phases of cycle, the 'elongated' daily time series of mean rainfall rate generated by the weather generator and snow depth and surface runoff computed by the hydrological component of CLICHE (cycle elongation factor = 1 kyr). E-F. Soil profile conditions—i.e., frozen (dark grey) or unfrozen (light grey)—as calculated by the thermal component of CLICHE for the same time spans than C-D. Note the presence of a seasonal active layer during the cold phase (E).

From a pure climatological point of view, the scenario defined here is somewhat inaccurate and unrealistic. However, as we have previously shown that the response of hillslope to abrupt climate changes may be a strongly non-linear function of the efficiency of soil transport (depending on the parameters of the soil transport laws), starting with a very simple climate scenario where abrupt transitions are limited in number should initially facilitate the interpretation of the results and the description of the modelled hillslope system during both cold and warm phases. The smooth climate variations in the scenario also allow us to choose a relative high value (1 ky) for CLICHE's cycle elongation factor and thus reduce the computational effort needed for the model runs.

3.3.2 Calibrating hydrological and thermal parameters

Table 3.III shows the values chosen for the fixed parameters of the CLICHE's hydrological and thermal components. Soil temperature damping depth—i.e. the single parameter of the thermal component —is generally of the order of 0.5-1.0 (m) (Kirkby, 1995). The hydrological parameters were calibrated by Bogaart (2003) using, for temperate conditions, data on present-day discharges of the Meuse River close to our study area (southern Netherlands), and for cold conditions, model tests on the periglacial Tana catchment (northern Norway/Finland). Bogaart (2003) also discussed the values of each parameter. Here we arbitrarily modified the calibrated value of some of these parameters (i.e. the soil layer storage capacities and the runoff separation coefficient) to produce more realistic runoff rates for both temperate and cold conditions, as observed from actual discharge data of the Vesdre river (temperate conditions) and reported in high latitude cold environments by several authors (e.g. studies of Bengtsson and Westerström, 1992; Stähli et al., 2001; Rawlins et al., 2003, at different spatial scales). During the cold phase of the climate cycle, runoff occurs during the spring and is mainly due to snow melt (Figure 3.4 C), while annual rates reach $\sim$ 300 mm·yr^{-1}. By contrast, the temperate conditions are characterized by much lower annual runoff rates with only an average of 5-6 daily events per year of average rate $\sim$ 3 mm·day^{-1} (Figure 3.4 D). However, due to the daily temporal resolution of the hydrological time series, it does not include runoff resulting from short convective rainfall events. Note that the generated runoff is spatially uniform because the CLICHE's hydrological component is lumped over the whole synthetic hill. Overland flow discharge is approximated by integrating runoff over drainage area.

Table 3.III: Parameters values fixed for CLICHE's hydrological and thermal components.

parameter description	parameter	value	(units)
Soil temperature damping depth	h_T	0.7	(m)
Snowmelt coefficient	c_s	0.7	(mm °C^{-1})
Soil storage capacity (cold phase)	$S_{\mathrm{smax}}\vert_{\mathrm{cold}}$	20.0	(mm)
Soil storage capacity (warm phase)	$S_{\mathrm{smax}}\vert_{\mathrm{warm}}$	80.0	(mm)
Runoff separation coefficient (cold phase)	$r\vert_{\mathrm{cold}}$	0.9	
Runoff separation coefficient (warm phase)	$r\vert_{\mathrm{warm}}$	0.7	

3.3.3 Setting the shape of the synthetic hill

Perron and Fagherazzi (2011) have recently demonstrated why it is important to consider the influence of initial conditions when comparing the results of landscape evolution models with natural topography. In our case, simulating hillslope erosion over the whole extent of the study area, at an acceptable resolution required by soil production and soil transport processes, would take to much computational time. On the other hand, gathering all hillslope configurations met in the study area into a small synthetic hill is nearly impossible, but it is necessary in order to produce simulation results consistent with the observations. We therefore adjust the shape and the geometry of the synthetic hill, by a combination of cosines and other functions, to generate a variety of slope, curvature and drainage area values as similar as possible to those observed in the Ardennian hillslopes (Figure 3.5B). The resulting hill extends 920 m in the x direction and 1150 m in the y direction, has a maximum height of about 80 m and presents both convergent and divergent zones (Figure 3.5A). Moreover, to account for the dual character of the Ardenne landscape, we create asymmetrical hillsides with a very different relief in terms of slope and curvature on either side of the main divide.

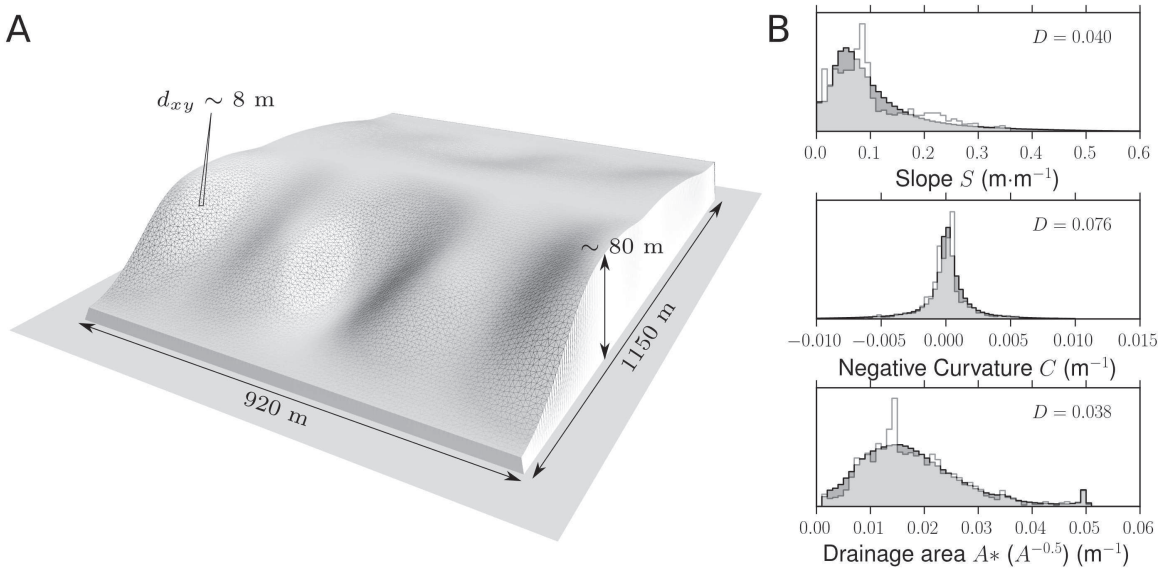

Figure 3.5: A. Shape and geometry of the synthetic hill used to simulate hillslope erosion. B. Distributions of slope, curvature and drainage area values, observed in the Ardenne (dark grey) and derived from the synthetic hill (light grey). Observed values are derived from the IGN's DEM and are sampled by a 100 m buffering around the selected soil units. Synthetic hill values are obtained after re-interpolation on a 20x20 m square grid (see section 3.4.1). Small D values are the Kolmogorov-Smirnov statistics resulting from the comparison of each couple of distributions.

Note that we use the observed present-day topography to define the initial topography of the synthetic hill. Previous simulations have shown that, at the scale of a glacial-interglacial cycle, the climate variations affect hillslope morphology to a much lesser degree than soil thickness (Chapter 2). Other observations support only slowly changing morphology of hillslopes under active erosion (e.g., Heimsath et al., 1997, 1999). Furthermore, Roering et al. (2004) have also demonstrated from the results of multiple numerical simulations that varying erosion regimes can result in similar hillslope morphologies. At the temporal scale considered here, the tectonic control on the evolution of hillslope topography can also be neglected (allowing us to make

hillslope erosion simulations with no uplift). Authors which have recently reconstructed the post-0.73 Ma tectonic uplift of the Rhenish Massif suggest a total amount of uplift between 50 and 200 m within our study area (Van Balen et al., 2000; Meyer and Stets, 2002; Demoulin and Hallot, 2009), but resulting from varying uplift rates that increased in NE Ardennes and Eifel between 730 and 400 ka before coming back to tectonic quiescence in recent times (Van den Berg, 1996; Van Balen et al., 2000). Moreover, the tectonically-induced fluvial incision wave has not so much propagated into the Ardenne Massif during the last 100 ky to steepen the slopes beside the channel reaches (Rixhon et al., 2010; Demoulin et al., 2011). Although the response of fluvial systems to Quaternary climate variations in NW Europe has been intensively studied on a qualitative basis (e.g., Mol et al., 2000; Houben, 2003; Vandenberghe, 2008), the climate control on river incision or aggradation has still not been formally quantified. Without sufficient knowledge on the quantitative coupling between hillslopes and rivers, we assume that all sediment supplied by the synthetic hill is easily evacuated by the river at the base of both hill sides, thus fixing constant soil thickness and elevation at these hill boundaries ('river' nodes of the mesh).

3.4 Model inversion: comparison between observations and simulation outputs

To extract constraints on the relative importance of the modelled transport mechanisms from the observations, we use an inversion method: the neighbourhood algorithm (NA) (Sambridge, 1999a,b). The purpose of this mathematical procedure is to objectively characterize the discrepancy between observations and model predictions in a space defined by the model parameters, through the sampling of a misfit function. The NA-sampler is an iterative, derivative free method making use of simple geometrical concepts to search the multidimensional parameter space and produce an accurate approximation of the misfit function, preferentially where the misfit values are small. At the first iteration, a set of models (i.e. points in the parameter space) are randomly and uniformly generated within the bounded parameter space. During each subsequent iteration, the entire space is discretized into a set of Voronoi cells, one cell about each previously sampled model. Voronoi cells represent the nearest neighborhood around each model. These cells are then used to guide the next sampling step, in a pseudo-randomized fashion. As iterations proceed, the algorithm concentrates sampling in regions of the parameter space where the data misfit, through the misfit function, is minimized (Figure 3.6). Full details of NA can be found in Sambridge (1999a,b).

Unlike other derivative free 'direct search' methods (e.g. genetic algorithms and simulated annealing), the NA approach is conceptually simple with only a few control parameters, but yet is able to exhibit complex self-adaptive behaviour in searching parameter space (Sambridge, 1999a). The main control parameters are the number of models generated at the first iteration, the number of models generated at each subsequent iteration and the number of Voronoi cells re-sampled by these new generated models. The NA method is also well suited for our problem because it is designed to perform an ensemble inversion rather than only a global optimization (i.e. find the optimal model(s) that are best fitted to the data). In our case, we might expect

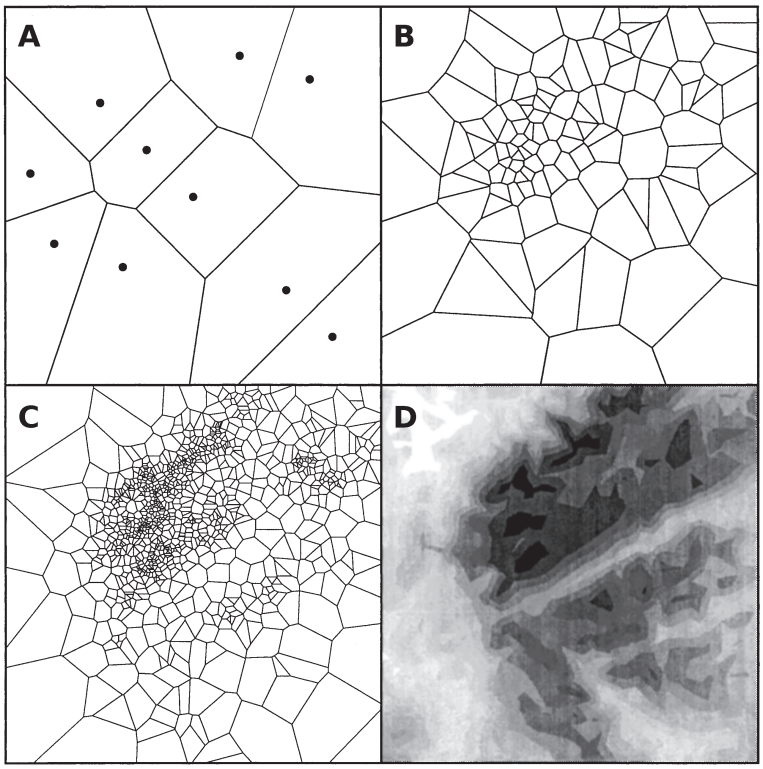

Figure 3.6: Example of the behaviour of the NA-sampler algorithm in a 2 dimension parameter space, from Sambridge (1999a). A. 10 models generated at the first iteration and their Voronoi cells. B. The Voronoi cells about the 100 samples generated at the 2nd iteration. C. Similar to B, but for 1000 samples. D. Contours of the misfit function (black areas indicate low values for the misfit function).

that no or many models may have an acceptable data fit. In an ensemble inversion, all models in the parameter space, not just the acceptable ones, provide us useful information.

In order to reduce the dimension of the parameter space and because our study focuses on the relative efficiency—in space and time—of soil transport processes rather than on the behaviour of each process taken separately, we assume here that the physics of soil production and soil transport is well-known (although nowadays the parameterization of soil transport laws is still discussed). The parameter search-space of the inversion comprises only the maximum soil production rate parameter P_0 and the 'K' coefficients of the transport laws used in CLICHE, in addition to the initial thickness h_{t0} of the uniform soil mantle imposed on the synthetic hill. Without any prior information on the value of these parameters for the Ardenne case, we define a large range of acceptable values for each parameter, which requires searching on a logarithmic scale for a uniform sampling (except for h_{t0}). All other parameters of soil production and transport laws (i.e. the equation exponents) in CLICHE are supposed to be already well constrained and their values are taken from previous studies (Braun et al., 2001; Herman and Braun, 2006), excepted for the solifluction law (see chapter 2). Furthermore, as we have a-priori no idea of the behaviour of the data misfit in the parameter space, we tune the NA control parameters so that the behaviour of the NA-sampler is more exploratory than exploitative, keeping a good compromise between computational efficiency and robustness against entrapment in local minima. Ranges or values for CLICHE and NA parameters are shown in Table 3.IV.

We also have to define the misfit function that drives the NA algorithm. This function is here

Table 3.IV: Parameters values or search ranges for CLICHE and the NA inversion algorithm. For the NA-sampler search ranges, 'log' means searching on a logarithm scale and 'lin' on a linear scale.

parameter description	parameter	value or range	(units)	scale
CLICHE fixed parameters				
Soil production damping depth	h_0	0.5	(m)	
Ratio of bedrock to soil bulk density	κ	2.0		
Overland flow exponents	m	1.7		
	n	1.3		
Depth-dependent creep exp.	p	1.2		
	l	0.7		
Solifluction exponents	e	1.7		
	g	0.5		
CLICHE inversion parameters				
Max. rate of soil production	P_0	$2.5 \cdot 10^{-7}; 2.5 \cdot 10^{-4}$	(m yr^{-1})	log
Overland flow coef.	K_r	$10^{-7}; 5 \cdot 10^{-3}$	(m^{2-2m}yr^{n-1})	log
Simple creep coef.	K_d	$10^{-4}; 5 \cdot 10^{-2}$	(m^{2}yr^{-1})	log
Depth-dependent creep coef.	K_{dd}	$5 \cdot 10^{-4}; 0.5$	(m^{2-p}yr^{-1})	log
Solifluction coef.	K_g	$5 \cdot 10^{-4}; 1.0$	(m^{2-e}yr^{-1})	log
Initial soil thickness	h_{t0}	$0.0; 3.0$	(m)	lin
NA control parameters				
Nb. of models for initial sample	N_{s1}	1024		
Nb. of models for other iterations	N_{s2}	96		
Nb. of Voronoi cells re-sampled	N_r	32		

based on (1) the comparison between observed and predicted distributions of surface derivatives for each thickness class defined from the soil map, and (2) the discrepancy between the relative coverage of the thickness classes observed in the Ardenne Massif and these of the thickness classes predicted on the synthetic hill. The computation of the misfit function is not straightforward in our case as it requires several processing stages from the raw model outputs. These stages are summarized in Fig 3.7 and are detailed in the following sections.

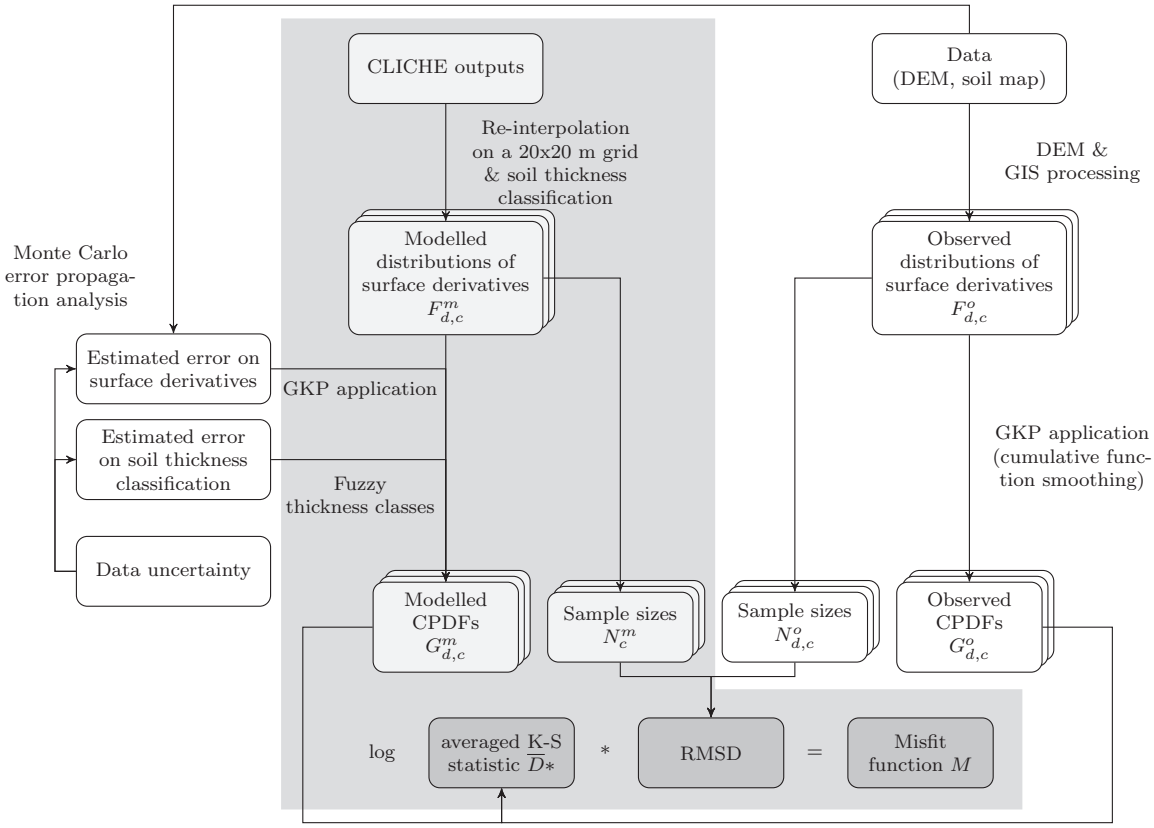

Figure 3.7: Summary of the inversion procedure. The grey-filled area indicates the stages that are repeated each time when a model is generated by the NA-sampler (once the CLICHE run is completed). Details on these processing steps can be found in the sections below.

3.4.1 Simulated surface derivatives vs. soil thickness

The mesh used for the simulations is a quasi-regular grid created by connecting nodes where the solution is calculated by a Delaunay triangulation, where the mean distance between a node and its neighbours $\sim$ 8m (Figure 3.5). As the values of DEM derivatives change according to the DEM grid-size (Deng et al., 2007), we need to interpolate after each model run the computed elevation and soil thickness values on a 20x20m regular grid (a linear interpolation scheme from the Delaunay triangulation is used here). Slope, curvature and drainage area are then calculated from the interpolated elevation values by the same algorithms and with the parameters than those used for the data. Soil thicknesses are also classified based on the class limits given above to finally form the 'predicted' cumulative distributions:

$$F^m_{d,c}(x) = \frac{1}{N^m_c} \sum_{i=1}^{N^m_c} I_{d_i}(x) \tag{3.2}$$

where N^m_c is the number of nodes of the regular grid that belong to the soil class c (see also equation 3.1). Note that in this case the sample size of each soil class is the same for all DEM derivatives ($N^m_c = N^m_{C,c} = N^m_{S,c} = N^m_{A,c}$).

3.4.2 Application of the Kolmogorov-Smirnov statistic

We apply the Kolmogorov-Smirnov (K-S) statistic (Press et al., 1992) to describe the similarity between observed and predicted distributions. The K-S test is a useful nonparametric method generally accepted to compare a sample with a reference distribution or to compare two samples. It has been used in many geomorphological or geochronological applications (e.g. Snyder et al., 2003; Giannoni et al., 2005; Lovera et al., 1999). The K-S statistic D is defined as the maximum value of the absolute difference between two cumulative distribution functions. In our case, for each of the 12 observed/modelled couples of distributions we can then calculate a K-S statistic as follows:

$$D_{d,c} = \sup_x \mid F^m_{d,c}(x) - F^o_{d,c}(x) \mid \tag{3.3}$$

In the case of a two-samples test, the K-S method is easier to apply than the χ^2 test because the sample sizes don't need to be equal (Borradaile, 2003). The wide range of possible applications of the K-S method also comes from the fact that it does not require that the samples come from normal distributions (Davis, 1986; Rock, 1988) while being sensitive to differences in the overall character of the cumulative distribution functions (regarding both location and shape). However the K-S statistic is relatively insensitive to differences at the extreme ends of the distributions (Press et al., 1992). In our case, the compared distributions may not be concerned by this limitation except for the distributions of drainage area values that are characterized by a long right tail and might then provide less meaningful values of D. The insensitivity of the K-S test to outliers can be remedied for example by the use of the Anderson-Darling test, a more sophisticated variant of the K-S test (Anderson and Darling, 1952; Press et al., 1992), but here we have instead chosen to remove the long tail of the distributions by transforming the drainage area variable itself ($A* = A^{-0.5}$) before applying the K-S statistic.

3.4.3 Dealing with observational errors

Another limitation of the standard K-S method is that it does not account for experimental errors on the samples (Sircombe and Hazelton, 2004). Yet in our case, the data we use are the product of many acquisition and processing steps, including field measurements and cartographic and numerical post-processing, that have obviously generated and propagated multiple errors citepVeron2005. By contrast, the errors made during forward modelling only comes from the accuracy of the numerical scheme used to solve the partial differential equations (PDEs) and from the re-interpolation of elevations and soil thicknesses on a regular grid. The magnitude of uncertainty in the observed cumulative distributions is expected to be much higher than in the modelled cumulative distributions. This uncertainty should therefore be taken into account while comparing the distributions. This is made by comparing cumulative probability density functions (CPDFs) rather than the cumulative distribution functions $F^m_{d,c}(x)$ and $F^o_{d,c}(x)$, as shown below.

Error estimation

The DEM derivatives and soil thickness classification errors contribute to the global uncertainty on the observed distributions. Slope, curvature and drainage area values which were assigned to each soil unit have an uncertainty that result from the combination of the positional error of the delineated soil units, the propagation of the DEM error trough the calculation of the surface derivatives and the averaging of these derivatives over the extent of each soil units.

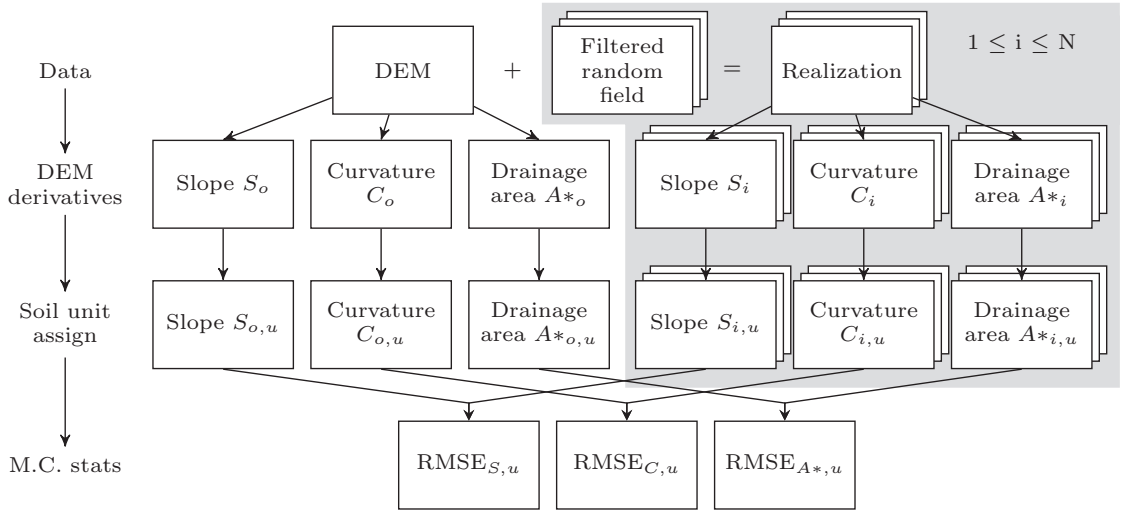

Figure 3.8: Outline of the Monte Carlo procedure applied to estimate error on DEM derivatives values that were assigned to the selected soil units.

Fine geometric corrections were achieved during the digitalization of the soil map, taking the IGN topographic background at 1/10 000 as a reference (Veron et al., 2005). The positional precision of the elements in this reference map is $\sim$ 1m (IGN, 2007). Moreover, The IGN's DTM at 1/10 000 is reported to have Root Mean Square Errors (RMSE) between 0.6 and 1.6m on the position of the 3D points, depending on the acquisition technique. Given the estimation of the uncertainty of these data sources, one can apply a Monte Carlo method to estimate the error on the DEM-derived attributes. Monte Carlo methods are commonly applied to propagate error and quantify uncertainty in spatial data (see for example Fisher, 1991; Carlisle, 2005; Oksanen and Sarjakoski, 2005; Raaflaub and Collins, 2006; Wechsler, 2007). In this stochastic approach —as indicated by its name —, the DEM is assumed to be only one realization of an infinite number of potential realizations of the real topography. The elevation of each DEM cell can therefore be represented by a probability distribution function (PDF) (Wechsler, 2007). Assuming a random error for the DEM, a Gaussian PDF is commonly chosen, with a mean equal to zero and a standard deviation equal to the RMS vertical error of the DEM. Here we adopt a standard deviation of $\sim$ 2m, which is the highest possible value resulting from the combination of the positional errors given above.

As described in Wechsler (2007), the Monte Carlo approach that is applied here can be summarized as follows (see also Figure 3.8) :

1. An error map (random field) is generated based on the PDF selected for the DEM error;
2. The random field is added to the original DEM, resulting in a realization;

3. Terrain attributes are derived from the DEM and an average value of these attributes is then assigned to each selected soil unit;

4. Previous steps 1,2,3 are repeated many times based on the number of realizations deemed appropriate to capture the distribution of possible elevations;

5. Uncertainty on DEM derived attributes can then be quantified from the values obtained with the multiple realizations. We calculate, for each soil unit, RMS errors from the multiple values of slope, curvature and drainage area that were assigned to the soil unit during Monte Carlo simulations:

$$\mathrm{RMSE}_{d,u} = \sqrt{\frac{\sum_{i=1}^{N}(\hat{d}_{i,u} - \hat{d}_{o,u})^2}{N}} \tag{3.4}$$

where N is the total number of DEM realizations (or Monte Carlo simulations), $\hat{d}_{i,u}$ is the value of derivative d assigned to the soil unit u based on the realization i, and $\hat{d}_{o,u}$ is the correspondent value assigned from the original non-perturbed DEM.

Note that additional processing when generating the random field is required as it is admitted that the elevation errors in DEMs are spatially autocorrelated (Oksanen and Sarjakoski, 2006). Among the multiple methods that have been developed to account for spatial dependence in random fields (Fisher, 1991; Hunter and Goodchild, 1997), we decided to apply to the uncorrelated random field a filtering algorithm implemented in the 'r.random.surface' module of GRASS GIS (Ehlschlaeger et al., 1997). This algorithm consists of applying a weighted low-pass filter, where the size of the filter corresponds to the distance of spatial dependence of the DEM error. Without the availability of higher accuracy elevation data, we set the maximum distance of spatial dependence to 500m which corresponds approximately to the mean horizontal length of the hillslopes in our study area. A total of 100 Monte Carlo simulations are performed to propagate DEM error. The resulting RMS errors on DEM derivatives are then combined with the standard deviations of the derivatives values sampled within the soil units to finally obtain an overall estimation of the uncertainty on observed surface derivatives. We can see in Table 3.V that the drainage area error estimated from Monte Carlo simulations increases significantly with increasing soil thickness, while slope and curvature errors remain quasi-constant. As the fixed maximum area of spatial dependence of the DEM error is much larger than the local neighborhood used to compute slope and curvature, the estimated accuracy of these attributes does not depend on the location of the soil units. But this is not the case with drainage area for which the estimated error does grow with increasing upslope contributing areas that become larger than the spatial dependence of the DEM error. Thick soil units, which have higher values of drainage area, have also a higher uncertainty on this derivative. Moreover, uncertainty due to slope and curvature averaging in soil units slightly decreases with soil thickness, because shallow soils are often located in steep and/or highly convergent—or divergent—areas while thick soils are more concentrated on flat terrains. It is therefore preferable to differentiate the estimated uncertainties following the soil thickness classes.

Table 3.V: Estimation of error related to the values of DEM-derived attributes that were assigned to the soil units. $\overline{\text{RMSE}}_{d,c}$ is the average, over the soil class c, of $\text{RMSE}_{d,u}$ values (equation 3.4) obtained from the Monte Carlo simulation results. $\sigma^s_{d,c}$ is the soil class average of the derivatives standard deviations that are calculated from the DEM grid cells sampled inside each soil unit. $\sigma^o_{d,c}$ is the overall error resulting from the combination of $\overline{\text{RMSE}}_{d,c}$ and $\sigma^s_{d,c}$, assuming that these two sources of error are independent.

# soil class c	$\overline{\text{RMSE}}_{d,c}$	$\sigma^s_{d,c}$	$\sigma^o_{d,c}$
	Slope S		
1 (0 to 20 cm)	$1.22 \cdot 10^{-2}$	$1.41 \cdot 10^{-2}$	$1.87 \cdot 10^{-2}$
2 (20 to 40 cm)	$1.20 \cdot 10^{-2}$	$1.17 \cdot 10^{-2}$	$1.67 \cdot 10^{-2}$
3 (40 to 80 cm)	$1.18 \cdot 10^{-2}$	$0.97 \cdot 10^{-2}$	$1.53 \cdot 10^{-2}$
4 ($>$ 80 cm)	$1.17 \cdot 10^{-2}$	$0.94 \cdot 10^{-2}$	$1.54 \cdot 10^{-2}$
	Curvature C		
1 (0 to 20 cm)	$3.13 \cdot 10^{-4}$	$6.14 \cdot 10^{-4}$	$6.89 \cdot 10^{-4}$
2 (20 to 40 cm)	$2.89 \cdot 10^{-4}$	$5.78 \cdot 10^{-4}$	$6.46 \cdot 10^{-4}$
3 (40 to 80 cm)	$2.99 \cdot 10^{-4}$	$5.37 \cdot 10^{-4}$	$6.15 \cdot 10^{-4}$
4 ($>$ 80 cm)	$3.19 \cdot 10^{-4}$	$5.42 \cdot 10^{-4}$	$6.29 \cdot 10^{-4}$
	Drainage area $A*$		
1 (0 to 20 cm)	$1.53 \cdot 10^{-3}$	$8.06 \cdot 10^{-4}$	$1.73 \cdot 10^{-3}$
2 (20 to 40 cm)	$1.84 \cdot 10^{-3}$	$8.74 \cdot 10^{-4}$	$2.03 \cdot 10^{-3}$
3 (40 to 80 cm)	$2.23 \cdot 10^{-3}$	$8.48 \cdot 10^{-4}$	$2.39 \cdot 10^{-3}$
4 ($>$ 80 cm)	$2.42 \cdot 10^{-3}$	$9.11 \cdot 10^{-4}$	$2.59 \cdot 10^{-3}$

Beside the estimation of the DEM derivatives uncertainties, we also need to estimate the error on soil thickness data. As, in the soil map, soil thickness is categorized into an ordinal variable—and given the non-availability of the initial augerings data in the map's database—, its level of uncertainty can be defined by (1) the probability that the 'real' aggregated thickness value for a soil unit effectively belongs to the class in which the soil unit has been categorized, and (2) the probabilities that this real value belongs to the other classes. One can easily estimate these probabilities, e.g. on the basis of a contingency table obtained by a cross-validation procedure. Unfortunately, at our knowledge no validation has been made yet for gravel soils in the Ardenne. Without any information available, we have chosen probability values in order to obtain an acceptable mid-level error (Table 3.VI).

Table 3.VI: Probabilities that the soil units, categorized into the thickness classes of the table's rows, belong to the thickness classes of the table's columns. The values are arbitrarily defined to reach a mid-level error, accounting for the variable class widths and the higher chance to underestimate than overestimate soil thickness when measuring the depth of the substratum by augerings in medium to high gravelly soils.

# soil class c	1 (0 to 20 cm)	2 (20 to 40 cm)	3 (40 to 80 cm)	4 ($>$ 80 cm)
1 (0 to 20 cm)	0.80	0.20	0.00	0.00
2 (20 to 40 cm)	0.06	0.80	0.14	0.00
3 (40 to 80 cm)	0.00	0.03	0.90	0.07
4 ($>$ 80 cm)	0.00	0.00	0.03	0.97

Incorporating error into cumulative distribution functions

We assumed that uncertainty on the model outputs can be neglected in comparison with uncertainty on the observations. To properly compare observed and modelled distributions of surface derivatives, the modelled cumulative distributions are re-calculated with the integration of the observational errors estimated above, prior to calculate the K-S statistic. This process consists of two stages. In the first stage, we have developed a simple algorithm that redistributes randomly selected values of surface attributes—derived from the re-interpolated CLICHE outputs (see section 3.4.1)—from one to the other soil thickness classes, according to the 'belonging' probabilities defined above. Rather than class permutation, the selected values in one class are added (copied) to the samples of the other classes, resulting in fuzzy classes of soil thickness. After this first stage, the size N_c^m of the sample of each soil class c is more or less enlarged. Nevertheless, due to the fixed mid-level error and partially overlapping distributions for contiguous thickness classes, the aspect of the modelled cumulative distributions doesn't drastically change in most cases (Figure 3.13).

In the second stage, we use Gaussian Kernel Probability (GKP) functions to represent the modelled cumulative distribution functions weighted by the error on observed values of DEM derivatives. For each sample obtained at the previous stage, the punctual values d_i are replaced by Gaussian PDFs centred on the values themselves and with a standard deviation $\sigma_{d,c}^o$ taken from Table 3.V. The GKP function is defined as the normalized sum of all the Gaussian PDFs (Silverman, 1986) and the cumulative probability density function (CPDF) is given by the integral of the GKP function. For the modelled distributions we thus calculate the CPDFs as follows:

$$G_{d,c}^m(x) = \frac{1}{N_c^m} \int_{-\infty}^{x} \sum_{i=1}^{N_c^m} \frac{\exp\left[-\frac{(x'-d_i)^2}{2(\sigma_{d,c}^o)^2}\right]}{\sigma_{d,c}^o \sqrt{2\pi}} dx' \tag{3.5}$$

where $x \in [-\infty; +\infty]$ and $G_{d,c}^m(x) \in [0; 1]$. Depending on the value of $\sigma_{d,c}^o$ and the tightness of the distributions, the obtained CPDFs are smoothed to a variable degree with respect to the original cumulative distributions $F_{d,c}^m(x)$, thus having a significant impact on the results of the K-S test.

Note that because the probabilities of values d_i to belong to other thickness classes are rather small, both the redistribution process and the CPDF computation are repeated many times (100x), reducing the risk of a high stochastic bias. The resulting CPDFs are then averaged into a unique CPDF. Moreover, an equation similar to equation 3.5 is used to calculate the CPDFs $G_{d,c}^o(x)$ from the observed distributions $F_{d,c}^o(x)$, but in this case the impact on the results of the K-S test is quasi-negligible due to the smoothness of the distributions $F_{d,c}^o(x)$. Finally, the K-S statistic that account for observational errors are calculated as follows:

$$D*_{d,c} = \max_{-\infty \leq x \leq \infty} \mid G_{d,c}^m(x) - G_{d,c}^o(x) \mid \tag{3.6}$$

3.4.4 The misfit function

As a measure of the data fit, we initially used the mean of the K-S statitic calculated for each surface derivative (S,C,A*) and each soil thickness class (equation 3.7). The mean is preferred to the product of the K-S statistics because we are searching for an acceptable fit for all the distributions, rather than a perfect fit—i.e., a value of $D*_{d,c}$ very close to zero—for at least one or a few of the distributions. Moreover, depending on the CLICHE's soil production and transport parameters set by the inversion algorithm, the size of some of the predicted samples can be too small to accurately characterize their distribution. The mean of the K-S statitic is thus weighted by a non-linear function of the sample size (equation 3.8).

$$\overline{D}* = \frac{\sum_d \sum_c w_c \, D*_{d,c}}{\sum_d \sum_c w_c} \tag{3.7}$$

$$w_c = \frac{2}{\pi} \arctan\left(N_c^m \frac{80}{\pi}\right) \tag{3.8}$$

However, as we noted after several inversion tests, the model that corresponds to the smallest value of the misfit function $\overline{D}*$ produces on the synthetic hill a spatial distribution of the soil mantle that may greatly differ from the observed distribution reconstructed with the soil map, notably characterized by an extended coverage of shallow soils (thickness < 20 cm). Possible explanations for that particular behaviour are: (1) the extraction of slope, curvature and drainage area attributes is not sufficient to fully characterize the spatial distribution of soil thickness, (2) the limited extent of the synthetic hill is sufficient to reproduce the global distribution of the DEM-extracted surface derivatives but not large enough to reproduce the distribution of these derivatives for the soil thickness classes taken separately, and (3) the broad classification of soil thickness values smoothed out the possible highly non-linear relations between surface derivatives and soil thickness. In addition to $\overline{D}*$, we therefore decided to apply another, somewhat arbitrary constraint based on the relative coverage of each thickness class. As, for the predictions, soil samples correspond to the 20x20m grid cells resulting from the re-interpolation and, for the observations, the areas of selected soil units are rather similar from one to another thickness class, sample sizes can be used instead of areas for both predictions and observations. The misfit function M that drives the inversion algorithm is thus defined by multiplying $\overline{D}*$ by the Root Mean Squared Differences (RMSD) between observed and predicted relative sample sizes (equation 3.9). The logarithm of this product—whose values theoretically vary between 0 and 1—is chosen to increase the variability of the misfit function (equation 3.10).

$$\text{RMSD} = \sqrt{\frac{\sum_c (p_c^m - p_c^o)^2}{4}}$$
$$\text{where } p_c^m = \frac{N_c^m}{\sum_c N_c^m} \text{ and } p_c^o = \frac{\overline{N}_c^o}{\sum_c \overline{N}_c^o} \text{ with } \overline{N}_c^o = \frac{1}{3}\sum_d N_{d,c}^o \tag{3.9}$$

$$M = \log(\overline{D}* \cdot \mathrm{RMSD}) \tag{3.10}$$

3.5 Inversion results

Results of the inversion are summarized in Figures 3.10 and 3.11. Each dot in these figures represents a forward model, i.e., a CLICHE run corresponding to a set of model parameters generated by the NA-sampler algorithm (red dots correspond to a small misfit value while blue dots correspond to a poor data fit). The results were obtained after 20 iterations (Figure 3.9B), when new generated models begun to be entrapped in local minima of the misfit function. A total of 2830 models were generated by the inversion algorithm. We see a remarkable convergence pattern for all parameters. Despite the generally accepted meter- to sub-meter scale required to study soil transport mechanisms on hillslopes, the 20 m resolution data we used have apparently constrained the soil production and soil transport parameters with a surprising efficiency. As the data also cover an extended region including variable hillslope geometries and—small but existing—lithological and soil heterogeneities, the good convergence rate achieved by the inversion scheme supports the assumption of a 1st order control of climate on hillslope erosion.

However, Figure 3.10 shows that the comparison between observed and modelled relative sample sizes of each soil class has mainly driven the NA-sampler algorithm to converge towards values of RMSD close to zero, thus producing low misfit values (Figure 3.11), while the comparison of cumulative distributions brought poorer results with $\overline{D}*$ values more spread over the parameter space, emphasized by the logarithm search scale of P_0 and the 'K' transport parameters. Consequently, the inversion results obtained here can't be used to determine the calibrated, precise or absolute values for these parameters. This was expected because of the low precision of the data and despite the incorporation of observational errors in the computation of data fit that probably enhanced the robustness of the results but certainly not their precision. Figures 3.10 and 3.9A also show that, although the lowest RMSD values do not correspond to the lowest $\overline{D}*$ values, a consistent, positive (though non-linear) relationship between RMSD and $\overline{D}*$ emerges from the whole inversion ensemble. For the lowest RMSD values, $\overline{D}*$ bottoms out between 0.2 and 0.3. This characteristic range and the inability of reaching lower $\overline{D}*$ values can be explained by several factors including the discrepancy between the climate scenario defined here and the real climate history of the past 120 kyr in the Ardenne which might play an important role, as well as the comparison of only broad classes of soil thickness (as previously discussed) or the possible incorrect parametrization of soil production and transport used for forward modelling (which will be discussed later).

Moreover, the results highlight that constraining CLICHE with data on present-day soil thickness didn't provide a unique solution of soil production and transport, i.e., the NA-sampler didn't converge towards one best-fit model. We indeed distinguish in Figure 3.11 multiple well-delimited areas of the parameter space characterized by low values of the misfit function. It confirms the expectation that searching for the best-fit model makes no sense in our case. Nevertheless, the number and the extent of these low-misfit areas are limited in the search ranges of all CLICHE constrained parameters. From the inversion ensemble, a set of three simulations

(S1-3) are chosen to be representative of the probable solutions (Table 3.VII). For each of these simulations, time series of sediment yield to the rivers (equal to the rate of soil loss through the lower boundaries of the synthetic hill), averaged denudation rate and averaged soil thickness are shown in Figure 3.12. The contrasted evolution of these variables from one simulation to another demonstrates the need for additional data—most probably time-dependent data—to constrain soil production and transport more efficiently. Focussing on the denudation rates, we see similarities between the time series of simulations S1 and S2 while simulation S3 presents much lower rates due its lower values of P_0 and the 'K' parameters. The multiple low misfit regions located below $P_0 \sim 2.8 \cdot 10^{-5}$ m·yr^{-1} suggest a positive correlation of data fit between P_0 and the transport parameters, but at this characteristic P_0 value, the low misfit models become spread over a large part of the search ranges of the other parameters (excepted for K_g). Among these models, S1 and S2 predict denudation rates that are more consistent with the rates measured in catchments of the Ardenne and the Reinish Massif (Schaller et al., 2002, 2004; Meyer et al., 2008). Therefore, the discussion below will be essentially based on the two solutions S1 and S2 (the predicted vs. measured denudation rates will be also discussed in more detail). A fourth simulation (S4) is chosen to show an example of a small $\overline{D}*$ value obtained from a model with P_0 close to $2.8 \cdot 10^{-5}$. Figures 3.13 and 3.14 illustrate respectively the data fit (through modelled and observed distributions of surface derivatives) and the state of the hillslope system (in both glacial and actual temperate periods) for simulation S1. The same figures for S2-4 can be found as a supplement at the end of this chapter (section 3.8). Comparisons of distributions of the topographic index, shown for control purpose (Figure 3.13), are consistent with the comparison of the other distributions. The distribution fit is generally better for the middle thickness classes (20 to 40 cm; 40 to 80 cm) than for the extreme classes, but note that the size of the samples for the shallowest class (0 to 20 cm) is often small while the thickest class has no upper boundary.

Beside the location of areas of low misfit in the parameter space, the density of models generated by the NA-sampler is also a good indicator of probable solutions for the parameters values, with the added benefit that this indicator is characteristic of the whole inversion ensemble, as the density progressively increased during the inversion process in the areas where misfit was minimized. The diagonal of the matrix in Figure 3.10 shows the marginal densities estimated for each constrained parameter. Density distributions for P_0, K_d and K_g have a single, narrow mode. The K_g mode indicates very high solifluction fluxes, and the K_d mode around $\sim 1.5 \cdot 10^{-3}$ is in the range of the simple creep 'K' values which were obtained with the multi-parametrized model of soil production and soil transport used by Braun et al. (2001) and Herman and Braun (2006). These values will be further discussed together with the characteristic P_0 value $\sim 2.8 \cdot 10^{-5}$. For the other constrained parameters, distributions of density are rather multimodal (the 2nd order maxima reflecting the entrapment in local minima of the misfit function). The density of forward models increases between 10^{-4} and $1.5 \cdot 10^{-2}$ for K_{dd}, while the modes are less marked for K_r indicating the poor constraint level brought by the data on transport by overland flow. The simulations S1 and S2 were thus specifically chosen to encompass cases for which the value of K_r is respectively very low and very high. The NA-sampler has converged towards either small values of h_{t0} (< 1 m) or around 2 m. Considering the periodicity of the Quaternary climate and the similarities between the Eemian and the Holocene climates, we expected a convergence

towards h_{t0} values close to the present-day mean soil thickness. However, such an interpretation is difficult due to the possible self-adapting behaviour of the hillslope system to evolve away from the uniform soil thickness initially assigned to the synthetic hill (the imposed uniform thickness might greatly differ from the probable spatially variable soil thickness distribution found at the end of the Eemian).

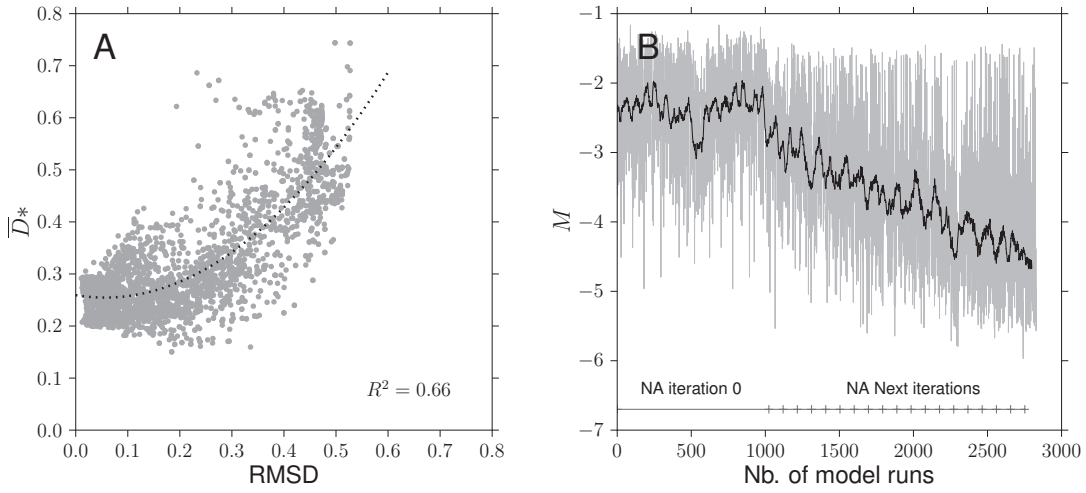

Figure 3.9: A. $\overline{D}*$ vs. RMSD values for all models generated by the NA inversion algorithm. R^2 is the coefficient of determination of the 2nd order polynomial adjustment between the two variables (dotted line). B. Evolution of the misfit function M values (grey line) as the iterations of the NA-sampler proceeded (the black line corresponds to the moving average over 30 successive models generated by the NA-sampler).

Table 3.VII: A set of models representative of the multiple solutions obtained from the inversion: description, parameter values and data fit. The parameter values correspond to models which were effectively generated by the NA-sampler (see Table 3.IV for parameter units).

	S1	S2	S3	S4
Description	$P_0 \sim 2.8 \cdot 10^{-5}$; high K_r; high K_g	$P_0 \sim 2.8 \cdot 10^{-5}$; low K_r; high K_g	Low P_0; low transport params.	Example of low $\overline{D}*$; P_0 close to $2.8 \cdot 10^{-5}$
P_0	$2.73 \cdot 10^{-5}$	$2.89 \cdot 10^{-5}$	$5.63 \cdot 10^{-7}$	$2.25 \cdot 10^{-5}$
K_r	$3.47 \cdot 10^{-5}$	$5.00 \cdot 10^{-7}$	$1.51 \cdot 10^{-6}$	$6.02 \cdot 10^{-5}$
K_d	$1.54 \cdot 10^{-3}$	$2.96 \cdot 10^{-4}$	$1.74 \cdot 10^{-3}$	$2.79 \cdot 10^{-2}$
K_{dd}	$2.23 \cdot 10^{-2}$	$3.20 \cdot 10^{-2}$	$3.07 \cdot 10^{-3}$	$8.51 \cdot 10^{-4}$
K_g	$5.45 \cdot 10^{-1}$	$7.31 \cdot 10^{-1}$	$7.90 \cdot 10^{-4}$	$8.91 \cdot 10^{-3}$
h_{t0}	0.08	1.83	0.64	2.64
$\overline{D}*$	0.30	0.27	0.23	0.20
RMSD	0.015	0.025	0.020	0.200
M	-5.40	-5.01	-5.33	-3.21

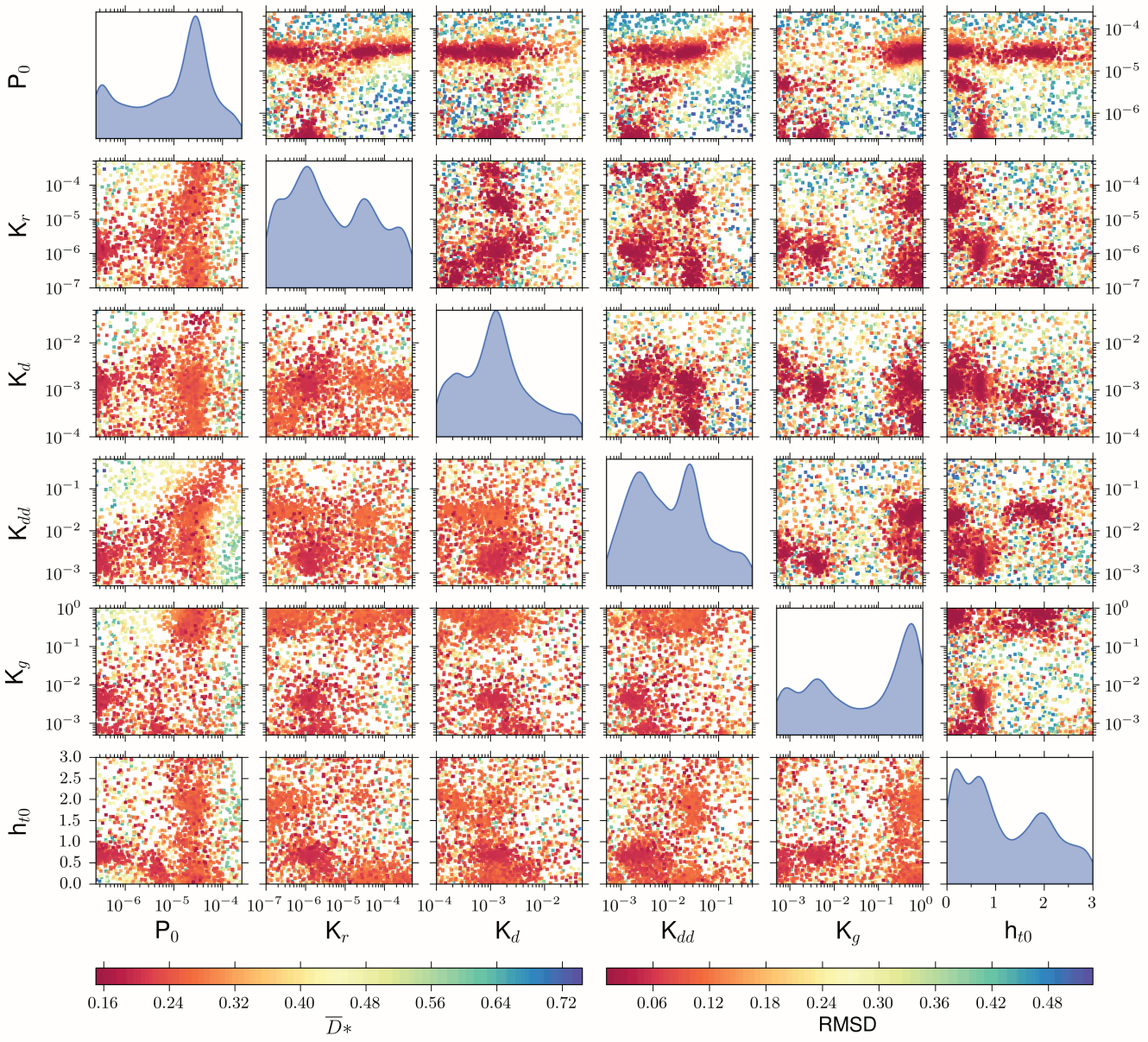

Figure 3.10: Results from the inversion (NA-sampler): matrix of two-dimensional cross sections in multi-dimensional parameter space (see Table 3.IV for parameter units). Each dot in the scatterplots represents a forward (CLICHE) model run. The color schemes are proportional to the $\overline{D}*$ (lower-matrix) and the RMSD (upper-matrix) values. In the scatterplots, red dots overlap the blue dots for more visibility of good data fit areas. The diagonal of the matrix shows the kernel density estimation of the models generated by the NA-sampler for each dimension of the parameter space (using a Gauss kernel with standard smoothing, see Scott (1992) for details on the calculation). As the NA-sampler iterations proceeded, the density increased in the regions where the misfit function were minimized. Note that the y-axis for the kernel density estimates differ from the y-axis of the scatterplots and also differ from one to another parameter for a better visualization.

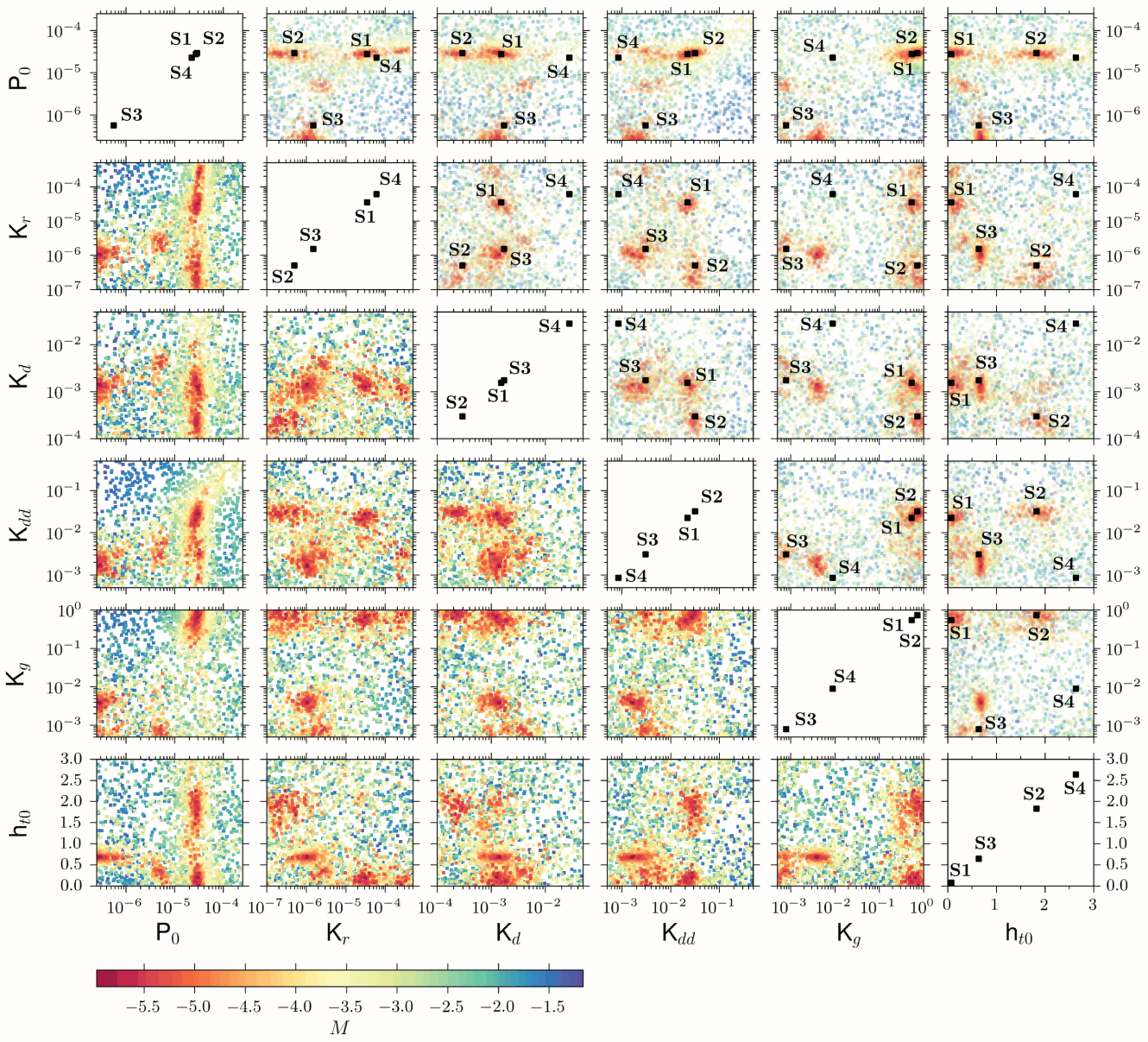

Figure 3.11: Results from the inversion (NA-sampler) and selected models: matrix of two-dimensional cross sections in multidimensional parameter space (see Figure 3.10 for more explanations). Here the color scheme is proportional to the misfit function M values (both lower-matrix and upper-matrix). Labelled Black squares in the diagonal and the upper-matrix indicate the locations of the selected models in the parameter space (see Table 3.VII for parameter values).

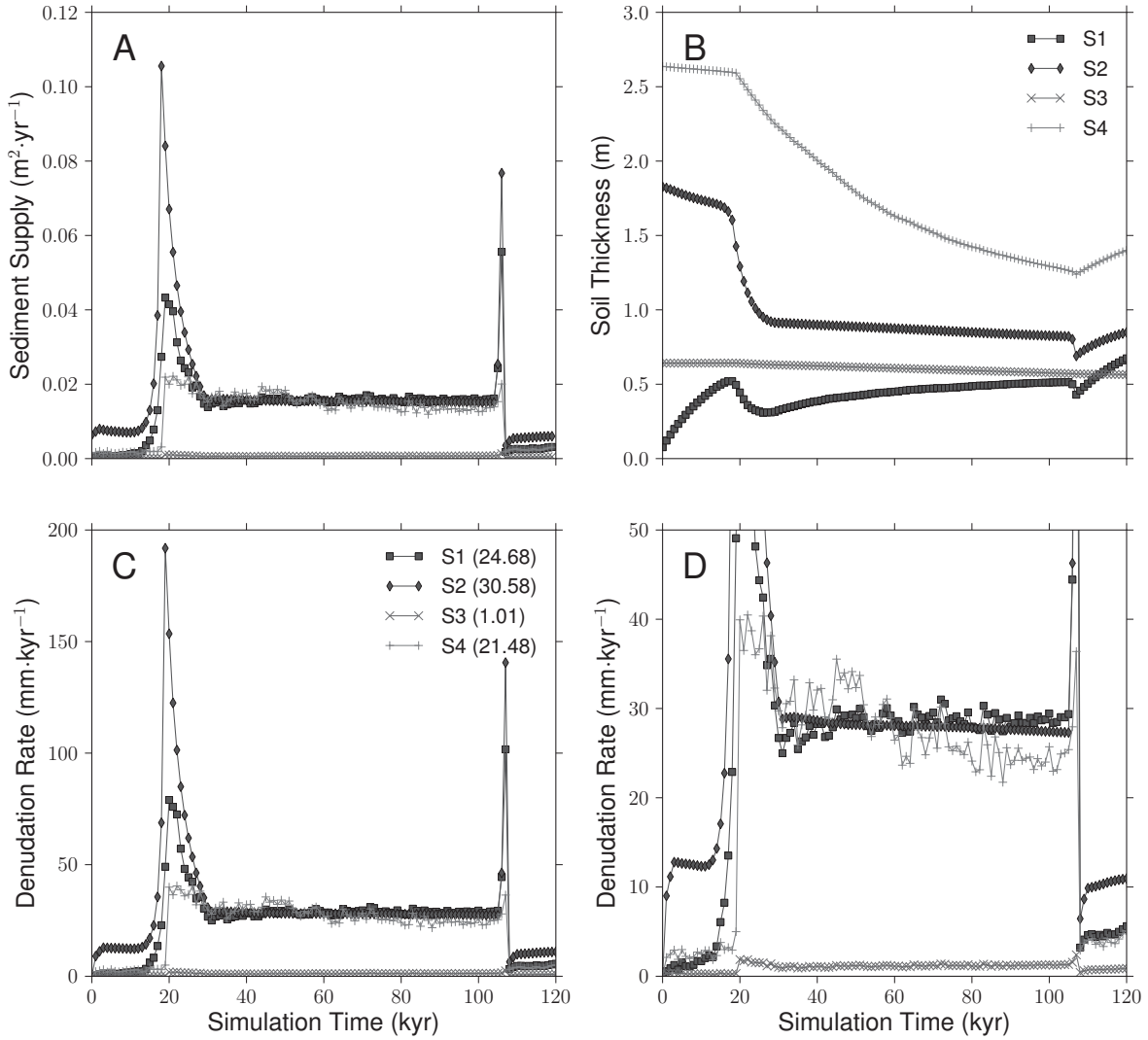

Figure 3.12: Time series for simulations S1,S2,S3 and S4 (see Table 3.VII). A. Sediment supply: output soil flux averaged over the fixed boundaries of the synthetic hill ('river' sides). B. Soil thickness averaged over the whole synthetic hill. C. Denudation rate averaged over the whole synthetic hill (Values in the upper-left quadrant indicate the averages over the 120 kyr of the simulation for S1-4). D. Focus on the low part of C.

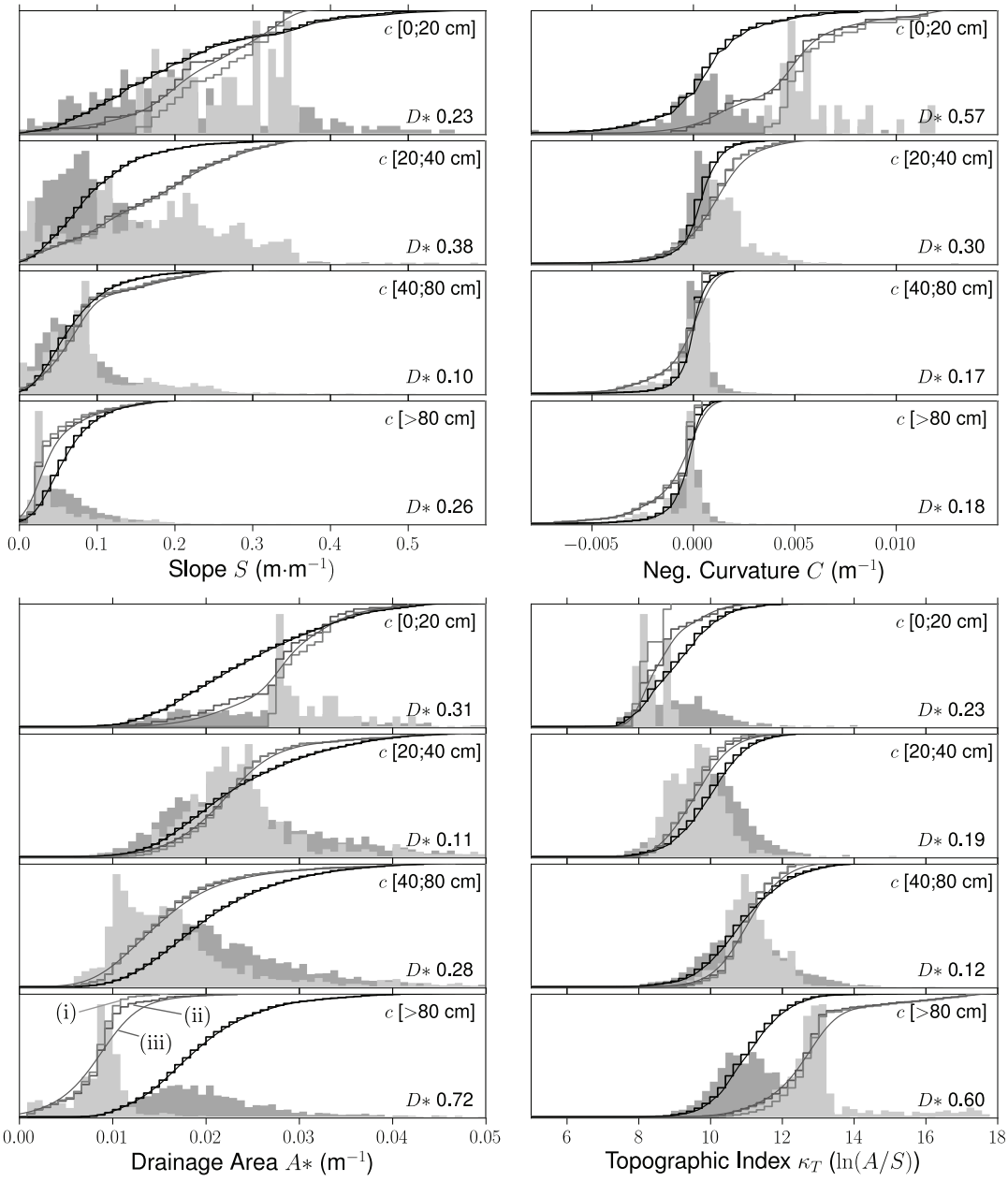

Figure 3.13: Simulation S1 (see Table 3.VII): Observed (dark grey) and modelled (light grey) distributions of terrain attributes for all soil thickness classes: normalized histograms, normalized cumulative distribution—before (i) and after (ii) sample redistribution for the modelled distributions—and Cumulative Probability Density Functions (CPDFs) (iii). Modelled distributions are computed from the distribution of soil thickness at the end of the simulation S1 (see Table 3.VII). Distributions of the topographic index were not involved in the misfit computation but are shown here for control purpose.

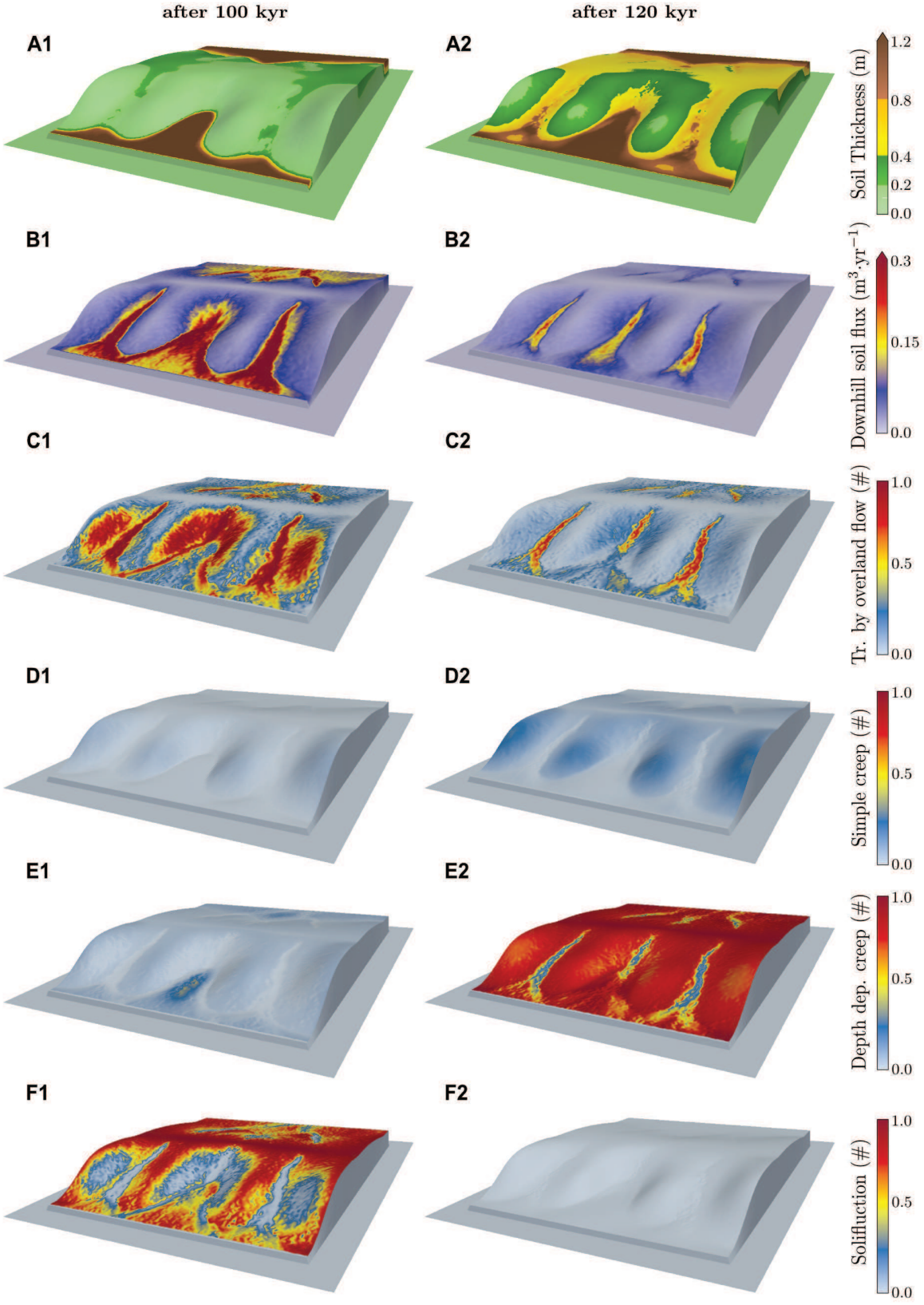

Figure 3.14: Snapshots of simulation S1 (see Table 3.VII) for Pleniglacial conditions (after 100 kyr of simulation, left hand-side) and present-day conditions (at the end of the simulation, right-hand side). A. Soil thickness. B. Local volumetric downhill soil flux (all processes). C-F. Contribution to the local downhill soil flux from transport by overland flow, simple creep, depth dependent creep and solifluction (unit-less). Note that the soil fluxes involved here are the averages over an entire elongated cycle in the simulation.

3.6 Discussion

The inversion results based on the comparison between the CLICHE model predictions with the soil thickness observations through the whole glacial-interglacial cycle yield a new and important amount of information that provides a strong quantitative basis for discussing a variety of unresolved problems concerning hillslope erosion under varying climate conditions. In the discussion below, based on our results and structured around key themes, we will try to give new insights on the following fundamental questions, with emphasis on whether the data we used here provide good constrains on hillslope dynamics:

- How can one characterize the hillslope system—weathering-limited vs. transport-limited—during 'cold' and 'warm' phases of the glacial-interglacial cycles ?
- Which weathering mechanisms prevailed under the cold and the temperate environments that followed each other in our study area and how has the rate of production of mobilizable regolith evolved during the past 120 kyr ?
- Is the present-day landscape in equilibrium ? Does the actual soil thickness distribution and/or landforms retain a 'memory' of the past environments or climatic events ?
- When and where did or do operate the predominant transport processes ?
- How are denudation rates and sediment delivery to channels influenced by climate ?

In addition to the hypothesis of a simple climate scenario fixed for the last glacial-interglacial cycle, we also discuss the consistency of several simplifications we made. In particular, the *a-priori* well-known physics of soil production and transport processes and the scale-dependence of transport processes are studied by analysing their influence on the value of the misfit function.

3.6.1 Transport-limited vs. weathering-limited landscape, and weathering mechanisms

At a first glance at the whole inversion ensemble, it is surprising to note that the bast constrained parameter is the maximum soil production rate P_0, whereas the map of soil thickness lets us to believe that the present-day landscape is transport-limited (Figure 3.2), corroborated by the model prediction of a low downhill soil flux at the end of the simulation, i.e., the Holocene (Figure 3.14B2). Because in transport-limited systems soil transport cannot mobilize all the produced regolith, soil mantle tends to become thicker, thus decreasing the soil production rates. Apart from possible variations in soil production rate related to variations in the underlying bedrock lithology (Ahnert, 1987), the spatial distribution of soil mantle in such systems is thus mainly controlled by the relative efficiency of transport processes, which depends mostly on hillslope morphology. In the extreme case, without any transport on a bare-bedrock hillslope, the soil cover would evolve towards a uniform thickness that is independent of the P_0 value (in that case, using the soil production law implemented in CLICHE, P_0 represents the rapidity at which soil mantle reaches a steady uniform thickness and h_0 represents its characteristic thickness). For these reasons, soil distributions in transport-limited systems do not provide good constraints on the maximum soil production rate. So, given the data, we did initially expect

a high constraint level on the soil transport parameters and relatively poor results for the soil production parameter, but the inversion results revealed the opposite.

This paradox can be explained looking at the behaviour of the hillslope system during the cold phase of the simulation, when high runoff regimes and the presence of a thawing soil layer promoted high potential rates of seasonal solifluction and transport by overland flow. The good data fit found with high parameters values for at least the solifluction law turned these potential rates into very high effective transport rates during the glacial period (Figure 3.14B1). Figure 3.14A1 shows that, during this period, downslope soil transport limited the development of the soil mantle to a few centimeters on a large part of the synthetic hill—at least for the steepest hill side—while the mobilized material accumulated at the base of the hill, resulting in a typical weathering-limited hillsope system (Carson and Kirkby, 1972). As the cold phase represents most of the time of the simulation, the emergence of these weathering-limited conditions on the synthetic hill is the most likely explanation for why soil production has played an important role during the last glacial-interglacial cycle.

However, it is also surprising that the NA algorithm has well converged towards a unique value for P_0, around 28 mm·kyr^{-1}, whereas recent studies suggest a strong connection between weathering rates and climate. For example, high denudation rates have been reported in regions that experience or have experienced a sufficient climatic cooling to bring the ground temperatures into the "frost cracking window" (Anderson, 1998; Hales and Roering, 2007; Delunel et al., 2010; Tucker et al., 2011). This window, defined by a temperature range between -3 to -8 °C, is a proxy for the intensity of frost-cracking, which primarily results from the growth of segregation ice in rocks (supposing the presence of available water) (Hales and Roering, 2007). Such a positive correlation between erosion rates and frost-cracking intensity as mainly been observed and/or interpreted in mountainous and rocky environments, e.g., western European Alps (Delunel et al., 2010), southern New Zealand Alps (Hales and Roering, 2007) and Italian Appenines (Tucker et al., 2011), where steep slopes ensure an effortless removal of the breakdown products and leading to interpreting denudation rates as weathering rates. On the other hand, an opposite effect of the mechanical dislocation of rocks by water freezing and ice lens growth is that other possible rock breakdown mechanisms would cause increasing weathering rates during the transition from cold to warmer climate conditions. For example, pollen records in NW Europe show, for the last glacial-interglacial transition, dramatic changes in the relative proportions of woody and herbaceous species, characterized by an overall increase of the tree/non-tree (AP/NAP) pollen ratio (e.g., Hoek, 1997; Litt and Stebich, 1999; Hoek, 2001), therefore encouraging more efficient rock disruption by tree throw and woody root growth. Higher annual rainfall rates and temperatures may also promote biological and chemical weathering. Recent data suggest even a more complex control of climate on soil production, trough the combined effects of rainfall and temperatures in addition to feedbacks between soil weathering, saprolite weathering and soil transport (Dixon et al., 2009a,b).

To which mechanism(s) is the constrained P_0 value related ?

Given that the soil production function implemented in CLICHE is not climate-dependent, the characteristic value of P_0 obtained here can be interpreted in two possible manners: (1) P_0 reflects the maximum soil production rate due to either frost-cracking and the action of water freeze-thaw during the cold phase of the climatic scenario, or active biological and chemical processes during the warm phase; (2) both of the weathering mechanisms previously mentioned have been active respectively during the cold and warm phases and resulted in similar rates of rock breakdown or soil production. Unfortunately, our results do not provide sufficient information to definitively decide which solution is the most acceptable. An argument that supports good constraints on soil production rates under the temperate climate of the Holocene, independently of weathering rates under cold climatic conditions, is the clear positive correlation between P_0 and K_{dd} for high values of K_{dd} that emerges from the inversion (Figure 3.10), whereas the low misfits values found for P_0 around 28 mm·kyr^{-1} do not significantly vary across the inversion search range of the other transport parameters. In our case, without any *a-priori* external constraint applied to the geomorphic laws, it is logical that soil production and soil transport rates must increase together in order to reproduce identical data fit (i.e. identical soil thickness distributions). K_{dd} is precisely controlling the rate of depth-dependent creep which turns out to be the dominant process acting on the largest extent of the synthetic hill during the warm phase of the climatic scenario (Figure 3.14E2). A more elusive positive correlation between P_0 and K_r (the overland flow parameter) emerges for high values of K_r and low misfit values. This makes good sense because transport by overland flow prevails in areas of surface convergence of the synthetic hill during the last thousands of years of the simulation (Figure 3.14C2), but only for high values of K_r due to the low runoff regime of the Holocene. However, this result—i.e., no or positive data fit correlations found between P_0 and the transport coefficients—also suggests that the characteristic value of P_0 reflects the production of mobilizable material during the cold phase of the climatic scenario. Indeed, close to this characteristic maximum production rate, the inversion results suggest a good data fit but only for high values of K_g (main control parameter in the solifluction law). In CLICHE, the solifluction law is only active in the presence of a seasonally thawing soil layer. Consequently, the contribution of solifluction to the total soil flux becomes so important during the cold period (Figure 3.14F1) that only high values of K_r, K_d and/or K_{dd} controlling the other transport laws could have caused a significant rise in the total soil flux. This may explain the absence of any relationship in the inversion result between P_0 around 28 mm·kyr^{-1} and low values of K_r, K_d and K_{dd} and, inversely, the positive correlations for high values of K_{dd} and K_r. Note also that the lowest misfits values around the characteristic P_0 value are located near the upper bound of the K_g parameter search range and don't exclude a possible positive correlation for higher K_g values.

If our results do not allow us to relate the optimum P_0 value to specific mechanisms of soil production, additional information on rock breakdown and/or soil production rates—in both transport-limited and weathering-limited hillslopes—should fuel the debate. For example, Heimsath et al. (2000) used cosmogenic radionuclides (CRN) to estimate soil production rates in the Bega Valley, southeastern Australia, which shares many similarities with the present-day Ardenne landscape (soil mantled hillsopes with low to moderate relief, warmer climate than the

Ardenne but with quasi-uniform rainfall rates and an annual average $\sim$ 910 mm·yr^{-1}) despite slightly different geological settings (Late Silurian to Early Devonian granite and granodiorite). In their study site, soil production and transport appeared to be primarily controlled by biogenic processes, although there was some evidence of overland flow. Measurements of production rates against soil depth indicated that soil production declined exponentially with depth, with a maximum production rate $P_0 \sim 53$ mm·kyr^{-1}. This value was consistent with $P_0 \sim 80$ mm·kyr^{-1} obtained from other CRN-based measurements in the Tennessee Valley, California (Heimsath et al., 1997, 1999). Other examples in more bedrock-dominated landscapes include Tucker et al. (2011) which estimated erosion rates on a fault scarp located in the Central Apennines (Italy), using a numerical model of footwall growth and erosion in which erosion rate tracks the GISP2 $\delta^{18}O$ curve. For this weathering-limited scarp system, the authors reported very low Holocene erosion rates from 1 to 50 mm·kyr^{-1} and much higher 110-300 kyr averaged erosion rates, between 200 and 400 mm·kyr^{-1}, suggesting that erosion rate has varied by about a factor of 30 over the past one to two glacial cycles due to the strong climatic control on rock breakdown by frost cracking. As thin soils ($<$ 25 cm) mantle the steep slopes of the studied scarp, we can reasonably compare the erosion rates indicated above with the P_0 parameter of the soil production function in the context of a weathering-limited system.

The characteristic P_0 value of 28 mm·kyr^{-1} obtained here is in good agreement with values reported by Heimsath et al. (1997, 1999, 2000) and suggests therefore that the present-day soil thickness data in the Ardenne constrain the maximum production rate related to biogenic and chemical activity under the temperate environment of the Holocene. However, a straightforward comparison of the weathering rates reported by Tucker et al. (2011) may be disputable in the Ardenne's case. Evidences of a locally warmer—but still cold—climate in the Central Apennines than in the Ardenne during the Last Glacial Maximum (LGM) suggest that rock weathering rates measured in the Apennines are likely to be much higher than weathering rates due to frost cracking in the Ardenne. Pollen-based temperature reconstructions and multi-proxy model simulations (e.g., Watts et al., 1996; Vanandel, 2002) indicated temperatures comprised between -10 and 0 °C for winter months in Central and Southern Italy (the LGM climate in the Ardenne were previously discussed in section 3.3.1, this chapter). Moreover, the scarp studied by Tucker et al. (2011) is located below the minimum elevations—from 1600 to 2500 a.s.l.—of relict rock glaciers identified in the Central Apennines. These rock glaciers probably mark the lowermost limit of Pleistocene discontinuous alpine permafrost in the peninsula (Dramis and Kotarba, 1992; Giraudi and Frezzotti, 1997), in contrast to evidences of a former discontinuous permafrost found in the Ardenne (see section 3.3, this chapter). As suggested by Hales and Roering (2007), the presence of a permafrost limits the availability of water from the groundwater system for segregation ice growth, thus drastically reducing the maximum intensities of frost cracking compared to systems characterized by seasonal ice conditions without the occurrence of a permafrost.

Thus, assuming that the weathering rates reported by Tucker et al. (2011) do not apply to the Ardenne's case, can we conclude that if frost cracking and the biogenic activity prevailed under, respectively, the periglacial and temperate environments that followed each other in the Ardenne, they probably resulted in weathering rates not far from each other ? This scenario may initially explain why P_0 is well constrained. Moreover, by constraining the CLICHE model with

present-day soil thickness data, the rate of production of mobilizable regolith is determinant in both cold and warm phases of the climatic scenario, respectively in order to reproduce proper 'initial conditions' of soil thickness distribution at the beginning of the Holocene, and from that time to control the rapidity at which the soil mantle evolved towards its present-day state given the low transport rates of the Holocene. However, hereafter we argue that any other value of P_0, specific to the cold period of the climate scenario and possibly very different from the P_0 value constrained by our inversion, could reproduce the same initial conditions at the beginning of the Holocene. Changing the transport coefficients for overland flow and solifluction, which turn out to be the probable dominant transport processes during the cold period, has almost no impact on the transport of soil during the Holocene. Solifluction is inactive during the warm phase, and due to the contrasted overland flow regimes between the cold and warm periods, the present-day rates of soil transport by overland flow are much lower than those of the cold period, even for high values of K_r (for the simulation S1, the rates varied by up to three orders of magnitude, depending on the location on the synthetic hill). Therefore, if we admit a higher P_0 value for the cold period than for the warm period, then it is possible to reproduce the same ideal soil distribution at the beginning of the warm period by increasing the values of K_r and K_g, without altering the further evolution of the synthetic hill during the warm period. If P_0 is effectively higher for the cold period, then our inversion underestimated the rate of soil transport for this period. The reasoning is similar if we alternatively consider a lower P_0 value for the cold period. Thus, we conclude here that the apparently good constraint on the rate of soil production is most probably related to mechanisms which prevailed under the recent temperate climate of the Ardenne, and that the present-day soil thickness distribution cannot be used together with a unique parametrization of soil production independent of climate to precisely constrain both soil production and soil transport for the last glacial period.

3.6.2 Inherited soil thickness distribution, inherited hillslope morphology and the landscape equilibrium

In chapter 2, we have used sediment supply in addition to spatially averaged soil thickness and denudation rates as indicators of landscape equilibrium. The evolution of these variables in the last 10 kyr of the simulations S1 and S2 (and S4) clearly shows that, if these simulations are representative of the real behaviour of hillslopes in the Ardenne, the present-day hillslopes are not in dynamic equilibrium (Figure 3.12). We made an additional simulation with the same set of parameter values than S1 but for an extended simulation time of another 80 kyr of temperate Holocene climate. The resulting evolution of average soil thickness indicates a very long potential response time to the last glacial-interglacial transition (Figure 3.15A). However, it does not mean that the entire present-day Ardenne landscape is far from equilibrium. In our simulations, the variety of hillslope geometrical settings found in the Ardenne were lumped into a small synthetic hill, and because of their limited extent in the Ardenne Massif, the steepest slopes which probably respond more rapidly to the last climate transition (see chapter 2) are under-represented in our modelling. In addition, variable lithological and environmental settings in the massif do obviously imply differences in response to climate variations.

Simulation S1 shows that even at the scale of the synthetic hill, the time response is highly

variable. At the end of the simulation, a local steady-state soil thickness (SSST), i.e., a dynamic equilibrium in which soil thickness does not vary locally over time, is reached on divergent areas of the synthetic hill (hill 'noses'). We see in Figure 3.16 that on those noses, assuming that soil density is half the rock density (Table 3.IV), the surface denudation rate is perfectly balanced by the soil production rate. Figure 3.15 also shows significant changes in soil thickness for the highest values of negative curvature from 100 kyr to 120 kyr of simulation time (B-C), but almost no change beyond that time (C-D). The establishment of SSST on the hill noses has some important implications, notably on the applicability of CRN-based estimation of soil production rates which could potentially validate the well constrained value of P_0 obtained here (and also the fixed h_0 parameter). These estimates imply SSST, as frequently assumed in techniques used to estimate erosion and weathering rates (Phillips, 2010). Wilkinson et al. (2005) have demonstrated that an invalid SSST assumption would affect the apparent relationship between soil production estimates and soil depth. In the previously mentioned studies of Heimsath et al. (1997, 1999, 2000), the sampled sites were precisely located on the convex regions of the investigated hillslopes where the authors had good reasons to suppose SSST, as changes in soil production or transport with Pleistocene–Holocene climate change would have adjusted local soil thickness early in the Holocene (Heimsath et al., 1997). For the Ardenne's case however, the simulation S1 (and S2) suggests that SSST was later reached on the hill noses (only 3-4 kyr ago). The recent rapid evolution of soil thickness in our study area is therefore not favourable to CRN-based estimations of soil production rates using traditional methods. Nevertheless, the total change in thickness is limited to 15-30 cm, and our modelling provides a probable scenario of recent soil thickness evolution that can be used to derive more sophisticated estimates of soil production rates from CRN measurements.

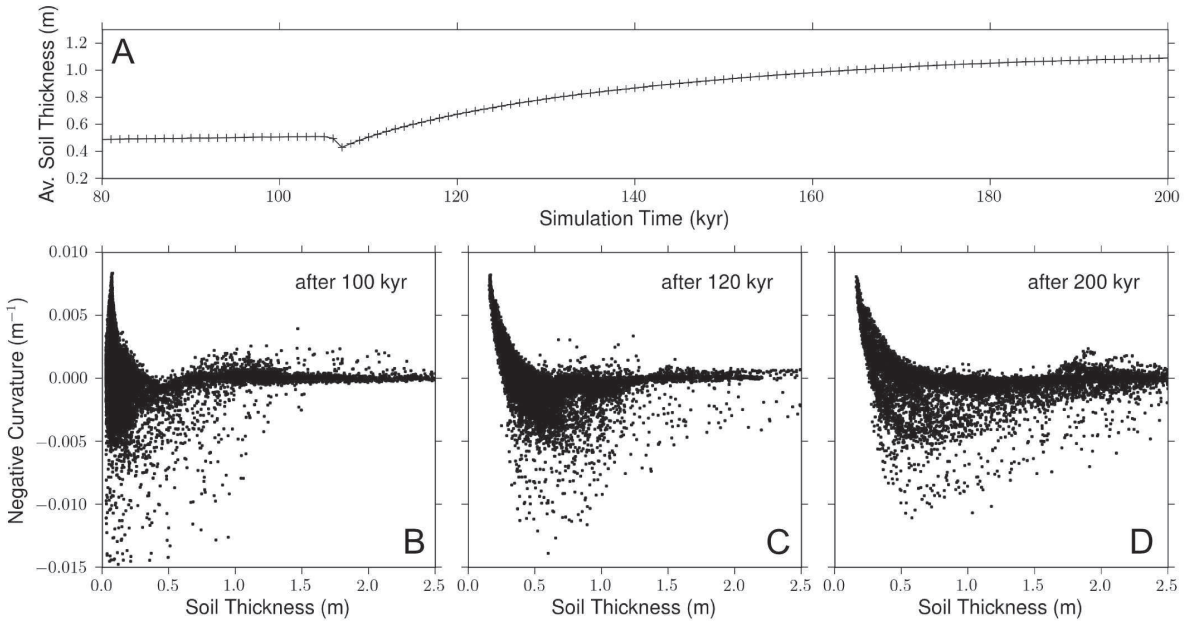

Figure 3.15: Evolution of soil thickness averaged over the synthetic hill (A) and evolution of the relationship of negative curvature vs. soil thickness (B,C,D) for the same set of parameter values than S1, but here with 80 kyr of additional simulation time during which the warm phase of the climate scenario is kept constant. Surface curvature is computed directly from the mesh nodes, without re-interpolation, using a finite volume scheme. The topography is prior smoothed to reduce the scatter of curvature values introduced by local disturbances, resulting itself from the intermittent transport by overland flow.

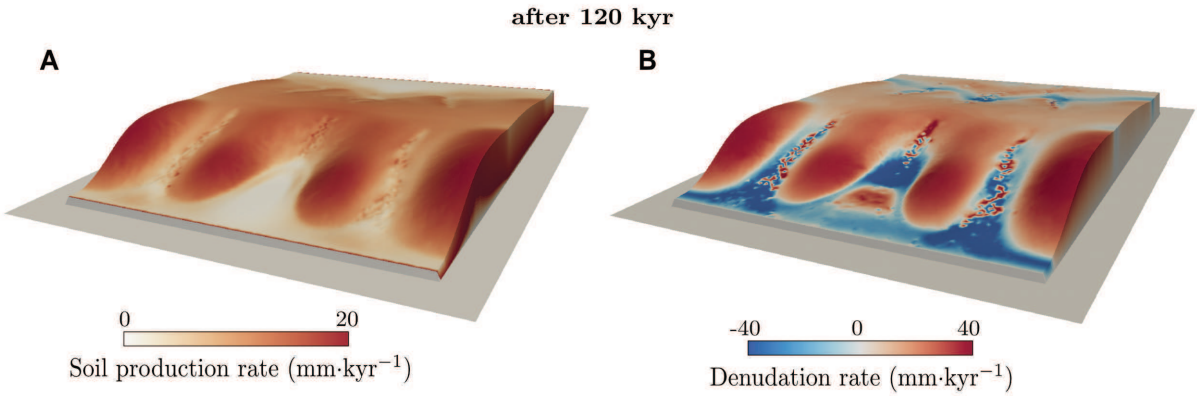

Figure 3.16: Soil production rates (A) and denudation rates (B) at the end of simulation S1. Deposition occurs for negative values of denudation rate.

Simulations S1 and S2 also show that changes in soil thickness since the transition from the cold to the warm climatic phase are more marked in convergent areas (i.e., negative curvature values in Figure 3.15 B-C-D) than on the noses of the synthetic hill. From the beginning of the warm phase, soil coming from the convex regions cannot be any longer evacuated by solifluction and/or highly efficient transport by overland flow. Deposition occurs in the concave regions (Figure 3.16B), resulting in a typical diffusive shape for the synthetic hill. Due to the overall low transport rates and given the slowly increasing depth-dependent creep fluxes along with the increase in soil thickness, the time needed for soil production and transport to reach SSST is quite long (a significant evolution of soil thickness vs. curvature is shown between Figure 3.15C and D for positive curvature values and thick soils), though the response is non-linear. Beside the possible control of vegetation and/or lithology on soil thickness, outlined by e.g. Wilkinson et al. (2005) and for which further investigations are needed in the Ardenne, it is therefore probable that the present-day shallow soils characteristic of convergent areas are the relics of a soil thickness distribution that formed during the glacial period and that has not yet been entirely overprinted by present-day processes. From data collected by Heimsath et al. (2000) on hill noses in the Bega Valley, Herman and Braun (2006) have demonstrated that soil thickness versus local curvature relationships do not provide good constraints on whether a soil distribution has reached steady state. But if our interpretation is correct, our results suggest that, focusing on convergent areas of the hillslopes, these relationships are very informative on whether a soil distribution has fully readjusted to a major climate change event. The relationships between soil thickness and other terrain attributes (slope, drainage area and topographic index) are also useful indices of the transition from cold to warm climate. The model predicts that these relationships change during the climate transition with a decline of their non-linearity. Note however that the shallow soils (< 20 cm) observed on the Ardenne soil map in convergent hillsope areas are not reproduced in the selected simulations S1 and S2 (Figures 3.13 and 3.16C for S1). This discrepancy between observations and model predictions may be explained by the possible incorrect parametrization we used for soil production in the Ardenne. A solution might be to use a 'humped' production function, which is assumed in many landscapes and that predicts a maximum production rate at a finite soil depth and smaller rates for both thinner and thicker soils (see chapter 1). It may either cause the soil to thicken to a stable depth, equal to or greater than the optimal depth,

or strip the hillside to bedrock (Carson and Kirkby, 1972; Dietrich et al., 1995; Heimsath et al., 1999). High transport rates during the cold period would have locally lowered soil thickness below its optimal depth, and the positive feedback between soil production and soil thickness has not permitted soil to thicken during the Holocene. Although only sparse bare bedrock areas are found in the Ardenne landscape, suggesting that the optimal production depth is likely to be small, we cannot, in this study, definitively demonstrate which soil production function between the simple exponential and the humped functions is more appropriate.

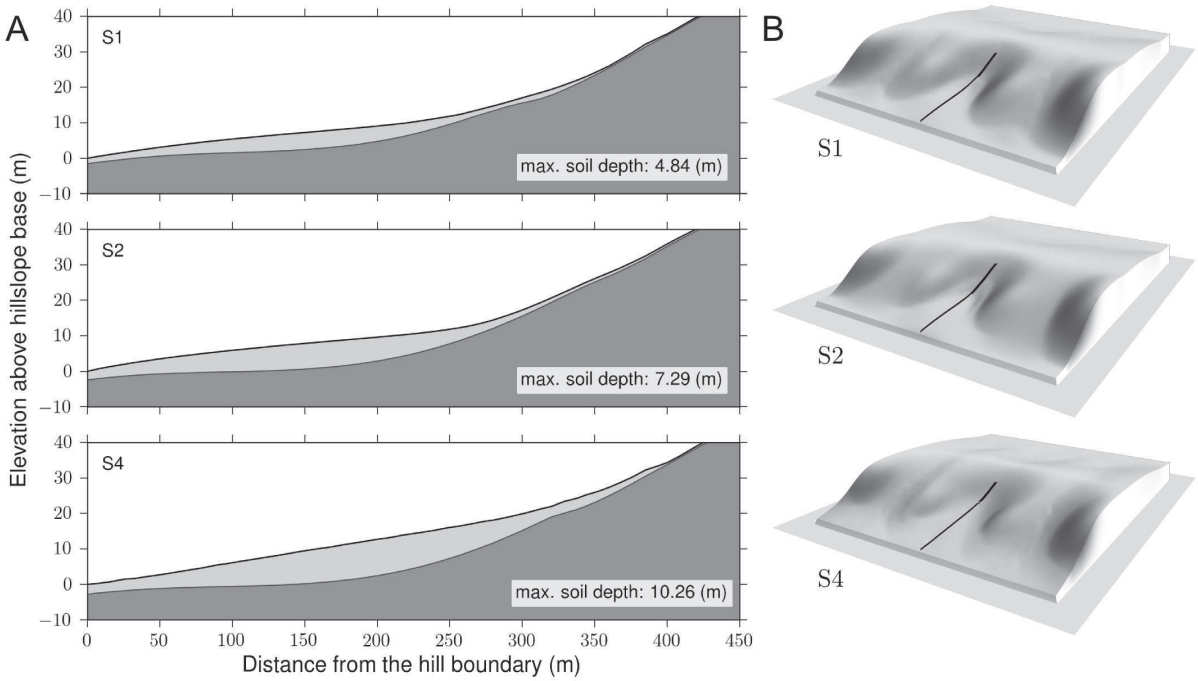

Figure 3.17: A. Vertical profiles at the middle of the steepest side of the synthetic hill for simulations S1 (both transport by overland flow and solifluction), S2 (predominant solifluction) and S4 (predominant transport by overland flow and high simple creep fluxes), at the end of the simulations. Dark-grey and light-grey filled areas correspond respectively to bedrock and mobilizable regolith (soil). B. Shape of the synthetic hill at the end of the simulations (greyscale is proportional to slope) and localization of the profiles (thick black line).

Beside thinning the soil over a large part of the synthetic hill, the high transport rates of the cold period also caused considerable accumulation of soil at the base of the hill, preferentially downslope of the convergent areas (Figure 3.14 A1). At the surface, these high accumulation rates result in gentle, quasi-linear slopes (Figure 3.17). Such slopes are also observed in the present-day Ardenne landscape. For example, Rixhon and Juvigné (2010) have attributed large, thick-mantled 'benches' found in the Ninglinspo valley (Amblève basin) to the former action of periglacial slope processes. All of these benches display a gentle transversal slope towards the current river channel and the most extended ones are located at the base of concave 'amphi-theatres'. Although the predicted and observed transversal slopes can't be directly compared due to the specific boundary conditions used in the model, our predicted maximum soil depths, between 4 and 10 m, are consistent with the maximum depths observed by Rixhon and Juvigné (2010) (from 2-3 m to 6-7 m). This suggests that despite our inability to constrain both soil production and transport rates related to the cold period, the predicted erosion rates for this period are probably close to real rates (note however that the hill sides of the Ninglinspo valley

are among the steepest slopes found in the Ardenne). The active periglacial processes proposed by Rixhon and Juvigné (2010) include mudflow events and solifluction, which is also consistent with our predictions, as similar features can be reproduced with either dominant solifluction, dominant transport by overland flow or both processes (Figure 3.17), and which would possibly indicate that the modelled transport by overland flow may involve the averaged effect of rapid and short events of flowing sediments in periglacial environments.

3.6.3 Efficiency and spatial segregation of soil transport processes

The overall efficiency of soil transport and the predominance of specific transport processes under cold and temperate conditions have been already discussed. It is important, however, to remind the reader that, using CLICHE, our scenario of varying climate only affected soil transport, which is thereby the driver of hillslope dynamics discussed so far. It is also important to note that the alternation of predominant transport mechanisms from cold to warm climatic phases is not the result of predetermined threshold parameters (although the presence of the frozen/non-frozen soil state for soil transport), but is the primarily the result of the dynamic interplay between the modelled processes.

Although our inversion highlighted this likely temporal alternation of transport mechanisms, the spatial partitioning of these mechanisms on the synthetic hill remains unclear in both the cold and warm climatic phases. The relative importance of soil transport mechanisms greatly differs between the two models S1 and S2, especially for overland flow and simple creep, resulting in contrasted patterns in the contribution from each transport process to the total downhill soil flux (Figures 3.14 and 3.22). Model S1 predicts that all transport mechanisms have been more or less active in separate regions of the hill, depending on the local combination of slope, soil thickness and drainage area, while model S2 predicts that solifluction and depth-dependent creep are the dominant mechanisms everywhere, for the cold and warm phases respectively. Despite these two different configurations, both models have produced similar distributions of soil thickness. The major differences in soil depth are restricted to areas of strong drainage convergence, where the action of overland flow prevents the accumulation of soil in model S1. These results contrast with those of Braun et al. (2001) in which the spatial segregation of transport processes is critical for fitting their model to an observed curvature vs. soil thickness relationship. However, both the data and the parameterization of soil transport are different here. Note also that runoff generation schemes different from the uniform excess storage capacity runoff used here (e.g., spatially variable saturation-excess runoff; see chapter 1) may drastically change the spatial distribution of overland flow. If sufficient weight is given to the overland flow mechanism, it should therefore considerably affect the partitioning of the transport processes.

3.6.4 Climate control on denudation rates and sediment supply

Quaternary denudation rates in the Meuse catchment and other catchments of the Renish Massif have been recently estimated on different time scales (Schaller et al., 2001, 2002, 2004; Meyer et al., 2008). A discrepancy is generally observed between Late Pleistocene to 'mordern' denudation rates derived from CRN concentrations (E_C)—measured in basal fluvial terrace or

active bedload samples—and present-day erosion rates inferred from river load gauging (E_G). The former rates, integrated through the last 10-30 kyr, vary between 30 and 80 mm·kyr^{-1} while the latter, which integrate the record over periods of a few years to decades, are only about one-third of the E_C estimates (from 9 to 25 mm·kyr^{-1}). Although these observed denudation rates correspond to averages over medium-size catchments, it is interesting to compare them with our predictions, as the change in predominant soil transport mechanisms suggested by our results may have caused major changes in denudation rates during the last glacial-interglacial cycle (Figure 3.12 C-D).

Simulations S1 and S2 show a similar ratio between erosion rates corresponding to the cold and warm stable phases of our climatic scenario, though both of these rates are less than the observed E_C and E_G estimates (predicted rates are about 30 mm·kyr^{-1} for the cold phase and range between 5 and 10 mm·kyr^{-1} for the warm phase). This may be due—at least for the underestimation of modern erosion rates—to the high value chosen for the cycle elongation factor (see chapter 1). This is also expected as, contrary to our model predictions, observed catchment-wide erosion rates do also include the contribution from river incision. However, we have previously mentioned in this chapter that the Late Quaternary propagation of a potential river incision wave into the Ardenne is likely to take place over a longer period than the time scales involved here. Unpublished CRN-derived erosion rates, measured in the Amblève basin, don't show any significant differences between samples collected above and downstream of the knickpoints (Schaller, 2011, pers. comm.). Moreover, a significant downstream increase of CRN concentrations was not observed by Schaller et al. (2001) who collected multiple samples along the main streams of several middle European catchments, including the Meuse catchment. As suggested by these authors, this demonstrates that the CRN concentration was governed by the residence time of the sediment in the hillslope weathering and mass wasting system, rather than by fluvial transfer. These evidence comfort us in our assumption that the observed E_C estimates can be directly compared with our predictions, after integrating the latter over similar time spans.

The mean predicted denudation rates over the past 10 to 30 kyr range between 5 and 25 mm·kyr^{-1} for S1 and S2. The discrepancy between these rates and the E_C estimates may be explained by an underestimation of soil production and transport rates for the cold period (as discussed in section 3.6.1). An alternate explanation may reside in the evolution of predicted denudation rates during the transitions between the cold and warm phases of the climate scenario. Both simulations S1 and S2 display during these transitions short peaks of very high erosion rates that reach 150 to 200 mm·kyr^{-1} for S2 and 80 to 100 mm·kyr^{-1} for S1. This is due to the high values of K_g, used in these model runs, and the maximum efficiency of solifluction when MAAT is close to 0°C (see chapter 1). If the parameterization and the relative importance of solifluction is correct, a more realistic climate scenario, with increased instabilities during the last glacial cycle (D-O events) and/or the last glacial-interglacial transition (Younger Dryas), would result in more frequent occurrences of these erosion peaks, resulting in higher time-integrated denudation rates. Schaller et al. (2001) and Meyer et al. (2008) proposed several explanations for the discrepancy between E_C estimates (from samples taken in stream sediment) and E_G estimates: (1) rare flood events that are not captured in the short-term erosion record obtained from river load gauging,

(2) spatially non-uniform erosion or (3) CRN concentration inheritance due to enhanced erosion during the Late Pleistocene. Our predictions strongly support the last explanation, though the other propositions cannot be excluded.

The simulated climate control on sediment supply to channels is strongly correlated to the evolution of denudation rates (Figure 3.12 A-C). This may also explain why E_G estimates are generally greater than our predicted erosion rates for the Holocene. During the Late Pleistocene, high predicted solifluction rates may have yielded a greater amount of material to the channels that has been more or less rapidly evacuated by the rivers, depending on their transport capacity. If we assume rather low transport capacities, as expected in the presence of coarse-grained material and low and rare peak discharges, it is then plausible that the rivers are still evacuating this accumulated material nowadays. Although solifluction allows the mobilization of material of heterogeneous granulometric composition, granulometry is not handled in CLICHE and the assumption of inefficient removal of slope deposits by the rivers cannot be verified here. It has however been discussed by Rixhon and Juvigné (2010) in the case of the Ninglinspo valley where these authors reported that the river removed more than 90 % of the periglacial material provided by hillslope erosion. Note, however, that the Ninglinspo River corresponds to an extreme case in the Ardenne where the average longitudinal gradient of the channel is very steep.

3.6.5 Scale dependence and influence of the physics of soil production and transport processes on the data fit

We made additional simulations, similar to model S1, to test whether the fit to data is sensitive to the scale used to represent the transport processes on one hand, and to the geomorphic law parameters that were not constrained by the inversion on the other hand. Sets of model runs were performed by varying each of a finite number of model parameters within a given range while keeping all other parameters constant. Results are shown in Figure 3.18. Note that the minimum of each of these curves does not necessarily correspond to the most probable value, as the data misfit may further change for different combinations of other parameter values.

The results indicate that the data fit is almost insensitive to variations in the pseudo-grid size of the synthetic hill above 5 m but seems to be scale-dependent below this value (note that the original mesh is still being re-interpolated on a 20x20 m grid prior to the calculation of the misfit). This characteristic value of 5 m is precisely the resolution above which Heimsath et al. (1999) found that the curvature derived from their topographic grid became relatively scale-independent. This agreement is difficult to explain, but may be due to the use of a similar exponential soil production function in both studies, and the dominance, assumed by Heimsath et al. (1999), of diffusive sediment transport which also prevails in the later part of our model evolution. These authors also suggest that the optimal scale is likely to be different for landscapes under different dominant processes or climates. However, our results do not support this conclusion as the scale does not appear to depend on the existence of a cold climate and the associated solifluction (and transport by overland flow), but as our modelling of these processes possibly involves both slow and rapid processes, their scale-dependence remains unclear (Furbish and Haff, 2010).

By constrast, we see that the data fit is most sensitive to the characteristic soil depth (h_0)

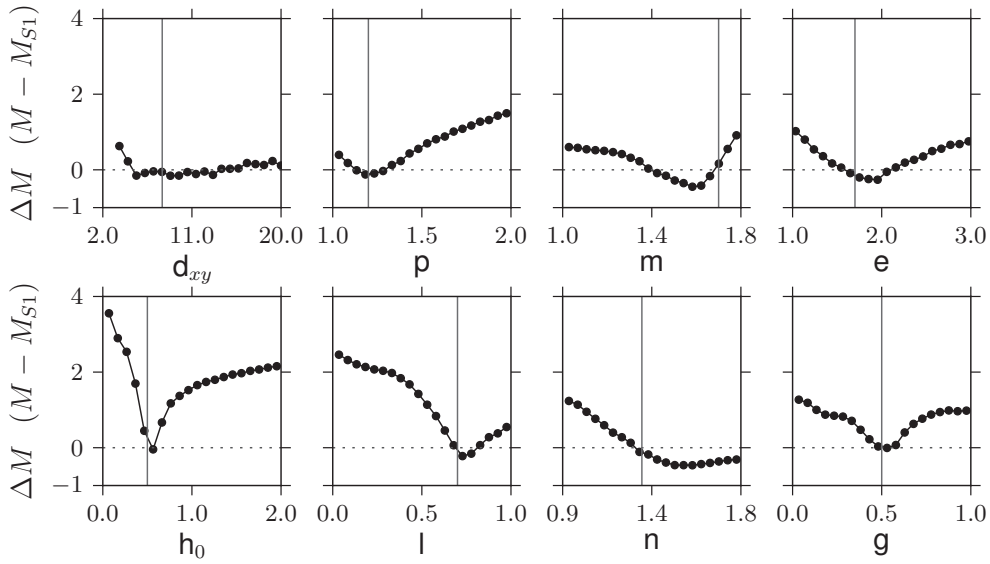

Figure 3.18: Differences ΔM between the misfit value of simulation S1, M_{S1}, and misfits resulting from varying the values of the mean distance between mesh nodes (d_{xy}), the exponents of the soil transport laws (p, l, m, n, e, g) and the parameter h_0 of the soil production function (see Table 3.IV). Vertical lines indicate the values fixed for S1 and all other simulations in this study.

of the exponential soil production function. This reinforces our conclusion that soil production is controlling parameter in reproducing the observed present-day distribution of soil thickness in the Ardenne. Further inversions should therefore also include h_0 in the parameter space, or even use another parameterization for soil production (as we previously proposed). We also see that the sensitivity of the depth-dependent creep exponents (p,l) is found to be slightly higher than the sensibility of those for solifluction and transport by overland flow (m,n and e,g, respectively). We thus show that the results presented here are consistent with the remarks we made in section 3.6.1.

3.7 Conclusions and perspectives

From a unique dataset of soil thickness vs. topography, coupled with a novel numerical model which handles in detail the physical influence of climate on soil transport, we have derived here an original and rigorous inference of soil production and transport in a region that underwent drastic environmental changes during the glacial-interglacial cycles of the Quaternary. Despite the coarse resolution of the data, very interesting and relevant results emerged from our inversion. Predictions from some of the best-fitted models are relatively consistent with independent observations of denudation rates estimated in the Renish Massif and soil production rates measured in other temperate environments, as well as landforms and broad features of soil thickness distribution observed in our study area, which has been identified as remnants of the former periglacial activity. These predictions suggest that Quaternary climate variations deeply affected hillslope dynamics, through the successive establishment of weathering-limited and transport-limited conditions due to alternating dominant transport processes of variable efficiency. This implied substantial changes in the relationship between soil thickness and to-

pography, and also contrasted time responses to climate variations. Consequently, we propose that the time response for transition from cold to temperate climates is much longer than for transition from temperate to cold climates, and therefore that the current distribution of soil thickness still retains a signature of the distribution in place during the last glacial period. Additionally, high peaks of sediment fluxes are predicted to occur during climate transitions and may have important implications on the fluvial response to these transitions.

Beside giving new insights into hillslope evolution under varying climatic conditions, we have also demonstrated that we cannot fully rely on data of present-day soil thickness and topography to accurately and precisely constrain both soil production and transport for the climates that preceded the Holocene. Additional data are needed, and should most probably comprise estimates of erosion, weathering and/or soil production rates at different time scales in the Ardenne or in comparable hilly landscapes which actually experience climates similar than those experienced in the past in our study area. Moreover, we have shown that the parametrization of soil production is determinant in reproducing observed distributions of soil thickness. Although we propose that, in our case, varying the dominant weathering mechanism might possibly result in similar weathering rates, further modelling efforts should be put towards better representing these mechanisms and their link to climate, as done for example by Hales and Roering (2007) and Dixon et al. (2009a,b). The inversion also highlighted the limits of using a simple climatic scenario and/or low precision data, as it was not possible to obtain a good fit between predicted and observed relationships between soil thickness and surface derivatives. It would therefore be interesting to consider using high resolution topographic and soil thickness measurements and take advantage of recent advances in modelling past climates. Yet, because our model allows a long-term integration of hillslope dynamics at a high temporal resolution, our method provides a powerful tool which can, for example, be used to more easily interpret erosion and soil production estimates that are often sparsely distributed in time.

3.8 Supplement: simualtion results for models S2, S3 and S4

In this supplement, modelled vs. observed distributions of surface derivatives, simulation snapshots and surface curvature vs. soil thickness relationships are shown for the selected simulations S2, S3 and S4. Results from simulation S1 were shown in the previous sections. See Table 3.VII for parameter values.

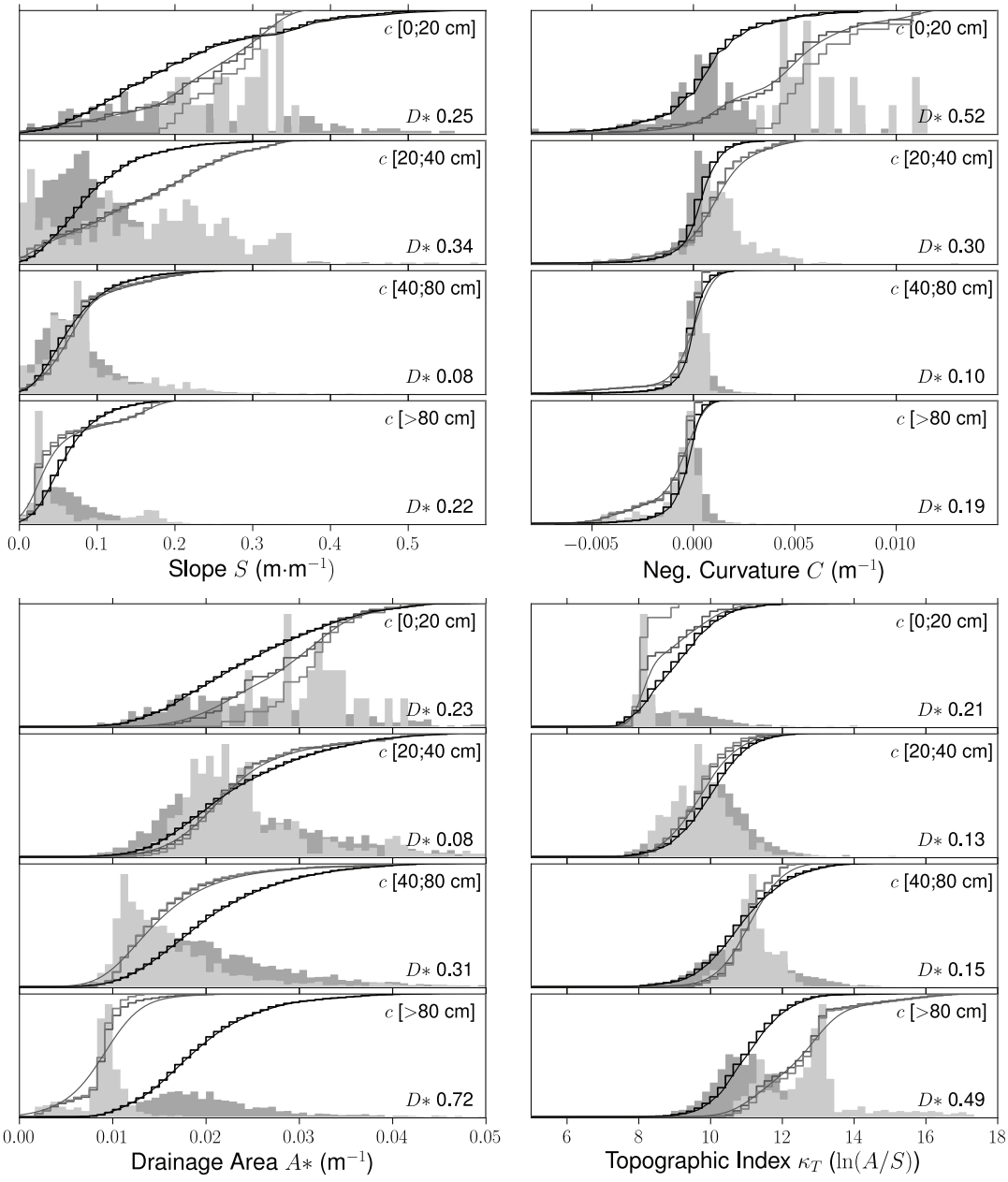

Figure 3.19: Simulation S2: observed (dark grey) and modelled (light grey) distributions of terrain attributes for all soil thickness classes. See Figure 3.13 for more details

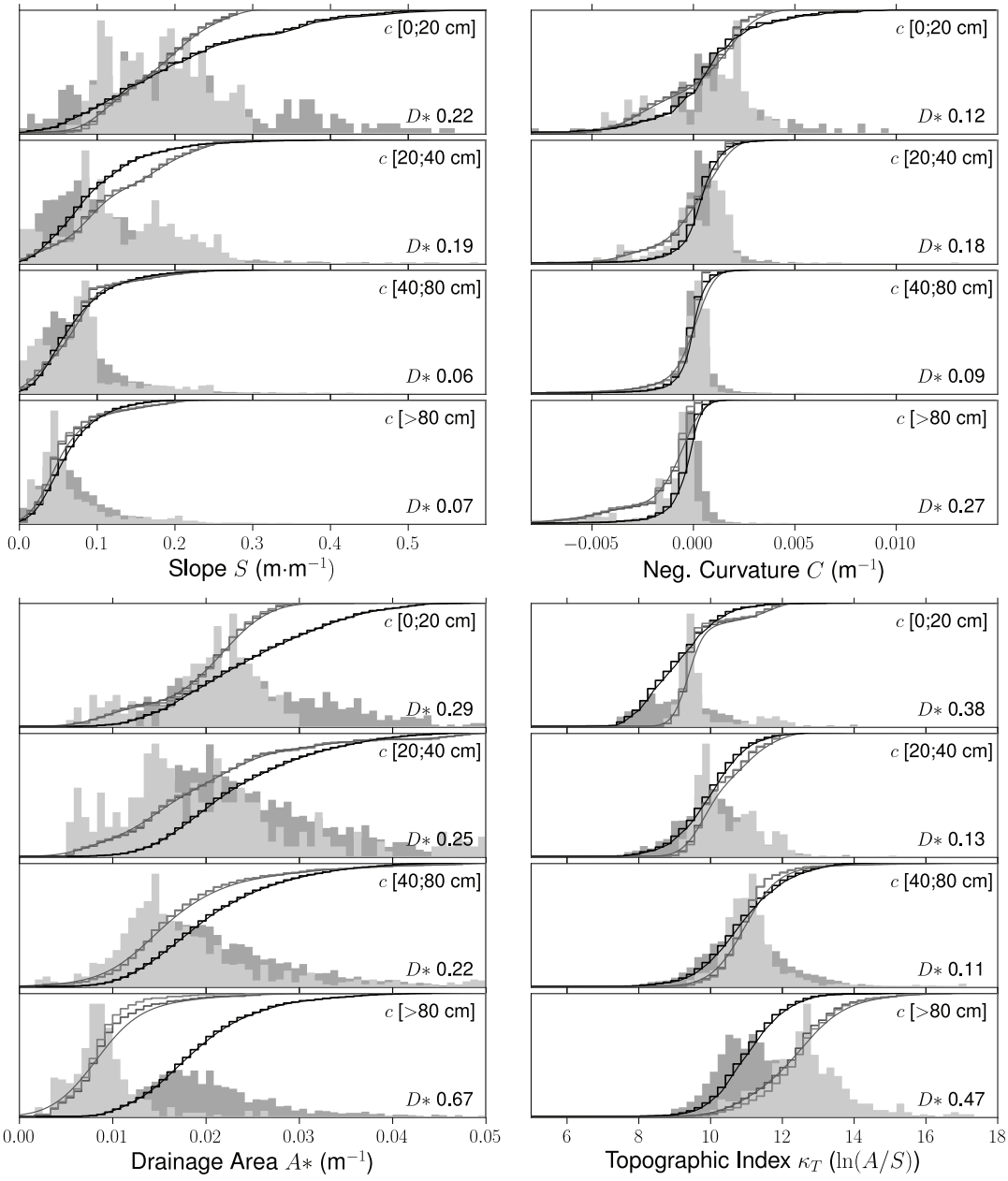

Figure 3.20: Simulation S3: observed (dark grey) and modelled (light grey) distributions of terrain attributes for all soil thickness classes. See Figure 3.13 for more details

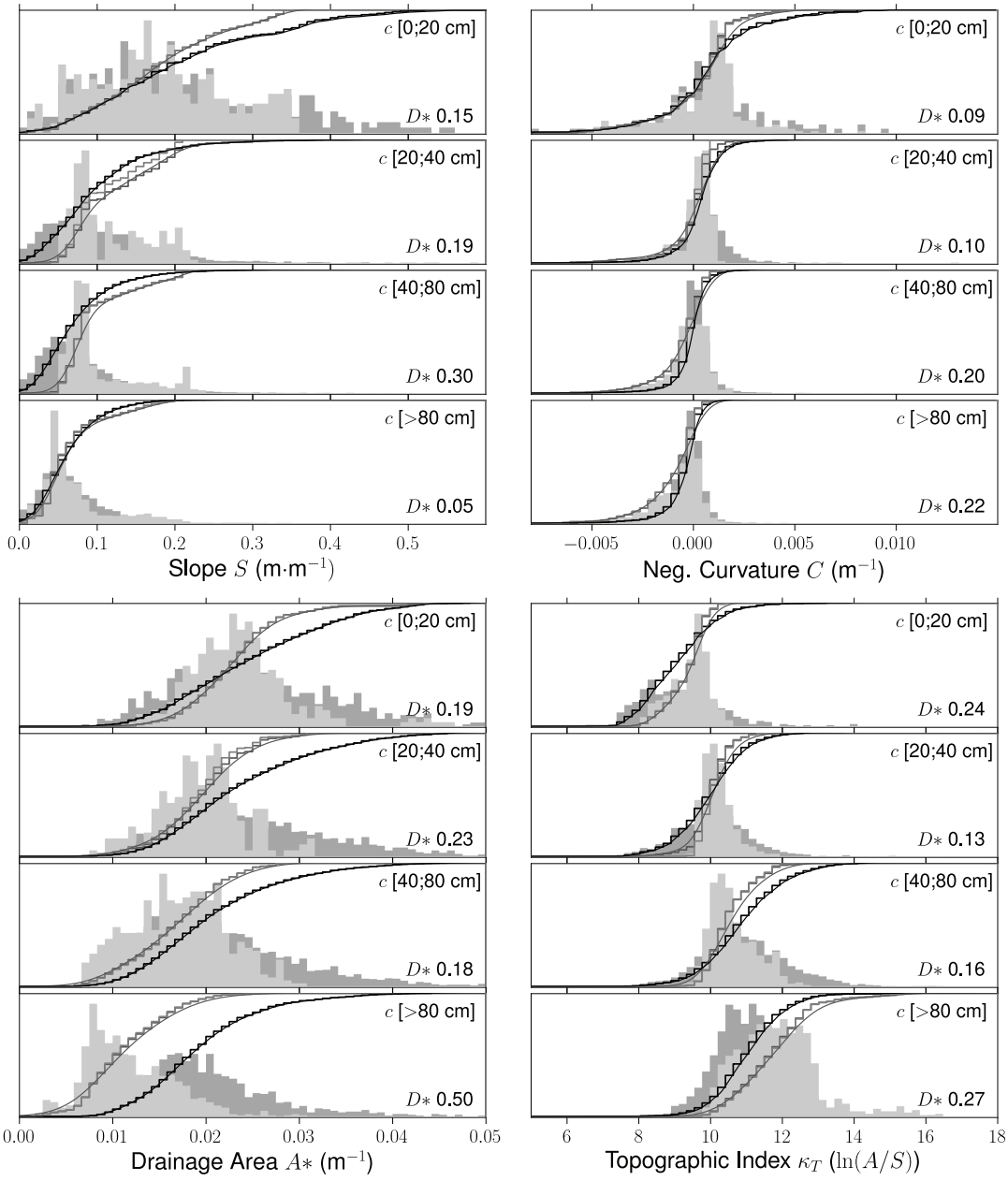

Figure 3.21: Simulation S4: observed (dark grey) and modelled (light grey) distributions of terrain attributes for all soil thickness classes. See Figure 3.13 for more details

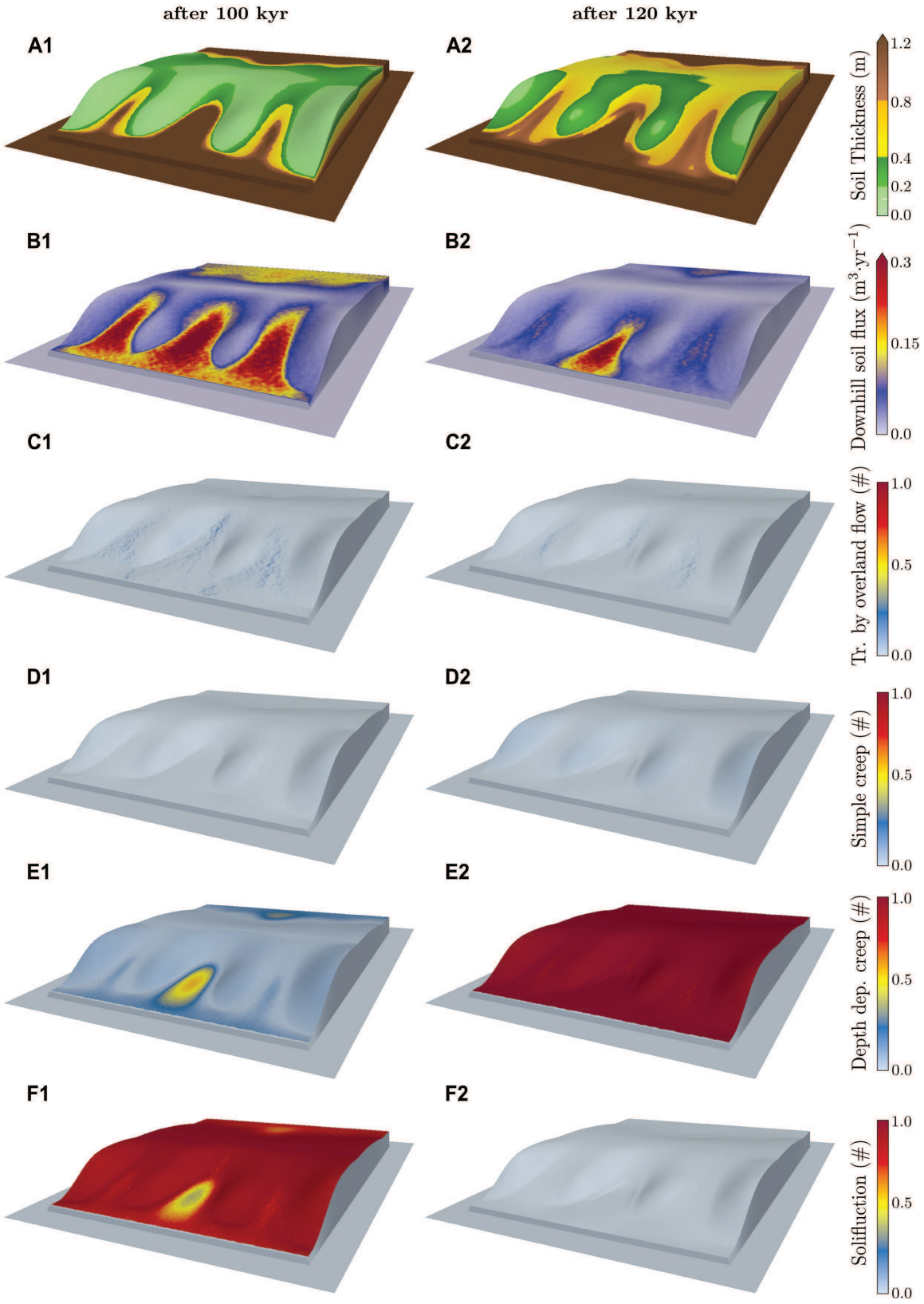

Figure 3.22: Snapshots of simulation S2. See Figure 3.14 for more details.

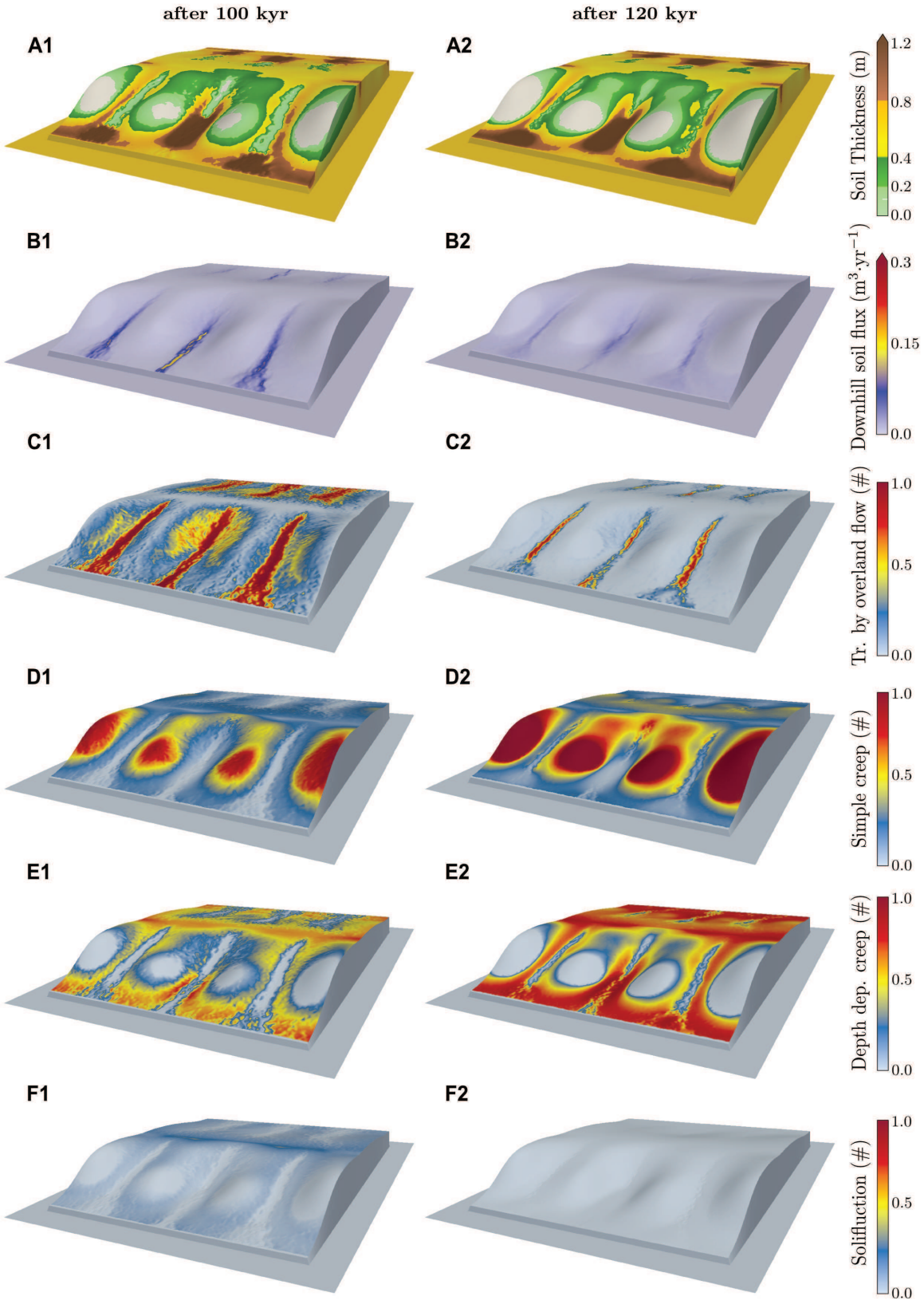

Figure 3.23: Snapshots of simulation S3. See Figure 3.14 for more details.

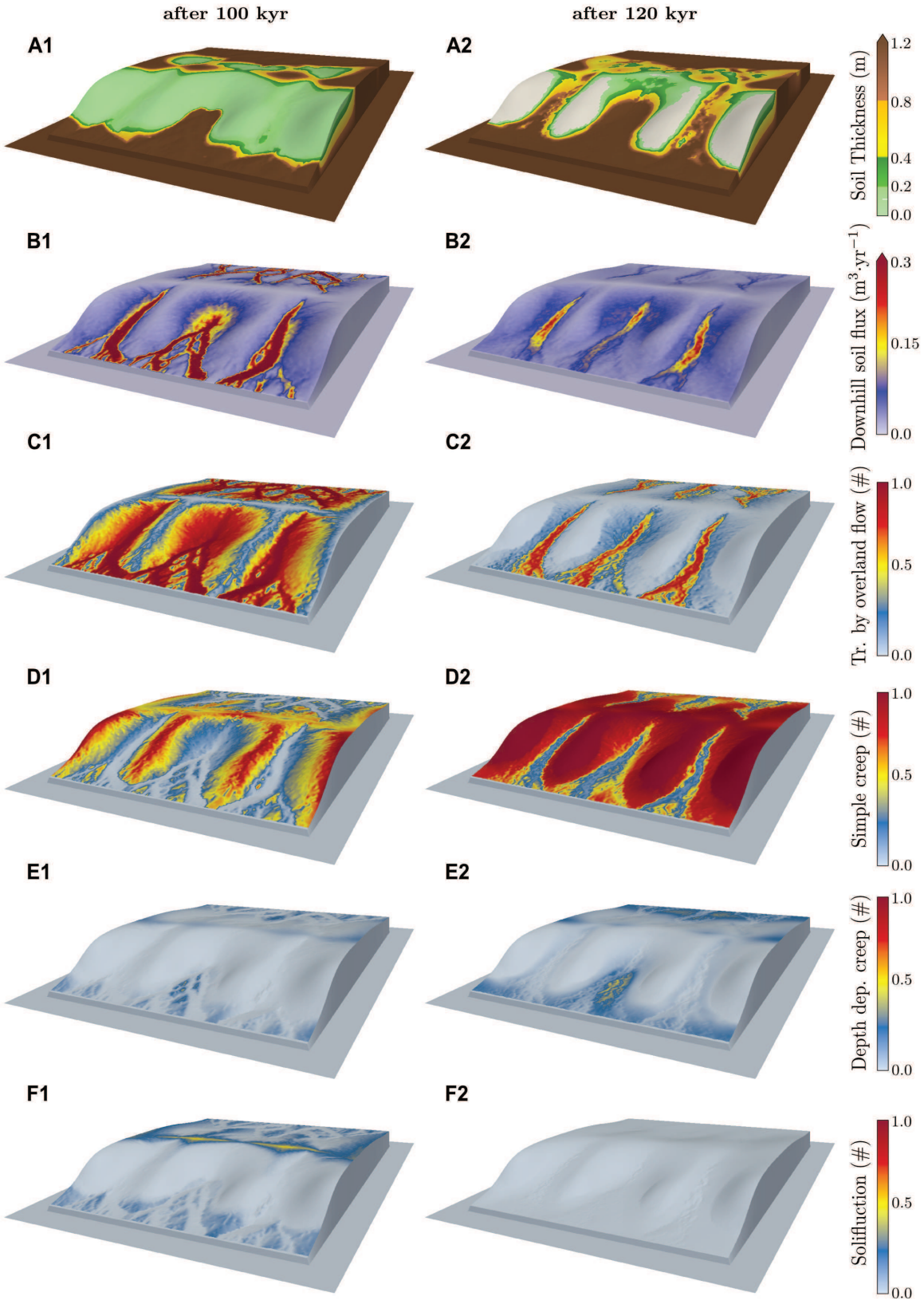

Figure 3.24: Snapshots of simulation S4. See Figure 3.14 for more details.

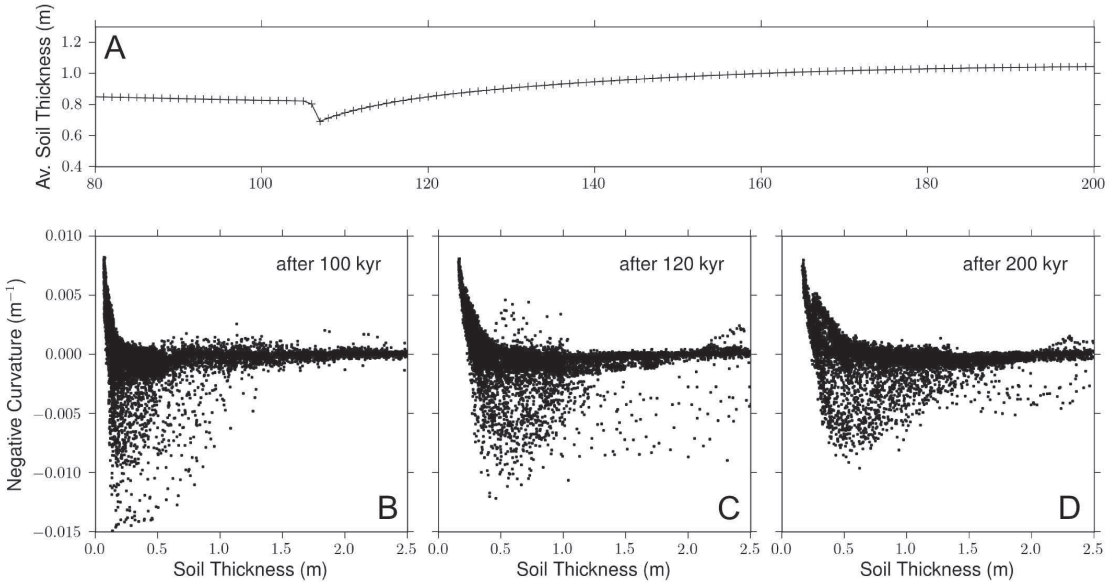

Figure 3.25: Evolution of soil thickness averaged over the synthetic hill (A) and evolution of the relationship of negative curvature vs. soil thickness (B,C,D) for the same set of parameter values than S2 (see Figure 3.15 for more details).

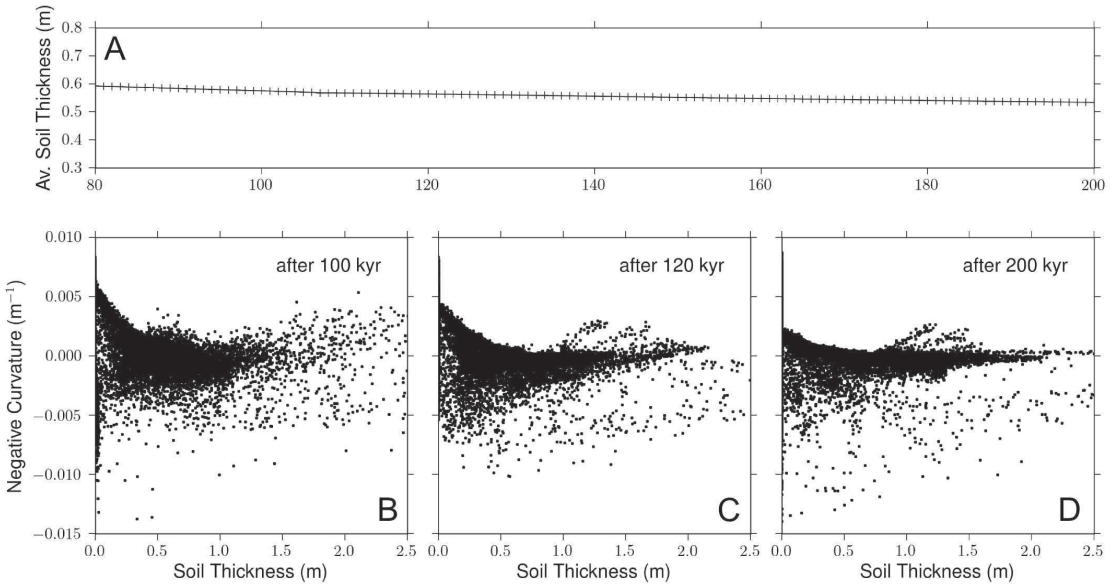

Figure 3.26: The same than 3.25 for the set of parameter values of S3.

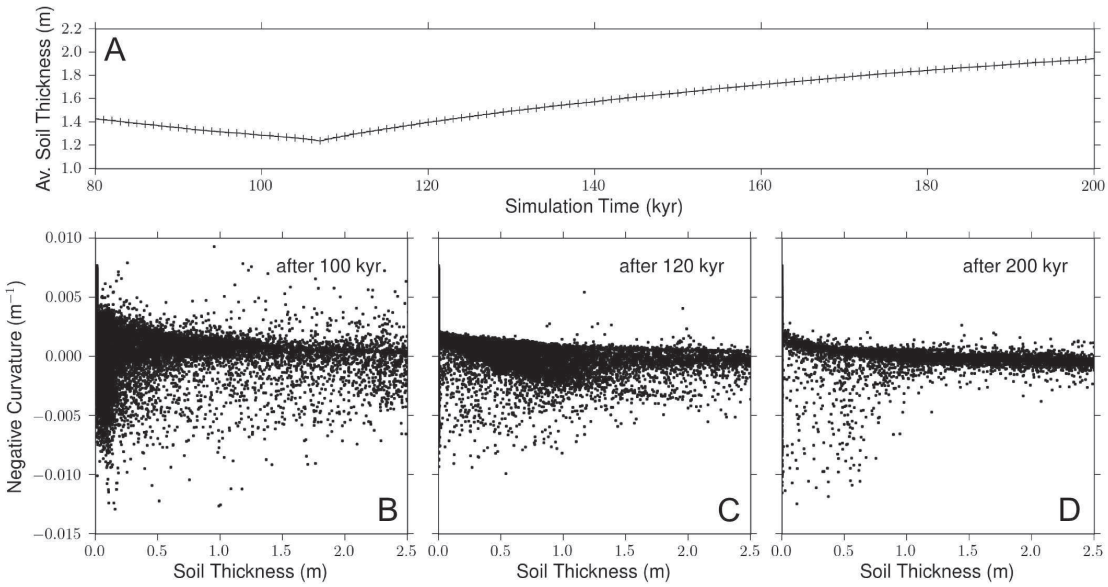

Figure 3.27: The same than 3.25 for the set of parameter values of S4.

Conclusion

In this thesis manuscript, we have presented CLImate Control on Hillslope Erosion (CLICHE), a new numerical modelling framework that has been specifically developed for simulating the evolution of soil mantle and hillslope morphology in response to climatic variations at different time scales (from diurnal or seasonal to millennial or Quaternary time scales). By using a multi-process parameterization of soil transport mechanisms, which includes variables that are related to climatic properties (i.e., temperature and precipitation) through the use of ground heat transfer and hydrological models, and by defining a soil mobilization threshold which depends on the frozen/unfrozen soil state, we have (partially) addressed the problem of the climate-dependence of the parameters of soil transport laws implemented in most of the hillslope erosion models. Our model therefore provides a useful framework for studying landscape evolution in regions that have experienced drastic climate variations in the past (e.g., during the glacial-interglacial cycles of the Quaternary) or that may undergo climate change in near future.

In chapter 1, we have shown through some examples that the efficiency of soil transport processes modelled in CLICHE is highly sensitive to climate variations. It is for example the case for solifluction rates that depend on active-layer depth, which itself varies non-linearly with mean annual air temperature. It is also the case for transport by overland flow, as climate variations can deeply affect the surface runoff regime on hillslopes. More generally, each transport processes are affected by variations in mean annual temperature or its annual amplitude, due to the frozen/unfrozen soil criterion for mobilization. Furthermore, sensitivity analyses, which have been presented in chapter 2, demonstrate that the general behaviour of the model under varying climates—considering all soil transport processes—is highly sensitive to hillslope geometry and the combination of parameter values chosen for soil transport. In other words, these analyses highlight how differently each modelled transport process responds to climate change and affects the evolution of the hillslope system towards an equilibrium. There is thus the hope that each transport parameter may be calibrated by using observations under a range of climatic and geometric conditions.

Hence, we may explain why the soil thickness/topographic dataset used in the inversion, presented in chapter 3, provides relatively good, though non-unique, constraints on the CLICHE soil transport parameters. Indeed, this dataset has been collected in a region (i.e., the Ardenne Massif) that underwent drastic climate changes during the glacial-interglacial periods of the Quaternary, and which encompass a variety of hillslope geometries that range from the low relief

found in the massif uplands to the steeper slopes along the main streams. In fact, a key point in the constraining of the CLICHE parameters is the ability of the model to produce a spatio-temporal segregation of soil transport mechanisms. The inversion results reveal the dominance of solifluction (and possibly transport by overland flow) under cold climates and the dominance of creep and depth-dependent creep under temperate climates. This temporal segregation of transport processes allowed the prediction of highly variable transport rates between cold and temperate climates, which in turn may explain the good constraint level obtained for soil production, as the rate of soil production is implicitly controlled by soil transport through soil thickness (see chapter 3 for full discussion).

Perspectives

The CLICHE applications presented in this manuscript have provided new interesting insights that improve our quantitative understanding of hillslope erosion processes under varying climates (see conclusion of chapter 3); They are, however, only a small overview of the possibilities offered by the numerical model. Indeed, we have used very simple climatic scenarios in these applications, whereas CLICHE has been specifically designed to allow the use of complex, realistic climatic inputs. Simple climatic scenarios helped to understand the basic aspects of the model behaviour and to give an outline of soil and slope dynamics under both cold and temperate climates, representative of the Quaternary glacial-interglacial cycles. Applications related to the Quaternary evolution of hillslopes may, however, take advantage of recent advances in modelling past climates (e.g., Flückiger et al., 2008; Kageyama et al., 2010; Singarayer and Valdes, 2010). Nowadays, global or regional climate models can be used to define realistic, high-resolution climatic scenarios for the last glacial-interglacial cycle (e.g., Singarayer and Valdes, 2010). In turn, these scenarios permit to study hillslope evolution in response to continuously changing climate, similarly to previous studies that have used δ^{18}O records as proxy for erosion rates (e.g., Schaller and Ehlers, 2006; Tucker et al., 2011), but in a much more advanced manner with CLICHE. Interesting future work therefore consists to apply the inversion procedure presented in chapter 3, considering such realistic climatic scenarios. Additionally, there is a need for exploring the influence of the climatic instabilities of the last glacial period (e.g., the 'Dansgaard-Oeschger' events) on hillslope erosion, as our inversion results suggest very high soil transport and denudation rates during cold/temperate climate transitions. At longer temporal scales, CLICHE may be used to investigate the response of hillslopes to changes in the period and amplitude of the Quaternary climatic oscillations, by comparing model predictions with, e.g., cosmogenic nucleide-derived erosion rates estimated at different ages and for different time spans (e.g., Schaller and Ehlers, 2006).

Other possible applications would only require a few model improvements. An interesting problem is for example the formation of asymmetrical valleys in periglacial environments. This phenomenon is widely described in the literature, although it remains poorly studied at a quantitative level. The formation of E-W aligned asymmetrical valleys, characterized by north-facing slopes steeper than south-facing slopes, is usually explained by greater mass-wasting activity on south-facing slopes, due to greater solar radiation and, consequently, thicker active layers

(French, 1996). CLICHE would provide a framework suited to the quantification of the processes controlling this phenomenon, but only if it allows spatially variable climatic inputs (at least for temperature), which is a feature not yet implemented in the model. Another, more general problem is hillslope/channel coupling. On one hand, channels act as lower boundary conditions and thus control hillslope evolution (e.g., Mudd and Furbish, 2005). Lateral migration of the boundary nodes is not yet implemented in CLICHE, although this feature is included in the CASCADE libraries (Braun and Sambridge, 1997) used by CLICHE. On the other hand, hillslopes yield sediments to channels, which influence the rate of river incision through the tool and cover effects (Turowski and Rickenmann, 2009; Lague, 2010). CLICHE can provide accurate, stream-variable predictions of hillslope sediment supply to channels, and is thus likely to be coupled with sediment-flux dependent river incision models in order to study the response of landscape as a whole to climate variations (at least, CLICHE could provide better constraints to the parameters of the sediment-supply formulations in these incision models). Recently, Valla et al. (2010b) compared different river incision models in their ability to predict the evolution of gorges incising glacial hanging valleys in the Western Alps (France). The authors have demonstrated the importance of considering sediment supply from the gorge sidewalls while reproducing the observed channel geometry. This example reminds the need to make CLICHE applicable in steep slope environments, either by including additional soil transport laws (e.g., Roering et al., 1999) or by the implementation of slope failure algorithms (e.g., Tucker and Bras, 1998).

Besides improvements needed to enlarge the range of potential CLICHE applications, and despite the relative complexity of the model in its current version, important modelling efforts are still required to pursue our goal towards a better climate forcing of weathering and soil transport processes, as we discussed in chapter 1. The inversion results presented in chapter 3 have highlighted the limitations of using a single, climate-independent soil production law. To overcome these limitations, a possible solution is to use a multi-process parameterization of soil production that should distinguish dominant weathering processes under cold climates (e.g., frost cracking) (Hales and Roering, 2007) from dominant processes under temperate climates (e.g., biogenic activity). But such a parameterization will indubitably introduce additional parameters. Chemical weathering should also be included by the distinction of soil and saprolite within the regolith layer (Dixon et al., 2009a). Furthermore, the parameterization of soil transport may suffer from the 'overlapping' of the processes involved in each transport law (see chapter 2). A solution would consist to define transport laws that each focus on specific processes, such as solifluction, but it will also introduce many parameters that have to be calibrated. We note that, from a technical point of view, these suggested modifications can rapidly be achieved as they mainly concern the parameterization of soil production and transport, which is handled in a very flexible fashion in the CLICHE framework.

References

Abrahams, A., Howard, A. D., Parsons, A., 1994. Rock-mantled slopes. In: Abrahams, A., Parsons, A. (Eds.), Geomorphology of Desert Environments. Chapman & Hall, London, Ch. 8, pp. 173–212.

Abu-Hamdeh, N., Sep. 2003. Thermal Properties of Soils as affected by Density and Water Content. Biosystems Engineering 86 (1), 97–102.

Abu-Hamdeh, N., Reeder, R., 2000. Soil thermal conductivity: Effects of density, moisture, salt concentration, and organic matter. Soil Science Society of America Journal 64 (4), 1285–1290.

Ahnert, F., 1967. The role of the equilibrium concept in the interpretation of landforms of fluvial erosion and deposition. In: Macar, P. (Ed.), L'evolution des versants. University of Liège, Liège, pp. 23–41.

Ahnert, F., 1970. A comparison of theoretical slope models with slopes in the field. Zeitschrift für Geomorphologie 9, 88–101.

Ahnert, F., 1976. Brief description of a comprehensive three-dimensional process-response model of landform development. Zeitschrift für Geomorphologie 25, 29–49.

Ahnert, F., 1987. Approaches to dynamic equilibrium in theoretical simulations of slope development. Earth Surface Processes and Landforms 12, 3–15.

Akerman, H., 1996. Slow mass movements and climatic relationships, 1972–1994, Kapp Linne, West Spitsbergen. In: Anderson, M., Brooks, S. (Eds.), Advances in Hillslope Processes (vol. 2). Wiley, Chichester, pp. 1219–1256.

Alexandre, J., 1958. Le modelé quaternaire de l'Ardenne Centrale. Annales de la société Géologique de Belgique 81 (M), 213–331.

Anderson, R., 1994. Evolution of the Santa Cruz mountains, California, through tectonic growth and geomorphic decay. Journal of Geophysical Research 99, 20161–20179.

Anderson, R., 1998. Near-surface thermal profiles in Alpine bedrock: implications for the frost weathering of rock. Arctic and Alpine Research 30, 362–372.

Anderson, R., Humphrey, N., 1989. Interaction of weathering and transport pro- cesses in the evolution of arid landscapes. In: Cross, T. (Ed.), Quantitative dynamic stratigraphy: Englewood Cliffs. Prentice Hall, New Jersey, pp. 349–361.

Anderson, R. S., 2002. Modeling the tor-dotted crests, bedrock edges, and parabolic profiles of high alpine surfaces of the Wind River Range, Wyoming. Geomorphology 46, 35–58.

Anderson, T. W., Darling, D. A., 1952. Asymptotic theory of certain "goodness-of-fit" criteria based on stochastic processes. Annals of Mathematical Statistics 23, 193–212.

Armstrong, A., 1987. Slopes, boundary conditions, and the development of convexo-concave forms—some numerical experiments. Earth Surface Processes and Landforms 12 (1), 17–30.

Ballantyne, C., Harris, C., 1994. The Periglaciation of Great Britain. Cambridge University Press, Cambridge.

Banninger, D., 2007. Technical Note: Water flow routing on irregular meshes. Hydrology and Earth System Sciences 11 (4), 1243–1247.

Beaumont, C., Kooi, H., Willett, S., 1999. coupled tectonic-surface process models with applications to rifted margins and collisional orogens. In: Summerfield, M. (Ed.), Geomorphology and Global Tectonics. Wiley, New York, pp. 29–55.

Bell, F., 2000. Engineering properties of soils and rocks, 4th Edition. Wiley-Blackwell.

Bengtsson, L., Westerström, G., Jun. 1992. Urban snowmelt and runoff in northern Sweden. Hydrological sciences journal 37 (3), 263–275.

Beven, K. J., 1997. TOPMODEL: A Critique. Hydrological Processes 11 (9), 1069–1086.

Beven, K. J., Kirkby, M. J., 1979. A physically based, variable contributing area model of basin hydrology. Hydrological Sciences Bulletin 24, 43–69.

Bishop, P., 2007. Long-term landscape evolution: linking tectonics and surface processes. Earth Surface Processes and Landforms 32 (3), 329–365.

Blyth, E., 2001. Relative influence of vertical and horizontal processes in large-scale water and energy balance modelling. In: Soil-vegetation-atmosphere transfer schemes and large-scale hydrological models. Sixth Scientific Assembly of the International Association of Hydrological Sciences (IAHS), Maastricht, pp. 3–10.

Bogaart, P. W., 2003. Process-based modelling of the fluvial response to rapid climate change. Phd, Vrije Universiteit Amsterdam.

Bogaart, P. W., Tucker, G. E., Vries, J. J. D., 2003a. Channel network morphology and sediment dynamics under alternating periglacial and temperate regimes: a numerical simulation study. Geomorphology 54, 257 – 277.

Bogaart, P. W., Van Balen, R., Kasse, C., Vandenberghe, J., 2003b. Process-based modelling of fluvial system response to rapid climate change II. Application to the River Maas (The Netherlands) during the Last Glacial–Interglacial Transition. Quaternary Science Reviews 22 (20), 2097–2110.

Bogaart, P. W., Van Balen, R., Kasse, C., Vandenberghe, J., 2003c. Process-based modelling of fluvial system response to rapid climate change—I: model formulation and generic applications. Quaternary Science Reviews 22 (20), 2077–2095.

Borradaile, G. J., 2003. Statistics of earth science data: their distribution in time, space, and orientation. Springer.

Braun, J., 2002. Estimating exhumation rate and relief evolution by spectral analysis of age–elevation datasets. Terra Nova 14 (3), 210–214.

Braun, J., Heimsath, A. M., Chappell, J., 2001. Sediment transport mechanisms on soil-mantled hillslopes. Geology 29 (8), 683–686.

Braun, J., Sambridge, M., 1995. A numerical method for solving partial differential equations on highly irregular evolving grids. Nature 376, 655–660.

Braun, J., Sambridge, M., 1997. Modelling landscape evolution on geological time scales: a new method based on irregular spatial discretization. Basin Research 9 (1), 27–52.

Braun, J., van der Beek, P., Batt, G., 2006. Quantitative Thermochronology. Cambridge University Press, Cambridge.

Brovelli, M. A., Cannata, M., Longoni, U. M., 2004. LIDAR Data Filtering and DTM Interpolation Within GRASS. Transactions in GIS 8 (2), 155–174.

Brown, R. J. E., Péwé, T. L., 1973. Distribution of permafrost in North America and its relationship to the environment: A review, 1963– 1973. In: Permafrost: The North American Contribution to the Second International Conference, Yakutsk. National Academy of Sciences, Washington D.C., pp. 71–100.

Bull, W., 2001. Geomorphic responses to climatic change. Oxford University Press, New York.

Carlisle, B. H., 2005. Research Article Modelling the Spatial Distribution of DEM Error. Transactions in GIS 9 (4), 521– 540.

Carson, M., Kirkby, M., 1972. Hillslope form and process. Cambridge University Press, New York.

Castelltort, S., Van Den Driessche, J., Mar. 2003. How plausible are high-frequency sediment supply-driven cycles in the stratigraphic record? Sedimentary Geology 157 (1-2), 3–13.

Cerling, T., Craig, H., 1994. Geomorphology and in-situ cosmogenic isotopes. Annual Reviews Earth Planetary Sciences 22, 273–317.

Chen, W., 2003. Changes in soil temperature and active layer thickness during the twentieth century in a region in western Canada. Journal of Geophysical Research 108 (D22), 1–13.

Codilean, A., Bishop, P., Hoey, T. B., 2006. Surface process models and the links between tectonics and topography. Progress in Physical Geography 30 (3), 307.

Costa-Cabral, M., Burges, S., 1994. Digital Elevation Model Networks (DEMON): a model of flow over hillslopes for computation of contributing and dispersal areas. Water Resources Research 30 (6), 1681–1692.

Coulthard, T., 2001. Landscape evolution models: a software review. Hydrological Processes 15, 165–173.

Coulthard, T. J., Macklin, M. G., Kirkby, M. J., 2002. A cellular model of Holocene upland river basin and alluvial fan evolution. Earth Surface Processes and Landforms 27 (3), 269–288.

Cox, N., 1980. On the relationship between bedrock lowering and regolith thickness. Earth Surface Processes 5, 271–274.

Crave, A., Davy, P., 2001. A stochastic "precipiton" model for simulating erosion/sedimentation dynamics. Computers and Geosciences 27 (7), 815–827.

Culling, W., 1960. Analytical theory of erosion. Journal of Geology 68, 336–344.

Culling, W. E. H., 1963. Soil creep and the development of hillside slopes. The Journal of Geology 71 (2), 127–161.

Czurda, K., Hohmann, M., Jun. 1997. Freezing effect on shear strength of clayey soils. Applied clay science 12 (1-2), 165–187.

Davis, J. C., 1986. Statistics and data analysis in geology. Wiley, New-York.

Davis, W. M., 1892. The convex profile of badland divides. Science 20, 245.

De Ploey, J., Savat, J., 1968. Contribution à l'étude de l'érosion par le splash. Zeitschrift für Geomorphologie 12, 174–193.

de Vries, D., 1963. Thermal properties of soils. In: van Wijk, W. (Ed.), Physics of plant environment. North-Holland, Amsterdam, pp. 210–235.

de Vries, D. A., 1975. Heat transfer in soils, Wiley. In: de Vries, D. A., Afgan, N. H. (Eds.), Heat and mass transfer in the biosphere. Part I: Transfer processes in plant environment. Wiley, New-York, pp. 4–28.

Delaunay, B., 1934. Sur la sphère vide. Akademii Nauk SSSR, Otdelenie Matematicheskikh i Estestvennykh Nauk 7, 793–800.

Delisle, G., May 2007. Near-surface permafrost degradation: How severe during the 21st century? Geophysical Research Letters 34 (9), 2–5.

Delunel, R., van der Beek, P. A., Carcaillet, J., Bourlès, D. L., Valla, P. G., Apr. 2010. Frost-cracking control on catchment denudation rates: Insights from in situ produced 10Be concentrations in stream sediments (Ecrins–Pelvoux massif, French Western Alps). Earth and Planetary Science Letters 293 (1-2), 72–83.

Demoulin, A., Beckers, A., Bovy, B., Sep. 2011. On different types of adjustment usable to calculate the parameters of the stream power law. Geomorphology.

Demoulin, A., Bovy, B., Rixhon, G., Cornet, Y., Oct. 2007. An automated method to extract fluvial terraces from digital elevation models: The Vesdre valley, a case study in eastern Belgium. Geomorphology 91 (1-2), 51–64.

Demoulin, A., Hallot, E., 2009. Shape and amount of the Quaternary uplift of the western Rhenish shield and the Ardennes (western Europe). Tectonophysics 474 (3-4), 696–708.

Demoulin, A., Hallot, E., Rixhon, G., 2009. Amount and controls of the Quaternary denudation in the Ardennes massif (western Europe). Earth Surface Processes and Landforms 1496 (June), 1487–1496.

Deng, Y., Wilson, J. P., Bauer, B. O., 2007. DEM resolution dependencies of terrain attributes across a landscape. International Journal of Geographical Information Science 21 (2), 187–213.

Densmore, A., Ellis, M., Anderson, R., 1998. Landsliding and the evolution of normal-fault-bounded mountains. Journal of Geophysical Research 103, 15203–15219.

Dewitte, O., Jasselette, J., Cornet, Y., Vandeneeckhaut, M., Collignon, A., Poesen, J., Demoulin, A., Jun. 2008. Tracking landslide displacements by multi-temporal DTMs: A combined aerial stereophotogrammetric and LIDAR approach in western Belgium. Engineering Geology 99 (1-2), 11–22.

Dietrich, W., Reneau, S., Reneau, C., 1987. Overview: 'Zero-Order Basins' and Problems of Drainage Density, Sediment Transport and Hillslope Morphology. In: Erosion and Sedimentation in the Pacific Rim. IAHS Publication No. 165. International Association of Hydrological Sciences, Washington, DC, pp. 27–37.

Dietrich, W. E., Bellugi, D., Sklar, L. S., Stock, J., Heimsath, A. M., Roering, J. J., 2003. Geomorphic transport laws for predicting landscape form and dynamics. In: Wilcock, P. R., Iverson, R. M. (Eds.), Prediction in Geomorphology. Vol. 135. AGU American Geophysical Union, Washington DC, pp. 103–132.

Dietrich, W. E., Reiss, R., Hsu, M. L., Montgomery, D. R., 1995. A process-based model for colluvial soil depth and shallow landsliding using digital elevation data. Hydrological Processes 9 (3-4), 383–400.

Dixon, J. L., Heimsath, A. M., Amundson, R., 2009a. The critical role of climate and saprolite weathering in landscape evolution. Earth Surface Processes and Landforms 1521 (June), 1507–1521.

Dixon, J. L., Heimsath, A. M., Kaste, J., Amundson, R., 2009b. Climate-driven processes of hillslope weathering. Geology 37 (11), 975–978.

Donnelly, T., 1982. Worldwide continental denudation and climatic deterioration during the late Tertiary: evidence from deep-sea sediments. Geology 10, 451–454.

Dosseto, a., Hesse, P. P., Maher, K., Fryirs, K., Turner, S., Apr. 2010. Climatic and vegetation control on sediment dynamics during the last glacial cycle. Geology 38 (5), 395–398.

Dramis, F., Kotarba, A., 1992. Southern limit of relict rock glaciers, Central Apennines, Italy. Permafrost and Periglacial Processes 3 (3), 257–260.

Du, C., 1996. An algorithm for automatic Delaunay triangulation of arbitrary planar domains. Advances in Engineering Software 27, 21–26.

Dunne, T., Malmon, D. V., Mudd, S. M., Jan. 2010. A rain splash transport equation assimilating field and laboratory measurements. Journal of Geophysical Research 115 (F1), 1–16.

Eagleson, P., 1978. Climate, soil, and vegetation, 2, The distribution of annual precipitation derived from observed storm sequences. Water Resources Research 14, 713–721.

Ehlers, J., Gibbard, P. (Eds.), 2004. Extent and chronology of Glaciation. Volume 1: Europe. Elsevier Science, Amsterdam.

Ehlschlaeger, C. R., Shortridge, A. M., Goodchild, M., 1997. Visualizing spatial data uncertainty using animation. Computers & Geosciences 23 (4), 387–395.

Elias, E., Cichota, R., Torriani, H., Quirijn de Jong van Lier, Q., 2004. Analytical soil-temperature model: Correction for temporal variation of daily. Soil Science Society of America Journal 68, 784–788.

Eymard, R., Gallouët, T., Herbin, R., 2000. Finite Volume Methods. In: Ciarlet, P., Lions, J. (Eds.), Handbook of Numerical Analysis, Vol. VII. Vol. M. North Holland, Amsterdam, pp. 713–1020.

Ferguson, R., 1999. Snowmelt runoff models. Progress in Physical Geography 23, 205–227.

Fernandes, N., Dietrich, W. E., 1997. Hillslope evolution by diffusive processes: The timescale for equilibrium adjustments. Water Resources Research 33 (6), 1307–1318.

Fisher, P. F., 1991. First experiments in viewshed uncertainty: the accuracy of the viewshed area. Photogrammetric Engineering and Remote Sensing 57 (10), 1321–1327.

Flückiger, J., Knutti, R., White, J. W. C., Renssen, H., Feb. 2008. Modeled seasonality of glacial abrupt climate events. Climate Dynamics 31 (6), 633–645.

Fortune, S., 1992. Voronoi diagrams and Delaunay triangulations. In: Du, D., Hwang, F. (Eds.), Computing in Euclidian Geometry. World Scientific, pp. 193–233.

Foufoula-Georgiou, E., Ganti, V., Dietrich, W. E., Jun. 2010. A nonlocal theory of sediment transport on hillslopes. Journal of Geophysical Research 115, 1–12.

Fourier, J., 1955. The Analytical Theory of Heat. English translation by Freeman (1878), republication by Dover Publications, New-York.

François, L., Delire, C., Warnant, P., Munhoven, G., 1998. Modelling the glacial–interglacial changes in the continental biosphere. Global and Planetary Change 16-17, 37–52.

Frechen, M., van Vliet-lanoe, B., van den Haute, P., 2001. The Upper Pleistocene loess record at Harmignies/Belgium: high resolution terrestrial archive of climate forcing. Palaeogeography, Palaeoclimatology, Palaeoecology 173 (3), 175–195.

Freeman, T., 1991. Calculating catchment area with divergent flow based on a regular grid. Computers & Geosciences 17, 413–422.

French, H., Slaymaker, O., 1993. Canada's Cold Land Mass. In: French, H., Slaymaker, O. (Eds.), Canada's Cold Environments. McGill-Queen's University Press, pp. 3–28.

French, H. M., 1996. The Periglacial Environment, 2nd Edition. Longman Harlow.

Furbish, D. J., 2003. Using the dynamically coupled behavior of land-surface geometry and soil thickness in developing and testing hillslope evolution models. In: Wilcock, P. R., Iverson, R. M. (Eds.), Prediction in Geomorphology. AGU American Geophysical Union, Washington DC, pp. 169–181.

Furbish, D. J., Fagherazzi, S., 2001. Stability of creeping soil and implications for hillslope evolution. Water Resources 37 (10), 2607–2618.

Furbish, D. J., Haff, P. K., Jul. 2010. From divots to swales: Hillslope sediment transport across divers length scales. Journal of Geophysical Research 115 (F3), 1–19.

Furbish, D. J., Haff, P. K., Dietrich, W. E., Heimsath, A. M., Sep. 2009. Statistical description of slope-dependent soil transport and the diffusion-like coefficient. Journal of Geophysical Research 114 (1), 1–19.

Garbrecht, J., Martz, L. W., 1999. Digital Elevation Model Issues in Water Resources Modeling. In: Proceedings from Invited Water Resources Sessions, ESRI International User Conference. Environmental Systems Research Institute, San Diego, California, pp. 1–17.

Genty, D., Combourieunebout, N., Hatte, C., Blamart, D., Ghaleb, B., Isabello, L., Aug. 2005. Rapid climatic changes of the last 90 kyr recorded on the European continent. Comptes Rendus Geosciences 337 (10-11), 970–982.

Giannoni, F., Roth, G., Rudari, R., Jun. 2005. A procedure for drainage network identification from geomorphology and its application to the prediction of the hydrologic response. Advances in Water Resources 28 (6), 567–581.

Gilbert, G., 1877. Report on the Geology of the Henry Mountains. U.S. Geographical and Geological Survey of the Rocky Mountain Region, Washington, D.C.

Gilbert, G., 1909. The convexity of hilltops. Journal of Geology 17, 344–350.

Giraudi, C., Frezzotti, M., 1997. Late Pleistocene Glacial Events in the Central Apennines, Italy. Quaternary Research 290 (48), 280–290.

GRASS Development Team, 2008. Geographic Resources Analysis Support System (GRASS GIS) Software. Open Source Geospatial Foundation.
URL `http://grass.osgeo.org`

Hales, T., Roering, J. J., 2005. Climate-controlled variations in scree production, Southern Alps, New Zealand. Geology 33 (9), 701.

Hales, T. C., Roering, J. J., Jun. 2007. Climatic controls on frost cracking and implications for the evolution of bedrock landscapes. Journal of Geophysical Research 112 (F2), 1–14.

Hancock, G. S., Anderson, R. S., 2002. Numerical modeling of fluvial strath-terrace formation in response to oscillating climate. Geol. Soc. Am. Bull. 114, 1131–1142.

Hann, C. T., 1977. Statistical Methods in Hydrology. Iowa State University Press, Ames.

Harris, C., 1981. Periglacial Mass-Wasting: A Review of Research. In: Geo Abstracts (Ed.), BGRG Research Monograph. Vol. 4. Norwich, p. 204.

Harris, C., Davies, M. C. R., Rea, B. R., Nov. 2003. Gelifluction: viscous flow or plastic creep? Earth Surface Processes and Landforms 28 (12), 1289–1301.

Harris, C., Kern-Luetschg, M., Murton, J., Font, M., Davies, M., Smith, F., 2008. Solifluction processes on permafrost and non-permafrost slopes: results of a large-scale laboratory simulation. Permafrost and Periglacial Processes 19 (4), 359–378.

Haxeltine, A., Prentice, I., 1996. BIOME3: An equilibrium terrestrial biosphere model based on ecophysiological constraints, resource availability, and competition among plant functional types. Global Biogeochemical Cycles 10, 693–709.

HDFGroup, 2011. The Hierarchical Data Format.
URL `www.hdfgroup.org`

Heimsath, A., Chappell, J., Dietrich, W., Nishiizumi, K., Finkel, R., 2000. Soil production on a retreating escarpment in southeastern Australia. Geology 28 (9), 787.

Heimsath, A., Dietrich, W., Nishiizumi, K., Finkel, R., 1997. The soil production function and landscape equilibrium. Nature 388 (6640), 358–361.

Heimsath, A., Dietrich, W. E., Nishiizumi, K., Finkel, R. C., 1999. Cosmogenic nuclides, topography, and the spatial variation of soil depth. Geomorphology 27, 151–172.

Heimsath, A. M., Chappell, J., Spooner, N. a., Questiaux, D. G., 2002. Creeping soil. Geology 30 (2), 111.

Heimsath, A. M., Furbish, D. J., Dietrich, W. E., 2005. The illusion of diffusion: Field evidence for depth-dependent sediment transport. Geology 33 (12), 949.

Herman, F., Braun, J., 2006. A parametric study of soil transport mechanisms. GSA Special Papers 398 (11), 191.

Hillel, D., 1980. Fundamentals of soil physics. Academic Press, New-York.

Hirakawa, K., 1989. Downslope movement of solifluction lobes in Iceland: a tephrostratigraphic approach. Geogr. Rep. Tokyo Metropolitan Univ. 24, 15–30.

Hoek, W. Z., Dec. 1997. Late-glacial and early Holocene climatic events and chronology of vegetation development in the Netherlands. Vegetation History and Archaeobotany 6 (4), 197–213.

Hoek, W. Z., Sep. 2001. Vegetation response to the ˜14.7 and ˜11.5 ka cal. BP climate transitions: is vegetation lagging climate? Global and Planetary Change 30 (1-2), 103–115.

Holmgren, P., 1994. Multiple flow direction algorithms for runoff modelling in grid based elevation models: An empirical evaluation. Hydrological Processes 8 (4), 327–334.

Horn, B. K. P., 1981. Hill Shading and the Reflectance Map. Proceedings of the IEEE 69 (1), 14–47.

Houben, P., 2003. Spatio-temporally variable response of fluvial systems to Late Pleistocene climate change: a case study from central Germany. Quaternary Science Reviews 22 (20), 2125–2140.

Hovius, N., 1998. Controls on sediment supply by large rivers, Relative Role of Eustasy, Climate, and Tectonism in Continental Rocks. Society of Sedimentary Geology. Special Publication 59, 3–16.

Hovius, N., Stark, C., Allen, P., 1997. Sediment flux from a mountain belt derived from landslide mapping: Geology. Geology 25, 231–234.

Howard, A., 1980. Thresholds in river regimes. In: Coates, D. R., Vitek, J. D. (Eds.), Thresholds in Geomorphology. George Allen & Unwin, London, pp. 227–258.

Howard, A., 1994. A detchment limited model of drainage basin evolution. Water Resources Research 30, 2261–2285.

Howard, A., Dietrich, W., Seidl, M., 1994. Modeling fluvial erosion on regional to continental scales. Journal of Geophysical Research 99, 13971–13986.

Huijzer, A., Isarin, R., 1997. The reconstruction of past climates using multi-proxy evidence: an example of the Weichselian Pleniglacial in northwest and central Europe. Quaternary Science Reviews 16 (6), 513–533.

Huijzer, B., Vandenberghe, J., 1999. Climatic reconstruction of the Weichselian Pleniglacial in northwestern and Central Europe. Journal of Quaternary Science 13 (5), 391–417.

Humphreys, G. S., Wilkinson, M. T., Apr. 2007. The soil production function: A brief history and its rediscovery. Geoderma 139 (1-2), 73–78.

Hunter, G., Goodchild, M., 1997. Modeling the Uncertainty of Slope and Aspect Estimates Derived From Spatial Databases. Geographical Analysis 29 (1), 35–49.

IGN, 2007. Website of the National Geographical Institute of Belgium.
URL `www.ngi.be (Last visit on August 2007)`

Ijjasz-Vasquez, E., Bras, R., Moglen, G., 1992. Sensitivity of a basin evolution model to the nature of runoff production and to initial conditions. Water Resources Research 28, 2733–2741.

Jenson, S., Domingue, J., 1988. Extracting topographic structure from digital elevation data for geographic information system analysis. Photogrammetric Engineering and Remote Sensing 54, 1593–1600.

Jiménez-Hornero, F., Laguna, A., Giraldez, J., 2005. Evaluation of linear and nonlinear sediment transport equations using hillslope morphology. Catena 64, 272 – 280.

Johnsen, S., Clausen, H., Dansgaard, W., Gundestrup, N., Hammer, C., Andersen, U., Andersen, K., Hvidberg, C., Dahl-Jensen, D., Steffensen, J., Shoji, H., Sveinbjörnsdóttir, A., White, J., Jouzel, J., Fisher, D., 1997. The d18O record along the Greenland Ice Core Project deep ice core and the problem of possible Eemian climatic instability. Journal of Geophysical Research 102, 26397–26410.

Jones, N., Wright, S., Maidment, D., 1990. Watershed delineation with triangle-based terrain models. Journal of Hydraulic Engineering 116, 1232–1251.

Juvigné, E., 1993. Contribution à la téphrostratigraphie du Quaternaire et son application à la géomorphologie. In: Mém. Expl. Cartes Géol. en Min. de la Belgique. p. 66.

Kageyama, M., Laîné, A., Abe-Ouchi, A., Braconnot, P., Cortijo, E., Crucifix, M., de Vernal, A., Guiot, J., Hewitt, C., Kitoh, A., Sep. 2006. Last Glacial Maximum temperatures over the North Atlantic, Europe and western Siberia: a comparison between PMIP models, MARGO sea–surface temperatures and pollen-based reconstructions. Quaternary Science Reviews 25 (17-18), 2082–2102.

Kageyama, M., Paul, A., Roche, D. M., Van Meerbeeck, C. J., Oct. 2010. Modelling glacial climatic millennial-scale variability related to changes in the Atlantic meridional overturning circulation: a review. Quaternary Science Reviews 29 (21-22), 2931–2956.

Kane, D., Hinkel, K., Goering, D., Jun. 2001. Non-conductive heat transfer associated with frozen soils. Global and Planetary 29 (3-4), 275–292.

Kelly, J. J., 2006. Graduate Mathematical Physics, 1st Edition. Wiley-VCH, Berlin.

Kienzle, S. W., 2008. A new temperature based method to separate rain and snow. Hydrological Processes 22, 5067–5085.

Kirkby, M., 1986. A two-dimensional simulation model for slope and stream evolution. In: Abrahams, A. (Ed.), Hillslope processes: Winchester, Mass. Allen and Unwin, pp. 203– 222.

Kirkby, M., 1987. Modelling some influences of soil erosion, landslides and valley gradient on drainage density and hollow development. Catena Supplement 10, 1–14.

Kirkby, M., 1994. Thresholds and instability in stream head hollows: a model of magnitude and frequency for wash processes. In: Kirkby, M. (Ed.), Process Models and Theoretical Geomorphology. Wiley, New-York, Ch. 14, pp. 295–314.

Kirkby, M., 2008. Erosion, Weathering and Landform Evolution. In: Holden, J. (Ed.), An Introduction to Physical Geography and the Environment, 2nd Edition. Pearson Education, Ch. 11, pp. 295–326.

Kirkby, M., Cox, N., 1995. A climatic index for soil erosion potential (CSEP) including seasonal and vegetation factors. Catena 25 (1-4), 333–352.

Kirkby, M. J., 1971. Hillslope process-response models based on the continuity equation. Inst. Brit. Geogr., Spec. Publ. 3, 15–30.

Kirkby, M. J., 1995. A model for variations in gelifluction rates with temperature and topography: Implications for global change. Geografiska Annaler 77 (4), 269–278.

Klein Tank, a. M. G., Wijngaard, J. B., Können, G. P., Böhm, R., Demarée, G., Gocheva, A., Mileta, M., Pashiardis, S., Hejkrlik, L., Kern-Hansen, C., Heino, R., Bessemoulin, P., Müller-Westermeier, G., Tzanakou, M., Szalai, S., Palsdottir, T., Fitzgerald, D., Rubin, S., Capaldo, M., Maugeri, M., Leitass, A., Bukantis, A., Aberfeld, R., van Engelen, a. F. V., Forland, E., Mietus, M., Coelho, F., Mares, C., Razuvaev, V., Nieplova, E., Cegnar, T., Antonio Lopez, J., Dahlström, B., Moberg, A., Kirchhofer, W., Ceylan, A., Pachaliuk, O., Alexander, L. V., Petrovic, P., Oct. 2002. Daily dataset of 20th-century surface air temperature and precipitation series for the European Climate Assessment. International Journal of Climatology 22 (12), 1441–1453.

Kwadijk, J., van Deursen, W., 1993. Development and testing of a GIS-based water balance model for the river Rhine drainage basin. In: Kwadijk, J. (Ed.), The impact of climate change on the River Rhine. Netherlands Geographical Studies, KNAG, Utrecht, Ch. 3, pp. 51–101.

Kwadijk, J., van Deursen, W., 1995. Development and testing of a GIS based water balance model for the Rhine drainage basin. Tech. rep., Internationale Komission für die Hydrologie des Rheingebietes / Commission internationale de l'Hydrologie du bassin du Rhin.

Laflen, J., Lane, L., Foster, G., 1991. WEPP: A new generation of erosion prediction technology. Journal of Soil and Water Conservation 46, 34–38.

Lague, D., 2010. Reduction of long-term bedrock incision efficiency by shor-term alluvial cover intermittency. Journal of Geophysical Research 115 (2), 1–23.

Lague, D., Hovius, N., Davy, P., 2005. Discharge, discharge variability, and the bedrock channel profile. Journal of Geophysical Research 110, 1–17.

Laîné, a., Kageyama, M., Salas-Mélia, D., Voldoire, A., Rivière, G., Ramstein, G., Planton, S., Tyteca, S., Peterschmitt, J. Y., Apr. 2008. Northern hemisphere storm tracks during the last glacial maximum in the PMIP2 ocean-atmosphere coupled models: energetic study, seasonal cycle, precipitation. Climate Dynamics 32 (5), 593–614.

Lal, D., 1991. Cosmic ray labeling of erosion surfaces: in situ nuclide production rates and erosion models. Earth and Planetary Science Letters 104, 424–439.

Leeder, M., Harris, T., Kirkby, M., 1998. Sediment supply and climate change: implications for basin stratigraphy. Basin Research 10 (1), 7–18.

Lewkowicz, A., 1990. Morphology, frequency and magnitude of active layer detachment slides, Fosheim Peninsula, Ellesmere Island, NWT. In: Permafrost-Canada, Proceedings of the Fifth Canadian Permaf rost Conference: Université Laval, Nordicana. pp. 111–118.

Lindström, G., Johansson, B., Persson, M., Gardelin, M., Bergström, S., 1997. Development and test of the distributed HBV-96 model. Journal of Hydrology 201, 272–288.

Litt, T., Stebich, M., 1999. Bio- and chronostratigraphy of the lateglacial in the Eifel region, Germany. Quaternary International 61 (1), 5–16.

Lovera, O. M., Grove, M., Kimbrough, D. L., Abbott, P. L., 1999. A method for evaluating basement exhumation histories from closure age distributions of detrital minerals. Journal of Geophysical Research 104 (B12), 29419–29438.

Mackay, J., 1981. Active layer slope movement in a continuous permafrost environment, Garry Island, Northwest Territories, Canada. Canadian Journal of Earth Sciences 18, 1666–1680.

Martin, Y., 2000. Modelling hillslope evolution: linear and nonlinear transport relations. Geomorphology.

Martin, Y., Church, M., 1997. Diffusion in landscape development models: on the nature of basic transport relations. Earth Surface Processes and Landforms 22, 273–279.

Martin, Y., Church, M., 2004. Numerical modelling of landscape evolution: geomorphological perspectives. Progress in Physical Geography 28 (3), 317 – 339.

Matsuoka, N., 2001. Solifluction rates, processes and landforms: a global review. Earth-Science Reviews 55 (1-2), 107–134.

Matsuoka, N., 2006. Monitoring periglacial processes: Towards construction of a global network. Geomorphology 80, 20 – 31.

Matsuoka, N., Moriwaki, K., 1992. Frost heave and creep in the Sør Rondane Mountains, Antarctica. Arctic and Alpine Research 24, 271–280.

McKean, J., Dietrich, W., Finkel, R., Southon, J., Caffee, M., 1993. Quantification of soil production and downslope creep rates from cosmogenic 10Be accumulations on a hillslope profile. Geology 21 (4), 343.

Melloh, R., 1999. A synopsis and comparison of selected snowmelt algorithms. Tech. rep., US Army Corps of Engineers, Cold Regions Research & Engineering Laboratory (CCREL report 99-8), Hanover, New Hampshire.

Merritt, W., Letcher, R., Jakeman, A., Oct. 2003. A review of erosion and sediment transport models. Environmental Modelling & Software 18 (8-9), 761–799.

Meyer, H., Hetzel, R., Strauss, H., Nov. 2008. Erosion rates on different timescales derived from cosmogenic 10Be and river loads: implications for landscape evolution in the Rhenish Massif, Germany. International Journal of Earth Sciences 99 (2), 395–412.

Meyer, W., Stets, J., 2002. Pleistocene to recent tectonics in the Rhenish Massif (Germany). Netherlands Journal of Geosciences 81, 217–221.

Miller, J., Germanoski, D., Waltman, K., Tausch, R., 2001. Influence of late Holocene hillslope processes and landforms on modern channel dynamics in upland watersheds of central Nevada. Geomorphology 38, 373–391.

Mol, J., Vandenberghe, J., Kasse, C., 2000. River response to variations of periglacial climate in mid-latitude Europe. Geomorphology 33 (3-4), 131–148.

Molnar, P., May 2004. Late Cenozoic Increase in Accumulation Rates of Terrestial Sediment: How Might Climate Change Have Affected Erosion Rates? Annual Review of Earth and Planetary Sciences 32 (1), 67–89.

Montgomery, D., Dietrich, W., 1994. Landscape dissection and drainage area-slope thresholds. In: Kirkby, M. (Ed.), Process Models and Theoretical Geomorphology. John Wiley, New York, pp. 221–246.

Mudd, S. M., Furbish, D. J., 2005. Lateral migration of hillcrests in response to channel incision in soil-mantled landscapes. Journal of Geophysical Research 110 (F4), 1–18.

Nash, D., 1980. Forms of bluffs degraded for different lengths of time in Emmet County, Michigan, USA. Earth Surface Processes and Landforms 5, 331–345.

Nelson, E., Jones, N., Miller, A., 1994. Algorithm for precise drainage-basin delineation. Journal of Hydraulic Engineering 120, 298–312.

Nemcok, A., Pasek, J., Rybar, J., Oct. 1972. Classification of landslides and other mass movements. Rock Mechanics and Rock Engineering 4 (2), 71–78.

Nishiizumi, K., Kohl, C., Arnold, J., Dorn, R., Klein, J., Fink, D., Middleton, R., Lal, D., 1993. Role of in situ cosmogenic nuclides 10Be and 26Al in the study of diverse geomorphic processes. Earth Surface Processes and Landforms 18, 407– 425.

Ochsner, T., Horton, R., Ren, T., 2001. A new perspective on soil thermal properties. Soil science society of America Journal 65 (6), 1641.

Oksanen, J., Sarjakoski, T., 2005. Error propagation of DEM-based surface derivatives. Computers & Geosciences 31 (8), 1015–1027.

Oksanen, J., Sarjakoski, T., 2006. Uncovering the statistical and spatial characteristics of fine toposcale DEM error. International Journal of Geographical Information Science 20 (4), 345–369.

Ouimet, W. B., Whipple, K. X., Granger, D. E., 2009. Beyond threshold hillslopes: Channel adjustment to base-level fall in tectonically active mountain ranges. Geology 37 (7), 579–582.

Overduin, P., Kane, D., van Loon, W., Jun. 2006. Measuring thermal conductivity in freezing and thawing soil using the soil temperature response to heating. Cold Regions Science and Technology 45 (1), 8–22.

O'Callaghan, J., Mark, D., 1984. The extraction of drainage networks from digital elevation data. Computer Vision, Graphics, and Image Processing 28, 323–344.

Palacios-Velez, O., Cuevas-Renaud, B., 1986. Automated river-course, ridge and basin delineation from digital eleva- tion data. Journal of Hydrology 86, 299–314.

PCNSW, 2007. Projet du Gouvernement wallon (GW VIII / 2007 / Doc.58.12 / 12.07 / B.L & GW VII / 2000 / Doc.1331 / 07.12 / JH.). Tech. rep.

Pelletier, J. D., 2008. Quantitative Modeling of Earth Surface Processes. Cambridge University Press, Cambridge.

Pelletier, J. D., Rasmussen, C., Sep. 2009. Geomorphically based predictive mapping of soil thickness in upland watersheds. Water Resources Research 45 (9), 1–15.

Perron, J. T., Fagherazzi, S., Aug. 2011. The legacy of initial conditions in landscape evolution. Earth Surface Processes and Landforms.

Perron, J. T., Hamon, J. L., 2011. Equilibrium form of retreating hillslopes. Journal of Geophysical Research in review.

Petit, C. C., Lambin, E. F., Jul. 2002. Long-term land-cover changes in the Belgian Ardennes (1775-1929): model-based reconstruction vs. historical maps. Global Change Biology 8 (7), 616–630.

Phillips, J. D., May 2010. The convenient fiction of steady-state soil thickness. Geoderma 156 (3-4), 389–398.

Pissart, A., 1976. Les dépôts et la morphologie périglaciaire de la Belgique. In: Pissart, A. (Ed.), Géomorphologie de la Belgique. Laboratoire de Géologie et de Géographie Physique, Université de Liège, Liège, pp. 115–135.

Pissart, A., 1995. L'Ardenne sous le joug du froid. Le modèle périglaciaire du massif ardennais. In: Demoulin, A. (Ed.), L'Ardenne. Essai de Géographie Physique. Département de Géographie Physique et Quaternaire, Université de Liège, Liège, pp. 136–154.

Pissart, A., Gullentops, F., 1967. Compte rendu de l'excursion du vendredi 10 juin 1966. Liège - Nessonvaux - Louvegné - Theux - Baraque Michel - Stavelot - Grand Halleux - Baraque

Fraiture - La Roche. In: Macar, P. (Ed.), L'évolution des versants. Symposium international de géomorphologie. Union géographique internationale, Liège-Louvain, pp. 307–324.

Poesen, J. W., van Wesemael, B., Bunte, K., Benet, A. S., Jun. 1998. Variation of rock fragment cover and size along semiarid hillslopes: a case-study from southeast Spain. Geomorphology 23 (2-4), 323–335.

Press, W. H., Teukolsky, S. A., Vetterling, W. T., Flannery, B. P., 1992. Numerical Recipes in C: The Art of Scientific Computing. Vol. 1 of ISBN 0-521-43108-5. Cambridge University Press.

Priestley, C., Taylor, R., 1972. On the Assessment of Surface Heat Flux and Evaporation Using Large-Scale Parameters. Monthly Weather Review 100, 81–92.

Prosser, I., Rustomji, P., 2000. Sediment transport capacity relations for overland flow. Progress in Physical Geography 24, 179–193.

Qin, C., Zhu, A. X., Pei, T., Li, B., Zhou, C., Yang, L., 2007. An adaptive approach to selecting a flow-partition exponent for a multiple-flow-direction algorithm. International Journal of Geographical Information Science 21 (4), 453–458.

Quine, T., Walling, D., Chakela, Q., Mandiringana, O., Zhang, X., ., 1999. Rates and patterns of tillage and water erosion on terraces and contour strips: evidence from caesium-137 measurements. Catena 36 (1-2), 115–142.

Quinn, P., Beven, K., Chevallier, P., Planchon, O., 1991. The prediction of hillslope flowpaths for distributed hydrological modeling using digital terrain models. Hydrological Processes 5, 59–80.

Raaflaub, L., Collins, M., 2006. The effect of error in gridded digital elevation models on the estimation of topographic parameters. Environmental Modelling & Software 21 (5), 710–732.

Rawlins, M. a., Lammers, R. B., Frolking, S., Fekete, B. M., Vorosmarty, C. J., Sep. 2003. Simulating pan-Arctic runoff with a macro-scale terrestrial water balance model. Hydrological Processes 17 (13), 2521–2539.

Renard, K., Laflen, J., Foster, G., McCool, D., 1994. The revised universal soil loss equation. In: Lad, R. (Ed.), Soil Erosion: Research Methods. pp. 105–126.

Renssen, H., Isarin, R. F. B., 2001. The two major warming phases of the last deglaciation at ˜14.7 and ˜11.5 kyr cal BP in Europe: climate reconstructions and AGCM experiments. Global and Planetary Change 30, 117–153.

Restrepo, J., Kjerfve, B., Hermelin, M., Jan. 2006. Factors controlling sediment yield in a major South American drainage basin: the Magdalena River, Colombia. Journal of Hydrology 316 (1-4), 213–232.

Richardson, C. W., 1981. Stochastic simulation of daily precipitation, temperature, and solar radiation. Water Resources Research 17, 182–190.

Riebe, C., Kirchner, J., Granger, D., Finkel, R., 2001. Strong tectonic and weak climatic control of long-term chemical weathering rates. Geology 29 (6), 511.

Riebe, C. S., Kirchner, J. W., Finkel, R. C., Aug. 2004. Erosional and climatic effects on long-term chemical weathering rates in granitic landscapes spanning diverse climate regimes. Earth and Planetary Science Letters 224 (3-4), 547–562.

Rixhon, G., Braucher, R., Bourlès, D., Siame, L., Bovy, B., Demoulin, A., Nov. 2010. Quaternary river incision in NE Ardennes (Belgium)–Insights from 10Be/26Al dating of river terraces. Quaternary Geochronology 6 (2), 273–284.

Rixhon, G., Juvigné, E., 2010. Periglacial deposits and correlated processes in the Ninglinspo Valley (Ardenne massif, Belgium). Geologica Belgica 13 (1-2), 49–60.

Rock, N., 1988. Numerical geology: A source guide, glossary, and selective bibliography to geological uses of computers and statistics. Springer-Verlag, Berlin-New-York.

Roering, J., Kirchner, J., Dietrich, W., 1999. Evidence for nonlinear, diffusive sediment transport on hillslopes and implications for landscape morphology. Water Resources Research 35 (3), 853–870.

Roering, J. J., Dec. 2004. Soil creep and convex-upward velocity profiles: theoretical and experimental investigation of disturbance-driven sediment transport on hillslopes. Earth Surface Processes and Landforms 29 (13), 1597–1612.

Roering, J. J., 2008. How well can hillslope evolution models "explain" topography? Simulating soil transport and production with high-resolution topographic data. Geological Society of America Bulletin 120 (9), 1248.

Roering, J. J., Almond, P., Tonkin, P., Mckean, J. A., 2004. Constraining climatic controls on hillslope dynamics using a coupled model for the transport of soil and tracers: Application to loess-mantled hillslopes, South Island, New Zealand. Journal of Geophysical Research 109 (F1), 1–19.

Rohli, R. V., Vega, A. J., 2011. Climatology, 2nd Edition. Jones & Bartlett.

Rosenbloom, N. a., Anderson, R. S., 1994. Hillslope and channel evolution in a marine terraced landscape, Santa Cruz, California. Journal of Geophysical Research 99 (B7), 14013–14029.

Salas, J., 1993. Analysis and modeling of hydrologic time series. In: Maidment, D. (Ed.), Handbook of Hydrology. McGraw Hill, New York, Ch. 19, p. 72.

Sambridge, M., 1999a. Geophysical inversion with a neighbourhood algorithm-I. Searching a parameter space. Geophysical Journal International 138 (3), 479–494.

Sambridge, M., 1999b. Geophysical inversion with a neighbourhood algorithm-II. Appraising the ensemble. Geophysical Journal International 138 (3), 727–746.

Sambridge, M., Braun, J., McQueen, H., 1995. Geophysical parametrization and interpolation of irregular data using natural neighbours. Geophysical Journal International 122 (3), 837–857.

Schaetzl, R. J., Anderson, S., 2005. Soils: genesis and geomorphology. Cambridge University Press, New York.

Schaller, M., Ehlers, T., 2006. Limits to quantifying climate driven changes in denudation rates with cosmogenic radionuclides. Earth and Planetary Science Letters 248 (1-2), 153–167.

Schaller, M., Von Blanckenburg, F., Hovius, N., Kubik, P., 2001. Large-scale erosion rates from in situ-produced cosmogenic nuclides in European river sediments. Earth and Planetary Science Letters 188 (3-4), 441–458.

Schaller, M., von Blanckenburg, F., Hovius, N., Veldkamp, A., VAN DEN, B., Meindert, W., Kubik, P., 2004. Paleoerosion rates from cosmogenic 10Be in a 1.3 Ma terrace sequence: response of the River Meuse to changes in climate and rock uplift. The Journal of geology 112 (2), 127–144.

Schaller, M., Von Blanckenburg, F., Veldkamp, A., Tebbens, L. A., Hovius, N., Kubik, P. W., 2002. A 30 000 yr record of erosion rates from cosmogenic Middle European river terraces 10 Be in river terraces. Earth and Planetary Science Letters 204, 307–320.

Scheidegger, A., 1961. Mathematical models of slope development. Geological Society of America Bulletin 72, 37–50.

Schoorl, J. M., Sonneveld, M. P. W., Veldkamp, A., 2000. Three-dimensional landscape process modelling: the effect of dem resolution. Earth Surface Processes and Landforms 25, 1025–1034.

Schoorl, J. M., Veldkamp, A., Bouma, J., 2002. Modeling Water and Soil Redistribution in a Dynamic Landscape Context. Soil Science Society of America Journal 66, 1610–1619.

Scott, D. W., 1992. Multivariate density estimation: theory, practice, and visualization. John Wiley & Sons, New-York.

Seibert, J., McGlynn, B. L., 2007. A new triangular multiple flow direction algorithm for computing upslope areas from gridded digital elevation models. Water Resources 43, 1–8.

Selby, M., 1993. Hillslope materials and processes, 2nd Edition. Oxford University Press.

Sharma, H., 1982. Perspectives in geomorphology. Concept Publishing Company.

Silverman, B. W., 1986. Density Estimation for Statistics and Data Analysis. In: Chapman, Hall (Eds.), Monographs on Statistics and Applied Probability (26). Vol. 37. London, p. 175.

Singarayer, J. S., Valdes, P. J., Jan. 2010. High-latitude climate sensitivity to ice-sheet forcing over the last 120kyr. Quaternary Science Reviews 29 (1-2), 43–55.

Singh, P., Kumar, N., Arora, M., 2000. Degree-day factors for snow and ice for the Dokriani Glacier, Garhwal Himalayas. Journal of Hydrology 235, 1–11.

Sircombe, K., Hazelton, M., Oct. 2004. Comparison of detrital zircon age distributions by kernel functional estimation. Sedimentary Geology 171 (1-4), 91–111.

Sklar, L. S., Dietrich, W. E., 2006. The role of sediment in controlling steady-state bedrock channel slope: Implications of the saltation–abrasion incision model. Geomorphology 82, 58 – 83.

Small, E., Anderson, R., Hancock, G., 1999. Estimates of the rate of regolith production using 10Be and 26Al from an alpine hillslope. Geomorphology 27, 131–150.

Smith, D., 1988. Rates and controls of soil movement on a solifluction slope in the Mount Rae area, Canadian Rocky Mountains. Zeitschrift für Geomorphologie N.F. Suppl 71, 25–44.

Smith, D., 1996. Cold regions utilities monograph, 3rd Edition. Technical Council on Cold Regions Engineering, Canadian Society for Civil Engineering. Cold Regions Engineering Division. ASCE Publications.

Snyder, N. P., Whipple, K. X., Tucker, G. E., Merritts, D. J., 2003. Channel response to tectonic forcing: field analysis of stream morphology and hydrology in the Mendocino triple junction region, northern California. Geomorphology 53, 97–127.

Sougnez, N., Vanacker, V., Apr. 2011. The topographic signature of Quaternary tectonic uplift in the Ardennes massif (Western Europe). Hydrology and Earth System Sciences 15 (4), 1095–1107.

Stähli, M., Nyberg, L., Mellander, P.-E., Jansson, P.-E., Bishop, K. H., Apr. 2001. Soil frost effects on soil water and runoff dynamics along a boreal transect: 2. Simulations. Hydrological Processes 15 (6), 927–941.

Stallard, R., 1998. Terrestrial sedimentation and the carbon cycle: Coupling weathering and erosion to carbon burial. Global Biogeochemical Cycles 12, 231–252.

Stark, C. P., Feb. 2010. Oscillatory motion of drainage divides. Geophysical Research Letters 37 (4), 1–5.

Tarboton, D., 1997. A new method for the determination of flow directions and upslope areas in grid digital elevation models. Water Resources Research 33 (2), 309 –319.

Thornthwaite, C., Mather, J., 1955. The water balance. Centerton, NJ: Drexel Institute of Technology - Laboratory of Climatology (Publications in Climatology, vol. VIII, n.1).

Thornthwaite, C., Mather, J., 1957. Instructions and tables for computing potential evapotranspiration and the water balance. Centerton, NJ: Drexel Institute of Technology - Laboratory of Climatology (Publications in Climatology, vol. X, n.3).

Trauth, M., Bookhagen, B., 2003. Late pleistocene climate change and erosion in the Santa Maria basin, NW Argentina. Journal of sedimentary 73, 82–90.

Tucker, G., Slingerland, R., 1996. Predicting sediment flux from fold and thrust belts. Basin Research 8, 329–349.

Tucker, G. E., 2009a. Natural experiments in landscape evolution. Earth Surface Processes and Landforms 34 (10), 1450–1460.

Tucker, G. E., 2009b. Natural experiments in landscape evolution. Earth Surface Processes and Landforms 34 (10), 1450–1460.

Tucker, G. E., Bradley, D. N., Mar. 2010. Trouble with diffusion: Reassessing hillslope erosion laws with a particle-based model. Journal of Geophysical Research 115, 1–12.

Tucker, G. E., Bras, R. L., 1998. Hillslope processes, drainage density, and landscape morphology. Water Resources Reasearch 34 (10), 2751–2764.

Tucker, G. E., Bras, R. L., 2000. A stochastic approach to modeling the role of rainfall variability in drainage basin evolution. Water Resources Research 36 (7), 1953–1964.

Tucker, G. E., Hancock, G., 2010. Modelling landscape evolution. Earth Surface Processes and Landforms 35 (1), 28–50.

Tucker, G. E., Lancaster, S. T., Gasparini, N. M., Bras, R. L., Rybarczyk, S. M., 2001a. An object-oriented framework for distributed hydrologic and geomorphic modeling using triangulated irregular networks. Computers & Geosciences 27, 959–973.

Tucker, G. E., Lancaster, S. T., Gasparini, N. M., L, R., 2001b. The channel-hillslope integrated landscape development (CHILD) model. In: Harmon, R. S., Doe, W. (Eds.), Landscape Erosion and Evolution Modeling, iii Edition. Kluwer Academic/Plenum, New York, Ch. 12, pp. 349–388.

Tucker, G. E., McCoy, S. W., Whittaker, A. C., Roberts, G. P., Lancaster, S. T., Phillips, R., Mar. 2011. Geomorphic significance of postglacial bedrock scarps on normal-fault footwalls. Journal of Geophysical Research 116 (F1), 1–14.

Tucker, G. E., Slingerland, R. L., 1997. Drainage basin responses to climate change. Water Resources Reasearch 33 (8), 2031–2047.

Turcotte, D., Schubert, G., 2002. Geodynamics, 2nd Edition. Cambridge University Press, New-York.

Turowski, J., Rickenmann, D., 2009. Tools and cover effects in bedload transport observations in the Pitzbach, Austria. Earth Surface Processes and Landforms 34 (1), 26–37.

Valla, P. G., Herman, F., van der Beek, P. a., Braun, J., Jul. 2010a. Inversion of thermochronological age-elevation profiles to extract independent estimates of denudation and relief history — I: Theory and conceptual model. Earth and Planetary Science Letters 295 (3-4), 511–522.

Valla, P. G., van der Beek, P. a., Lague, D., May 2010b. Fluvial incision into bedrock: Insights from morphometric analysis and numerical modeling of gorges incising glacial hanging valleys (Western Alps, France). Journal of Geophysical Research 115 (F2), 1–25.

Van Balen, R., Houtgast, R., Van der Wateren, F., Vandenberghe, J., Bogaart, P., 2000. Sediment budget and tectonic evolution of the Meuse catchment in the Ardennes and the Roer Valley Rift System. Global and planetary change 27 (1-4), 113–129.

Van den Berg, M., 1996. Fluvial sequences of the Maas, a 10 Ma record of neotectonics and climate change at various timescales. Ph.D. thesis, University of Wageningen.

Van Den Eeckhaut, M., Poesen, J., Verstraeten, G., Vanacker, V., Moeyersons, J., Nyssen, J., Vanbeek, L., Apr. 2005. The effectiveness of hillshade maps and expert knowledge in mapping old deep-seated landslides. Geomorphology 67 (3-4), 351–363.

Van der Zwan, C., 2002. The impact of Milankovitch-scale climatic forcing on sediment supply. Sedimentary Geology 147, 271 – 294.

Vanandel, T., Jan. 2002. The Climate and Landscape of the Middle Part of the Weichselian Glaciation in Europe: The Stage 3 Project. Quaternary Research 57 (1), 2–8.

Vandenberghe, J., 2008. The fluvial cycle at cold–warm–cold transitions in lowland regions: A refinement of theory. Geomorphology 98 (3-4), 275–284.

Vandenberghe, J., Lowe, J., Coope, R., Litt, T., Zöller, L., 2004. Climatic and environmental variability in the mid-latitude Europe sector during the Last Interglacial-Glacial Cycle. In: Battarbee, R. W., Gasse, F., Stickley, C. E. (Eds.), Past Climate Variability trough Europe and Africa. Springer, Dordrecht, The Netherlands, Ch. 19, pp. 393–416.

Vandenberghe, J., Pissart, A., 1993. Permafrost changes in Europe during the last glacial. Permafrost and Periglacial Processes 4, 121–135.

Veron, P., Bah, B. B., Bracke, C., Lejeune, P., Rondeux, J., Bock, L., Mokadem, A. I., 2005. The digital soil map of wallonia (DSMW/CNSW). In: XXII International Cartographic Conference (ICC2005), A Coruña, Spain. p. 8.

Voronoi, G., 1908. Nouvelles applications des paramètres continus à la théorie de formes quadratiques. Journal für die reine und angewandte Mathematik 134, 198–287.

Wanner, H., Beer, J., Bütikofer, J., Crowley, T. J., Cubasch, U., Flückiger, J., Goosse, H., Grosjean, M., Joos, F., Kaplan, J. O., Küttel, M., Müller, S. a., Prentice, I. C., Solomina, O., Stocker, T. F., Tarasov, P., Wagner, M., Widmann, M., Oct. 2008. Mid- to Late Holocene climate change: an overview. Quaternary Science Reviews 27 (19-20), 1791–1828.

Washburn, A., 1967. Instrumental observations of mass-wasting in the Mesters Vig district, Northeast Greenland. , 318 pp. Meddelelser. Groenland 166 (4), 292.

Washburn, A., 1979. Geocryology: A Survey of Periglacial Processes and Environments. Edward Arnold, London.

Watts, W., Allen, J., Huntley, B., 1996. Vegetation history and palaeoclimate of the last glacial period at Lago Grande di Monticchio, southern Italy. Quaternary Science Reviews 15 (2-3), 133–153.

Wechsler, S., 2007. Uncertainties associated with digital elevation models for hydrologic applications: a review. Hydrology and Earth System Sciences 11 (4), 1481–1500.

Whipple, K., Tucker, G., 1999. Dynamics of the stream-power river incision model: Implications for height limits of mountain ranges, landscape response timescales, and research needs. Journal of Geophysical Research 104 (B8), 17661–17.

Whipple, K., Tucker, G. E., 2002. Implications of sediment-flux-dependent river incision models for landscape evolution. Journal of Geophysical Research 107 (2039), 10–1029.

White, A., Blum, A., 1995. Effects of climate on chemical weathering in watersheds. Geochimica et Cosmochimica Acta 59, 1729– 1747.

Wilkinson, M., Humphreys, G., 2005. Exploring pedogenesis via nuclide-based soil production rates and OSL-based bioturbation rates. Australian Journal of Soil Research 43 (6), 767–779.

Wilkinson, M. T., Chappell, J., Humphreys, G. S., Fifield, K., Smith, B., Hesse, P., Aug. 2005. Soil production in heath and forest, Blue Mountains, Australia: influence of lithology and palaeoclimate. Earth Surface Processes and Landforms 30 (8), 923–934.

Willenbring, J. K., von Blanckenburg, F., May 2010. Long-term stability of global erosion rates and weathering during late-Cenozoic cooling. Nature 465 (7295), 211–4.

Willett, S. D., 2010. Late Neogene Erosion of the Alps: A Climate Driver? Annual Review of Earth and Planetary Sciences (February), 409–435.

Willgoose, G., 2005. Mathematical Modeling of Whole Landscape Evolution. Annual Review of Earth and Planetary Sciences 33 (1), 443–459.

Willgoose, G., Bras, R. L., Rodriguez-Iturbe, I., 1991. A Coupled Channel Network Growth and Hillslope Evolution Model 1. Theory. Water Resources Research 27 (7), 1671–1684.

Wu, J., Nofziger, D. L., 1999. Incorporating Temperature Effects on Pesticide Degradation into a Management Model. Journal of Environmental Quality 28 (1), 92–100.

Yair, A., 1990. The role of topography and surface cover upon soil formation along hillslopes in arid climates. Geomorphology 3 (3-4), 287–299.

Zhang, P., Molnar, P., Downs, W. R., Apr. 2001. Increased sedimentation rates and grain sizes 2-4 Myr ago due to the influence of climate change on erosion rates. Nature 410 (6831), 891–7.